Nearby Spiral Galaxies at Low Frequencies

Dissertation
zur
Erlangung des Doktorgrades (Dr. rer. nat.)
der
Mathematisch-Naturwissenschaftlichen Fakultät
der
Rheinischen Friedrich-Wilhelms-Universität Bonn

von
David D. Mulcahy
aus
Cork,Irland

Bonn, 13.01.2014

Dieser Forschungsbericht wurde als Dissertation von der Mathematisch-Naturwissenschaftlichen Fakultät der Universität Bonn angenommen und ist auf dem Hochschulschriftenserver der ULB Bonn http://hss.ulb.uni-bonn.de/diss_online elektronisch publiziert.

1. Gutachter:	Prof. Dr. Ulrich Klein
2. Gutachter:	Prof. Dr. Michael Kramer
Tag der Promotion:	07.07.2014
Erscheinungsjahr:	2015

Abstract

The low frequency regime (less that 300 MHz) of radio astronomy, while been its birthplace, has been neglected in the past several decades due to the challenges of calibration. External galaxies have hardly been observed at these frequencies with several exceptions. Such observations always suffered from poor angular resolution and therefore accurate flux measurements were nearly impossible. In addition virtually no research in polarization has been performed at these frequencies due to various physical and instrumental depolarization processes. Observing external galaxies at low frequencies would enable us to study the propagation of low energy electrons and in turn weak magnetic fields.

Thankfully, a revival in low frequency radio astronomy is now in full force with interferometers such as the GMRT being constructed. This is especially so with the construction of the Low Frequency Array (LOFAR) which officially opened in 2012. This thesis took place during the commissioning phase of LOFAR and therefore contains many technical commissioning tasks mainly addressing the calibration of LOFAR data which were essential for the wider community. This includes developing software to interpolate gain solutions in frequency, enabling more bandwidth on the observational target and thus increasing sensitivity.

This thesis presents the first arcsecond observations of nearby galaxies at low frequencies with LOFAR. We mapped the face-on interacting galaxy M51 and the edge-on galaxy NGC891 to study the propagation of low energy cosmic ray electrons especially in the extended disk and halo. We also employ the novel method of RM synthesis to search for linear polarization in these galaxies and their surrounding fields for polarized background sources.

In M51 we observe no break in the integrated spectrum but there are signs of thermal absorption in center of the galaxy. We observe a radial break of the radio continuum emission beyond M51's star forming disk, demonstrating that detecting the extended disk in radio contiuum will still be difficult even at low frequencies.

We have created a program to model the cosmic ray electron distribution for M51 and we find that a diffusion coefficent of approximately 7.5×10^{28} cm^2 s^{-1} is needed to describe the radial spectral index of M51. From these models we can also determine the thermal fraction in the center of M51 and spiral arms at 151 MHz. We also see that the magnetic field in the outer disk obtained from observations are underestimated due to assumptions made using equipartition. Through this observation and model we conclude that diffusion is the dominate process in the cosmic ray electron propagation in M51. The observed frequency dependence of radial scalelengths and the radio-infrared correlation of M51 both confirm our diffusion model.

In M51 and NGC891, no diffuse linear polarization was detected showing that detecting diffuse polarization in star forming galaxies at low frequencies will be impossible at current sensitivities. In the M51 field, we detect six polarized extragalactic sources, resulting in a polarization detection for every 2.9 square degrees, making previous plans of using RM grids of background polarized sources to probe the weak magnetic fields of nearby galaxies quite unrealistic.

We confirm the spectral break in NGC891 seen in previous studies and we observe significant signs of thermal absorption within the disk of NGC891. We argue that increased thermal absorption by classical HII regions due to the path length and hence inclination causes the flatting of the integrated spectral index at low frequencies. Also it is found that a low temperature ionized gas component as proposed by Israel & Mahoney (1990) is not needed to explain the thermal absorption. We detect the supernova SN1986J at 146 MHz with a peak flux of 8.8 mJy. We observe significant outflows in the halo via the spectral index map and also observe a new feature not seen in higher frequencies, possibly created via increased star formation in the disk. We see that the bulk velocity of the galactic wind speed is relatively constant for only one half of the galaxy making NGC891 different from NGC253.

New observations of the nearly face on galaxy NGC628 were also taken with the Effelsberg 100m telescope and the Jansky Very Large Array in order to detect rotation measure gradients signifying outflows from the disk to the halo of the galaxy. Preliminary results do detect such RM gradients and reversals.

Finally this thesis also contains work done on the calibration and processing of the MSSS (Multi Frequency Snapshot Survey) survey for which linear polarization was detected, thus opening up the first low frequency polarization survey of the entire northern sky.

Acknowledgements

Now that I'm approaching the end of this work that is my doctoral thesis, I need to acknowledge all those who were with me ever step of the way. Completing a thesis consisting of LOFAR data is a small miracle and without the help of many people it would have never happened.

First of all I want to thank my supervisor Dr. Rainer Beck. It was a honor and a pleasure to have a supervisor who was so patient and willing to help. His love and deep knowledge for all things magnetic fields was a great inspiration. His excitement when a new result would pop it's head gave me the energy to keep pushing forward. His constant words of encouragement were so important to me especially in a project like this with its many disappointments.

Many thanks must go to Prof. Dr. Uli Klein who's deep knowledge in many areas especially in radio astronomy were a great inspiration. I always loved listening to your stories of the early days of your career as well as your talks and lectures of radio astronomy and magnetic fields. Thank you for giving me the chance for being part of a such great and professional research group.

Thanks to Prof. Dr. Michael Kramer for supporting me for the final six months of this thesis and for letting me be a part of your fantastic group. Also for being so friendly and approachable whenever I had a problem, even with your busy schedule.

To the entire Fundamental of Physics group, it was a great experience and pleasure to work with such a professional and diverse group. Many thanks to you all.

Thanks must go to Gabi Breuer who sadly passed away during this thesis. You were always so pleasant to me and always looked after my needs even when you were so busy with everyone else. You will be sorely missed.

Thanks to Dr. Andrew Fletcher from Newcastle University, for hosting me in Newcastle for the months of September and October 2013. Thank you for giving me to chance to develop our CRE code. Without your knowledge and expertise, it would have never have happened. I look forward to working with you in the future.

Many thanks must go to Dr. Andreas Horneffer who helped me so much with the calibration of the LOFAR data and without your help this thesis would have been impossible.

Thanks to Dr. George Heald of ASTRON for all his help and practical advice when it came to radio astronomy. Having a chat about things with you always made a trip to ASTRON worthwhile. Many thanks to ASTRON Science Support especially Dr. Roberto Pizzo and Dr. Emanuela Orru for being so quick in resolving problems. Thanks to Dr. Rodian Stepanov & Dr. Peter Frick for their help and advice concerning the wavelet analysis of M51.

Thanks to all members of the LOFAR Magnetism Key Science Project especially Dr. Cathy Horellou for her interest on this project and critical comments and Dr. Anna Scaife for letting me become a part of her group in the future and of course for being so friendly.

Thanks to all the students of the 'dungeon' EK0.9, past & present especially Dr. Rene Gießübel for always being there to answer PYTHON questions, Jana Kohler & Charlotte Sobey for understanding the

pain of LOFAR data reduction, Ancor Damas, Philip Schmidt & Carolina Mora. Thanks to Dr. Bjorn Adebahr for all interesting discussions on interferometry calibration and for the Sharknado night. It was awesome! Thanks to everyone of the DFG Research Unit 1254, for the cooperation and encouragement at our yearly conferences. Thanks to Elizabeth Kramer for being so helpful with any problems I had and for the organization of all the DFG conferences. Thanks to Dr. Nadya Ben Bekhti for being awesome! I'm sorry I killed your plant. I will miss you but we will always have our memories of Hamburg. Thanks to Dr. Rick Perley for making me so welcome in Soccoro and for the fantastic interferometry tutorial and trip of the VLA. Thanks to Jeremy, Tessa, Andra, Phil, Kristina, Jeff, Philip and Hana for making my trip in New Mexico awesome!

Thank you to my family who I miss everyday, especially to my parents, Declan and Deirdre, for always supporting me in everything I do. Words cannot express my gratitude for all that you have done for me through all the years that have gone by. For my mother Mary, even though you are not here, I hope you are proud of me wherever you are.

Finally I want to thank the love of my life, my darling wife, Sawa. You have have been a source of constant support through these three and a half years and the thought of spending the rest of my life fills me with much excitement and happiness. We did it!

This research was performed in the framework of the DFG Forschergruppe 1254 "Magnetization of Interstellar and Intergalactic Media: The Prospects of Low-Frequency Radio Observations". LOFAR, designed and constructed by ASTRON, has facilities in several countries, that are owned by various parties (each with their own funding sources), and that are collectively operated by the International LOFAR Telescope (ILT) foundation under a joint scientific policy. The JVLA is operated by the National Radio Astronomy Observatory which is a facility of the National Science Foundation operated under cooperative agreement by Associated Universities, Inc. This thesis contains observations with the 100-m telescope of the MPIfR (Max-Planck-Institut für Radioastronomie) at Effelsberg.

Contents

CHAPTER 1

The science of low frequency radio astronomy

1.1 Introduction

Magnetic fields are ubiquitous in the Universe and are an essential part in understanding it. They have been studied extensively at all scales, from solar to galaxy cluster magnetic fields. But many questions still exist such as the origin and amplification of magnetic fields. The role of magnetic fields is probably crucial to explain galactic evolution. The absence of these fields strongly inhibit star formation as it is essential to transport angular momentum outwards during cloud collapse.

While magnetic fields cannot have dynamical significance on large scales, they can play their role on smaller, local scales, especially in star-forming regions.

Another very important role of magnetic fields is the cosmic ray propagation and their containment within galaxies. Low frequency observations (< 200 MHz) are essential to detect the radio emission in galactic gaseous features at the distance of tens of kpc from the star-forming disk, like the extended gaseous halos and disks. Using these observations, it would be possible to learn more about the nature of the magnetic field and cosmic ray propagation at the furthest reaches of galaxies. This is the scientific motivation of this thesis.

In this chapter, the history and motivation of low frequency radio astronomy will be presented. The important physical emission and absorption processes will be presented and explained. What is known about nearby galaxies at low frequencies will be shown. Finally, the polarization properties of galaxies at low frequencies and methods to detect polarization will be discussed.

1.2 A brief history of low frequency radio astronomy

The beginnings of low frequency radio astronomy date back to the 1930s when Bell Labs tasked Karl Jansky to investigate the source of radio frequency interference (RFI) disrupting early transatlantic wireless communication. With his broad-side array tuned to a frequency of approximately 20 MHz, he found that this 'RFI' was actually extraterrestrial in origin. For the next ten years, Grote Weber continued this work alone experimenting at various frequencies such as 160 MHz where he observed non thermal emission from the Milky Way. Thanks to an injection of innovated technology from the Second World War (such as radar), radio astronomy really started to take off. Large synthesized telescopes like the Cambridge interferometer which discovered pulsars and produced the 2C & 3C catalogues, were the first to use the then new technique of aperture synthesis and could produce 16 independent beams separated in

declination.

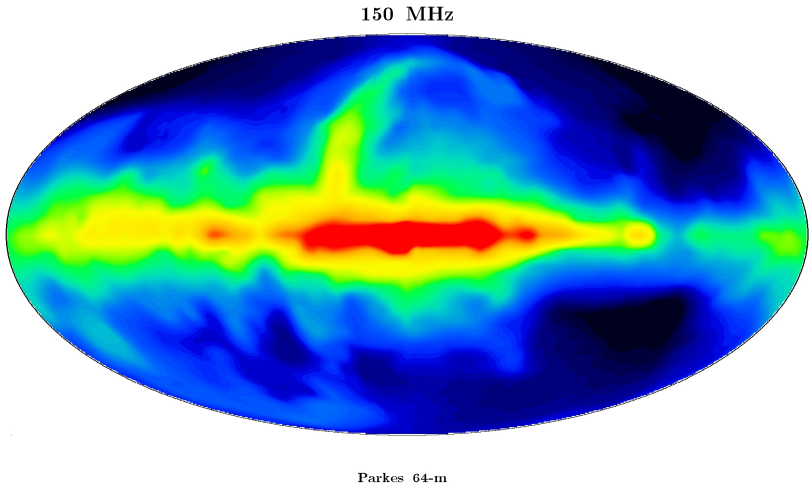

Figure 1.1: An all sky image at a frequency of 150 MHz observed with the Parkes telescope with the northern sky observed by the Cambridge radio interferometer. From Landecker & Wielebinski, 1970 [1].

However, due to the need of higher angular resolution along with the problems of Radio Frequency Interference (RFI) and the difficulties of calibration due to the turbulent ionosphere, most large radio telescopes were built for higher frequencies (above 1 GHz) especially after the discovery of the HI line at 1.4 GHz. Naturally due to these demands, parabolic dishes led the way in radio astronomy at cm, mm and sub-mm wavelengths.

However, several telescopes were built in Clark Lake which defied this trend, most well known is the TPT telescope (Erickson et al. 1982)[2] operating at 57.5 MHz. Even though it was an pioneering instrument in its time, the TPT was dismantled in the early 1990s. Following the TPT, NRAO implemented the 74 MHz system at the VLA in the early 1990s (Kassim et al. 2007) [3]. It was seen early on with a 8-antenna system that self-calibration could remove ionospheric effects on baselines < 35km. The 74 MHz system at the VLA became a real pathfinder and showed that low frequency radio astronomy is not only possible but can produce interesting scientific data.

The VLA Low-Frequency Sky Survey (VLSS) (Cohen et al. 2007) [4] showed that it is possible to create low frequency sky survey at a reasonable resolution ($80''$) and rms noise (median rms noise level being at 0.1 Jy beam^{-1} at a frequency of 74 MHz. With a source count of 70,000 sources, this survey is invaluable for the calibration of LOFAR as will be seen in future chapters. Even more recently, the VLSS data has been re-reduced (VLSSr) (Lane et al. 2012) [5] with improved RFI mitigation techniques and calibration algorithms, thereby increasing the source count by 35 %. However, due to the uv-coverage used for these surveys, extended objects like galaxies, are not fully detected.

The Giant Meterwave Radio Telescope (GMRT) near Pune, India has also enabled astronomers to observe at MHz frequencies since the 1990's, with several receivers at 153, 233, 327, 610 and 1420 MHz.

This brings us to the present, where low frequency astronomy is finally achieving the resolution and low noise of GHz observations.

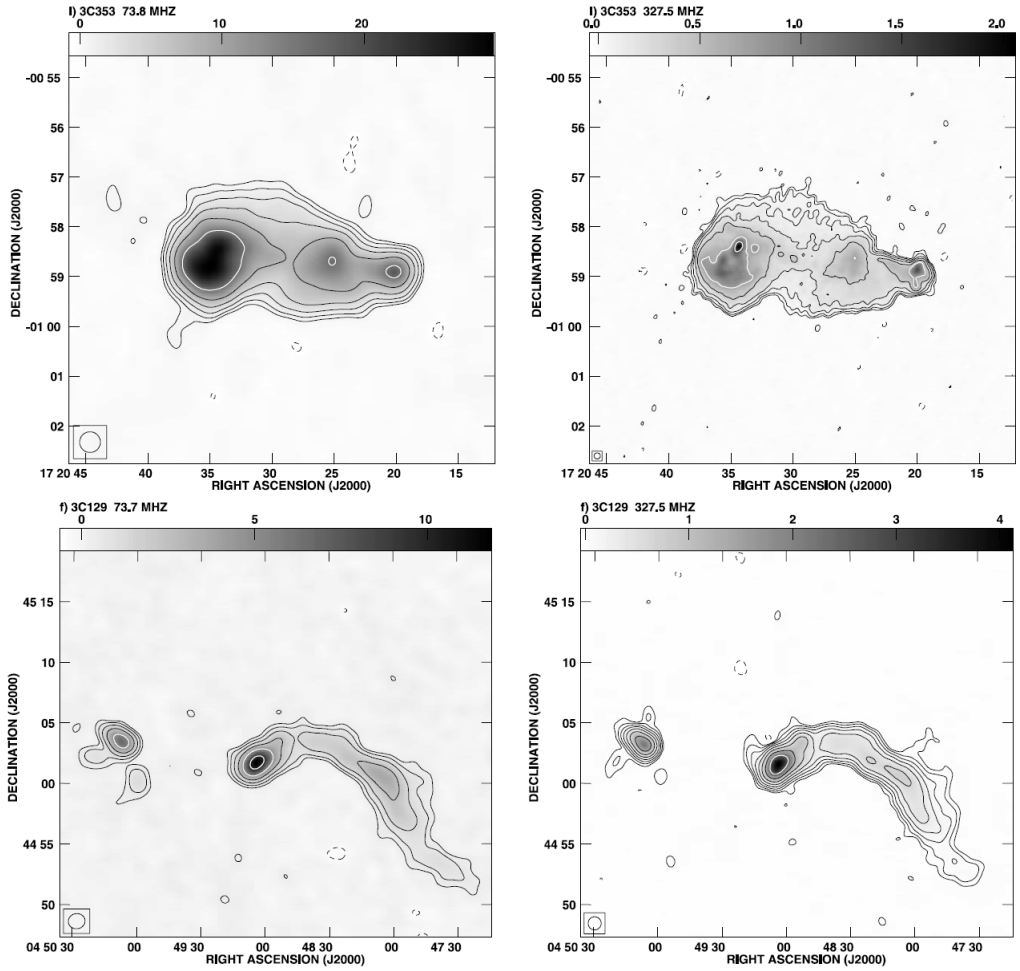

Figure 1.2: Comparing source morphology of 3C353 (top) and 3C129 (bottom) at 74 and 327.5 MHz with the VLA. From Kassim et al. (2007) [3].

1.3 Motivation for observing at low frequencies

In astronomical terms, observing at low frequencies has several advantages. The low frequency radio radiation coming from our own Galaxy or external galaxies is primarily from synchrotron emission produced by cosmic ray electrons gyrating around the magnetic field lines. There is only a small contribution from thermal emission. The power-law nature with a negative spectral index means that the intensity of synchrotron emission increases at lower frequencies, enhancing our ability to trace the component of the total field in the sky plane. To illustrate this point, in present day telescopes operating at frequencies from 1-10 GHz, synchrotron emission from electrons can be detected in a 5 μG magnetic field in external galaxies. The minimum detectable field strength varies with $\nu^{(\alpha/(\alpha+3)}$ (where α is the synchrotron spectral index $\alpha \approx 0.8$) and assuming everything else is equal, one would expect at frequencies ten times lower, to be able to detect magnetic fields two times weaker.

Synchrotron emission at these low frequencies emit from aging, low-energy electrons which suffer less from energy losses and therefore can propagate further from their site of origin into regions of lower magnetic field strength. The observable extent of radio emitters is limited by the diffusion speed if the

cosmic ray electrons (CREs) away from the sources of origin (i.e supernovas) and by the extent of the magnetic field. Therefore, one would expect to detect emission from the outer disk or haloes of galaxies and therefore weak magnetic fields, which would otherwise be invisible at higher frequencies. Galaxies are expected to be much larger than their optical sizes when observed at low radio frequencies.

An important technical advantage of low frequency radio astronomy is the fact that at long wavelengths λ, the large field of view Ω covered by an antenna of diameter d is:

$$\Omega \approx (\frac{\lambda}{d})^2 \tag{1.1}$$

Taking for example the 74 MHz VLA Low-frequency Sky Survey (VLSS) (Kassim et al. 2003) [6], the primary beamwidth of the 25 m VLA antennas are ≈ 0.2 rad FWHM, and only 523 partially overlapping fields are needed to cover the 9.4 sr of the sky north of declination of -30 degrees in comparison to the 1400 MHz NVSS survey (Condon et al. 1998) [7], needed 2×10^5 fields to cover the sky above -40 degrees in declination.

Finally, low frequencies also enhances our ability to detect the magnetic field component along the line of sight due to the wavelength squared dependency of Faraday rotation.

In the following sections, we shall explore the wide range of astrophysics which can be explored at the low frequencies that LOFAR will open up to us.

1.3.1 Epoch of Reionization

One of the central tasks of the new generation of low frequency arrays such as LOFAR and the MWA (Murchison Widefield Array) (Tingay et al. 2013) [8] is the search for the highly redshifted ($6 < z < 12$) neutral hydrogen emission from the Epoch of Reionization aka EoR. EoR is the period of when the first stars formed and initially the intergalactic medium is mostly neutral except in regions surrounding the first objects. But as the reionization progressed, an evolving patch work of neutral and ionized hydrogen formed. After a sufficient number of UV-radiation emitting objects formed, the temperature and ionized fraction of the gas in the Universe increased rapidly until eventually the ionized regions permeate to fill the whole Universe. Prior to EoR, the formation and evolution of the structure was dominated by dark matter alone, while baryonic matter played a marginal role (Zaroubi et al. 2012) [9].

However, many details need to be clarified, for example what controlled the formation of the first objects and how much ionizing radiation they produced or how the ionization bubbles expanded into the intergalactic medium and what did they ionize first?

LOFAR's frequency range will be able to observe a wide range of redshifts from z = 11.4 (115 MHz) to z = 6 (200 MHz). LOFAR EoR Key Science Project will observe a number of fields including the region around 3C196 and the North Celestial Pole with minimal Galactic foreground emission for a total of several thousands of hours.

1.3.2 Pulsars

Most studies of pulsars have been performed at the frequency range of 300 - 2000 MHz, where most pulsars are intrinsically brightest in this frequency. The main reasons are the dispersion and scattering from the interstellar medium, the effective background sky temperature and the ionosphere (Stappers et al. 2011) [10]. Above 2000 MHz pulsars are dim and hard to observe.

Observing pulsars at low frequencies is where propagation effects in the pulsar magnetosphere are expected to be the largest. Also LOFAR would be very sensitive to milli second pulsars (MSPs) and as they are generally much older than other neutron stars and have more time to leave their birthplace

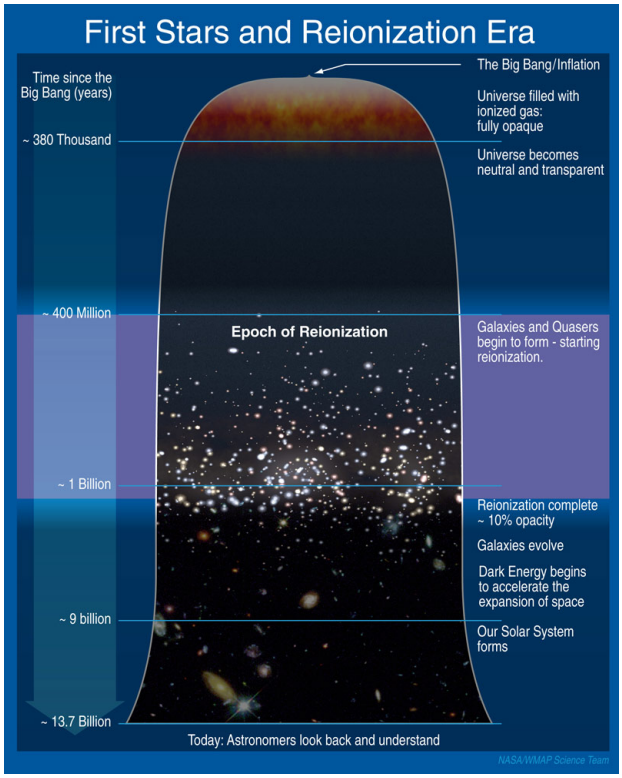

Figure 1.3: Diagram showing the timeline of the Universe, showing the Epoch of Reionization's place in cosmic history. Courtesy of WMAP Science Team (NASA).

in Galactic plane. In addition these MSPs will be much brighter with the flux density of some MSPs remaining steep down to 30 MHz (Kuzmin & Losovsky, 2001)[11], (Kramer et al. 1999) [12].

Pulsars can also be of vital importance in detecting and mapping out the magnetic field of the Milky Way (Noutsos 2012) [13]. Polarization has been observed for hundreds of pulsars which have been used to determine large scale features of the Galactic magnetic field. With the newly detected pulsars from LOFAR, it is hoped that the number of polarized pulsars used to chart the Galactic magnetic field will double. As many of the newly detected pulsars are expected to be located away from the Galactic plane, there will be a chance to probe the magnetic fields of these relatively unexplored regions such as the Galactic halo.

1.3.3 Radio recombination lines

Radio Recombination lines (RRLs) originate from different ionized elements in the ISM. RRLs are often weak but have an advantage over other tracers of ionized gas in that extinction due to dust and contamination from other sources are negligible. High frequency observations mainly detect hydrogen RRL emission, however fainter carbon RRLs dominate at frequencies of $\lesssim$ 300 MHz. There has been very few surveys to observe hydrogen and carbon RRLs and the poor angular resolution not only prevents the location of the line emitting gas to be found but also makes it more difficult to detect RRLs due to beam dilution.

Thankfully, now due to LOFAR's high spectral and angular resolution, carbon RRLs have been detected at frequencies from 40-50 MHz. This is the first time that spectra have been extracted from the

brightest hotspot in Cassiopeia-A at frequencies lower that 330 MHz (Asgekar et al. 2013) [14].

1.3.4 Transients

Incoherent synchrotron emission arises from the acceleration of relativistic electrons in a magnetic field, in the context of transients this includes all types of jets, nova and supernova explosions. These events tend to evolve slowly and especially at low frequencies where the optical depth is higher (Fender et al. 2011) [15]. With LOFAR, one would not expect to see variability on time scales shorter than 1-10 seconds. Coherent synchrotron emitters such as pulsars and masers on the other hand have much higher brightness temperature which means the variability time scales are much shorter.

Transient searches will benefit from low frequency observations especially with LOFAR due to its wide field of view, omni-directional antennae, high speed data transport and computing power.

Other transient phenomena that LOFAR could detect may be associated with black hole emissions, flares,radio bursts from exoplanets or even SETI signals.

1.4 Synchrotron emission

Synchrotron radiation is the main diagnostic tool to trace the extent and morphology of magnetic fields in the ISM. Relativistic electrons gyrating in a magnetic field emit synchrotron radiation in the radio regime. The following sections follow closely Longair (2010) [16] and the lecture notes of Prof. Uli Klein. [1]

We shall first consider the case of a single particle (of mass m, energy $E = \gamma mc^2$, and charge e) moving with velocity $\vec{v}$ in a uniform magnetic field of strength B . The equation of motion is

$$\frac{d}{dt}(\gamma m\vec{v}) = e(\vec{v} \times \vec{B}) \tag{1.2}$$

$\vec{v}$ can be projected into components $\vec{v}_{\parallel}$ which is parallel to $\vec{B}$ and $\vec{v}_{\perp}$ which is perpendicular to $\vec{B}$. The pitch angle α of the particle's trajectory is given by

$$\tan\alpha = \frac{\mid \vec{v}_{\perp} \mid}{\mid \vec{v}_{\parallel} \mid} \tag{1.3}$$

This is the angle between the vectors $\vec{v}$ and $\vec{B}$. It is found that

$$\frac{d\vec{v}_{\parallel}}{dt} = 0 \tag{1.4}$$

and

$$\frac{d\vec{v}_{\perp}}{dt} = \frac{e}{\gamma m}(\vec{v}_{\perp} \times \vec{B}) \tag{1.5}$$

The particle´s trajectory forms a spiral or a helix which is centered on the magnetic field line with a radius a and at a constant pitch angle α, due to the $\vec{v} \times \vec{B}$ force, with a constant orbital velocity $v_{\perp} =\mid \vec{v} \mid$. The angular frequency of the particle in its orbit ω_g is known as the angular cyclotron or angular gyrofrequency and is given by

[1] These notes are available at http://www.astro.uni-bonn.de/ uklein/teaching/B_Fields/MagneticFields.pdf

$$\omega_g = \frac{eB}{\gamma m_0} \tag{1.6}$$

From equation 1.5 we see that the electron is accelerating in its trajectory and since the electron is accelerating, it will radiate.

Now the electron will be accelerated to relativistic speeds and it is found that one important feature of the radiation of relativistic particles is the fact that it is beamed in the direction of motion of the particle. The relativistic motion causes the normal $\sin^2$ dipole radiation pattern that is emitted in the rest frame of the particle to be a strongly Lorentz-transformed beamed pattern in the observer's frame. The way this pattern transforms is governed by the following abberation formula:

$$\sin\phi = \frac{\sin\phi'}{\gamma(1+\beta\cos\phi')} \tag{1.7}$$

$$\cos\phi = \frac{\cos\phi' + \beta}{1+\beta\cos\phi'} \tag{1.8}$$

where a prime ($'$) indicates the particle´s rest frame. If we consider the angle $\phi' = \frac{\pi}{2}$, where there is zero power emitted and so in the lab frame we have $\sin\phi = 1/\gamma$. Therefore all the forward power is radiated in a beam of $2/\gamma$

The emission can be expressed in terms of components in two polarizations: perpendicular and parallel to the projected direction of the magnetic field. Longair (2010) [16] gives a complete derivation of these two components, but here I will just give the final result.

$$I_\perp(\omega) = \frac{\sqrt{3}e^2\gamma\sin\alpha}{8\pi\epsilon_0 c}[F(x)+G(x)] \tag{1.9}$$

$$I_\parallel(\omega) = \frac{\sqrt{3}e^2\gamma\sin\alpha}{8\pi\epsilon_0 c}[F(x)-G(x)] \tag{1.10}$$

where

$$F(x) = x\int_x^\infty K_{\frac{5}{3}}(z)dz \tag{1.11}$$

$$G(x) = xK_{\frac{2}{3}}(x) \tag{1.12}$$

where $K_{\frac{1}{3}}$ and $K_{\frac{2}{3}}$ are modified Bessel functions of order $\frac{1}{3}$ and $\frac{2}{3}$. Finally $x = 2\omega a/3c\gamma^3$.

In deriving the total emissivity of a single electron by synchrotron radiation we must add these two polarization expressions and divide by the period of the electron in orbit namely in time $T_r = \nu_r^{-1} = 2\pi\gamma m/eB$.

We finally get the emission spectrum for a single electron by synchrotron radiation.

$$j(\omega) = \frac{I_\perp(\omega)+I_\parallel(\omega)}{T_r} = \frac{\sqrt{3}e^3 B\sin\alpha}{8\pi^2\epsilon_0 cm}F(x) \tag{1.13}$$

Now we would like to look at the emission from a population of electrons which is much more interesting from an astronomical point of view. Such a population has a distribution of energies and pitch angles. The energy distribution is described by a power law distribution of energies, $N(E)dE = \kappa(\frac{E}{E_0})^{-p}dE$,where $N(E)dE$ is the number of electrons per unit volume in the energy interval E to $E+dE$.

κ is determined by the total number of relativistic electrons per cm^3 per energy interval and by the electron range over which the distribution is valid.

As before, Longair (2010) [16] shows the derivation of the total emission of such a population where he assumed the power-law distribution of electrons energies applies to electrons with a fixed pitch angle α. The total emissivity is

$$J(\omega) \propto \kappa B^{(p+1)/2} \omega^{-(p-1)/2} \tag{1.14}$$

From this equation it is evident that the spectral index of the synchrotron emission of these electrons is $\alpha = (p-1)/2$. Therefore, the above equation can written in terms of spectral index rather than the electron spectrum index as

$$J(\omega) \propto \kappa B^{1+\alpha} \omega^{-\alpha} \tag{1.15}$$

1.5 Free-free emission

Electrons and ions interact with each other through their electric charge in an ionized gas such as a HII region. This process cause the electrons to emit photons. The energy of a single photon emitted during this interaction is the difference of the kinetic energy of the electron before and after the interaction, (i.e., $h\nu = E' - E$) according to the principle of energy conservation. The spectral index of this emission at short wavelengths where the Wien approximation can be used is typically $\alpha = -0.1$, with the brightness temperature dropping off at $\nu^{-2.1}$. At long wavelengths, the intensity exhibits the slope of the Rayleigh-Jeans law $\alpha = 2$ with the observed brightness temperature equal to the physical temperature. Compared to the much steeper synchrotron spectrum of $\alpha = -0.7$, the contribution of free-free emission to the overall emission is more or less negligible compared to shorter wavelengths. Thermal free-free radiation is unpolarized as the trajectories of the electrons are randomly oriented.

1.6 Loss processes

It is natural that radiating particles such as electrons and positrons would lose their energies through their interaction with matter, magnetic and radiation fields and other processes. These include synchrotron losses, inverse Compton losses, adiabatic losses, ionization losses and bremsstrahlung losses.

1.6.1 Synchrotron losses

Synchrotron losses occurs as the electrons lose energy emitting synchrotron radiation. The total energy loss rate by synchrotron radiation is given by:

$$-\left(\frac{dE}{dt}\right)_{synch} = \frac{4}{3}\sigma_T c \gamma^2 U_{mag} = 6.6 \times 10^4 \gamma^2 B^2 \mathrm{eVs}^{-1} \tag{1.16}$$

where σ_T is the Thompson cross section and B is the magnetic field strength in Tesla. Synchrotron losses steepens the energy spectrum by $\Delta p = 1$.

1.6.2 Inverse Compton losses

Inverse Compton losses arises from the reverse of normal Compton scattering such that if a free electron has a sufficiently high kinetic energy, $mc^2 \gg h\nu$, the electron can impart it's energy when it impacts a

photon. In galaxies these photons can be boosted from the far infrared to the X-ray or even γ regime. All these losses have different timescales, τ, which is the time where the particles lost half of their energy and determine the lifetimes of the CREs which can be seen in Heesen et al. (2009) [17].

$$-(\frac{dE}{dt})_{IC} = \frac{4}{3}\sigma_T c\gamma^2 U_{rad} \tag{1.17}$$

where U_{rad} is the energy density of a radiation field.

Synchrotron and inverse Compton losses can combined into a single expression as they are in the same form:

$$-(\frac{dE}{dt}) = \frac{4}{3}\sigma_T c\gamma^2 (U_{rad} + U_{mag}) \tag{1.18}$$

Due to this, inverse Compton losses also steepen the energy spectrum by $\Delta p = 1$. It is important to note that energy density of the radiation field from the Cosmic Microwave Background (CMB) is:

$$U_{rad} \sim \frac{B_{CMB}^2}{8\pi} \tag{1.19}$$

where $B_{CMB} = 3.25\mu\mathrm{G}(1 + \mathrm{z})^2$.

1.6.3 Adiabatic losses

Adiabatic losses are due to the loss of internal energy of ultra relativistic gas via expansion. This energy loss can be calculated by:

$$-(\frac{dE}{dt})_{ad} = \frac{1}{3}(\boldsymbol{\nabla} \cdot \boldsymbol{v})E \tag{1.20}$$

Anytime the particles exert pressure which does work, adiabatic losses become important, for example the escape of particles from supernova remnants.

1.6.4 Ionization losses

Ionization losses occur when a cosmic ray particle collides with a neutral particle, imparting it's energy to the neutral particle and thus ionizing it. As hydrogen is the most abundant element in the Universe we find that:

$$-(\frac{dE}{dt})_i = 7.64 \times 10^{-15} N(3ln\gamma + 19.8)\mathrm{eVs}^{-1} \tag{1.21}$$

where $\gamma = (1 - v^2/c^2)^{-1/2}$ is the Lorentz factor of the electron and N is the number density of hydrogen atoms in particles per meter cubed. Usually ionization losses can be neglected for the typical conditions of the interstellar medium. But ionization losses can become important in the nuclear regions of starburst galaxies. Thompson et al. (2006) [18] shows that ionization as well as bremsstrahlung losses can flatten the nonthermal spectra of starburst galaxies in the presence of rapid cooling.

1.6.5 Bremsstrahlung losses

Bremsstrahlung is electromagnetic radiation produced by the deceleration of a charged particle when deflected by another charged particle. Due to this, the traveling particle loses kinetic energy which is converted into a photon. Bremsstrahlung losses can be calculated from the formula:

$$-(\frac{dE}{dt})_{brems} = 7.0 \times 10^{-23} N(ln\gamma + 0.36) s^{-1} \tag{1.22}$$

1.7 Absorption processes

As according to the principle of detailed balance, to every emission process there is a corresponding absorption process. As result of this we have synchrotron self absorption and free-free absorption.

In star forming regions, low-frequency radio emission can be reduced by thermal absorption or even by synchrotron self-absorption in galactic nuclei. Regions of much lower thermal electron density, away from the galactic disks and active nuclei, maintain their steep emission spectrum and should become much more prominent at low frequencies.

1.7.1 Synchrotron self absorption

At low enough frequencies the brightness temperature of a source of synchrotron radiation may approach the kinetic temperature of the radiating electrons. When this happens, self-absorption effects can become important since thermodynamically the radiating electrons cannot result in a brightness temperature greater than their kinetic temperature. The maximum brightness temperature of a synchrotron source is limited by synchrotron self-absorption to:

$$T_{max} \approx 3 \times 10^{12} \mathrm{K} (\frac{\nu}{\mathrm{GHz}})^{1/2} (\frac{\mathrm{B}}{100\mu\mathrm{G}})^{-1/2} \tag{1.23}$$

from Begelman, Blandford & Rees (1984)[19]

Lacki (2013) [20] shows that the maximum cutoff frequency of $\sim$ 20 MHz for synchrotron self-absorption in Arp 220 like starbursts and therefore not important at observable frequencies from earth.

1.7.2 Free-free absorption

Free-free absorption occurs when a photon is absorbed by a free electron in the presence of an ion which increases the electron energy and moves it into a higher energy orbit.

Free-free absorption in the case of an ionized foreground screen is given by:

$$I(\nu) = I_0 (\frac{\nu}{\nu_0})^{\alpha} e^{-\tau(\nu)} \tag{1.24}$$

where I is the measured flux in Jy, I_0 is the flux without any free-free absorption in Jy and τ is the optical depth which is expressed by:

$$\tau = 3.01 \times 10^{-2} EM \nu^{-2} T_e^{-1.5} g_{ff} \tag{1.25}$$

where T_e is the thermal electron temperature in multiples of 10^4 K, EM and g_{ff} are the emission measure and Gaunt factor respectively and can be described as:

$$EM = \int_0^{s_0} n_e^2 ds \tag{1.26}$$

$$g_{ff} = 12.5 + ln(Z^{-1} T_e^{-1.5} \nu^{-1}) \tag{1.27}$$

where n_e is the electron density in particles per cm^{-3}, where Z is the charge number of the ionized atom.

In case of free absorption inside the source:

$$I(\nu) = I_0(\frac{\nu}{\nu_0})^2(1 - e^{-\tau(\nu)}) \tag{1.28}$$

Free-free absorption becomes very important along lines of sight through dense H II regions and thus free-free absorption can flatten the low frequency radio spectrum of starbursts such as M82 [21, Klein et al., 1988]. Free-free absorption was seen by Adebahr et al. (2013)[22], where the emission of the core of M82 showed that free-free absorption is lowering the flux of the starburst region at wavelengths from 1.4 GHz and lower, whereas the halo shows no sign of this.

It's effect is easily recognizable at low frequencies in HII regions surrounding supernova remnants as can be seen in figure 1.4.

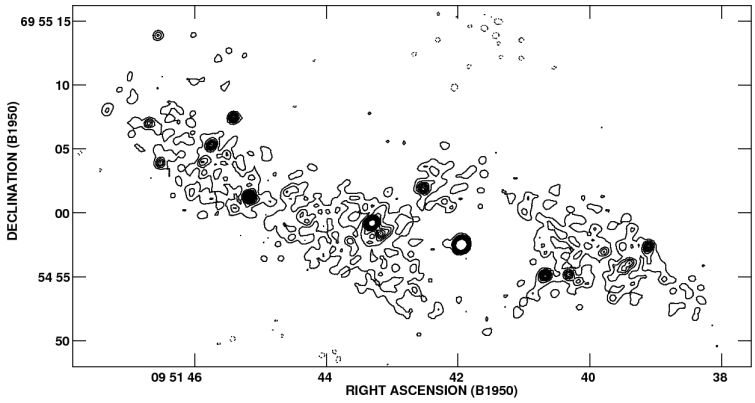

Figure 1.4: Contour map of M82 at 408 MHz observed with MERLIN. Resolution is 0.57×0.54″.Thermal absorption by a HII region is seen as a cavity ~ 100 pc across centered on the youngest and brightest supernova remnant 41.95+57.5. (From Wills et al. (1997) [23])

The Razin effect

Another process that can cut off the radio spectrum at low frequencies other than free-free absorption & synchrotron self absorption is the Razin effect. At low energies, the index of refraction of plasma suppresses the beaming of synchrotron radiation and causes it to fall off exponentially (Rybicki & Lightman 1979)[24]. From Schlickeiser (2002) [25], the frequency where this Razin effect becomes important is

$$\upsilon_R = 185\text{kHz}(\frac{\text{n}_\text{e}}{1\text{cm}^{-3}})(\frac{\text{B}}{100\mu\text{G}})^{-1} \tag{1.29}$$

The Razin effect is not important in spiral and starburst galaxies.

1.8 Galaxies at low frequencies

Low frequency radio emission traces low energy cosmic ray electrons that suffer less from energy losses and can propagate further away from their sources into regions with weak magnetic fields, therefore low frequency observations should also be able to probe these weak magnetic fields.

In star-forming regions, low frequency radio emission can be reduced by thermal absorption or even disappear by synchrotron self-absorption in galactic nuclei. Regions such as the halo and the extended

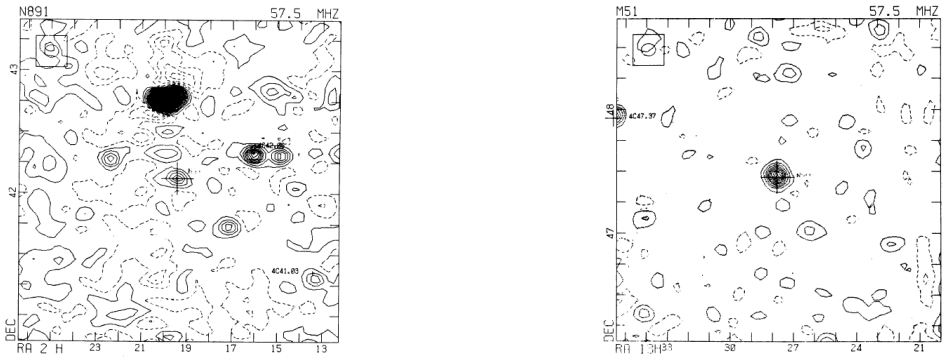

(a) NGC891 (b) M51

Figure 1.5: Images of NGC891 and M51 at 57.5 MHz observed with the TPT Clark Lake Telescope. From Israel & Mahoney (1990) [26].

disk which possess lower thermal electron density, away from the galaxy disks and active nuclei, maintain their steep spectrum and therefore become prominent at low frequencies, so that emission from weak magnetic fields should be observable.

Israel & Mahoney (1990) [26] used the Clark Lake Radio Observatory TPT array at a frequency of 57.5 MHz to produce a survey of 133 galaxies for which 68 galaxies were detected. NGC891 & M51 observed in this survey can be seen in figure 1.5. The observed 57.5 MHz integrated fluxes were systematically lower that the integrated fluxes extrapolated from 1.4 GHz. They also observed that this decrease correlates with the axial ratio of the observed galaxies and is smallest for edge-on galaxies. I&M interpreted this as increasing free-free absorption of nonthermal emission in galaxy disks with increasing tilt and proposed that it is caused by a smoothly distributed diffuse ionized gas component with a very low electron temperature $T_e \sim 50$K. However, there is no clear observational evidence for the presence of such gas in our own Galaxy. In addition, Israel et al. (1992) [27] observe a relatively flat spectral index below 500 MHz (α = -0.2) in the galaxy M33. Again, they explain this flat spectral index to be caused by free-free absorption of nonthermal emission by a cool ionized gas.

Hummel (1991) [28] reanalyzed the I&M 1990 data and while observed a change in spectral index with frequency, he did not see that the amount changed significantly on the inclination of the galaxies. Therefore this is still a matter for debate and will be answered in the near future with LOFAR.

The mean equipartition total magnetic field strength in spiral galaxies is on average 9 ± 3 μG. But the total magnetic field can be seen to be stronger within the spiral arms where the increased turbulence from star formation causes it to have a strength of 20 μG. The interarm region is filled with regular fields forming long filaments of polarized intensity such as IC342 (Krause et al. 1989) [29] or so called magnetic spiral arms like in NGC6946 (Beck & Hoernes, 1996) [30].

There is observational evidence that the magnetic field extends well beyond the star-forming region but the problem is that the synchrotron emission is weak due to the lack of cosmic-ray electrons far from the star-forming regions in the inner disk. Faraday rotation measures of polarized background sources behind the spiral galaxy M31 showed that the regular magnetic field of this galaxy extends to at least 25 kpc radius which is twice the extent of the optical disk without significant decrease in magnetic field strength (Han et al. 1998) [31]. For some galaxies we can see the polarized spiral pattern extends far from the optical disk as can be seen in figure 1.6.

Edge-on galaxies possess radio halos which can usually comprises of two exponential components, a thin disk component (~ 300 pc) and a thick disk component of about 1.8 kpc (Krause, 2011) [33].

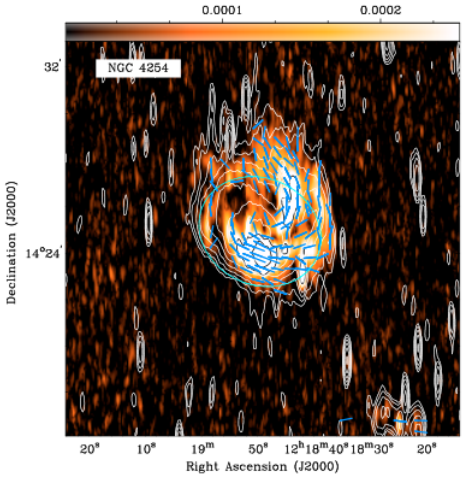

Figure 1.6: The galaxy NGC4254 at 1.4 GHz with total radio emission shown in contours and the background color image shows the polarized intensity. The cyan ellipse indicates D_{25}. From Heald et al. 2009 [32]

There is a wide variety of observational evidence that points to a connection between the supernova rate per unit area and the strength of the radio continuum, X-ray and Hα halo emission (Dahlem et al. 1995) [34], (Rossa & Dettmar, 2003) [35]. Low frequency measurements of edge on galaxies show that the z-extent of the radio halo changes with frequency and that the rate of change becomes smaller at lower frequencies (Hummel & Dettmar, 1990) [36]. They observed that the spectral index steepens with increasing height which indicates energy losses of the cosmic ray electrons originating in the disk and propagating into the halo.

In all of the edge-on spiral galaxies studied up to now, the large scale ordered fields in the disks lie plane-parallel along the disk of the galaxy and in the halo they have a X-shaped morphology. This is what is expected from observations of face-on galaxies and their magnetic field amplification by the action of a mean-field $\alpha\Omega$ (Beck et al. 1996) [37]. The large-scale magnetic field pattern seems not to depend on the star formation rate (Krause 2009) [38].

1.8.1 The FIR-radio correlation

The radio continuum and far-infrared (FIR) luminosities for a wide morphological class of galaxies are tightly correlated over five orders of magnitude (de Jong et al. 1985) [40], (Condon, 1992) [41]. From spatially resolved studies of normal and irregular galaxies it is seen that the correlation holds even at scales of tens to hundreds of parsecs (Beck & Golla, 1998) [42], (Tabatabaei et al. 2007a) [43]. It is through star formation that connects these two regimes (Harwit & Pacini, 1975) [44]. The radio continuum arises due to synchrotron emission from relativistic electrons originating from supernova remnants. The FIR emission arises from re-radiation by dust heated due to ultra violet (UV) photons emitted by massive, short lived stars. Since the mean free path of a dust-heating photon is smaller than the diffusion length of a CR electron, a radio image of a galaxy appears as a smoothed version of a FIR image and the retrieval of CRE scale lengths can provide important information on star formation and radiation intensity (Murphy et al. 2006) [45] and on CREs propagation (Tabatabaei et al. 2013)[46].

While the cause of the correlation is well understood, the tightness over several magnitudes still remains puzzling. This correlation can be used to give a rough estimate for the strength of the radiation fields and thus the connection between star formation and magnetic fields.

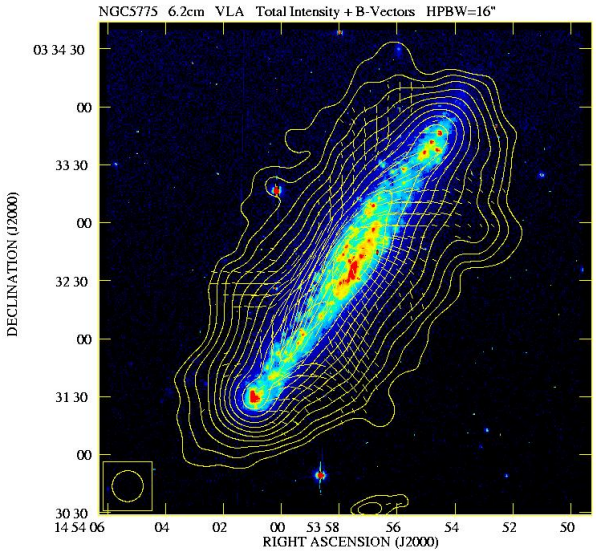

Figure 1.7: Total radio emission (shown in contours) and apparent B-vectors of NGC5775 at 4.8 GHz observed with the VLA overlayed on a Hα image. From Tüllmann et al. 2000 [39]

1.9 Polarization at low frequencies

Synchrotron emission from a plasma in a uniform magnetic field is naturally intrinsically highly polarized and depends on electron spectrum index as follows:

$$P = \frac{p+1}{p+7/3} \tag{1.30}$$

With a typical value for $p = 2.5$, the degree of polarization is to be about 72%. This is independent of frequency and viewing angle but assumes that the directions of the velocity vectors of the electrons are isotropically distributed in a magnetized plasma (Le Roux, 1961) [47]. The polarization of synchrotron emission on its own can contain much information on the ordered magnetic field of the astrophysical object in question, for example, the interarm regions of NGC6946 that show polarization in the form of 'magnetic arms'.

Maps produced in radio polarimetry are usually attributed to the Stokes parameters, namely I,Q,U,V. The total polarized intensity is found from:

$$I_{pol} = \sqrt{U^2 + Q^2 + V^2} \tag{1.31}$$

Normally we are dealing with linear polarization and therefore, $V = 0$, giving us:

$$I_{pol} = \sqrt{U^2 + Q^2} \tag{1.32}$$

The degree of linear polarization is thus:

$$p_{lin} = \frac{\sqrt{U^2 + Q^2}}{I} \tag{1.33}$$

However, this only gives us information on the magnetic field on the plane of the sky ($B_\perp$). But, due to birefringence of the magneto-ionic medium, the polarization angle of linearly polarized radiation that propagates through this plasma rotates as a function of frequency. This can give us information on the magnetic field in the line of sight, traditionally through the use of the rotation measure, defined as:

$$RM = \frac{\delta\chi}{\delta\lambda^2} \tag{1.34}$$

where χ is the polarization angle and is:

$$\chi = \frac{1}{2} tan^{-1} \frac{U}{Q} \tag{1.35}$$

However, as one will see, there are many complications when trying to detect polarizations at low frequencies such as:

- Beam depolarization: This occurs when the magnetic field is tangled on scales smaller that the resolution of the observation. The polarization with different polarization angles cancel each other out and therefore the original polarized signal depolarizes itself inside the beam. The only way to prevent this is to have better resolution on the target which isn't trivial at low frequencies.
- Bandwidth depolarization: This effect occurs when, depending on the RM of the source, the signal depolarizes itself within a frequency band. While the noise level is decreased proportionally to the square root of the bandwidth in terms of frequency, the polarized signal reduces proportionally to the sinc of the bandwidth in terms of wavelength squared. To combat this, the total bandwidth is divided into narrow channels of bandwidth. However, the signal to noise of one channel is much lower than the total bandwidth.
- Galactic foreground: At low frequencies, the Milky Way can dominate the polarized emission especially at low and intermediate galactic latitudes. This can make it difficult to distinguish the polarization properties of extra galactic sources.
- Internal/External Faraday dispersion: This effect occurs when the polarized emission is depolarized by the various amounts of Faraday rotation in the line of sight within the beam, either in an emitting region (internal) or outside the emitting region (external). An example of external Faraday dispersion would be the effect of the galactic foreground on a background polarized signal in that it can contribute in rotating the polarization angle of the signal and hence could depolarize the object of interest.

Quantifying depolarization effects between different frequencies can be done through the following equation from Beck (2007) [48]:

$$DP(\nu_1, \nu_2) = \frac{PI_1}{PI_2} \times (\frac{\nu_1}{\nu_2})^{\alpha_n} \tag{1.36}$$

where α_n is the synchrotron spectral index and ν_1 & ν_2 are the respective frequencies.

At low frequencies, depolarization is dominated by internal Faraday dispersion. From Burn (1966) [49]:

$$DP_{int} = \frac{1 - exp(-S)}{S} \tag{1.37}$$

with

$$S = 2\sigma_{RM}^2 \lambda^4 \tag{1.38}$$

where the term σ_{RM} describes the dispersion of the medium in rad m^{-2}. In a simplified model of a magneto-ionic medium it can be written as (Arshakian & Beck 2011) [50]:

$$\sigma_{RM}^2 = (0.81 n_e B_{\rm turb} d)^2 \frac{fL}{d} \tag{1.39}$$

$$\sigma_{RM}^2 \simeq (0.81 \langle n_e \rangle \langle B_{\rm turb} \rangle)^2 \frac{Ld}{f} \tag{1.40}$$

where $n_e = \langle n_e \rangle / f$ is the thermal electron density in cm^{-3} within the turbulent cells of size d in pc, $\langle n_e \rangle$ is the average electron density in the volume along the pathlength traced by the telescope beam in pc, f is the filling factor of the cells, $\langle B_{turb} \rangle$ is the strength of the turbulent magnetic field in μG and L is the pathlength along the line of sight through the Faraday-active emitting layer. The term in the brackets describes the rotation measure of a single turbulent cell, while $\frac{fL}{d}$ term gives the number of cells along the line of sight.

Another major source of difficulty in polarization is the ionosphere which will be dealt with in the next chapter.

As shown in equation 1.34, the traditional method of finding the rotation measure and therefore $B_{\parallel}$ is found by plotting the polarization angle as a function of λ^2 and then performing a least squares fit. However, if only a few data points are available, then multiple RM solutions are as good as each other. This is known as the $n\pi$ ambiguity problem (see Rand & Lyne 1994, [51] figure 1).

To remedy the problem of bandwidth polarization and $n\pi$ ambiguities, RM synthesis, a technique to analyze and interpret polarization data has been developed.

1.9.1 RM synthesis

The RM synthesis technique was first used by Burn (1966) [49] on the Crab Nebula, but was rarely used after as it required accurate polarization data at many frequency channels over a wide bandwidth which was impractical in those days. Now with the advent of multi-channel receivers, this technique can be fully utilized. From Burn (1966) [49], we take the definition of Faraday depth (ϕ) of a source as:

$$\phi(\mathbf{r}) = 0.81 \int_{there}^{here} n_e \mathbf{B} \mathrm{dr} \quad \mathrm{radm}^{-2} \tag{1.41}$$

where n_e is the electron density in cm^{-3}, $\mathbf{B}$ is the magnetic field in μGauss and $\mathbf{r}$ is an infinitesimal path length in parsecs. It is important to note here that the Faraday depth and rotation measure are equivalent to each other if and only if there exists just a background source with a dispersive Faraday Screen (often called a Burn's slab) in the foreground along the line of the sight. If a magnetized, emitting plasma exists in the line sight, then the RM is no longer valid. Therefore, Faraday Depth is a general definition with the RM an exceptional case of it. RM synthesis avoids bandwidth depolarization by averaging the complex polarization. The Faraday dispersion function is related to the complex polarization vector:

$$\tilde{F}(\phi) = F(\phi) * R(\phi) = K \sum_{i=1}^{N} w_i P_i e^{-2i\phi(\lambda_i^2 - \lambda_0^2)} \tag{1.42}$$

The RM Spread Function (RMSF) is defined as:

$$R(\phi) = K \sum_{i=1}^{N} w_i e^{-2i\phi(\lambda_i^2 - \lambda_0^2)} \tag{1.43}$$

$$K = (\sum_{i=1}^{N} w_i)^{-1} \tag{1.44}$$

where $*$ denotes convolution, w_i is the weight of the ith data point. The RMSF represents the response of the instrument, due to the discrete separation of the bandwidth into separate channels.

After performing RM synthesis, confusion with RMSF sidelobes can make the interpretation and locating the correct Faraday depth of a source difficult. Fortunately, a deconvolution routine know as RM clean (Heald 2009) [32] can improve the situation in that it performs a routine quite similar to one used in aperture synthesis radio telescope images but with a major difference being that this convolution is performed in 1-D (Faraday depth). The full description of the algorithm can be seen in Heald (2009) [32].

The usual method of applying RM-Synthesis to interferometric data involves the following steps:

- Calibrate the visibility data as usual
- Create images of the deconvolved Q and U images at each frequency channel. The weighting and tapering of the calibrated data must be in a way so that the resolution of the images are approximately equal in frequency. Each image must have the same pixel dimensions and size.
- These images are then stacked and RM synthesis is then performed pixel by pixel.
- A further ϕ-space deconvolution is performed namely RM-Clean

Using RM synthesis, shortcomings are easily noticeable. The first being that when creating the images, one needs to taper the visibility data so that the higher frequency images have the same resolution as those of lower frequencies which means a loss of resolution. Also this weighting and tapering can not be performed perfectly and variations in the polarized intensity arising from different resolutions would produce a shift in the Faraday depth of the emission and lead to systematic errors. Secondly, artifacts in the images caused by normal clean deconvolution will be further amplified during RM clean, further reducing image fidelity. Finally, incomplete λ^2 coverage can be a serious problem in order to interpret radio polarization data for extended sources like galaxies (Frick et al. 2011 [52]). Beck et al. (2012) [53], show that in order to reliably recognize magnetic field structures in spiral galaxies, one requires the analysis of data cubes observed over a wide and continuous frequency range with the SKA being close to fulfilling this need.

Bell and Ensslin (2011) [54] developed a new method called Faraday synthesis which addressed some of these shortcomings. With this approach, one reconstructs the Faraday spectrum directly from the visibility data. With Faraday Synthesis, the deconvolution is performed in one step using the entirety of the broadband data. In comparison, with RM-Synthesis, each frequency channel must be deconvolved individually. Faraday and RM synthesis are equivalent if deconvolution is not required. It was found from comparing both methods applied to mock data that Faraday synthesis had a 20% less noise, 30% better resolution and the strongest artifact was about half as bright compared to RM-Synthesis. However, Faraday synthesis has not been performed on real interferometric data.

RM synthesis has been performed on galaxies observed as part of the Westerbork SINGS survey (Braun et al. 2010) [55], where through RM synthesis the authors were able to detect faint secondary

polarized components in three relatively face on spiral galaxies. This supports the model that the polarized intensity observed at GHz frequencies from nearby galaxy disk is dominated by a region of emissivity located above the mid plane closer to the observer. This polarized emission would only suffer a Faraday rotation of a few tens of rad m^2 within the halo. These faint secondary components would be located from the far side of the mid plane and would undergo much more severe Faraday rotation and Faraday dispersive effects.

1.10 Outline of this thesis

In this thesis, I will present the first results of observations from LOFAR high band antenna (HBA) of nearby spiral galaxies. Chapter 2 will contain an overview of LOFAR, explaining the difficulties imposed on the observer at low frequencies as well as the tools created to combat these difficulties. A short introduction on the processing of LOFAR and the challenges this imposes on the observer. In this chapter, commissioning results which benefited the LOFAR community obtained during this thesis will be shown. Most notably, the development and testing of a procedure to transfer and interpolate the complex gains obtained from calibrators to target sources. Chapter 3 will present the results of a Cycle 0 LOFAR HBA observation on the face-on spiral galaxy M51 where the extended disk beyond 10 kpc will be studied. Chapter 4 will present the modelling of the cosmic ray distribution of M51 by solving the diffusion loss differential equation through approximation methods. Chapter 5 will show the results of a LOFAR HBA commissioning observation on the edge spiral galaxy NGC891 and explore the physical properties of the halo at low frequencies. Chapter 6 will detail observations of the nearly face on spiral galaxy NGC628 with the Effelsberg 100 meter radio telescope and the JVLA at GHz frequencies. Interesting preliminary results from the implementation of RM Synthesis will be shown. Chapter 7 will detail the work done during this thesis on the Multi-frequency Snapshot Sky Survey (MSSS) including the detection of nearby galaxies as well as polarization from the Galactic foreground opening up the exciting possibility of a MSSS polarization survey. Chapter 8 will summarize the main findings of this thesis and future prospects.

CHAPTER 2

Radio Interferometry with the Low Frequency Array

In this chapter we will explore the principals of interferometry in particular the problems that affect low frequency interferometry. The newly constructed low frequency telescope LOFAR will be introduced to the reader. Additional in this chapter, the hardware and software of LOFAR will be explained and several commissioning results will be presented.

2.1 A short introduction to Radio Interferometry

While the first radio telescopes were simple single dish antennas, they had one inherent weakness, namely it's relative low angular resolution which degrades even further at lower frequencies as the angular resolution of a single dish telescope is proportional to λ/D where λ is the observing wavelength and D is the dish diameter. Interferometers are apparatuses that consist of two or more antennas whose signals are combined in a correlator. This correlator output simulates a single dish radio telescopes but with a diameter equal to the distance of the maximum separation between any of antenna pairs (separation between antennas is called the *baseline*). This enables far better angular resolution.

Here I will discuss the fundamental principals of radio interferometry using the Radio Interferometry Measurement Equation (RIME) formalism created by Hamaker et al. (1996) [56], Sault et al. (1996) [57] and redeveloped by Smirnov (2011a,b) [58] [59]. Section 2.1.1 follows both these papers closely.

2.1.1 The RIME formalism

Firstly, we consider a quasi-monochromatic signal from a single point source. A signal is emitted from a fixed point in a orthogonal *xyz* coordinate system, with z being the direction of propagation. This signal can be represented as:

$$\boldsymbol{e} = \begin{pmatrix} e_x \\ e_y \end{pmatrix} \tag{2.1}$$

The single most important fundamental assumption for the RIME is *linearity*. Therefore all transformations along the signal path are linear with respect to $\mathbf{e}$. All linear transformations can be seen $\boldsymbol{e'} = \boldsymbol{Je}$ where $\mathbf{J}$ is a 2×2 complex matrix called the Jones matrix. Multiple effects along the signal propagation correspond to repeated matrix multiplications which form a Jones chain. The order of terms in a

Jones chain corresponds to the physical order in which the effect occurs in the signal path. As matrix multiplication is not commutative it is very important that the order of the Jones chain is in the right order.

When the signal hits the antennas' reciever, it is then converted into a complex voltage. v_a and v_b represents two polarizations. This is represented by:

$$\boldsymbol{v} = \begin{pmatrix} v_a \\ v_b \end{pmatrix} = \boldsymbol{J}\boldsymbol{e} \tag{2.2}$$

Equation 2.2 shows the linear relationship between the voltage vector $\boldsymbol{v}$ as measured by the antenna feeds and the original signal vector $\mathbf{e}$ at some arbitrarily distant point with $\boldsymbol{J}$ being the product of all propagation effects along the the signal path including electronic effects of the antenna and atmospheric effects.

Two spatially separated antennas p and q measure two independent voltage vectors $\boldsymbol{v_p}, \boldsymbol{v_q}$. These are fed into a correlator producing the following 4 pairwise correlations which are arranged into the *visibility matrix* (or *coherency matrix*) $\mathbf{V}_{pq}$:

$$\boldsymbol{V}_{pq} = 2\begin{pmatrix} \langle v_{pa} v_{qa}^* \rangle & \langle v_{pa} v_{qb}^* \rangle \\ \langle v_{pb} v_{qa}^* \rangle & \langle v_{pb} v_{qb}^* \rangle \end{pmatrix} = 2\langle \boldsymbol{v}_p \boldsymbol{v}_q^H \rangle \tag{2.3}$$

where H represents the conjugate transpose operation, otherwise known as the Hermitian operator.

Combining equations 2.2 & 2.3 and assuming that $\mathbf{J}_p$ and $\mathbf{J}_q$ are constant over the averaging interval:

$$\boldsymbol{V}_{pq} = 2\langle \boldsymbol{J}_p \boldsymbol{e} (\boldsymbol{J}_q \boldsymbol{e})^H \rangle = 2\langle \boldsymbol{J}_p (\boldsymbol{e}\boldsymbol{e}^H) \boldsymbol{J}_q^H \rangle = 2\boldsymbol{J}_p \langle \boldsymbol{e}\boldsymbol{e}^H \rangle \boldsymbol{J}_q^H = 2\boldsymbol{J}_p \begin{pmatrix} \langle e_x e_x^* \rangle & \langle e_x e_y^* \rangle \\ \langle e_y e_x^* \rangle & \langle e_y e_y^* \rangle \end{pmatrix} \boldsymbol{J}_q^H \tag{2.4}$$

The last bracketed quantities are related to the Stokes Parameters (Hamaker & Bregman 1996) [56]:

$$2\begin{pmatrix} \langle e_x e_x^* \rangle & \langle e_x e_y^* \rangle \\ \langle e_y e_x^* \rangle & \langle e_y e_y^* \rangle \end{pmatrix} = \begin{pmatrix} I + Q & U + iV \\ U - iV & I - Q \end{pmatrix} = \boldsymbol{B} \tag{2.5}$$

$\mathbf{B}$ is defined as the brightness matrix. This gives us the RIME of a single point source:

$$\boldsymbol{V}_{pq} = \boldsymbol{J}_p \boldsymbol{B} \boldsymbol{J}_q^H \tag{2.6}$$

Equation 2.6 holds in any coordinate system. $\boldsymbol{J}_p$ and $\boldsymbol{J}_q^H$ corresponds to the various effects that are applied to the original source brightness. Equation 2.6 can be written in the 'onion' form of the RIME:

$$\boldsymbol{V}_{pq} = \boldsymbol{J}_{pn}(...(\boldsymbol{J}_{p2}(\boldsymbol{J}_{p1} \boldsymbol{B} \boldsymbol{J}_{q1}^H)\boldsymbol{J}_{q2}^H)...)\boldsymbol{J}_{qm}^H \tag{2.7}$$

In this case $n \neq m$ for the outer indices as the two signal paths can be completely dissimilar to each other. Each propagation effect can be described by a different Jones matrix. For example:

- Phase Delay given by a scalar matrix, **K**-Jones
- Faraday rotation in the Earth's ionosphere given by a rotation matrix, **F**-Jones
- A possible rotation over a parallactic angle of the feed system with respect to the incident field, **P**-Jones
- Deviations of the actual feed from the ideal, **D**-Jones. If the feed is ideal then **D** is an identity matrix.

- The complex receiver gains given by a diagonal matrix, **G**-Jones

There is one fundamental effect that needs to be addressed namely the phase delay associated between voltages $\boldsymbol{v}_p$ and $\boldsymbol{v}_q$. The phase difference is due to the geometric path length difference from source to antennas p and q. If we consider antenna p located at coordinates $\boldsymbol{u}_p = (u_p, v_p, w_p)$, the phase difference at point $\boldsymbol{u}_p$ relative to a generic $\boldsymbol{u} = 0$ for a signal arriving from direction **s**, is given by:

$$\kappa_p = 2\pi\lambda^{-1}(u_p l + v_p m + w_p(n-1)) \tag{2.8}$$

where $l, m, n = \sqrt{1 - l^2 - m^2}$ are the direction cosines of **s** and λ is the signal wavelength. Defining **u** in terms of wavelength allows us to omit λ^{-1} term. The phase delay matrix can now be described as:

$$\kappa_p = e^{-i\kappa_p} = e^{-2\pi i(u_p l + v_p m + w_p(n-1))} \tag{2.9}$$

If we insert this into the RIME for a single point source (equation 2.6), we get:

$$\boldsymbol{V}_{pq} = \boldsymbol{K}_p \boldsymbol{B} \boldsymbol{K}_q^H \tag{2.10}$$

This visibility matrix is known as the *source coherency* and is written as $\boldsymbol{X}_{pq}$ and is the visibility that would be measured by a corruption-free interferometer. However, there is no such thing as a corruption-free interferometer and in reality there are several 'corrupting' effects along the signal path given by $\boldsymbol{G}$ as:

$$\boldsymbol{V}_{pq} = \boldsymbol{G}_p \boldsymbol{X}_{pq} \boldsymbol{G}_q^H \tag{2.11}$$

Let us now place N point sources in the sky. Each source contributes to the measured visibility matrix $\boldsymbol{V}_p q$ by linear addition. The signal propagation for each source s to each antenna p is different as it passes through different regions of the ionosphere. Thus, each path can be described by its own Jones matrix $\boldsymbol{J}_{sp}$. Equation 2.6 becomes:

$$\boldsymbol{V}_{pq} = \sum_s \boldsymbol{J}_{sp} \boldsymbol{B}_s \boldsymbol{J}_{sq}^H \tag{2.12}$$

Some elements in the Jones chain may be the same for all sources such as electronic gain. We can collapse the Jones chain into a product of three Jones matrices

$$\boldsymbol{J}_{sp} = \boldsymbol{G}_p \boldsymbol{E}_{sp} \boldsymbol{K}_{sp} \tag{2.13}$$

Here $\boldsymbol{G}_p$ is the source-independent term of the Jones chain, $\boldsymbol{K}_{sp}$ is the phase term and $\boldsymbol{E}_{sp}$ is the source dependent term. We can rewrite equation 2.12:

$$\boldsymbol{V}_{pq} = \boldsymbol{G}_p \Big(\sum_s \boldsymbol{E}_{sp} \boldsymbol{K}_{sp} \boldsymbol{B}_s \boldsymbol{K}_{sq}^H \boldsymbol{E}_{sq}^H\Big) \boldsymbol{G}_q^H \tag{2.14}$$

$\boldsymbol{G}_p$ describes the directional independent effects (DIEs) and $\boldsymbol{E}_{sp}$ the direction dependent effects (DDEs)

In the more general case, the sky is not a sum of discrete sources, but a continuous, brightness distribution $\boldsymbol{B}(\sigma)$, where σ is a unit direction vector. Jones matrices are now in the form $\boldsymbol{J}_p(\sigma)$. Integrating equation 2.6 over a unit sphere:

$$\boldsymbol{V}_{pq} = \int_{4\pi} \boldsymbol{J}_p(\sigma) \boldsymbol{B}(\sigma) \boldsymbol{J}_q^H(\sigma) d\Omega \tag{2.15}$$

If we perform a sine projection of the sphere onto a plane (l, m) tangential at the field center, we obtain:

$$\boldsymbol{V}_{pq} = \int_{lm} \int \boldsymbol{J}_p(\boldsymbol{l}) \boldsymbol{B}(\boldsymbol{l}) \boldsymbol{J}_q^H(\boldsymbol{l}) \frac{dldm}{n} \tag{2.16}$$

where $n = \sqrt{1 - l^2 - m^2}$.

Finally, we decompose the Jones matrix $\boldsymbol{J}_p$ into its components and putting together the $\boldsymbol{K}$ terms we get:

$$\boldsymbol{V}_{pq} = \boldsymbol{G}_p(\int_{lm} \int \frac{1}{n} \bar{\boldsymbol{E}}_p \boldsymbol{B} \bar{\boldsymbol{E}}_q^H e^{-2\pi i(u_{pq}l + v_{pq}m + w_{pq}(n-1))} dldm) \boldsymbol{G}_q^H \tag{2.17}$$

This is actually a more general formulation of the famous van Cittert-Zernike theorem. This states that the spatial autocorrelation function of the electromagnetic field is the Fourier transform of the brightness distribution.

This form of the RIME is implemented by the LOFAR calibration software. It is flexible as it can incorporate many different effects, and in particular the direction-dependent effects that are extremely important at low frequencies.

2.2 The difficulties of low frequency radio interferometry

In this section, the main problems of performing astronomy at low frequencies (< 300MHz) will be explored. Long wavelength observations have in the past been hindered by low angular resolution, low bandwidth, high noise temperature, strong confusion by sources in the field of view. Only recently, due to advances in technology and computing has this relatively unexplored region of the electromagnetic spectrum been open to the scientific community through the MWA, LWA and LOFAR.

2.2.1 The problem of the ionosphere

The greatest and most fundamental issue that has prevented low frequency radio astronomy from producing significant scientific results in recent decades is the corrupting influence of the earth's ionosphere on the measurement of the visibility phase on baselines longer than a few kilometers.

The ionosphere is a shell of electrons and ionized atoms and molecules that covers the earth at an altitude of about 50km to 1000km. It is a dynamic, inhomogeneous medium with electron densities varying as a function of position and time. The state of ionization is mostly caused by the Sun through photo-ionization. The free electron column density along the LOS through the ionosphere is generally referred to as the total electron content or TEC. The TEC unit is 10^{16} m^{-2}.

The refraction and propagation delay are caused by a varying refractive index n of the ionospheric plasma (Intema et al. 2009) [60]:

$$n^2 = 1 - \frac{\nu_p^2}{\nu^2} \tag{2.18}$$

with ν being the observing frequency and ν_p, the plasma frequency which is given by:

$$\upsilon_p = \frac{e}{2\pi} \sqrt{\frac{n_e}{\epsilon_0 m}} \tag{2.19}$$

The total propagation delay, integrated along the line of sight, causes a phase rotation of:

$$\varphi^{ion} = -\frac{2\pi\nu}{c}\int (n-1)\mathrm{dl} \tag{2.20}$$

with c being the speed of light in a vacuum.

Most variations observed however, are not caused by a differential variation through a smooth ionosphere, but due to varying horizontal gradients produced by traveling ionospheric waves (A Traveling Ionospheric Disturbance, TID). A medium-scale TID is observed at heights between 200 and 400 km, have a wavelength between 250 and 400 km and have a near horizontal velocity of 300 to 700 km per hour. Most crucially, these TIDs can cause TEC variations of 1-5 %. Due to these TEC variations in time, antenna position and viewing direction, visibility phases are distorted by time varying differential ionospheric phase rotations. These distorted visibility phases can lead to severe problems such as an instantaneous spatial phase gradient over the array in the direction of the source which causes an apparent position change in the image plane but causes no source deformation. However, source deformation can occur if the spatial phase behavior deviates from a gradient. What is worse is that this deformation can lead to greater residual sidelobes after deconvolution.

It is important to discuss the four different regimes discussed by Lonsdale (2005)[61] for instantaneous ionospheric phase calibration as it is essential to understand in terms of low frequency interferometry. A diagram illustrating the four regimes is presented on figure 2.1.

In the first regime (top left in figure 2.1), the projected size of the field of view V of each array element is small, much smaller than the scale size of ionospheric phase fluctuations S as well as the array size A. Here we do not have directional dependent effects and phase only self calibration on short enough timescales is sufficient to remove the ionospheric phase errors from the visibilities.

In the second regime (top right in figure 2.1), the array size A is much larger than the size of ionospheric phase fluctuations S and therefore the ionospheric phases are different for each array element. Fortunately, the station FoV is narrow so that it is possible to assign a single unknown ionospheric phase to each individual antenna. Thus, the regime reduces to that of the first regime and the same calibration solution applies.

In the third regime,(bottom left in figure 2.1), the station FoV is greater than the size of ionospheric phase fluctuations. The phase and gain of the station FoV is thus direction dependent but the array is compact and thus see the same ionosphere. It is then possible to make a coherent image but sources may have shifted positions.

Finally in the fourth regime,(bottom right in figure 2.1), is the most general case with a large array with a wide FoV (LOFAR is this case). Each station beam sees a multitude of sources and each station is distorted by different ionospheric gains and phases. This causes source position shifts and source shape deformations that both vary in time and viewing direction.

For unresolved sources, Cotton 2004 defines the *Strehl Ratio* as the ratio of observed peak over the true peak flux. In the case of Gaussian random phase errors, the *Strehl Ratio* is related to the rms phase error σ_ϕ by

$$R = exp[-\frac{\sigma_\phi^2}{2}] \tag{2.21}$$

A larger peak flux is equivalent to a smaller rms phase error. This is due to the fact that phase errors cause scattering of source power into sidelobes.

Due to the problems discussed that are caused by the ionosphere, radio interferometers observing at low frequencies were limited by short baselines (<5km), which severally reduces angular resolution. This led to a huge obstacle in the manifestation of confusion which would severely degrade the sen-

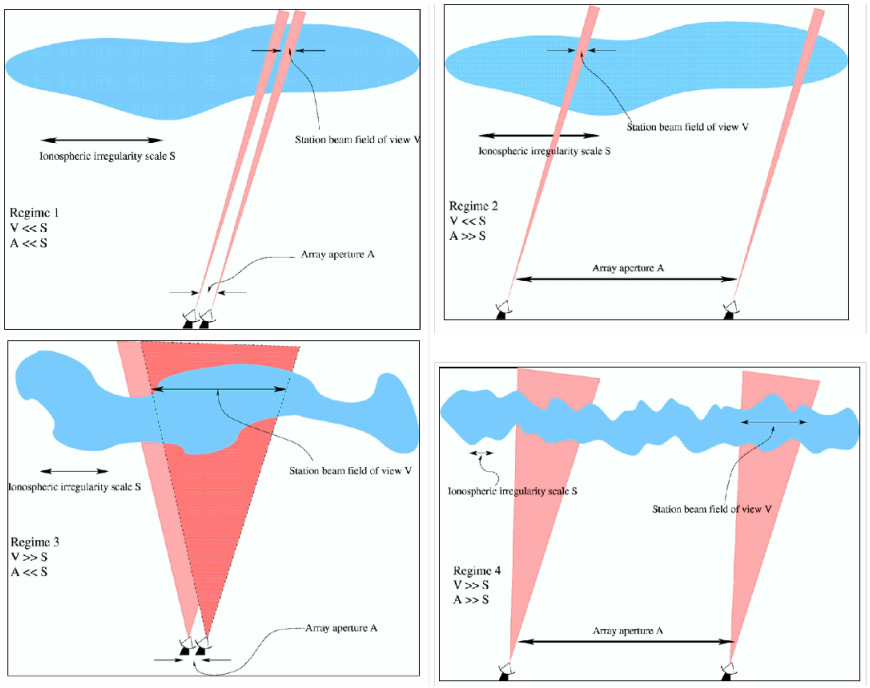

Figure 2.1: Diagrams showing each seperate regimes for instantaneous ionospheric phase calibration from Lonsdale (2005) [61]. From Wijnholds et al. (2010)[62].

sitivity of an interferometer. Confusion in radio astronomy is manifested in three different ways and all these three effects are roughly proportional to the square of the angular resolution. Therefore, if an interferometer has it's angular resolution decreased by a factor of 10, the sensitivity of the interferometer would decrease by 100. Further integration beyond this would not lower the rms noise. This is demonstrated on figure 2.2. The impact of this put low frequency radio astronomy in the backwater for several decades.

The ionosphere can also affect the polarization of an observation due to time variable Faraday rotation. Quantitatively, the angle variation is

$$\Delta\Phi = 2.6 \times 10^{-17} \nu^{-2} \int_{LoS} n_e B_{\parallel} \, \mathrm{d}l = \mathrm{RM}\nu^{-2} \, [\mathrm{rad}] \tag{2.22}$$

where ν [Hz] is the frequency, n_e [cm^{-3}] is the electron density,$B_{\parallel}$ [μ G] is the magnetic field in the line of sight, RM is the rotation measure and dl [m] is the path length along the line of sight (LoS). In the RIME formalism, in a linear-coordinate polarization basis, the Faraday rotation is simply a rotation matrix:

$$F = Rot\beta = \begin{pmatrix} cos\beta & -sin\beta \\ sin\beta & cos\beta \end{pmatrix} \beta \propto \nu^{-2} \int_{LoS} n_e B_{\parallel} \, \mathrm{d}l \tag{2.23}$$

This effect can be corrected for and will be presented in 2.9.2.

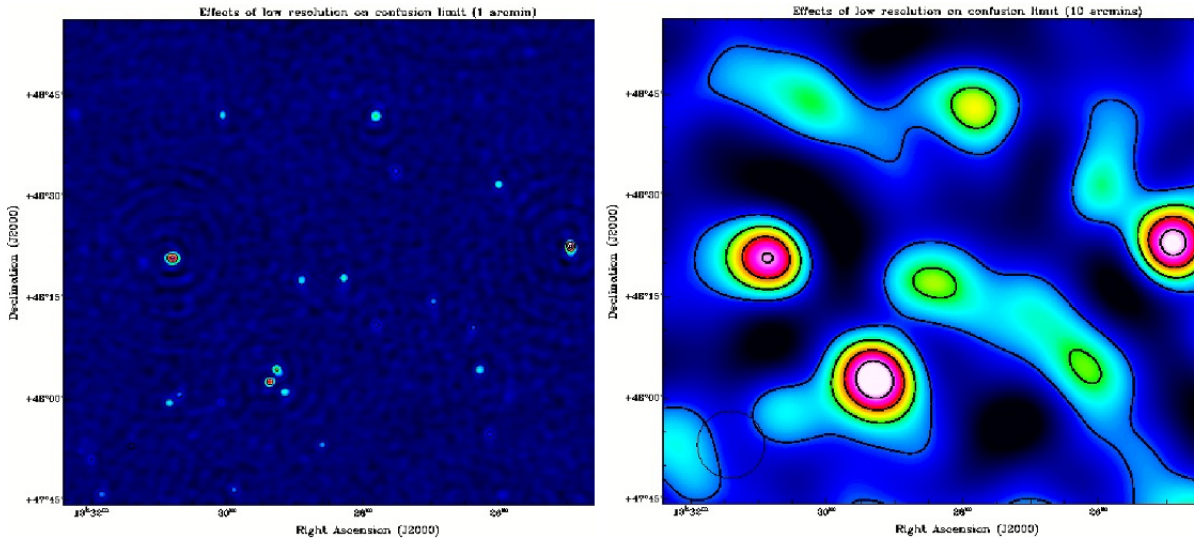

Figure 2.2: Two images showing the effect of how reduced resolution will impact the sensitivity of a LOFAR observation.

2.2.2 Absolute Flux Scale and the Need for Calibrators

Another difficulty imposed onto low frequency radio astronomy is the lack of a broadband flux scale which is essential for calibration of low frequency interferometers such as LOFAR and the SKA-low. The problem is especially acute in that the widely used Baars radio flux density scale (Baars et al. 1977)[63] is incomplete below 300MHz. The Baars' scale is based on absolute flux measurements of Cassiopeia A over a wide range of epochs and frequencies. The principal reason for using Cas-A is that many absolute flux measurements exist due to being the brightest radio source in the sky. However, as Rees (1989) [64] points out, the flux of Cas-A is decreasing with time and that this decrease also depends on frequency. Another low frequency absolute flux scale of Roger, Bridle and Costain (1973) [65] exists. This scale is based on observations of 225 sources with the Dominion Radio Astrophysical Observatory's 10-MHz and 22-MHz arrays between 1965 and 1973. This scale is accepted as the best low-frequency flux scale available. However, having more than one absolute flux scale isn't helpful and makes quantitatively combining and comparing data from various telescopes and surveys difficult. Therefore when comparing source fluxes it is essential that each catalog used is scaled to the same flux scale. The scale factors from various catalogs to convert to the RBC scale can be found in Scaife and Heald (2012) [66]. In addition, any comparison with higher frequency measurements, the higher frequency measurements needs to rescaled to the RBC scale. Fortunately, at frequencies $\gtrsim$ 300 MHz, the RBC scale is in agreement with the KPW scale (Kellermann et al, 1969)[67] and the conversion factors from the Baars et al. (1977)[63], table 7 can be used.

With regards to what calibrators to be used, Cas-A and Cygnus-A, while the brightest sources in sky have extremely detailed morphologies. This would make calibration of an interferometer array with arcsecond resolution difficult without a very detailed skymodel. Therefore, the calibrators need to not only dominate the visibility function but also be compact compared to the angular resolution of the interferometer. With LOFAR in mind, Scaife & Heald (2012) [66] created an initial list of bright compact sources from the 3C and revised 3C catalogue with the criteria that the sources:

- have positions above 30° declination.

- have a flux density at 178 MHz greater than 20 Jy.
- have an angular diameter less than 20 arcseconds.

Six sources were found to fit this criteria and are detailed in table 2.1 below.

Table 2.1: Calibration Source Sample taken from Scaife & Heald (2012)

Source	RA (J2000)	Dec (J2000)	S_{3C} (Jy)	$\Delta\theta$ (arcsec)
3C48	$01^h37^m41.3^s$	$+33°09'35''$	50 ± 11	< 1
3C147	$05^h42^m36.1^s$	$+49°51'07''$	63 ± 12	< 12
3C196	$08^h13^m36.0^s$	$+48°13'03''$	66 ± 20	< 12
3C286	$13^h31^m08.3^s$	$+30°30'33''$	21	< 3
3C295	$14^h11^m20.5^s$	$+52°12'10''$	74 ± 15	< 12
3C380	$18^h29^m31.8^s$	$+48°44'46''$	70 ± 10	< 20

More detailed models of these calibrators at higher resolutions are currently being worked upon by the LOFAR community for better calibration on the longest baselines. How to observe and use these calibrators to calibrate LOFAR data will be detailed in section 2.7.2.

2.3 Background to LOFAR

LOFAR, the Low Frequency Array,(van Haarlem et al. 2013) [68] is a new and innovative low frequency radio telescope designed and constructed by ASTRON. Its construction was motivated by the scientific aims described in the previous chapter and was originally intended to surpass the power of previous interferometers in it's frequency range by 2-3 orders of magnitude, providing a square kilometer of collecting area at 15 MHz, milliJansky sensitivity and arcsecond resolution.

However, due to funding constraints, the original collaboration was split into three ongoing projects, namely LOFAR, the Long Wavelength Array (LWA) (Ellingson et al. 2013) [69] and the International Murchison Widefield Array (MWA) (Lonsdale et al. 2009) [70].

As LOFAR is such a flexible but complicated instrument this chapter will only cover aspects applicable to interferometric imaging. For a complete coverage of LOFAR, please refer to van Haarlem et al. (2013).

2.4 Broad overview to the LOFAR system

LOFAR (van Haarlem et al. 2013) [68] currently consists of a total of 40 LOFAR stations located in the Netherlands with an additional 8 international stations located in various European countries. The amount of international stations is set to increase with additional countries opting to join. The majority of the stations are located in the LOFAR core near the town of Exloo which is a densely sampled, 2-km area (which can be seen in figure 2.3) which ensures excellent uv-coverage for detecting extended emission.

The LOFAR core is located where relatively low levels of RFI are present. LOFAR is capable of operating at frequencies from 10-240 MHz and has two types of antennas to detect radio waves from this radio range. The first is the LBA (Low-Band Antenna) which operate from the ionospheric cutoff near 10 MHz up to about 90 MHz due to the FM band. As this FM band is extremely strong RFI, filters are in place which limit bandwidth from 30-88MHz. This filter can be deselected by the user.

The LBA element is sensitive to two orthogonal linear polarizations. One LBA antenna can be seen in figure 2.4. The simple design of the LBAs make it sensitive to the entire visible sky. The HBA (High-band antenna) covers the frequency range from 110-250 MHz. This is split in the receiver into three parts namely HBA-low (110-190 MHz), HBA-mid (170-230 MHz) and HBA high (210 - 250 MHz). The observations presented in this thesis are from HBA-low only. At these frequencies the sky noise is not dominating unlike the LBAs and therefore the HBAs have a very different design in order to increase the sensitivity. HBAs are gathered together into 'tiles' of 16 antenna elements which include initial analogue amplification and the first stage of analog beam forming. A 'tile beam' is formed when combining the signals for each of these 16 elements in phase for a given direction in the sky. The HBAs are controlled by the Monitoring and Control system (MAC).

Figure 2.3: An overhead view of the LOFAR superterp.

The analogue data signals from the HBA tiles and LBA antennas are then transported via coaxial cables to the electronics cabinet which is located at the edge of every LOFAR station. The signals first reach the receiver unit (RCU) where they are filtered, amplified and then digitized. Once digitized, further processing is done by the remote station processing (RSP) boards. These RSP boards first separate the input signals from the RCU into 512 sub-bands via a polyphase filter (PPF). The sub-bands can have a bandwidth of 156 or 200 kHz depending on whether the 160 or 200 MHz sampling clock was selected. For HBA low and LBA, which are the bands used in this thesis, the sampling clock is always 200 MHz. Usually, the sample values are stored using 16 bit integer representations, which allows 244 sub-bands to be available for a total bandwidth of 48 MHz per polarization. But recently a 8 bit integer representations can be utilized which allows the user to have up to 488 sub-bands for a total bandwidth of 96 MHz per polarization. Tests showed that strong RFI that can saturate the 8 bit mode is extremely rare.

Once the sub-bands have been created, the next main processing step is the digital phase rotation based beam former. The beam former sums all the signals from selected RCUs after first multiplying them by a set of complex weights which take into account the phase rotation produced by geometrical and other delays. These weights are calculated in the local control unit (LCU). The beam forming is performed independently per sub-band and the resulting beam for each sub-band is called a beamlet. Theoretically, the user could point the same number of simultaneous beams on the sky as sub-bands available, for example, at 16 bit mode, the user would be able to point 244 independent beamlets on the sky. However, at the moment the independent directions per station is currently limited at eight by the

(a) LBA dipole

(b) HBA tile

Figure 2.4: Figures showing both types of LOFAR antennas.

system control software.

After the beam-forming step the data is then transferred to the correlator at the Central Processing (CEP) facility in Groningen.

2.5 LOFAR at station level

One can think of a LOFAR station as one of the dishes of a traditional radio interferometer. They provide collecting area and raw sensitivity as well as pointing and tracking capabilities. However, the antennas in a LOFAR station which form a phased array, do not physically move but use beam forming techniques to point and track targets in the sky. What is important is not only do LOFAR stations contain the necessary antennas, electronics etc, but also significant local computing resources as well. This allows for station level beam forming to allow for rapid pointing of the telescope as well as performing multiple observations at once. Each separate LOFAR station can be used as a single dish radio telescope.

LOFAR stations can be grouped into three categories, namely, core, remote and international; corresponding to their distance from the center of the array. For example, the stations CS001HBA0 & CS001HBA1 are the two ears of HBA core station number 001 whereas RS509HBA is a HBA remote station number 509. More importantly, each of these categories of stations have a different antenna configuration. Core and remote stations in the Netherlands have 96 LBA and 48 HBA antennas and a total of 48 digital receiver units (RCUs). It is also worth mentioning that the layout between the HBA tiles in core and remote stations differ in that, for remote stations, all HBA tiles are contained in a single field whereas in the core stations, the HBA tiles are contained in two sub stations of 24 tiles each. International HBA stations consists of a single HBA field of 96 tiles. For LBA, the antenna fields are about the same for all types of station. However the core and remote LBA stations only use half of the antennas. The station layouts for the different stations can be seen in figure 2.6.

2.6 LOFAR Radio Environment

Even though the superterp is located in the mostly rural area of Drenthe, households can still exist within 1km and even closer for some stations. Therefore, contamination of the celestial signal of interest by radio-frequency interference (RFI) has always been a major concern for LOFAR. During the hardware planning phase of LOFAR, these concerns played a big part in the hardware design. This included

Figure 2.5: A map showing the layout of the majority of the stations in the LOFAR core with the superterp in the center (source: OpenStreetMap).

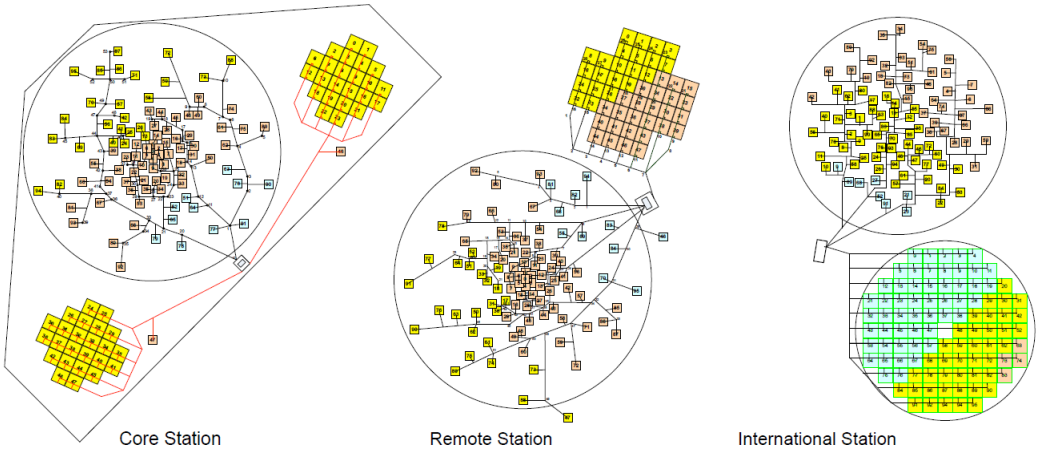

Figure 2.6: Layout diagram of the different LOFAR stations.

placing shielded cabinets around the electronics on site to prevent self-interference; applying steep analogue filters to suppress the FM bands and frequencies below 10 MHz; and applying strong digital sub-band filters to localize and confine RFI in frequency. The distribution of RFI in frequency can be seen in figure 2.7.

RFI tests were performed by Offringa (2012) [71] using surveys from 24 hour LBA & HBA observations. It was found that the HBA survey had a higher RFI occupancy of 3.18 % than the LBA survey

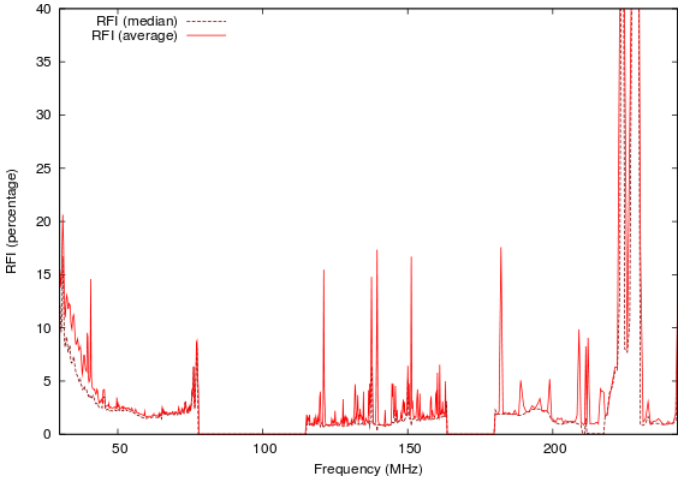

Figure 2.7: The RFI distribution in most frequencies observable with LOFAR. While at most frequencies, RFI is only at a few percent there are exceptions. Notably below 30 MHz which is plagued by RFI sources such as air traffic and short wave radio broadcasting. In addition, the effect of the FM band can be seen in the higher frequencies of the LBA frequencies. Image from the LOFAR Imaging cookbook and André Offringa.

of 1.77 % after correcting for the changing sky temperature. However, it was also seen that almost all stations have less than 2.5% RFI occupancy with exceptions of CS101HBA0 and CS401HBA0 with 3.9 % and 7.5 % which would suggest a local RFI source such as sparking electric fence or a lawn mower near the two stations.

Another important result from these surveys is that no significant relation was found between the hour of the day and the RFI occupancy due to less activity at night. This was found for LBA and HBA data. Overall, the LOFAR data loss due to RFI is low, which is surprising in that LOFAR is built in a populated area and operates at low frequencies. This is due to the fact that many interfering sources contaminate a narrow frequency and are of short duration. LOFAR's high time and frequency resolution can minimize the data loss due to these sources of RFI. Also the hardware design as stated above also matters as well as the sophisticated software used for the flagging process which will be discussed in the next chapter.

2.7 Processing LOFAR data

Processing LOFAR is a big challenge due to the vast amount of data been produced as a result of high resolution multi channel receivers. This has been the case for WSRT for the past number of years and now recently with the wideband receivers of the JVLA. So like these new instruments, LOFAR also investigates data handling management. For a normal HBA Dual 6 hour observation with 244 subbands with 64 channels at a 1 second visibility averaging, you would have a dataset of 25.7 Terabytes.

Obviously with this huge amount of data, automated routines need to be implemented as manual editing and reduction would take months if not years. The full processing flow chart can seen in figure 2.8.

The final correlated data ready for reduction is in the form of a Measurement Set (MS)[1].

[1] http://casa.nrao.edu/docs/UserMan/UserMansu82.html

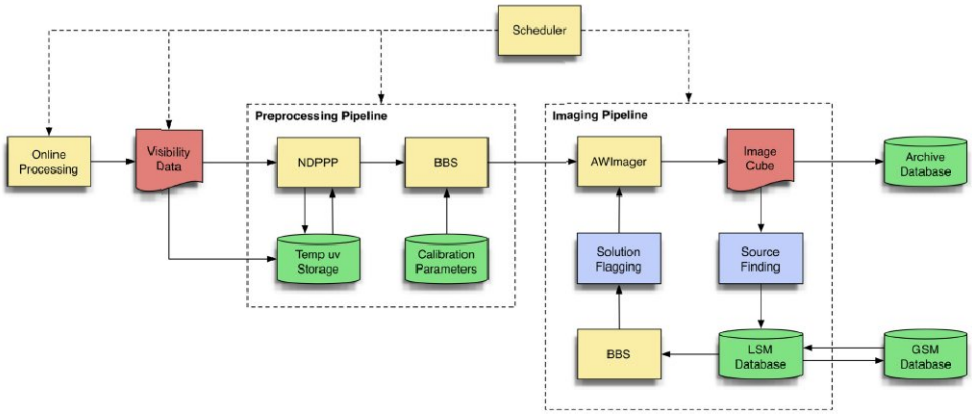

Figure 2.8: A flow chart showing the order of LOFAR data reduction and the main software used. From van Haarlem et al. 2013 [68].

2.7.1 Preprocessing LOFAR data

The first steps of LOFAR data reduction is termed preprocessing which has 3 main steps, namely in order:

- Flagging for Radio Frequency Interference (RFI).
- Subtraction of the brightest sources via demixing.
- Averaging or compression of data in frequency and time.

These data reduction steps can be implemented via the program called NDPPP (New Default Pre-Processing Pipeline). This routine can perform the above steps and much more including combining subbands into a single MS or add core stations to form a superstation, which is essential for VLBI work.

Flagging of residual RFI

As mentioned before, frequencies covered by LOFAR are considerably affected by RFI and therefore an efficient and automated method to edit the data of RFI is essential to obtain high quality images. While there are numerous possible techniques to remove RFI, almost every observation needs to be post-processed due to RFI effects.

The AOflagger (Offringa et al. 2012) [72] which can be called via NDPPP or run independently was originally written for the Epoch of Reionization key science project but has since been optimized to be accurate for any observation. The AOflagger (Offringa et al. 2012) [72] uses a SumThreshold method which detects series of samples with higher values than expected to detect RFI. An example of the flagging results that AOflagger can produce is shown in figure 2.9.

For a more detailed explanation of the flagging detection and editing alogrithm, more information can found in Offringa et al. (2010)[73], (2012)[72]).

For the best results, this flagging routine must be performed on the raw dataset, however, this leads to long processing times. Usually for LOFAR data, the default settings are sufficient. Such results can be seen in figure 2.9

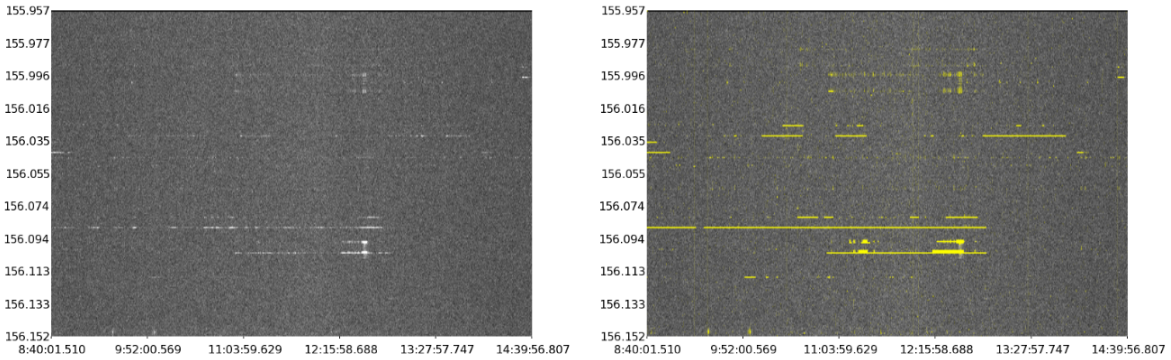

Figure 2.9: Flagging results on LOFAR data from a subband around 156MHz using AOFlagger. Left shows a time-frequency plot with amplitude as greyscale before flagging and right shows after flagging which are shown by the yellow pixels. From Offringa et al. (2010b)[73].

Demixing

One of the more challenging problems of processing LOFAR data is the contamination of very bright sources dominating the low frequency sky. This contamination is due to the strong sidelobes of the LOFAR station. These sources include Cassiopeia A, Cygnus A, Virgo A , Taurus A and Hercules A, which are known as the A-Team sources in the LOFAR community. The Sun can also pose problems to LOFAR data.

The process to remove these A-Team sources that is used in LOFAR is known as *demixing* (Van der Tol, 2007) [74] which consists of solving for the directional dependent gains towards the A-Team source/s which are problematic. Then the A-Team source can be then subtracted from the data but a very accurate model is required. This can be performed using NDPPP and can be invoked through the demixer step. Previously, a major problem was that demixing would not work sufficiently when the distance of the A-Team source to the observed field was less than 21 degrees at 60 MHz, but this has now being solved.

Usually when demixing, one would have to demix all subbands for all times ranges, however, the A-Team signal is highly time and frequency dependent. Due to this, high time and frequency resolution are needed to prevent smearing which makes this technique computationally expensive. In addition as the A-Team signal is highly time and frequency dependent, this breaks the basic calibration rule that sufficient S/N is required for solving throughout the whole observation. Fortunately, a 'smart' demixing algorithm is now being tested and will only demix when a A-Team source is detected in the sidelobes through simulations.

It is found that for LBA observations, demixing is always necessary as the observations are usually strongly affected by A-Team sources especially on the short baselines. In addition, it is often found that the A-Team signal dominates completely over the source signal.

For HBA, usually some A-Team flux is present but is usually more intermittent. This can be due to one or more of the A-Team sources passing through one of the sidelobes or worse still, the grating lobes.

Figure 2.10 shows the XX & YY phases for two example short baselines suffering from A-Team contamination.

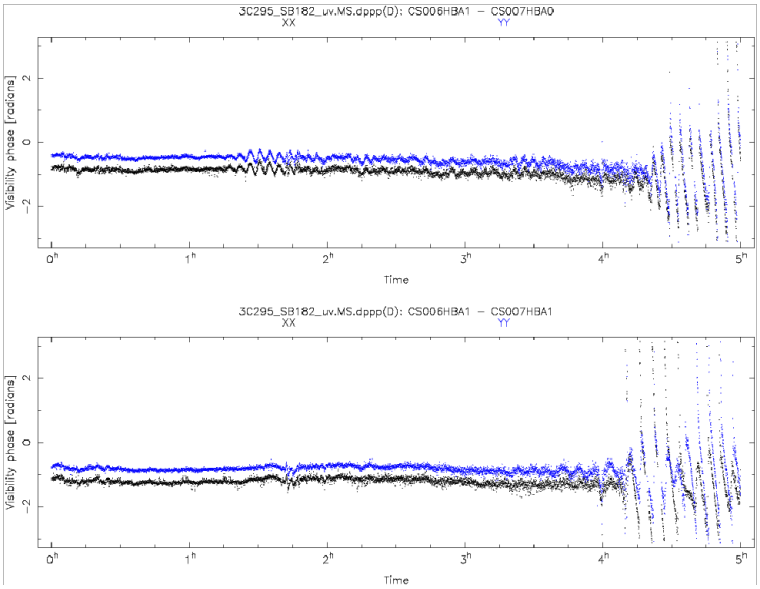

Figure 2.10: An example of two baselines suffering from A-Team contamination in the last hour of the observation.

Averaging of data

Averaging the data in time and frequency is important to minimize processing time to a more manageable duration especially with regards to calibration. But the user needs to take in account several factors when compressing. Firstly, averaging too much in time can produce time averaging smearing. While this isn't a huge concern when one is interested in the region around the phase center when using 20km baselines, it does become important when one is interested in the entire field at 5″ resolution (which is possible using all Dutch baselines) as this effect gets worse with increasing frequency and baseline length.

Secondly averaging too much in frequency can produce bandwidth smearing. The effect of bandwidth smearing on the final image radially smears sources located far from the phase center. In addition it also reduces the maximum RM that can be detected using RM Synthesis as this depends on the width of the channel. In effect, this is the same as bandwidth depolarization.

Averaging can be done again via NDPPP.

2.7.2 Calibration

Blackboard Selfcal (BBS) (Pandey et al. 2009) [75] is the main software that is designed for the calibration and simulation of LOFAR data. What is important to know about BBS is that it makes extensive use of the RIME formalism developed by Hamaker et al (1996) [56] and explained in section 2.1.1 in order to model and solve for the many complex effects explained before. The RIME provides a complete model of a generic interferometer. Each linear physical effect that transforms or changes the E-field vector in any way before correlation can be described by linear transformations, namely a 2×2 Jones matrix.

Most Jones matrices in BBS are general in nature, such as complex gain or Faraday rotation. The beam model is LOFAR specific, for example the array factor or dipole model. BBS requires an observation, a source catalogue i.e a skymodel and a configuration file known as a parset. Optionally,

model calibration parameters such as gain amplitudes obtained from an external calibrator contained in an instrument table can also be used to calibrate an observation with BBS.

The parset file is important as it specifies the operations that need to be performed on the observation. The bbs-controller process instructs the bbs-reducer process to load a chunk of time into memory and then performs all operations listed in the parset file on this chunk. BBS can also be very useful in simulating visibilities given a skymodel and the time of the observation. This allows the observer to check if a A-Team source would effect one's observation and enable them to select demixing for preprocessing. After the processed chunk is then written to disk, the next chunk is loaded and this process continues until the entire observation has been processed.

Calibration via gain solutions transfer

Usually in interferometry an external calibrator is used to solve certain elements of the RIME. These solved values can be then transferred to the target source. However, with normal radio interferometry such as the VLA this would mean slewing from target to calibrator and back to the target wasting precious time. As LOFAR can observe many parts of the sky at once due to it's beam-forming abilities, it can bypass this problem and give the observer far more freedom. With LBA, a calibrator source can be observed always simultaneously as the LBA dipoles are able to 'see' the entire sky. HBA on the other hand, a calibrator source can be observed simultaneously only if the calibrator and target source are within 10°, which is the FWHM of the tile beam.

For calibration of LOFAR HBA data, two main approaches are used:

1. If the target and calibrator sources are within 10°, the total bandwidth is divided equally between them. The drawback is of course the observer loses half of their bandwidth. The gain solutions found from the calibrator for one subband which are contained in an instrument table are then transferred to the target subband at the same frequency. This is illustrated in Figure 2.11.

2. If the target and calibrator sources are more than 10°, then the calibrator has to observed intermittently in blocks of 2 minutes between target observation blocks during the observation. The disadvantage of this method is that it creates many MS files (one MS for each block for each subband) which make calibration more tedious.

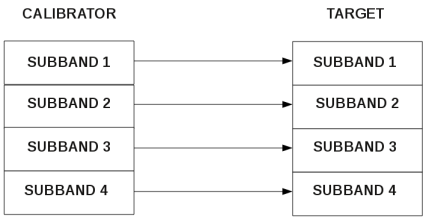

Figure 2.11: Illustration showing the concept of transferring gain solutions from calibrator to target subbands.

First commissioning tests using the first method explained above are presented in 2.8.1 on page 35 and improvements to it are shown in 2.8.2.

2.8 Commissioning results

During the course of this thesis, several commissioning tasks important to the LOFAR Magnetism Key Science Project were worked upon. It is important to remember that these tasks were performed when the understanding of LOFAR was low. Looking back on these tasks it is now easy in some cases to see what was the problem was but hindsight is a wonderful thing. In this section I will detail the commissioning tasks and testing I performed which benefited the LOFAR community and MKSP.

2.8.1 Comparison between selfcal and transfer of gains

The first observations of M51 took place in 2011, when much of the array and software were very much still incomplete. More importantly, the understanding of the system and methods to calibrate LOFAR data were still very much in it's infancy. This observation, along with NGC4631 were observed to test if the gain solutions obtained from a nearby external calibrator (in M51's case, 3C295) could be applied to the target source (Transfer of Gain Solutions Method–TGS method). These objects were chosen largely because the external calibrator was less than 10 degrees and therefore within the LOFAR HBA tile beam.

First attempts to self calibrate this M51 data were performed for a single subband of 200 kHz bandwidth at 139 MHz was to use a simple skymodel from the WENSS survey, namely a Gaussian source at the the location of M51. A normal self calibration was applied with BBS with the beam correction not applied. A reasonable but insufficient image was produced (see figure 2.12), as some kind of strange extended feature can be seen in the South East of the galaxy which is not seen at higher frequencies. This is due to two point sources which are located there and therefore this method has failed.

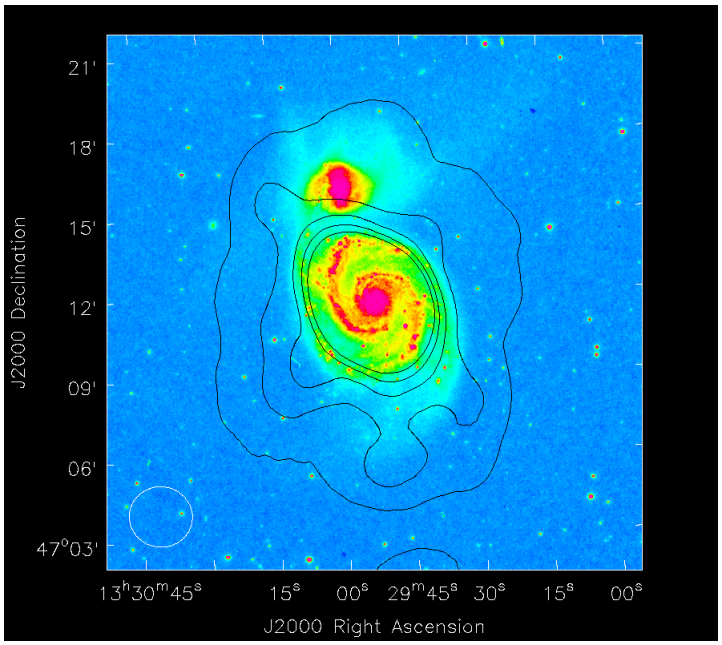

Figure 2.12: First attempt of creating an image of M51 using a skymodel from the WENSS survey for self calibration. The contours represent the LOFAR image starting at three times the rms noise. The background image is an optical image from the Digital Sloan Survey.

Efforts then moved on to do a self-calibration from a GMRT image at a frequency of 325 MHz

supplied by Andrew Fletcher. Attempts to extract the clean components in order to create a skymodel from the image failed. Creating a sky model through shaplets was then attempted. A point source model was first created which would be added to the extended flux later on. This point source model now had to be subtracted from the original image. However when subtracting, too much of the extended emission was subtracted by the shaplet software. This approach of creating a sky model was then abandoned.

Finally the source finding software PyBDSM[2] was used to create a skymodel, the best results were obtained with a threshold of 3σ.

From this skymodel an image was created (See figure 2.13). However, one can see again the very clear structure in the South-East due to 2 point sources. Due to this, the two most prominent sources from this region were left out from the skymodel to see the effects. What was seen was that the structure still appeared, but it did decrease in intensity, especially at the location where the sources were located. This suggested at the time that this structure was not entirely due to the skymodel. Since then, this structure has not been seen again in any other subbands using the TGS (Transfer of Gains Solutions) Method.

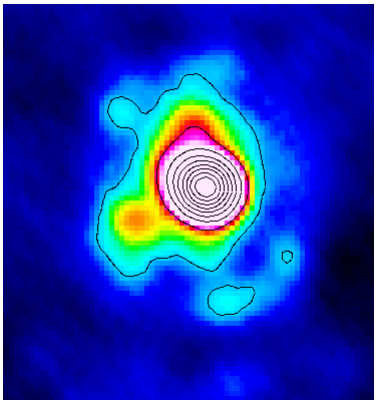

Figure 2.13: An image of M51 using a GMRT skymodel for self calibration.

When performing the TGS (Transfer of Gains Solutions) method, 3C295 was calibrated with a simple point source skymodel and from this, the electronic gain amplitudes and phases are determined. These gain solutions were then transferred to M51 with BBS. During the transfer, BBS corrects for beam effects. When comparing the complex gains for both XX and YY correlations, the TGS method gives a much clearer determination of the gain solutions than the self-cal method does.

Point sources were also compared between both methods, in many cases as can be seen in figure 2.14, no point sources could be seen at all in the self-cal image. Point sources look much more like point sources in TGS method as well as having a better local dynamic range. This is not a surprising as the self cal skymodel used was created from the M51 region only.

Therefore from this task we have learned that:

1. Using a selfcal model of just the galaxy leads to poor results, due to there being alot of extra flux in the field, that is not in the model.

2. Transfer of Gain Solutions Method has been found to work and produces better results than just self calibrating on the target only.

[2] http://www.lofar.org/wiki/doku.php?id=public:user_software:pybdsm

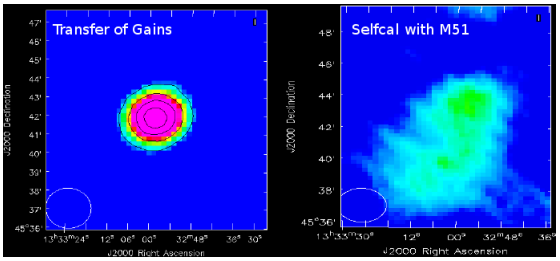

Figure 2.14: Comparison of a single point source from calibration methods. Left:TGS method, Right:Self calibration on M51 model.

2.8.2 Second M51 commissioning observation: interpolation of gain solutions

Motivation

With the 2011 M51 observation it was seen that transferring the gain solutions found from an external calibrator improved image fidelity and dynamic range. However, there was a major drawback in this method in that when using 16 bit mode (8 bit mode was not available at the time) the bandwidth had to be split into two, therefore only leaving 24 MHz of bandwidth remaining on the target. Increasing this bandwidth on the target would not only help in reducing the noise of the final image, it would also result in better λ^2 coverage for RM synthesis. Therefore, a new M51 commissioning observation took place to develop a method of interpolating gain solutions in frequency in order to reduce the number of subbands used on the calibrator. This is illustrated in the diagram 2.15.

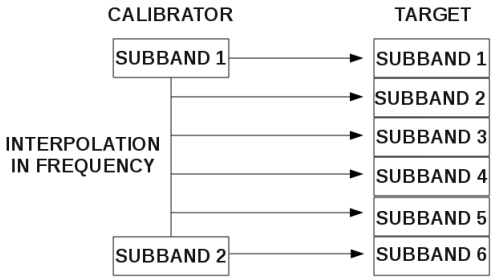

Figure 2.15: A diagram illustrating the benefits of interpolating the gain solutions in time.

Details of observation and initial calibration

The observation took place on April 16-17th 2012 for a duration of 6 hours during the night with a configuration of 54 high band antenna (HBA) stations. This configuration consisted of 23 core HBA stations with split HBA fields (thus acting as 46 stations in the correlator) and 9 HBA remote stations. No international stations were used in this observation. Dual Beam mode was utilized for this observation with one beam targeting M51 ($\alpha = 13^h29^m52.7^s$, $\delta = +47.11.43$) and one beam targeting 3C295($\alpha = 14^h11^m20.5^s$, $\delta = +52.12.10$) for the purposes of flux calibration. As 3C295 was within 10 degrees from the target and within the HBA tile beam, both calibrator and target could be observed simultaneously. 36 MHz were used to observe the target and 9.4 MHz were used to observe the calibrator for the purpose of flux and initial phase calibration. The target subbands were set up in groups or blocks

of 20 adjacent subbands seperated evenly along the entire frequency range. The observational setup is shown in table 2.2.

Table 2.2: Parameters of the M51 commissioning LOFAR observation

Start Date (UTC)	16-Apr-2012/20:30:15.0
End Date (UTC)	17-Apr-2012/02:29:46.7
Frequency Range	120-180.6 MHz
Total Bandwidth on Target	36 MHz
Total Bandwidth on Calibrator	9.4 MHz

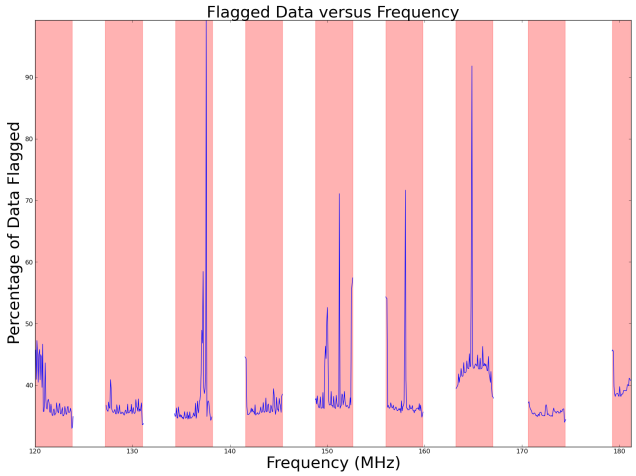

Figure 2.16: This plot shows the total amount of data flagged as a percentage against frequency with the red bars showing the frequency coverage. Note that the last 10 sub-bands at frequencies approximately above 180MHz which were flagged are not included in this plot.

For RFI detection, the AOFlagger pipeline (Offringa, 2010) [73] was performed on the raw data, with the greatest frequency and time resolution. The RFI detection algorithm was executed on all linear correlations which is most accurate. It was seen at frequencies greater than 180MHz were heavily affected by DAB 5 (Digital Audio Broadcast) RFI and 10 subbands were discarded. The total amount of data flagged in frequency can be seen in figure 2.16.

The removal of Cas A and Cyg A contamination was performed on both the calibrator and target data. Improvements was immediately apparent in the visibilities' phases.

At the time of observation, the limited timing synchronization between the station's RSP boards (which had jumps of 5 nanoseconds) caused the performance of several stations to be not optimal. This caused decorrelation of signals which resulted in beam shape deformation, mispointing and loss of sensitivity which worsened towards 100 MHz. This problem was only identified in early 2012 and required the installation of so called SyncOptic boards to correct this, which took place in October 2012. While this observation suffered from this problem and limited the achievable dynamic range and image fidelity, alot could be learned from it. We shall see in later chapters what a positive difference to the data quality these SyncOptic boards made.

The stations suffering from this '5ns problem' were identified by the low signal to noise ratio in visibilities shown in figure 2.17 and low gain solutions obtained from calibrating on the calibrator 3C295. The affected stations were then flagged.

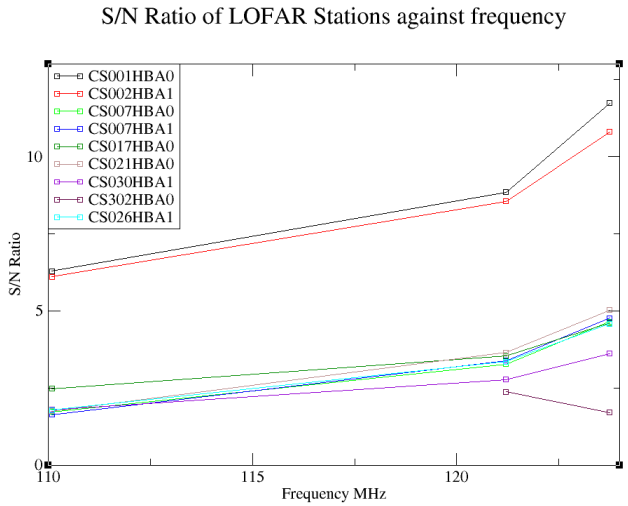

Figure 2.17: Several sub-bands are plotted here for several stations with frequency against S/N. All stations suffering from the '5ns problem' are plotted along with 2 stations that were not affected. The difference in the S/N ratio is very noticeable.

The data was then compressed in frequency to 6 channels per SB and 15 secs sampling time. This flagging and compression was performed using the New Default Pre-Processing Pipeline (NDPPP).

The calibrator subbands of 3C295 were calibrated using a skymodel from Scaife & Heald (2012) [66] using Black Board Selfcal (BBS) software (Pandey et al. 2009)[75].

Developing and testing gain interpolation

After all the calibrator subbands were calibrated and all preprocessing performed on the M51 target subands, development of the interpolation software could now begin which was done in PYTHON[3].

The calibrator gain solutions are contained in an instrument table which is a parmdb database and can be accessed via pyparmdb, a PYTHON class which is created to read LOFAR instrument tables. The gain solutions read from the instrument tables are in complex form and therefore have to be converted into amplitude and phase. As absolute phase is a meaningless quantity, a reference station needs to be chosen, usually a superterp station that wasn't suffering from this '5ns problem' so that it can be subtracted from the other station's phases.

When this is done, the frequency information of the target subband is found using PYRAP[4].

A correct interpolation in phase is impossible unless the phases are unwrapped to avoid any 2π jumps which is shown in Figure 2.18. In order to perform this unwrapping properly, calibrator subbands have to be spaced densely in frequency to avoid errors in unwrapping. In HBA, this is not so much of a problem, but in LBA, wrapping occurs much more in frequency and therefore more calibrator subbands are needed to unwrap properly.

[3] http://www.python.org/
[4] https://code.google.com/p/pyrap/

Also residual RFI can cause higher gains than usual and should be avoided. Therefore before the interpolation, any outlier gain amplitude solutions caused by RFI were found using a MAD (Median Absolute Deviation) threshold chosen by the user and the median gain value was assigned instead.

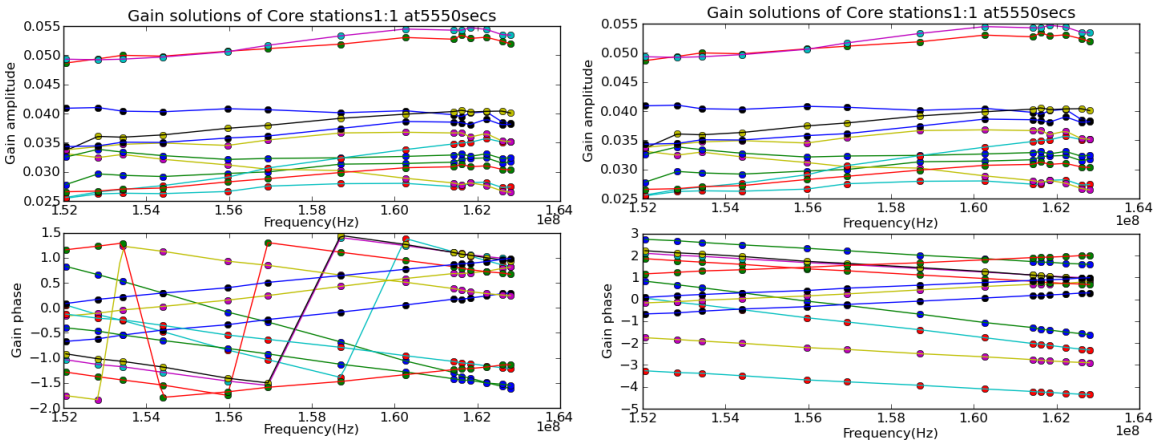

Figure 2.18: Testing of unwrapping phase solutions on a limited amount of frequency coverage. Left shows gain phases before unwrapping and right shows after unwrapping.

The full frequency coverage of the gain solutions for both amplitude and phase for one timestep and for the superterp stations can be seen in Figure 2.19. While the phases change quite linearly and should not be difficult to interpolate, the amplitude could be more difficult. This gain bandpass mirrors the HBA sensitivity profile in frequency. There are two main inflexions, that can be seen at 130 MHz & 150 MHz. Therefore, during observations, the calibrator should be observed more densely at these frequencies in order for interpolation to be more successful.

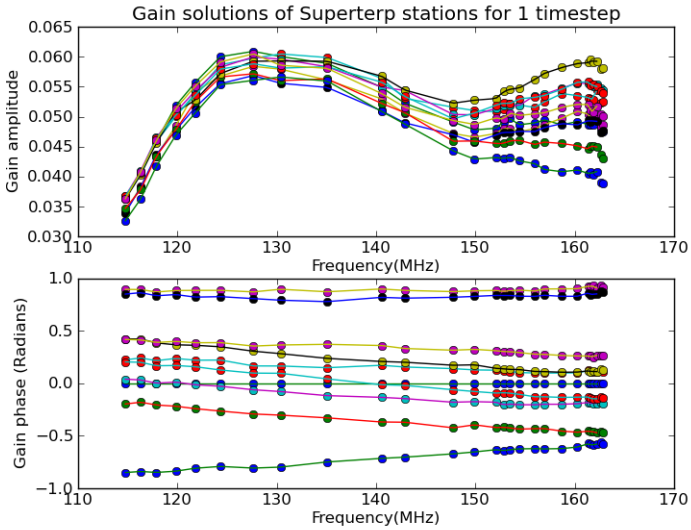

Figure 2.19: The gain solutions (top:amplitude bottom:phase) for the full calibrator frequency coverage of this observation for one timestep and for the superterp stations only.

The gain amplitude solutions for the parallel correlations (XX & YY) found were then interpolated in frequency. 2nd & 3rd order polynomials, direct and spline interpolation were tested to see which predicted the actual gain amplitude. This was done by interpolating between approximately 26 calibrator subbands and the interpolation solution was compared to another calibrator subband that was not used in the interpolation. It was found that direct interpolation worked best, giving an maximum error of 1-2 % throughout the observation. This test can be seen for two stations at one timestep in figure 2.20. What is also interesting about figure 2.20 is the difference between the two stations. The gains solutions in the station on the right plot are much lower than the station on the left. Secondly, the shape of the gain bandpass is very different. This suggests a major problem with this station, probably due to the '5ns problem' and should be flagged. Therefore plotting the gain amplitudes in frequency for a station is a good way to see if a station is misbehaving.

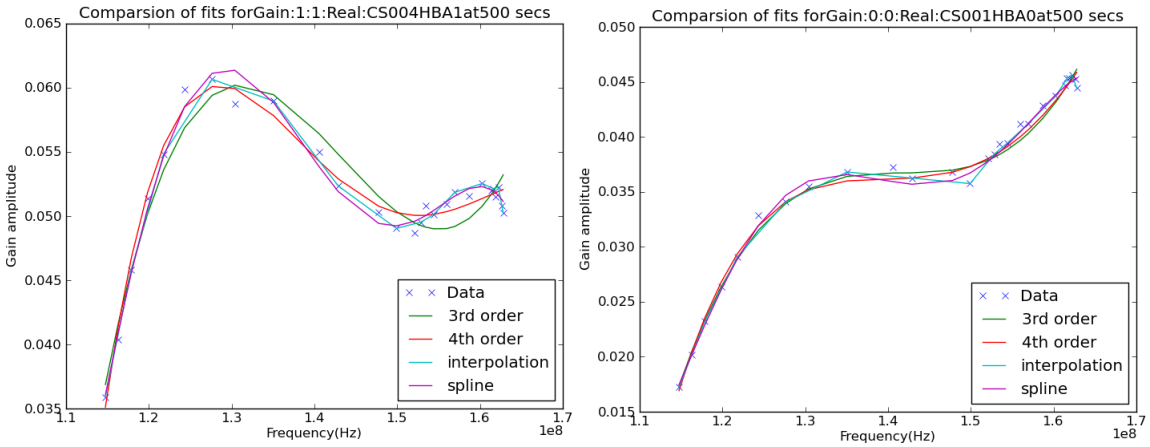

Figure 2.20: The different methods that were tested to see what method worked best for interpolation. Note the difference in shape of the gain bandpass between the stations, indicating a problem with the station on the right.

Once the interpolated values are found for the frequency desired they are written into a text file which is processed into an instrumental table with the parmdb tool. This table is then used to calibrate the target source for the subband at the desired frequency via BBS.

An overall summary of the gain interpolation code is as follows:

1. Read in calibrator instrument tables and target measurement set(s)
   - We use pyparmdb for the instrument tables and pyrap for the measurement set(s).
   - Read gain values, frequencies, and times from calibrator instrument tables.
   - Read target frequencies from target measurement set(s) or frequency list.
2. Open output instrument table(s)
   - We write to an instrument table by writing to a text file, that can then be piped into the parmdb program.
3. Write default values to the output instrument table(s).
4. Apply first filter:
   - Flag gain values that have REAL=1 AND IMAG=0 (or AMP=1 AND PHASE=0) by masking. These values correspond to flagged data.

5. Convert real & imaginary to amplitude & phase
6. Apply second filter:
   - Flag values with amplitude > threshold*MAD (Median Absolute Deviation)
   - MAD runs along the frequency axis (do this for every time-step separately)
   - Flag both amplitude & phase.
7. Reference phases to reference station:
   - final phase = phase − reference station phase
   - If a value of the reference station is flagged, then flag this time & frequency step for all stations
8. unwrap phases:
   - Perform unwrapping so that the phases 'line up' so that no 2π jumps occur
9. Interpolate gain values to target frequencies
   - Linear interpolation between the nearest neighbors in frequency
   - Interpolate amplitude & phases separately
10. Convert interpolated amplitude & gain to real & imaginary if requested
11. Write interpolated gain values to instrument table via parmdb

We can see in figure 2.21 the accuracy of this method for the XX correlation of station CS007HBA01 for the entire observation. The top two plots compares the actual gains (blue) and interpolated gains (green) for both amplitude and phases. For the gain phases we can see the difference in the bottom plot in figure 2.21. Here we see difference for most of the observation $\pm$ 1 $\sim$ 3 degrees except for the end of the observation. Here it seems that the interpolation method fails and this is believed to be due to the influence of the A-Team sources even though it has been demixed from the data.

This method was used for one target M51 subband with both amplitude and phase interpolated from the calibrator 3C295. An image was made and can be seen in figure 2.22. This image came out extremely well with all sources matching the NVSS catalog (showed with green circles). We also see new sources not included in the NVSS survey. This is the first time interpolating the instrumental gains has been done with LOFAR data and this method is now being used by various Key Science Projects for LOFAR.

This method was also tested for interpolating the XY and YX amplitudes but it was seen that the amplitudes are too noisy and interpolation is impossible. Making images using this method produced even greater instrumental polarization and therefore this was abandoned.

The target subands were then combined in frequency and copied using NDPPP into blocks of 20 subbands (4 MHz bandwidth) for a better signal to noise ratio. These blocks of 20 subbands were then phase calibrated using a global sky model. This global skymodel consists of positions of sources from the NVSSS catalogue with fluxes obtained from a power spectral fitting with data from the NVSS (1.4 GHz), WENSS (325 MHz) and VLSS (74 MHz) surveys. M51 itself is describe as a simple Gaussian source.

After this initial calibration, each subband was checked by eye and any RFI or bad solutions resulting from the calibration were flagged.

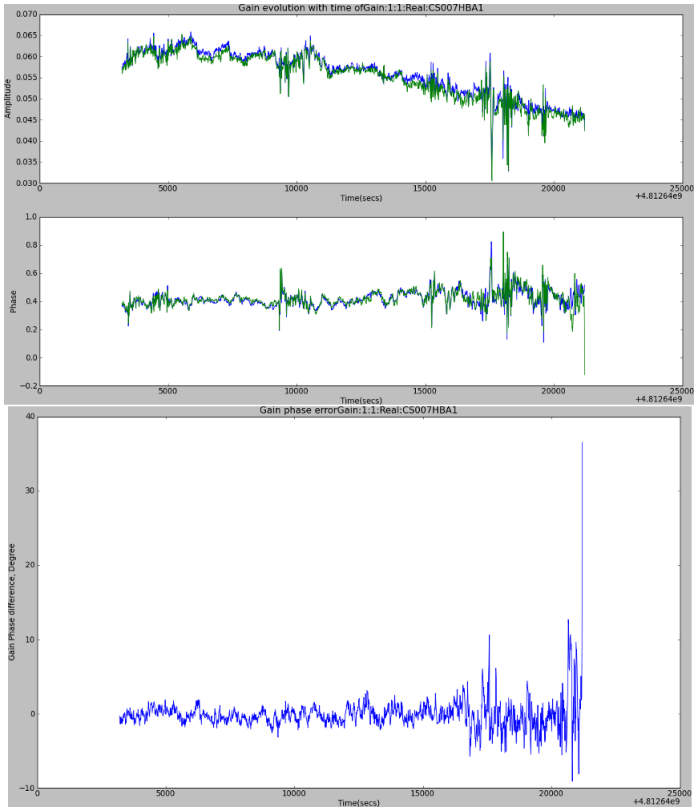

Figure 2.21: Top plots compares the actual gains (blue) and interpolated gains (green) for one LOFAR station. The bottom plot shows the difference between actual and interpolated gain phases in degrees.

2.8.3 Tests on Directional Dependent Calibration with BBS

The classical calibration algorithm used in radio interferometry associates a single direction-independent complex gain term with each antenna of the interferometer. This method of calibration has been extremely successful but only for relatively narrow fields. Now with the next generation of radio interferometers beginning science operations, the limitations of self-calibration are becoming apparent. With LOFAR, direction-dependent effects (DDEs) that vary across the field of view (FoV) as well as between antennas become significant enough to produce dynamic range limiting calibration artifacts.

In this commissioning task, we explain what is the most effective way of peeling with BBS and the effect this has on the extended emission of M51. The idea of peeling is to subtract strong off-axis sources together with their gains. A peeling strategy needs to be devise and the following method was found to be most effective:

1. Choose which sources are to be peeled. Usually the rule of thumb is not to peel more than 5 sources with BBS as the computation time increases drastically beyond this. Of course this may not be a sufficient amount of sources to peel depending on your field.

2. Subtract all other sources contained in the skymodel from the uv data.

3. Solve for the directional dependent gain solutions in the direction of these sources to be peeled for the XX and YY correlation.

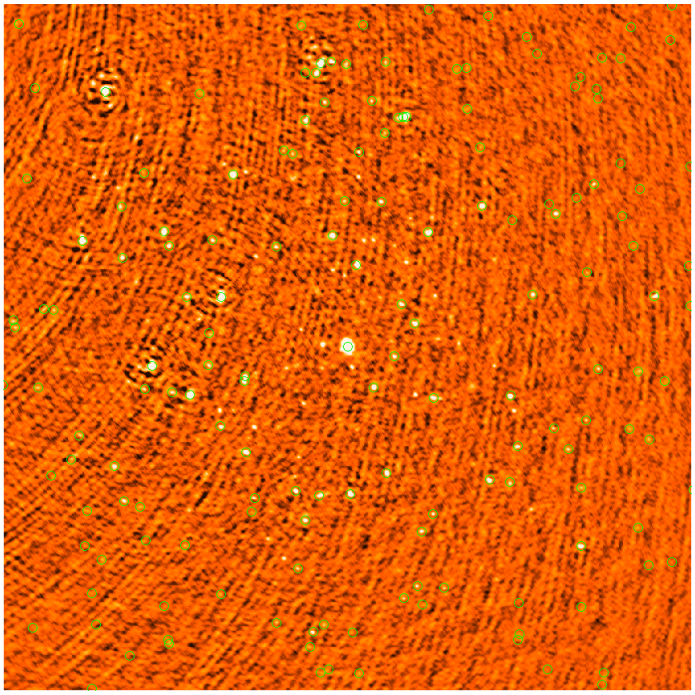

Figure 2.22: First test image of the M51 field using interpolated gains and phases from the calibrator 3C295. The sidelobes coming from outside the image is actually 3C295 which is located 10 degrees from the phase center.

4. Subtract these sources from the field after applying the gain solutions obtained from step 4.
5. Add the remaining sources to the uv data.
6. Solve and apply a directional independent calibration using these remaining sources.
7. Write out the results to corrected uv-data column.
8. Finally add the subtracted sources back into the corrected uv-data column.

This method of peeling produces positive results but much depends on the quality of the skymodel used. Near M51 a decrease of 20% in noise is seen using this method. While this is not a huge difference, the appearance of the field does improve dramatically with peeling and many more sources are visible just by eye.

What is also seen is that the flux of M51 has been significantly reduced. The approximate integrated flux of M51 before peeling is approximately 5 Jy at this frequency whereas after peeling it is 2.9Jy, a 40% reduction in flux. This effect is also seen in MSSS (Multi-frequency Snapshot Sky Survey) with IC342 in chapter 7.3. This of course is not acceptable in order to measure accurate flux densities and therefore had to be investigated.

First of all is seen that when solving for a directional independent calibration decreasing the time cell size by 5 times improved the situation marginally. Overall flux in M51 increases but it is still 35% lower than the prepeeled flux.

The residual maps between unpeeled and peeling state are shown on figure 2.24

Trying a second time but with a different approach on just concentrating in improving the skymodel used in calibration. Instead of using a normal skymodel generated from the NVSS (Condon et al. 1998)

[7], WENSS (Rengelink et al. 1997) [76] & VLSS (Kassim et al. 2003) [6] surveys, a skymodel was generated from the clean components of the initially calibrated data. Only normal Clark clean was used. AWimager was used to get these clean components with the number of clean iterations set to 2000 in order that the relative fluxes were correct as the primary beam is implemented. The threshold of the cleaning was set at the default value. This method actually resulted in better peeling for the brightest sources in field compared to using the gsm skymodel, where artifacts still occurred. This can be seen in figure 2.23

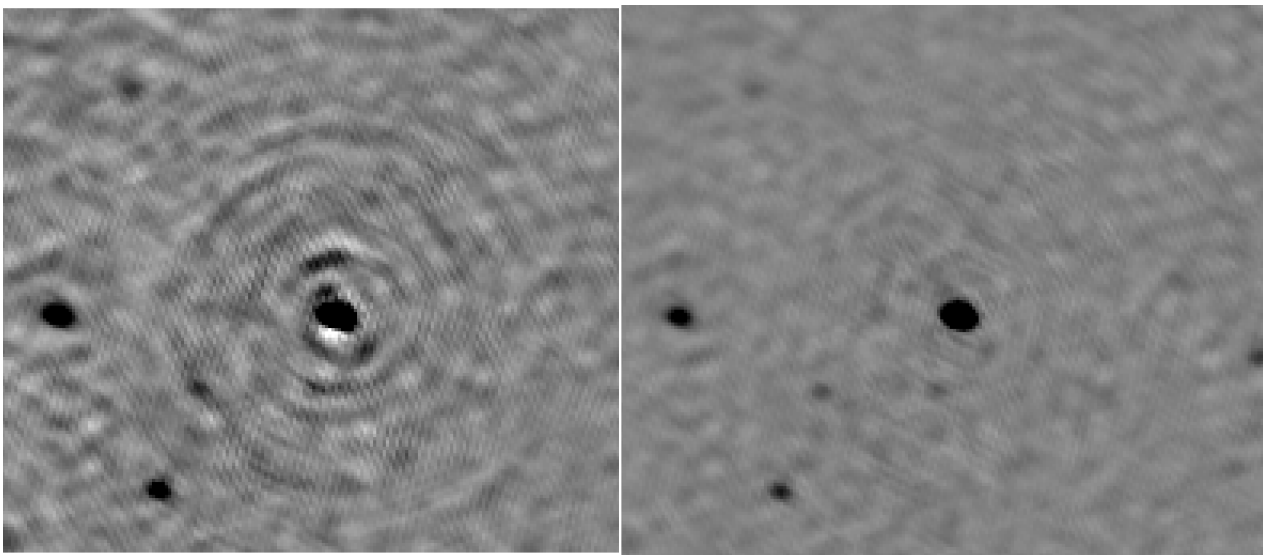

Figure 2.23: Comparison of peeling using different skymodels. Left: peeling with a GSM skymodel. Right: peeling with a skymodel extracted from AWimager clean components.

It was also found that using the skymodel taken directly from the clean components, the total flux of M51 is now only approximately 20% below what it was before peeling. Also it can be seen in the residual image in figure 2.24 which shows that the difference between the unpeeled image and the gsm skymodel peeled image occurs throughout most of the target. The original skymodel for M51 was only a Gaussian located at the central region. However, the difference between the unpeeled image and the AWimager clean component skymodel peeled image in figure 2.24 is mainly located in the central region and where the companion galaxy is. However there is still low level residuals appearing over most of the target. It seems that the reduction of flux of M51 is primarily due to the skymodel being used.

As a final test, a combination of CASApy and AWimager was used to obtain the clean components. First, CASA was used to clean M51 only, using multi-scale (Cornwell 2000) [77] clean making sure no residuals of M51 remained.

Using this hybrid skymodel for peeling, the measured total flux of M51 in this case is seen to be only 2% lower than the unpeeled map. In the residual map the only difference that can be seen is the central region. This confirms that when using a very detailed skymodel of the extended emission, one can retain nearly all the unpeeled flux. It is observed that there is about on average, a 30% decrease in the noise around M51. Artifacts around the peeled sources are removed like that shown in figure 2.23.

In recap, these tests show that the more accurate and detailed skymodel is essential for efficient directional dependent calibration with BBS. This is especially true for extended emission as with so many parameters present, flux that is not described adequately in the model can be subtracted via this method.

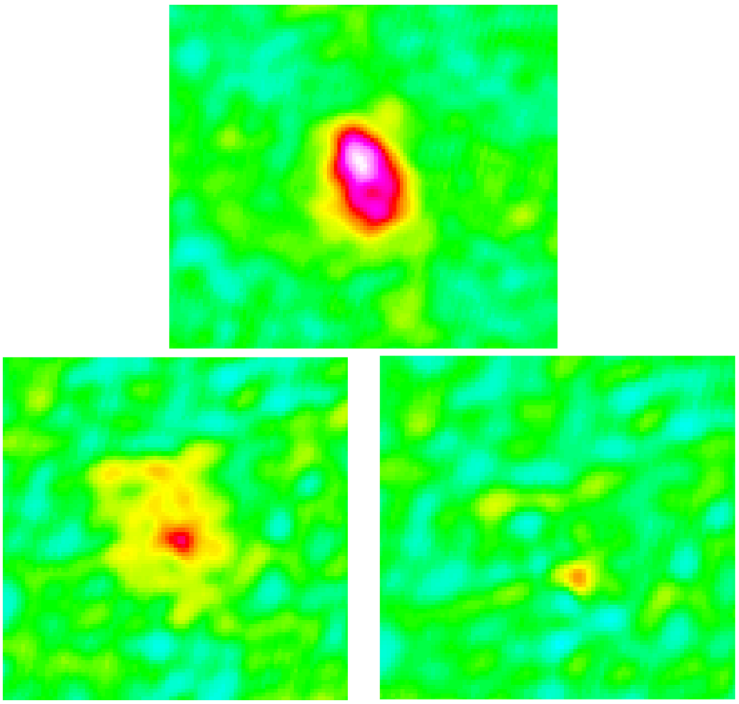

Figure 2.24: Flux difference (residual) M51 images from before and after peeling.Top image shows the greatest difference and for which only a gsm skymodel was used. Bottom left shows the same but for a skymodel taken from clean component from a normal clark clean and finally bottom right is for a skymodel taken from clean components from multi scale clean

Therefore, multi-scale clean is essential to create a good clean component model for the skymodel used in directional dependent calibration if extended emission is present in the field.

2.8.4 Final images of the M51 commissioning dataset

Once directional dependent self calibration was performed on all 8 frequency blocks of sub-bands, each block was then imaged. Images were made with the same imaging parameters and uv-distance for each frequency block with CASA in order to utilize multi-scale clean (Cornwell 2000) [77]. While AWimager would be preferable to use, utilizing a-projection (Bhatnagar et al. 2008) [78] and the primary beam correction, it did not have multi-scale clean as a feature at this time. Each frequency block image was smoothed to 20 arcsec and then all 8 images were averaged in the image plane using an inverse variance weighting scheme. Inverse-variance weighting is a method of aggregating two or more random variable to minimize the variance of the sum. Given a sequence of observations y_i with independent variances σ_i^2, the inverse variance weighted sum is given by:

$$\bar{y} = \frac{\sum_i y_i/\sigma_i^2}{\sum_i 1/\sigma_i^2} \tag{2.24}$$

Several point sources were compared to the Point Spread Function (PSF) to investigate if any point sources were broadened due to phase errors caused by the ionosphere but no significant broadening could be seen. In addition, the astrometry of these source were also checked before any averaging took place. The final image of M51 can be seen in figure 2.25.

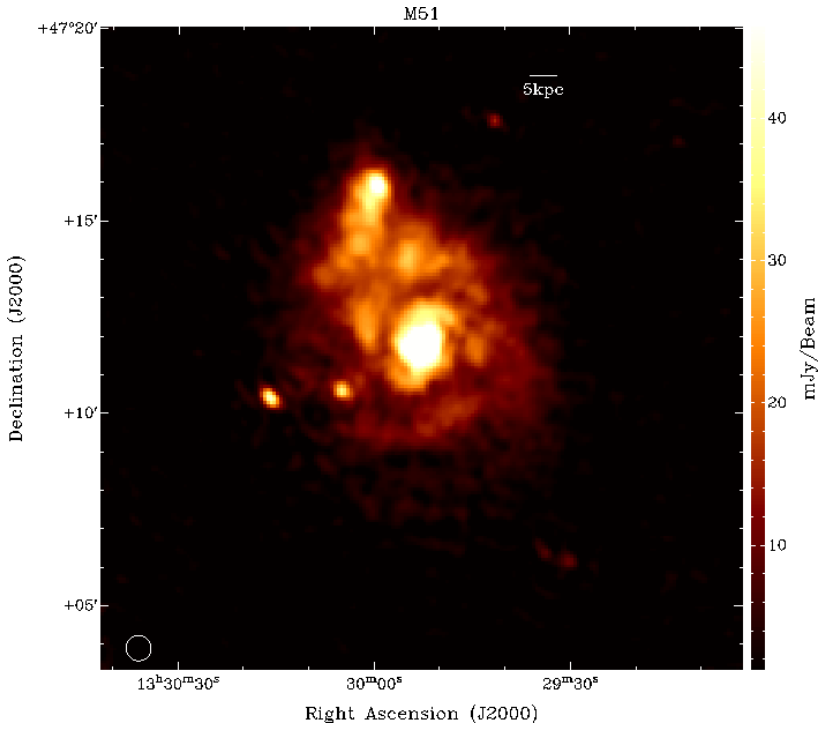

Figure 2.25: Final image of M51 at a central frequency 151MHz with a bandwidth of 34MHz. Resolution is 20″ and rms noise is approximately 1 mJy/beam. Uniform weighting was used.

From this image, we can see compared to the previous observation, a great improvement. Here we were able to achieve 20″ resolution and a noise of 1 mJy/beam using uniform weighting. While this is still far (22 times) from the thermal noise (40 μJ/beam), it is a step in the right direction. We see familiar point source which have been observed in previous observations. The central region and companion (NGC5195) can be observed but the spiral arms while observable are smeared. It should be noted that SN 2011dh (discovered on 01 June 2011 by the Palomar Transient Factory project (PTF)) (Silverman et al. 2011) [79]; (Arcavi et al. 2011)[80] was not detected with this observation. This gives an upper limit of the SNe flux at 150MHz at day 320 of approximately 8.9 mJy ±0.4

At first it was thought that this was similar to what was seen in Basu et al. (2012)[81], where they observed several galaxies including NGC6946 with the GMRT at 333 MHz. There the spiral arm and interarm region become indiscernible due to the low energy CREs diffusing further out than compared to higher frequencies. This would give the arms a smeared appearence. However, there is a danger that this smearing of the spiral arms could be instrumental due to poor phase calibration of the longer baselines. As we will see in Chapter 3 for M51, the overall data quality of this observation was still not sufficient enough to observe the extended disk of M51 mainly due to the 5ns delay in the RSP boards.

2.8.5 Polarization results from the M51 commissioning dataset

RM synthesis was performed on this dataset in order to detect polarization in M51, extra-galactic background sources and the Galactic foreground. First, correction of the ionospheric Faraday rotation was performed using the RMwriter (Mevius et al. in prep) which will be discussed further in section 2.9.2. The average RM correction was approximately 1 rad m^{-2}. All Q & U maps of all channels of the 170

subbands were imaged via CASA with 2′ resolution in order to detect the Galactic foreground polarized emission. RM Synthesis was performed using software written by Mike Bell for LOFAR MKSP purposes. The resulting RMSF is presented in figure 2.26. The Faraday depth resolution is approximately 1 rad m^{-2}. RM clean was then performed on the resulting Q & U cubes using a RM clean code from George Heald.

Unfortunately, no polarization could be detected in M51. With 2′ resolution this was not surprising as it would be expected that severe Faraday depolarization would play a part. In addition, Gießübel et al. (2013) [82] offered pessimistic predictions for LOFAR observations based on WSRT 333 MHz observations. Also the instrumental polarization is very severe for M51, and this makes identification of real polarized emission difficult.

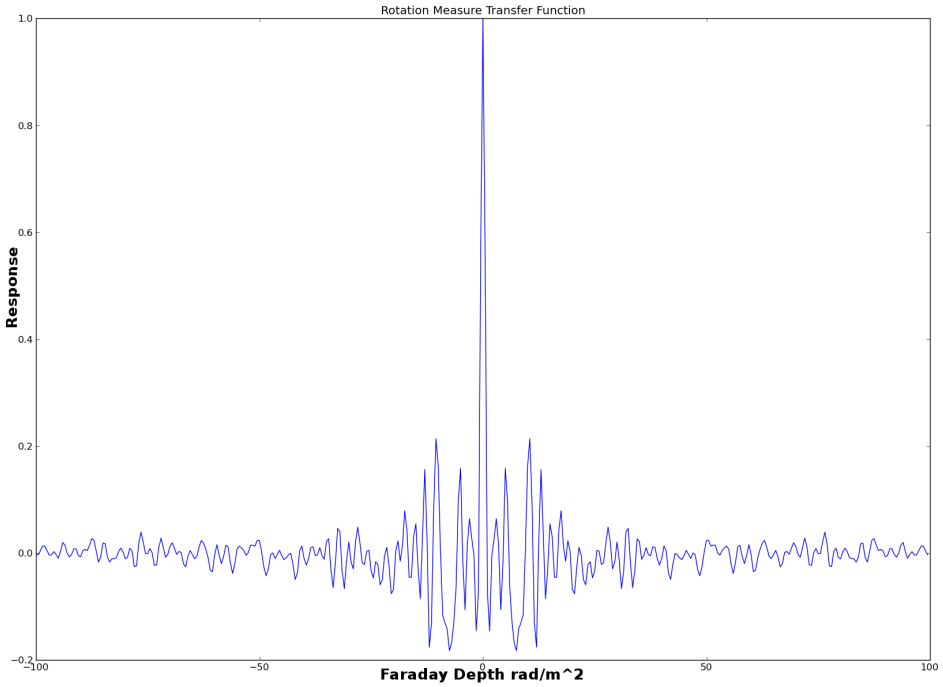

Figure 2.26: The RMSF of this observation using 170 subbands. The Faraday depth resolution is approximately 1 rad m^{-2}.

Whilst M51 is undetectable, we are still able to observe several interesting foreground structures as well as extra-galactic detections.

2.8.6 The Galactic foreground around the region of M51

LOFAR will make the investigation of the distribution of small clumps of thermal electrons and their relation to weak magnetic fields possible, due to its high Faraday depth resolution and Field of View (FOV) making it an ideal instrument to study the Galactic foreground. M51 is located at a high Galactic latitude of 68.5 degrees. At high Galactic latitudes, polarization angle and RM variations are expected to be low, making observations at long wavelengths essential in order to trace them.

De Bruyn et al. (2006) [83] observed the region centered at RA = 13^h14^m, Dec = +45° at 315-388 MHz where they discovered wide-spread polarized Faraday thin emission. However, their Faraday depth resolution was only 12 rad m^{-2}. LOFAR is to improve this by a factor of 12.

The result of RM Synthesis showed several interesting discrete features. The main component of the foreground can be seen as a wide-spread Faraday screen at approximately ϕ = +2 rad m^{-2} shown in figure 2.27. The Faraday spectra in figure 2.28, shows that the polarized emission first appears at ϕ = -10 rad m^{-}2 and continuing approximately to ϕ = +10 rad m^{-2}. This would suggest a magnetic field reversal in this direction. The large-scale diffuse polarized emission at low ϕ is very similar to the features seen in previous WSRT studies at 333 MHz (De Bruyn & Brentjens, 2005) [84].

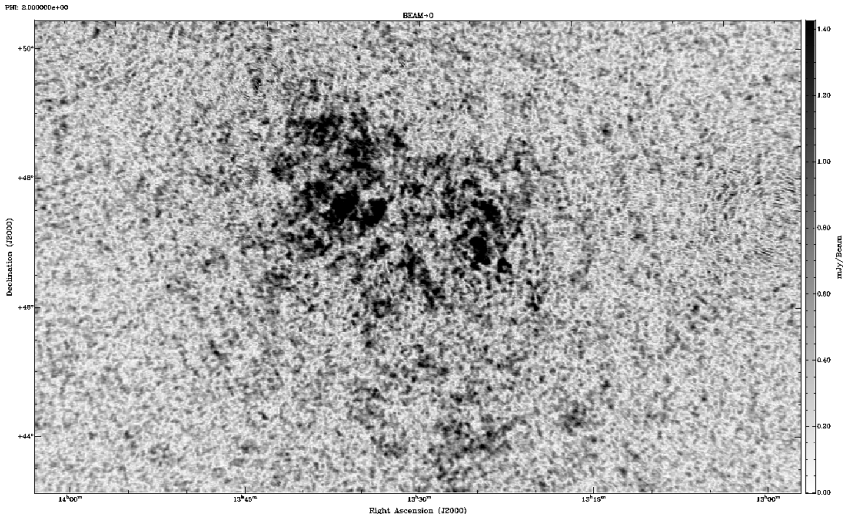

Figure 2.27: A slice in the Faraday cube showing the main Galactic foreground structure at ϕ = +2 rad m^{-2}.

An expanding bubble like structure which is shown in figure 2.29 is centered at RA = 13^h27^m, Dec = 47°53′. This feature expands from ϕ = 3.5 rad m^{-2} to 8 rad m^{-2} with a maximum diameter of 3.75° at ϕ = 7 rad m^{-2}. We see that the PI emission is greatest at the highest Faraday depth is located at the edges of this bubble. This would seem to indicate that we are seeing a shell surrounding a density depletion rather than a filled sphere. It is observed that polarized emission is stronger at around ϕ = 7 rad m^{-2} where the maximum polarized flux of 3.5 mJy/beam is detected. These kinds of expanding structures are also seen in the Fan Region (Iacobelli et al. 2013) [85] where the distance could be approximately estimated using a reference source (usually a pulsar) and the equation:

$$d_D = \frac{\phi_{OBS}}{\phi_{REF}} D_{REF}[\mathrm{pc}] \tag{2.25}$$

where ϕ_{OBS} is the measured Faraday depth of the bubble structure, and ϕ_{REF} the reference value of Faraday depth (or rotation measure) corresponding to the line of sight total which is a distance of D_{REF}.

However, after checking the ATNF catalogue (Manchester et al. 2005) [86] this region of the sky has no pulsars with the closest being 19 degrees away which is not too surprising given the Galactic latitude.

The Galactic foreground around M51 with Cycle 0 data with LOFAR will be studied further by Van Eck et al, in prep.

2.8.7 Extra-galactic polarization detections

In this field, two unresolved extra-galactic sources have been detected. The first is a 4C source, namely 4C +47.38 which is clearly detected at ϕ = +23 rad m^2 with a peak flux of 2.3 mJy. However, there is significant amounts of polarized emission along this line of sight at around ϕ = 0 rad m^{-2}, mostly

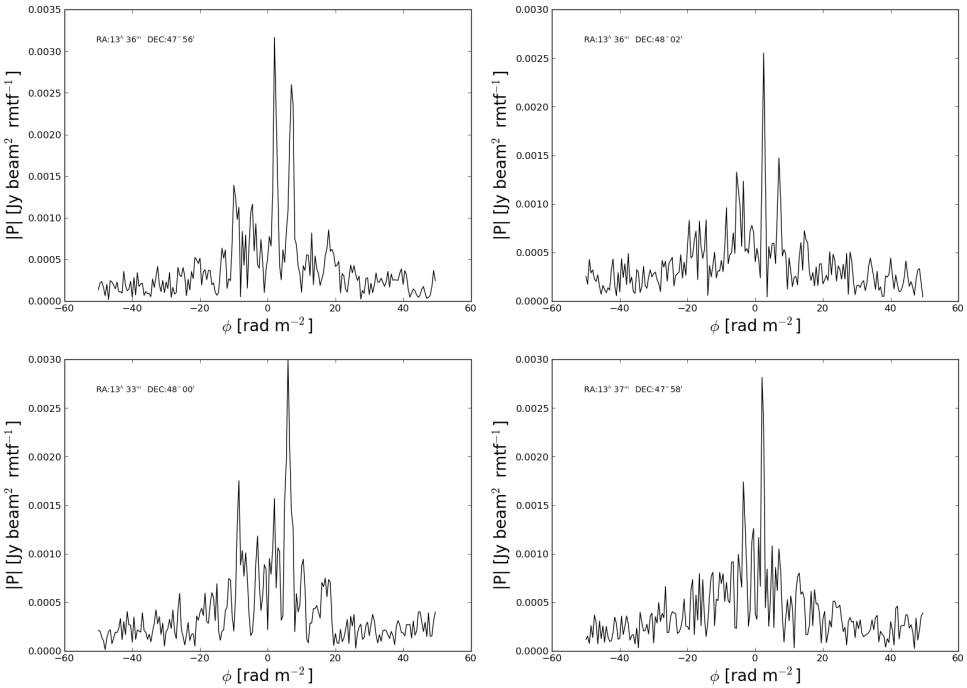

Figure 2.28: Four Faraday Spectra at representative locations. The location where the Faraday spectra was extracted is shown in the upper left of each plot.

instrumental or foreground in nature. Therefore, it is difficult to say at this time if there are multiple Faraday components present.

The second source is J133923+464008, which is detected at ϕ = +20.5 rad m^2 with a peak flux of 4.8 mJy. A slice of the Faraday cube at the location of this source can be seen in figure 2.31. The Faraday spectra for both sources is shown in figure 2.30.

These extra-galactic detections will be addressed in greater detail in the following chapter.

2.9 Additional commissioning tests

2.9.1 Testing of subbands near HBA-low filters

As part of the observation on M51 several subbands were allocated for commissioning purposes to the very extremities of the HBA bandpass, namely 110-115 MHz and 185-190 MHz regions. As the HBA filters are starting to have an effect at these frequencies, it is important to test whether or not these subbands at these frequencies can be used. Using these subbands can potentially increase our $\Delta\lambda^2$ space for RM synthesis, producing a narrower RMSF and hence increasing our Faraday resolution.

The amplitude gain solutions from all the calibrator 3C295 subbands were taken and plotted against frequency as seen in figure 2.32. It can be seen that after 165 MHz the gain decreases slowly up to 175 MHz and then falls sharply as the upper filter starts to take affect. As expected, the gain amplitude below 120 MHz decreases quite rapidly as well. It was seen that RFI above 180 MHz is especially bad and poses a problem to many stations.

The filter sub-bands at 110 MHz and 190 MHz for M51 were calibrated using normal direct amplitude gain transfer (no interpolation) and phase selfcal on the skymodel of the region. These two sub-bands

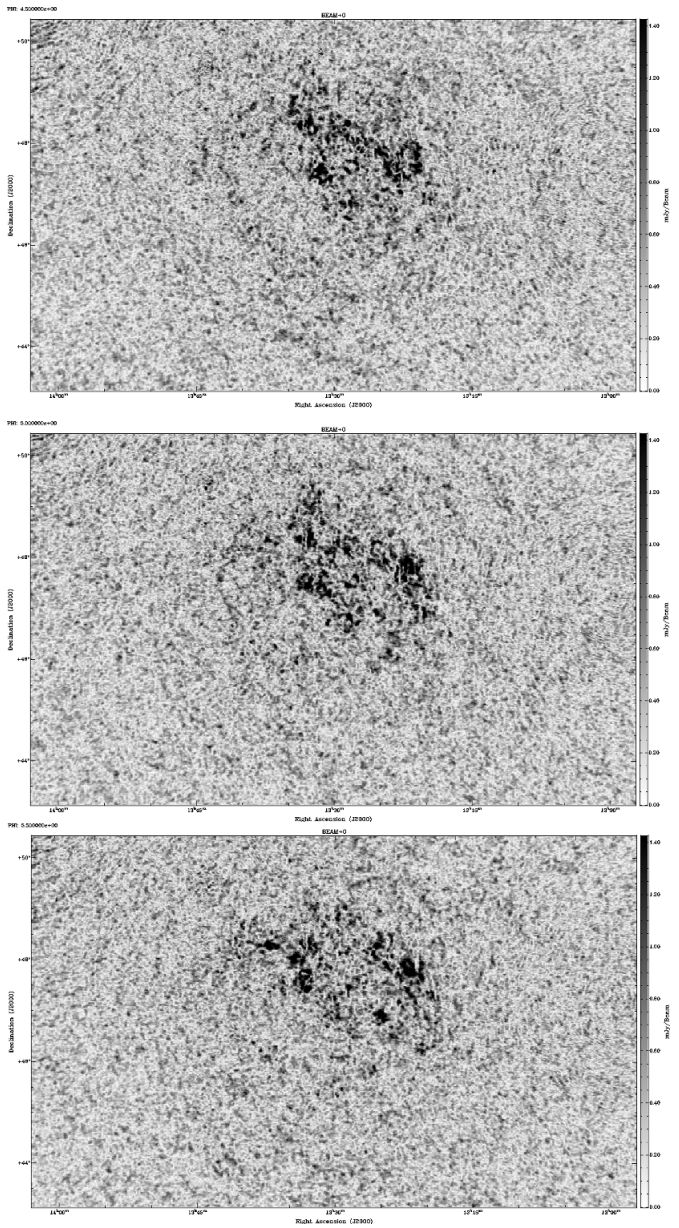

Figure 2.29: 3 slices (ϕ = 4.5,5.0,5.5 rad m^{-2}) of the Faraday cube showing the expansion of a foreground bubble like structure

were imaged and compared to a subband at 157.4 MHz which had undergone the same calibration routine. The local noise around M51 was found as well as finding the brightest pixel of M51 to calculate the signal to noise which is plotted for the 4 subbands tested in figure 2.35. The image quality overall for 110 MHz is quite poor, M51 itself is extremely distorted along with other point sources and the S/N is quite low compared to the subband at 157.4 MHz but surprisingly at 190 MHz, the image quality is quite good. A closeup of M51 can be seen in figure 2.33 and figure 2.34 for 190 MHz and 110 MHz, respectively.

Another lower band filter subband was checked at 114 MHz and showed an improvement in image

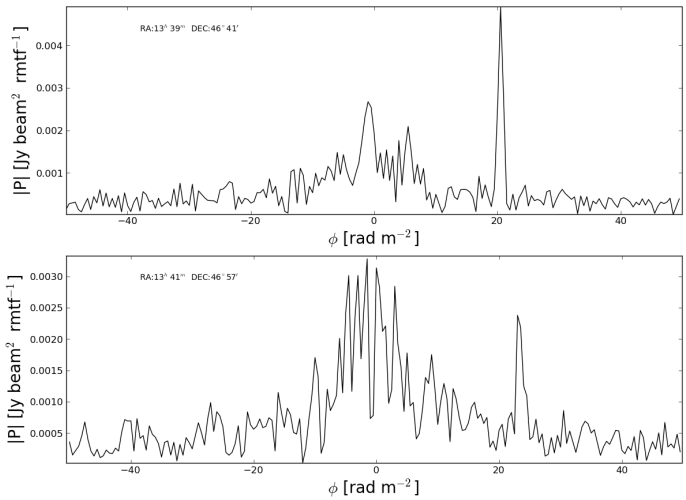

Figure 2.30: The Faraday spectra of both extra-galactic point sources. Top: J133923+464008 Bottom: 4C +47.38

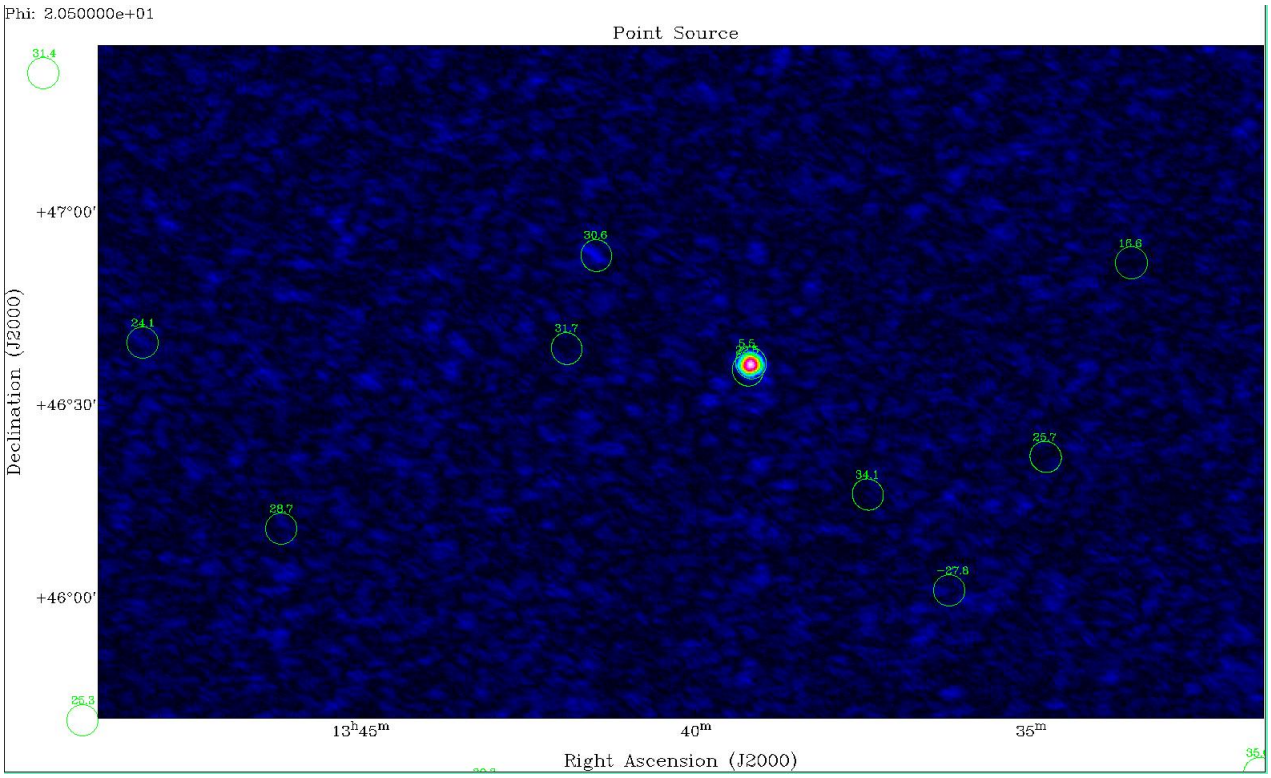

Figure 2.31: The unresolved extra-galactic source (J133923+464008) detected in the Faraday cube at ϕ = 20.5 rad m^{-2}.

quality as well as signal to noise. Observing close to the 190 MHz filter should be okay, however one

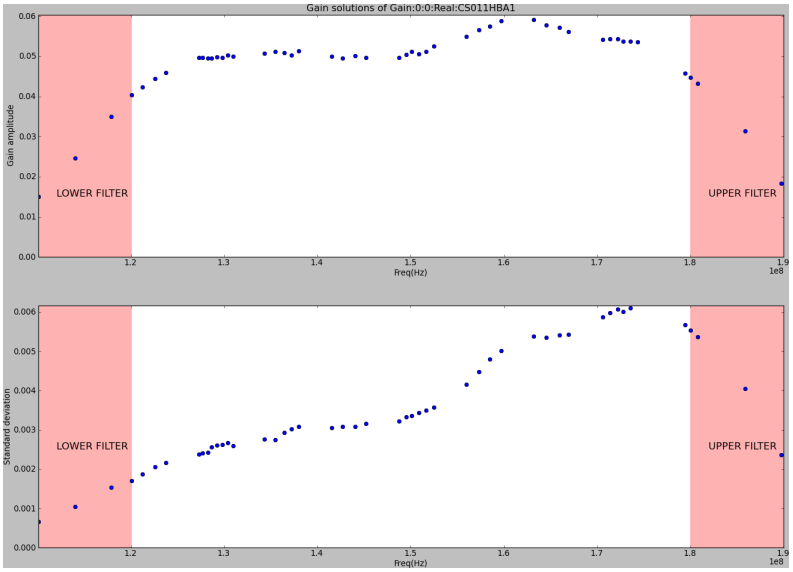

Figure 2.32: Mean gain amplitude solutions (top panel) and the standard deviation(bottom panel) for each calibrator subband for station CS011HBA1, XX correlation.

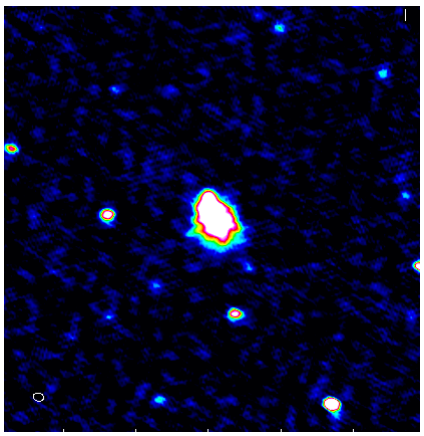

Figure 2.33: Closeup of M51 at 190MHz.

needs to mindful of RFI due to T-DAB.

Therefore the result of this small but interesting commissioning task shows that:

1. Observing down to 110 MHz is definitely not advisable due to poor image quality but the situation does improve rapidly with increasing frequency.

2. Observing up to 190 MHz seems to be okay, however, RFI can be extremely bad. Therefore the observer can observe the 180-190 MHz range of LOFAR HBA, but at their own risk due to RFI.

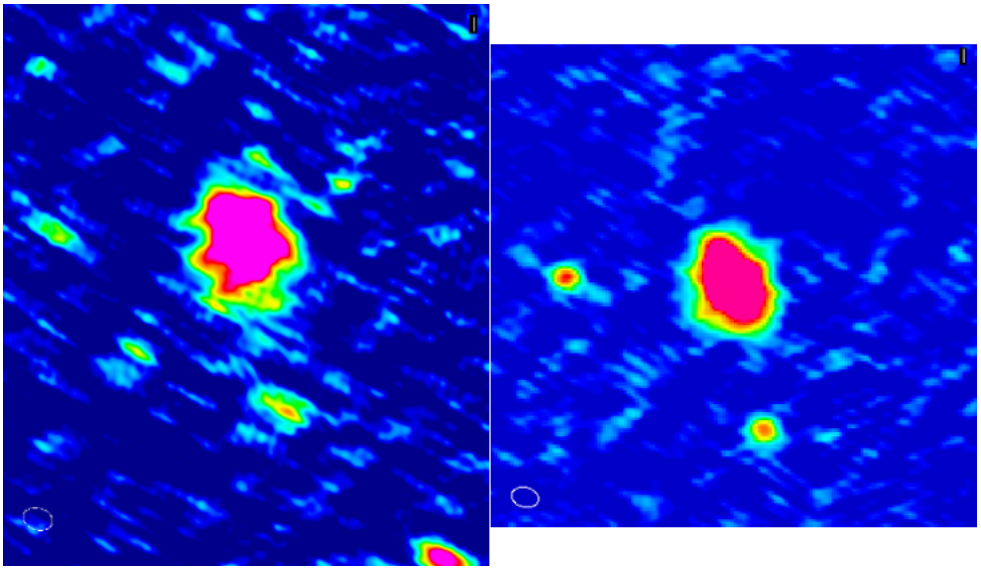

Figure 2.34: Closeup of M51 at 110MHz (left) & 114MHz (right).

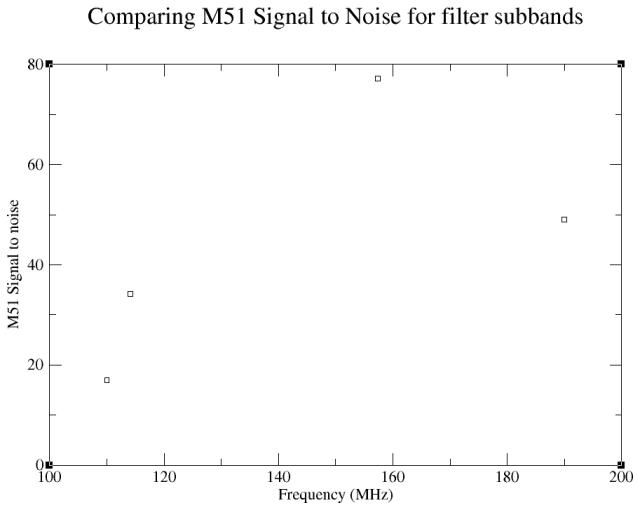

Figure 2.35: Signal to Noise ratio of M51 for the 4 subbands inspected.

2.9.2 Testing ionospheric RM correction on PSRJ0218+4232

Research in low frequency radio polarimetry is a relatively new area of research but again difficulties exist due to the ionosphere. The observed polarization angle for an astronomical source can be rotated significantly by the ionosphere, especially at low frequencies.

Calibration for this ionospheric Faraday rotation depends on the free electron content which varies with the time of day, season, level of solar activity and line of sight. Brentjens (2008)[87] and Pizzo et al. (2011)[88] show that ionospheric Faraday rotation usually changes on timescales shorter than a typical observation.

Sotomayor-Beltran et al (2013)[89] presented a code that calculates the ionospheric Faraday rotation

for a specific epoch, geographic location, and line-of-sight. In the calculations, Sotomayor-Beltran et al (2013)[89] assumed that the ionosphere is a spherical shell surrounding the Earth. The ionospheric Faraday depth is calculated at the ionospheric piercing point (IPP). The ionospheric Faraday depth is:

$$\phi_{ion} = 2.6 \times 10^{-17} \mathrm{TEC_{LOS}} \mathrm{B_{LOS}} \quad \mathrm{rad\ m^{-2}} \tag{2.26}$$

where TEC_{LOS} is the total electron content (TEC) at the geographic coordinates of the IPP and B_{LOS} is the geomagnetic field intensity at the IPP. The TEC_{LOS} is defined as:

$$\mathrm{TEC_{LOS}} = \int \mathrm{n_e dl} \quad \mathrm{m^{-2}} \tag{2.27}$$

However, this code doesn't output the ionospheric Faraday rotation correction in a format which is usable for LOFAR.

The program RM Writer (M.Mevius et al, in prep) which has been adapted from Sotomayor-Beltran et al. (2013)[89] for calibration of LOFAR data was used and is now the usual software that is being used for LOFAR polarization ionospheric calibration. The self calibrated data of NGC891 observed with LOFAR HBA (see chapter 5) was used to check the polarization properties of the millisecond pulsar PSRJ0218+4232 (Navarro et al. 1995) [90]. This pulsar has a RM of -61 rad $\mathrm{m^{-2}}$ and a polarization fraction of approximately 50%. Therefore it is an ideal calibrator for polarization.

In order to check that this RMwriter software performs correctly, RM synthesis was performed on a small region around PSRJ0218+4232 without any ionospheric Faraday correction. Only approximately 80 channels were used, therefore resulting in a broader RMSF than LOFAR is capable of but for the purpose of this commission test, this is sufficient. After this the data was copied and the ionospheric Faraday rotation correction for our line of sight was found using vertical TEC values from the center for Orbit Determination in Europe (CODE). The time resolution of CODE measurements is every 2 hours. This correction values were then applied to the data via BBS. Here the pointing direction via a skymodel needs to be specified for BBS. The results from both uncalibrated data and calibrated are compared in figures 2.36 & 2.37.

From this commissioning test it is evident that the ionospheric Faraday correction produced three positive changes to the data.

1. The Faraday depth has shifted from -59 rad $\mathrm{m^{-2}}$ in the uncorrected data to -61 rad $\mathrm{m^{-2}}$ in the corrected data which is the catalogue value. This shows that the RMwriter does correctly calibrate for the ionospheric Faraday correction.

2. Spurious polarization was seen at + 60 rad $\mathrm{m^{-2}}$ in the corrected data but this disappears in the corrected data.

3. Finally we see the polarized flux increase in corrected data by approximately 3%.

These results show two things, firstly correction for ionospheric Faraday rotation correction is essential if one wants to study polarization at low frequencies. Secondly, this test shows that for the direction the pulsar was located in, the RMwriter software works. However, it is important that this software is tested for different pulsars distributed in the sky. MSSS (Multifrequency Snapshot Sky Survey) (Heald et al, in prep) will allow us to do this and first tests on polarization using the RMwriter software have been successful (see chapter 7).

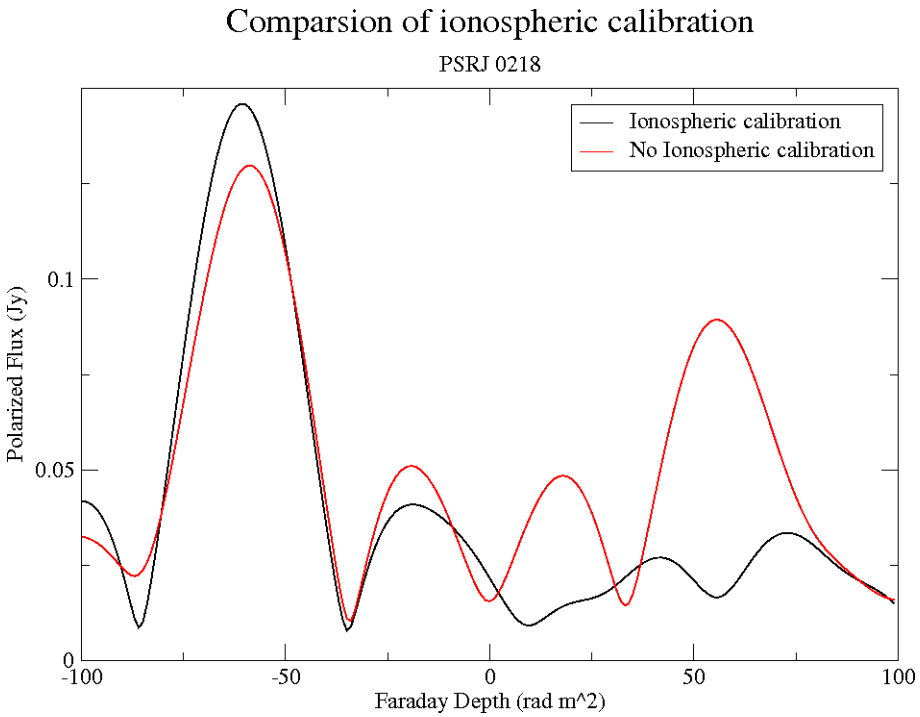

Figure 2.36: Faraday spectra of the pulsar PSRJ0218+4232 before and after ionospheric Faraday correction.

2.10 Conclusions and future work

Commissioning of LOFAR is still an ongoing project with participation from people and institutes around the world. With regards to software, much more work needs to be performed especially with regards to the AWimager which badly needs multiscale cleaning implemented. Much more work needs to done on polarization calibration. While much has been done to address the ionospheric Faraday rotations on the polarized signal, very little has been done to address the problem of polarization leakage. While usually this is located at a Faraday depth of zero, correction of the ionosphere will shift this by the average Faraday depth correction performed, making it harder to identify real polarization. In addition, the sidelobes from instrumental polarization leakage can make interpretation of Faraday spectra more difficult. This makes the use of RM clean essential. The observation of NGC891 with the polarized pulsar should be a good starting point to investigate how to solve and correct for the polarization leakage.

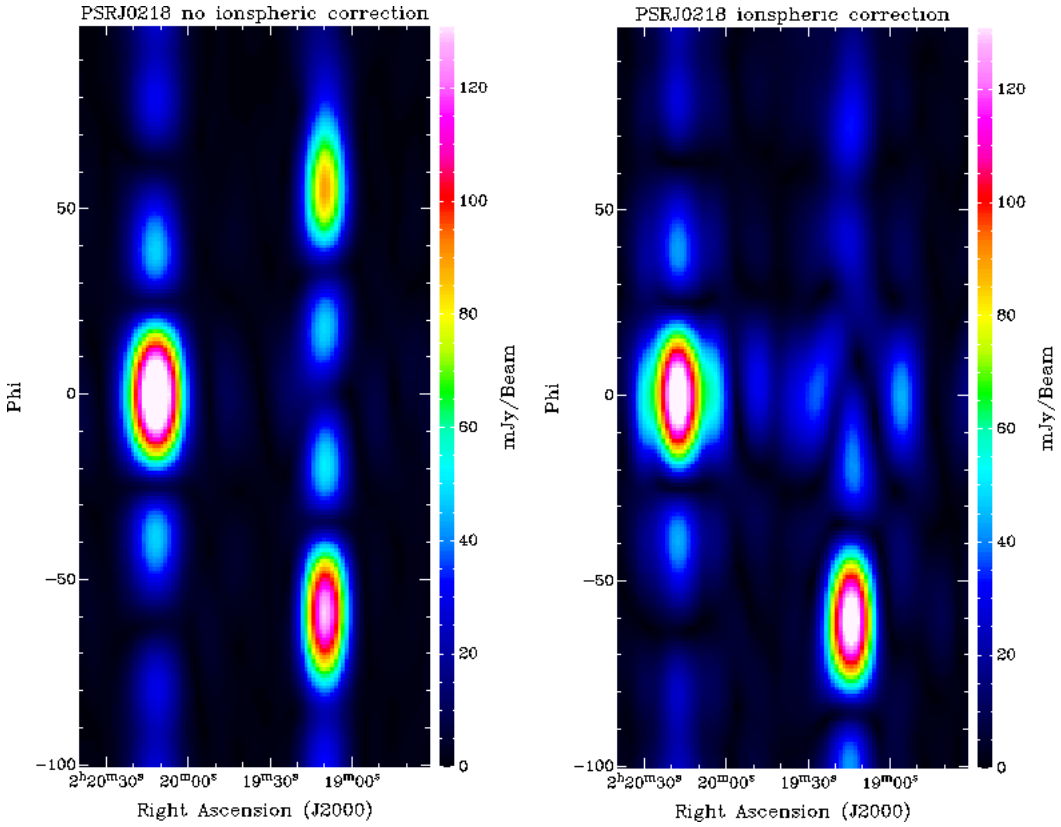

Figure 2.37: The Faraday spectra for a set declination, Faraday depth is the y-axis and Right Ascension on the x-axis. The left image is before ionospheric Faraday correction and the right image is after. The source at $\phi = 0$ rad m^{-2} is the instrumental polarization from a point source at the same declination.

CHAPTER 3

Observation of M51 at Low Radio Frequencies

3.1 Introduction

Messier 51 or NGC5194, aptly named the 'Whirlpool Galaxy' is one of the most widely studied galaxies as it is one of the most striking examples of a classical grand-design spiral galaxy. Spiral galaxies can exhibit a wide range of morphologies, from flocculent to grand-design and is important to note that these different morphologies can be due to small-scale gravitational instabilities in the stars and/or gas, or due to larger scale perturbations caused by global density waves, tidal interactions or bars. In the case of M51 itself, it has a companion galaxy NGC5195 for which many galactic interactions studies have been performed. For example Dobbs et al. (2010) [91] used hydrodynamical models to simulate the tidal induced spiral structure. In these studies the authors were able to replicate several features seen in observations such as the HI tidal tail as well as kinks and bifurcations in the spiral arms, thus showing that the internal structure of M51 is deceptively complicated. The physical parameters of M51 used in this chapter can be seen in Table 3.1.

M51 was also the first external galaxy where polarized radio emission was first detected by Mathewson et al. (1972) [92]. Polarized emission is present throughout most of the disc of M51, especially in the locations of the inner spiral arms coinciding with CO emission as seen by Fletcher et al. (2011) [93]. Horellou et al. (1992) [94] found that at wavelengths of 1.66 and 1.46 GHz, the distribution of polarized emission is strongly affected by Faraday depolarization, that the polarized emission being detected at these wavelengths is actually emerging from an upper layer of the disk and that the galaxy may not be transparent to polarized emission at decimeter wavelengths.

Heald et al. (2009) [32] observed polarization at approximately 1.4 GHz again throughout the whole disk, however it was seen that there were large variations with a 5% polarization fraction detected in the optical disk and 25-30% beyond the outer arms. Braun et al. (2010) [55] performed RM Synthesis on M51, detecting a main Faraday component at +13 rad m^{-2}, with two weaker secondary components near -180 and +200 rad m^{-2}.

Fletcher et al. (2011) [93] were able to identify two different regular magnetic field patterns. A regular field with a combination of $m = 0 + 2$ azimuthal modes was found in the disk. In the halo, however, a regular field with $m = 1$ azimuthal mode was found. The origin of this regular field in unknown.

However, considering how extensively M51 has being studied both observationally and theoretically, very few observations have being performed on M51 at frequencies below 500 MHz, primarily due to the difficulties of observing at low radio frequencies. Segalovitz (1977) [95] observed M51 with

the WSRT at 610 MHz as well as 1.4 GHz. But with a resolution of approximately $1'$ for the 610 MHz observation, few details of the inner galaxy could be observed. An extended component could be seen but this extended no further than the 1.4 GHz observation. Using both observations, Segalovitz (1977) [95] computed a spectral index map which was compared with analytical models of the cosmic ray diffusion equation. Two sets of parameters produced models which were fitted to the observations, namely: (a) a constant magnetic field and diffusion coefficient with leakage of electrons out of the galactic magnetic field in the z-direction or (b) no leakage but a magnetic field which is proportional to $1/r^{1/2}$ and a diffusion coefficient which is proportional to $1/r$ where r is the galactocentric distance. However, the step-like source function used in the analytical solutions is now outdated and unrealistic.

M51 was also observed at low frequencies as part of a survey of 133 spiral galaxies performed by Israel & Mahoney (1990) [26] using the Clarke Lake Telescope at 57.5 MHz. M51 was seen to have 11 ± 1.5 Jy in flux. However, with a resolution of $7'$, results are not very accurate. Overall in this survey it was seen that the measured flux in nearly all the galaxy observed was lower than expected through extrapolating from higher frequencies. In addition, they found that more highly inclined galaxies had lower fluxes than moderate inclined galaxies. I&M explained this flatten of the radio spectrum through free-free absorption especially due it's dependence on inclination. I&M explained that such an effect could be explained by the existence of a clumpy medium of well mixed non thermally emitting and thermally absorbing gas with a small filling factor and an electron temperature of 500 to 1000 Kelvin. To complicate things further, Hummel (1991) [28] reanalyzed the same data and while he does see a spectral index flattening, the magnitude of the flattening does not depend on the inclination of the galaxy. This discrepancy is one of the main issues that needs to be addressed with low frequency observations especially with the upcoming Multi frequency Snapshot Sky Survey (MSSS) Heald et al (2014).

Observing at lower frequencies enables us to observe synchrotron emission from the oldest and lowest-energy electrons which are the least affected by energy losses and therefore can propagate further away from their site of origin. One would expect to see a huge radio disk around M51. Little is known about conditions in the ISM of the outer disk ($R > R_{25}$). Thornley et al. (2006) [96] using IR, UV, Hα and HI found that star formation in the outer disk of M51 is about an order of magnitude less efficient that at smaller radii. Braine & Herpin (2004) [97] observed carbon monoxide (CO) in the outer disk of NGC4414 at regions of high HI column density regions. At these regions, Bigiel et al, (2010)[98] found that despite widespread star formation the outer disk star formation is extremely inefficient, i.e the gas depletion time is very low and which increases with radius. It could be the case in that turbulence caused by magneto-rotation instability [99, Sellwood & Balbus 1999] could be stronger than turbulence caused by star formation in the outer regions of the galaxy thereby increasing the turbulent energy density and scale length (Beck 2007) [48].

It is hoped with these low frequency observations that the extended disk can be observed in radio continuum and thus revealing weak magnetic fields.

Table 3.1: Physical parameters of NGC5194

Morphology	SAbc
Position of the nucleus	$\alpha(2000) = 13^h29^m52^s.709$
	$\delta(2000) = +47°11'42.59''$
Position angle of major axis	-10° (0° is North)
Inclination	-20° (0° is face on)
Distance	7.6 Mpc
Optical Radius (R_{25})	$3.9'$ (8.5 kpc)

In this paper, we shall outline the results from the first LOFAR [1] observations of a nearby galaxy, namely M51. In section 3.2, we will describe the observational setup along with the data reduction process. In section 3.3, we will present the LOFAR HBA 151 MHz map of M51 and investigate the radial profile of LOFAR emission while comparing to higher frequencies. In section 3.4, we will present and discuss the spectral index and total magnetic field strength maps derived from the LOFAR 151 MHz and VLA 1.4 GHz map from Fletcher et al. (2011) [93]. Section 3.5, the cosmic ray propagation in M51 will be discussed. In section 3.6, we shall present results from the wavelet analysis on the 151 MHz along with 1.4 GHz and Far Infrared maps. In section 3.7, we shall also present results from performing rotation measure synthesis on this region and the analysis of detected background sources in the field. Finally, conclusions and prospects for future work will be presented in section 3.8.

3.2 Observation and preprocessing data reduction

The observation took place on the night of April 22-23rd 2013 for a duration of 8 hours with a configuration of 61 high-band antenna (HBA) stations. This configuration consisted of 24 core HBA stations (counting the two HBA 'ears' for core HBA stations makes this 48) and 13 HBA remote stations. No international stations were used in this observation. Dual beam mode was utilized for this observation with one beam targeting M51 ($\alpha = 13^h29^m52^s$, $\delta = +47°11'43''$) and one beam targeting 3C295($\alpha = 14^h11^m20^s$, $\delta = +52°12'10''$) for the purposes of flux calibration. As 3C295 was within 10 degrees from the target and within the HBA tile beam, both calibrator and target could be observed simultaneously. In addition, 8-bit sampling mode was used in order to observe with an instantaneous bandwidth of 96 MHz. This total bandwidth is split into 488 subbands each with bandwidth of 0.18 MHz. Due to the dual-beam mode observation, the subbands had to be split evenly between calibrator (244 subbands) and target (244 subbands). The target subbands were split into 8 blocks of approximately 30 subbands. LOFAR has the ability to observe up to 180 MHz but DAB 5 (Digital Audio Broadcast) RFI is very strong above 175 MHz [71, Offringa et al. 2013] and therefore was avoided. Details of the observation can be seen in table 3.2.

Table 3.2: Parameters of the M51 LOFAR observation

Start Date (UTC)	22-Apr-2013/20:08:07.0
End Date (UTC)	23-Apr-2013/04:04:04.7
Frequency Range	115.9-175.8 MHz
Total Bandwidth on Target	48.8 MHz
Total Bandwidth on Calibrator	48.8 MHz

The majority of the data reduction of this data was performed with the LOFAR pipeline. A full description of this pipeline can be seen in (van Haarlem et al. 2013) [68] & (Heald et al. 2010) [100].

For RFI detection, the AOFlagger pipeline (Offringa et al. 2012) [72] was performed on the raw data, with the greatest frequency and time resolution resulting in superior RFI detection and flagging. The algorithm was executed on all linear correlations which is most accurate. The visibility data was checked to see if any contamination from the A-Team (Cas-A, Cygnus-A, Virgo-A, etc.) entered the sidelobes. It was seen not to be the case and therefore 'demixing' (van der Tol, 2007) [74] was not applied. The

[1] [68, van Haarlem et al. 2013]

data was then compressed in frequency to 8 channels per SB and 14 secs sampling time. These flagging and compression operations were performed using the New Default Pre-Processing Pipeline (NDPPP).

3.2.1 Initial calibration

The calibrator subbands of 3C295 were calibrated using a skymodel from Scaife & Heald (2012) [66] using Black Board Selfcal (BBS) software (Pandey et al. 2009) [75]. It must be noted that the flux scale is that of Roger et al. (1973)[65] (hereafter RBC). This scale is used to avoid the suggested issues (Rees 1990) [64] with the secular decrease in the flux density of Cas A at low frequencies existing in the Baars et al. (1977) [63] scale. From Scaife & Heald (2012) this sky model was a spectral model of the form:

$$\log S = \log A_0 + A_1 \log \nu + A_2 \log^2 \nu + ... \tag{3.1}$$

was used. The model was applied in linear frequency space, ie

$$S[\mathrm{Jy}] = A_0 \prod_{i=1}^{N} 10^{A_i \log^i[\nu/150\mathrm{MHz}]} \tag{3.2}$$

in order to retain Gaussian noise characteristics. Both determination of the optimal order (N) of polynomial model and maximum likelihood parameter estimation were performed using a Markov Chain Monte Carlo (MCMC) implementation. The gain amplitude solutions found from the calibrator subbands were then directly transferred to the target M51 subbands. The target subands were then combined in frequency and copied using NDPPP into blocks of approximately 30 subbands (6 MHz bandwidth) for a better signal to noise ratio.These blocks of 30 subbands were then phase calibrated using a global sky model. This global sky model consists of positions of sources from the NVSS catalogue (Condon et al. 1998) [7] with fluxes obtained from a power spectral fitting with data from the NVSS, WENSS (Rengelink et al. 1997) [76] and VLSS (Cohen et al. 2007) [4] surveys. M51 itself is described as a simple Gaussian source in this sky model.

After this initial calibration, each block of subbands was checked by eye for any RFI and any bad solutions resulting from the calibration were flagged.

3.2.2 Self calibration

Once the initial direction-independent calibration had been completed, a new sky model was created in the following way. First of all, a point source model was created from the clean components using AW-imager (Tasse et al. 2013) [101] which is part of the LOFAR software. This software utilizes the A-projection algorithm (Bhatnagar et al. 2008) [78] to image wide fields of view (due to direction-dependent effects resulting from beam and ionospheric effects) and therefore is necessary to extract accurate fluxes for sources far away from the phase center. Next, a second image was created using CASA [2] and utilizing it is multiscale clean (Cornwell 2008) [77] and w-projection (Cornwell et al. 2005) [102] tasks solely for creating a detailed model for M51 itself. This could not be done with AWimager due to the nonavailability of multiscale clean at the time of reduction. This feature will be added to the AWimager in the near future. As M51 is very small compared to size of the primary beam and at the phase centre of our observation, errors due the primary beam correction are small. A uv coverage of 12 klambda was used to create these self calibrated sky models. This corresponds to 20-25 arcsec resolution at uniform weighting. These two sky models are then combined so that it can be

[2] http://casa.nrao.edu/

used to perform a direction-independent self calibration step solving only for the phases of the parallel correlations.

This whole process was performed on each of the 8 blocks of 30 subbands.

At these low frequencies, calibration for ionospheric Faraday rotation is essential in order to study polarization accurately. Therefore, this rotation must be corrected for. Values of the RM correction were obtained using the method from Sotomayot-Beltran et al. (2013)[89]. Measurements of the vertical total electron content (VTEC) were obtained from the Center for Orbit Determination in Europe (CODE). The time resolution of CODE measurements is every 2 hours. In addition, the Earth's magnetic field was calculated using the eleventh generation of the International Geomagnetic Reference Field (IGRF11; [103]). The calculated RM correction for the entire observation can be seen in Figure 3.1.

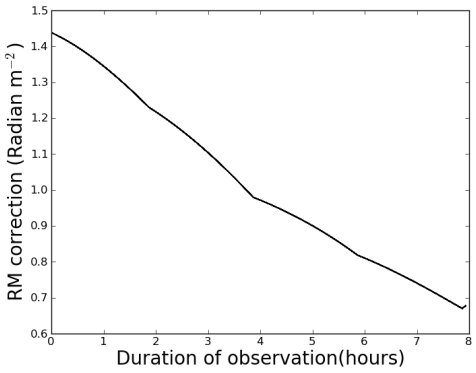

Figure 3.1: Calculated RM ionospheric correction applied for the duration of the observation.

3.3 Final M51 total power image

Images were made with the same imaging parameters and uv-distance (16 kλ) for each of the 8 subband blocks with CASA in order to utilize multi-scale clean with w-projection. Several point sources were compared to the Point Spread Function (PSF) to investigate if the point sources were broadened due to phase errors caused by the ionosphere but no significant broadening could be seen. Also astrometry of these point sources were checked with catalogue values but no major deviations could be seen.

Each frequency block image was smoothed to 20″ and then all 9 images were averaged in the image plane using an inverse variance weighting scheme. The final image of M51 at 15″ resolution with uniform weighting can be seen in Figure 3.3, whilst figure 3.5, shows M51 at 20″ resolution with a robust weighting scheme of -0.5 which shows the extended disk well.

The noise in quiet regions close to the edges of the FOV is found to be approximately 150 μJy/beam. Closer to M51 the noise is found to be between 200-300 μJy/beam.

At 151 MHz, the grand design spiral arms of M51 still can be clearly seen. The arm and interarm contrast is highly visible in M51 at these low frequencies and comparable at first glance to higher frequencies (Fletcher et al. 2011) [93]. This is in stark contrast to the galaxies observed by Basu et al. 2012 [81] at 333 MHz with the GMRT where the spiral arms and inter arm regions were often indiscernible from each other. According to Fletcher et al. (2011) [93], this is primarily caused by the low energy cosmic ray electrons (CREs) diffusing from star forming regions in the spiral arms without

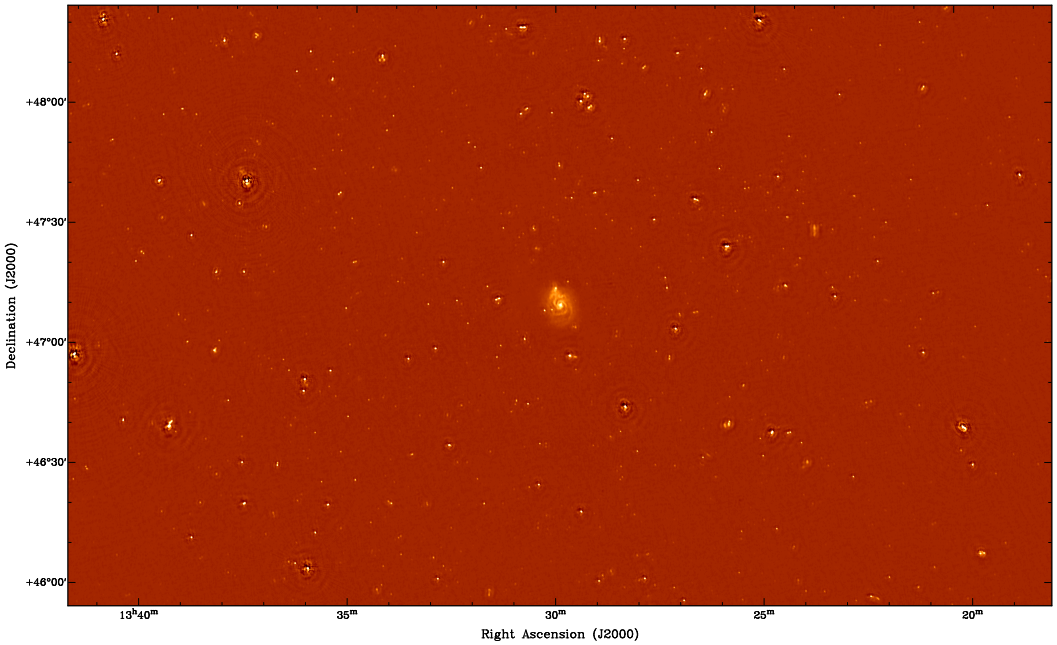

Figure 3.2: Widefield image of the region around M51. Note that calibration errors still occur around bright sources. Directional dependent calibration is essential to remove these types of errors.

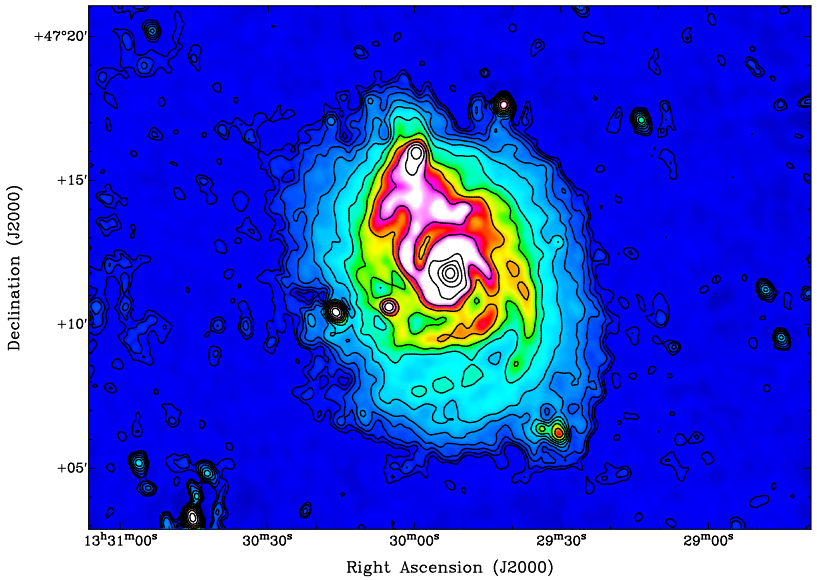

Figure 3.3: Image of M51 at a central frequency 151 MHz with a bandwidth of 48.8 MHz. Resolution is 20″ at a robust weighting of -0.5. The rms noise is approximately 300 μJy/beam. The contours start at 3 times the rms noise and increases at levels of 1.5.

losing much energy compared to higher energy electrons seen at higher frequencies. This may enable the lower energy electrons to diffuse further and thus filling up the inter arm region.

CREs diffusion from the spiral arms into the interarm region can be seen in the 151 MHz image,

Table 3.3: Integrated Fluxes for M51 from literature rescaled to the RBC scale

ν (GHz)	Flux Density (Jy)	Ref
22.8	0.147 ± 0.0155	Klein et al. (1984)
14.7	0.19665 ± 0.0207	Klein et al. (1984)
10.7	0.241 ± 0.0143	Klein & Emerson (1981)
8.46	0.308 ± 0.1026	Dumas et al. (2011)
4.86	0.604 ± 0.201	Fletcher et al. (2011)
2.604	0.771 ± 0.049	Klein et al. (1984)
1.49	1.36 ± 0.097	Fletcher et al. (2011)
0.61	2.629 ± 0.062	Segalovitz (1977)
0.408	3.53 ± 0.1	Gioia & Gregorini (1980)
0.15	8.1 ± 0.55	this work

especially when compared to images at higher frequencies. One can see especially in the northern region that the interarm region is becoming squeezed as the CREs diffuse into the interarm region. However, it is not as severe compared to the galaxies observerd by Fletcher et al. (2011) [93].

The region between the companion and the northern arm of NGC5194 is very distinct at 151 MHz. It is much brighter compared to the 8.4, 4.9 GHz maps from Dumas et al. (2011) [104] making it consistent with synchrotron emission that is enhanced by the ongoing interaction.

It should be noted that SN 2011dh (discovered on 01 June 2011 by the Palomar Transient Factory project (PTF)) (Silverman et al. 2011 [79]; Arcavi et al. 2011 [80]) was not detected with this observation. This gives an upper limit of the SNe flux at 150 MHz at day 691 of approximately 11.3 ±0.7 mJy/beam.

3.3.1 Integrated radio continuum spectrum

To calculate the integrated flux for M51 we fitted concentric rings whilst taken into account the inclination and major axis of the galaxy. We obtain an integrated flux measurement of 8.1 ± 0.55 Jy out to a radius of 16 kpc. The star forming region ($R < 10$ kpc) contains 6.98 Jy of flux and the extended disk ($R > 10$ kpc) contains approximately 1.1 Jy of flux.

We use other measurements from higher frequencies to compute the spectral index of M51 as shown in table 3.3. As we have used the RBC flux scale for scaling our LOFAR data, measurements at other frequencies must be rescaled. Fortunately, at frequencies $\gtrsim$ 300MHz, the RBC scale is in agreement KPW scale Kellermann et al. (1969) [67] and therefore we can use the conversion factors from the Baars scale, Baars et al. (1977) [63], table 7. We use integrated fluxes from Klein et al. (1984) [105], Klein & Emerson (1981) [106], Dumas et al. (2011) [104], Fletcher et al. (2011) [93], Segalovitz (1977) [95] and Gioia & Gregorini (1980) [107].

Comparing this to previous flux measurements, the LOFAR flux agrees very well with other lower frequency data. As a further check, the integrated flux of the star forming region of M51 found here was compared to the integrated flux found in the MSSS survey (Heald et al. in prep) and was found to be very close to the flux of the star forming region as MSSS wouldn't have the sensitivity to detect the extended disk of M51. The 4 and 8 GHz fluxes shown have significant errors due to addition of single dish data to interferometry data (see Fletcher et al. 2011 [93]). We fit a power law in the form of $S \propto \nu^{\alpha}$ with a spectral index of α = -0.81 ± 0.02, shown in figure 3.4. There is no indication of any flattening of the spectrum for M51 up to 151 MHz.

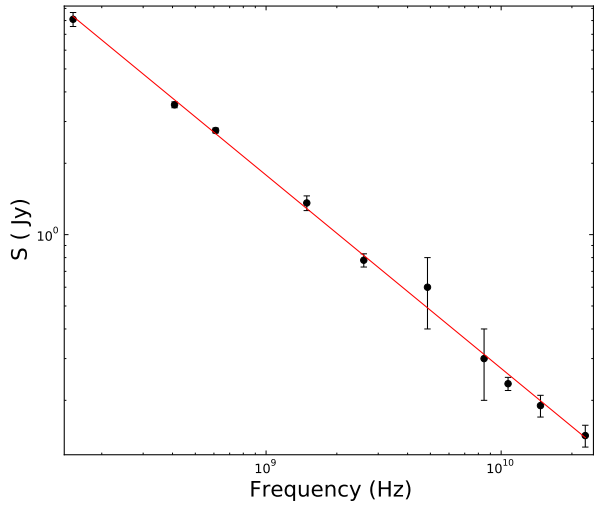

Figure 3.4: The integrated flux of M51 with a power law fit.

3.3.2 The extended disk of M51

Figure 3.5 shows M51 at 20″ resolution with a robust weighting scheme of -0.5 which shows the full extent of the disk of M51.

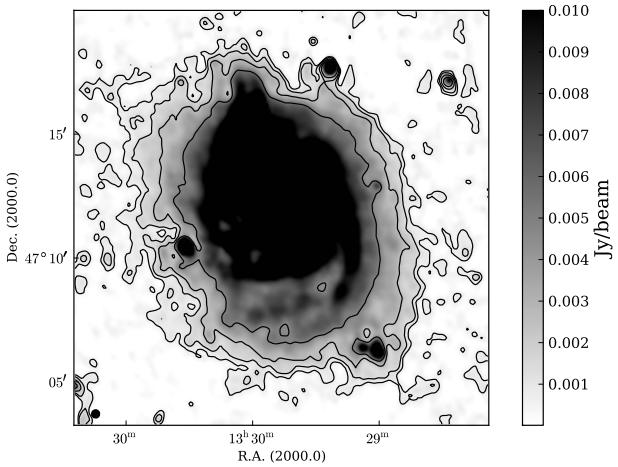

Figure 3.5: Image of M51 at 20″ resolution with a robust weighting of -0.5. Here the extended disk is seen more clearly. Contour levels are at 4,8,16,32 × 150 μJy/beam.

The extended disk is detected as far out as 16 kpc away from the galactic center. We observe that the disk is not increasing uniformly with radius as we see a further extension of the disk to the northwest possible due to an outflow caused by the interaction with the companion.

The total extent of disk emission is insufficient as a measure of how far the disk extends out to as we

Table 3.4: Scale lengths for the inner (l_i) and outer (l_o) disk of M51

ν (MHz)	l_i (kpc)	l_o (kpc)
1400	3.4 ± 0.2	1.28 ± 0.02
151	5.32 ± 0.4	2.06 ± 0.06

are limited by the sensitivity of our observation. Therefore, we use the scale length l which prescribes the emission along the disk as an exponential function i.e. $\propto exp(-r/l)$ where r is galactocentric distance.

The radial profile of M51 was taken by the mean in concentric rings with the position angle of the major axis and the inclination of the galaxy taken into account using the values from table 3.1. Surrounding background point sources were removed by fitting Gaussians before measuring the radial profile. Several background point sources located in disk were blanked out. The same was also done to a VLA 1.4 GHz map rescaled to the RBC flux scale from Fletcher et al. (2001) [93] which was placed on the same grid and resolution as the 151 MHz map. The interarm region of M51 can be seen in the radial profile at 3.3 kpc at both frequencies but at 151 MHz is not as apparent.

Usually a single exponential profile is fitted onto the emission profile (Dumas et al. 2011)[104], but it was seen that a break occurs at around 10 kpc at both frequencies, just beyond the star forming region of M51 (Kennicutt et al. 2007) [108] (refer to figure 3.7) and therefore a separate exponential was fitted for the inner and outer disk for both maps using the following function

$$I(R) = \begin{cases} I_0 exp(-R/l_i) & \text{R} \leq 10 \text{ kpc} \\ I_{10} exp(-R/l_o) & \text{R} \geq 10 \text{ kpc} \end{cases} \tag{3.3}$$

The radial profile of M51 continuum emission at 151 MHz and 1.4 GHz with the above function fitted is shown in figure 3.6. The obtained scale lengths for the inner and outer parts of the galaxy are shown in table 3.4.

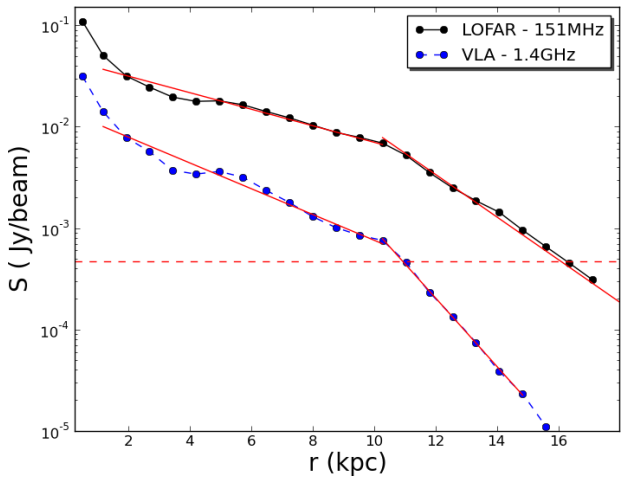

Figure 3.6: Radial profile of M51 at 151 MHz and 1.4 GHz. The horizontal red line shows the sensitivity limit (3σ) of the 151 MHz image.

As expected, we see that the scale lengths in the inner and outer disk are larger at 151 MHz than 1.4 GHz, due to the fact that CREs energy loss processes are much more dominant at higher frequencies. In addition, nonthermal emission becomes more dominate at lower frequencies and the radial diffusion

of CREs becomes much more important and leads to larger scale lengths. The scale length in the outer disk for both frequencies is > 50% less than the inner scale length. This has also been seen in M33 (Tabatabaei et al. 2007b) [109] where 2 exponential scale lengths were fitted. The scale length of region < 4 kpc was seen to be twice as large as the scale length $R > 4$ kpc. In HI, a break in the radial profile of M51 is also seen in Bigiel et al. (2010) [98].

It is very unlikely that the lack of short spacings can cause this effect. LOFAR has excellent inner uv coverage and is sensitive to structures over a half of a degree. The same holds for the 1.4 GHz VLA observation, at D-configuration it is sensitive to structures up to 15′.

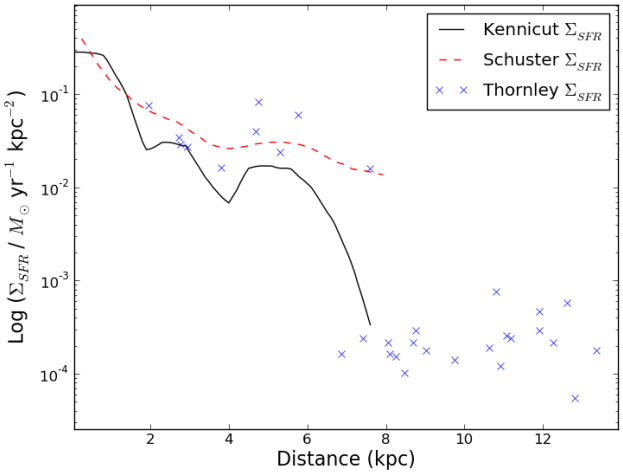

Figure 3.7: The radial profile of the star formation rates of M51 taken from Kennicut et al. (2007) [108], Schuster et al. (2007) [110] and Thornley et al (2006) [96].

3.4 M51 spectral properties and total magnetic field

A VLA map of M51 from Fletcher et al. (2011) [93] at 1.4 GHz which was rescaled to the RBC flux scale was used along with the 151 MHz LOFAR map to create a spectral index map. Both maps were convolved to the same resolution (20″) and placed on the same grid. Nearby point sources were either subtracted by fitting a Gaussian component and then subtracted or for sources within M51 manually blanked out. The spectral index was computed pixel by pixel and is shown in Figure 3.8 along with the error map.

The spiral arm and interarm contrast can be easily seen in the spectral index map indicating energy losses of the CREs as they propagate from the star forming regions into the interarm regions. In the arm regions, the strongest HII regions can be seen easily. We also see that in regions of high star formation a bulging into interarm region specifically in the inner South East HII region. The extended disk shows a steeping of α, with $\alpha > -0.9$, this indicates energy losses through synchrotron cooling and inverse Compton losses. In figure 3.9, beyond 10 kpc we observe a very sharp decrease in α, as the SFR here is a magnitude smaller than it is in the central disk (Thornley et al. 2006) [96] resulting in hardly any fresh injection of CREs.

A spectral index of $-0.47 \leq \alpha \geq -0.52$ (see figure 3.10) is present in the central region and inner spiral arms of M51 which is flatter than the normal injection spectrum of CREs, signifying free free absorption.

Primary CR electrons are injected into galaxies via SNR with a power-law spectra $Q(E) = CE^{-p}$ where the energy spectrum p is related to the spectral index α via $\alpha = \frac{-(p-1)}{2}$. Observational results based on Galactic SNR from Kothes et al. (2006) [111] & Green (2009) [112] suggest a mean nonthermal spectral index of -0.5 which is indicative of a mature adiabatically expanding SNR (Kothes et al. 2006) [111]. Scoville et al. (2001)[113] found that 1373 Hα emission regions exist within the central region with sizes up 100 pc and therefore free free absorption would be expected especially in these regions of intense star formation. Recently, Adebahr et al. (2013)[22] observed a spectral flattening in the core region of M82 where intense star formation is known to be occurring. On the other hand, if this is simply thermal emission, a thermal fraction of approximately 20% at 151 MHz would be needed to explain this spectral index, assuming that that the non-thermal spectrum is -0.8. This seems very high for such low frequencies making thermal absorption more likely.

Observations at lower frequencies specifically with LOFAR LBA may show this region become opaque and will be performed at a later date.

The arc shaped structure located just below the companion galaxy NGC5195 seen in radio continuum (Dumas et al. 2011)[104] and in Hα (Greenawalt et al. 1998) [114] can be seen with a spectral index of ~ -0.74. We also see that the region between the companion and the northern arm of NGC5194 has a spectral index of ~ -0.8. Also to the left of the companion, NGC5195, the northern spiral arm can be seen continuing beyond what is seen in the normal radio continuum maps.

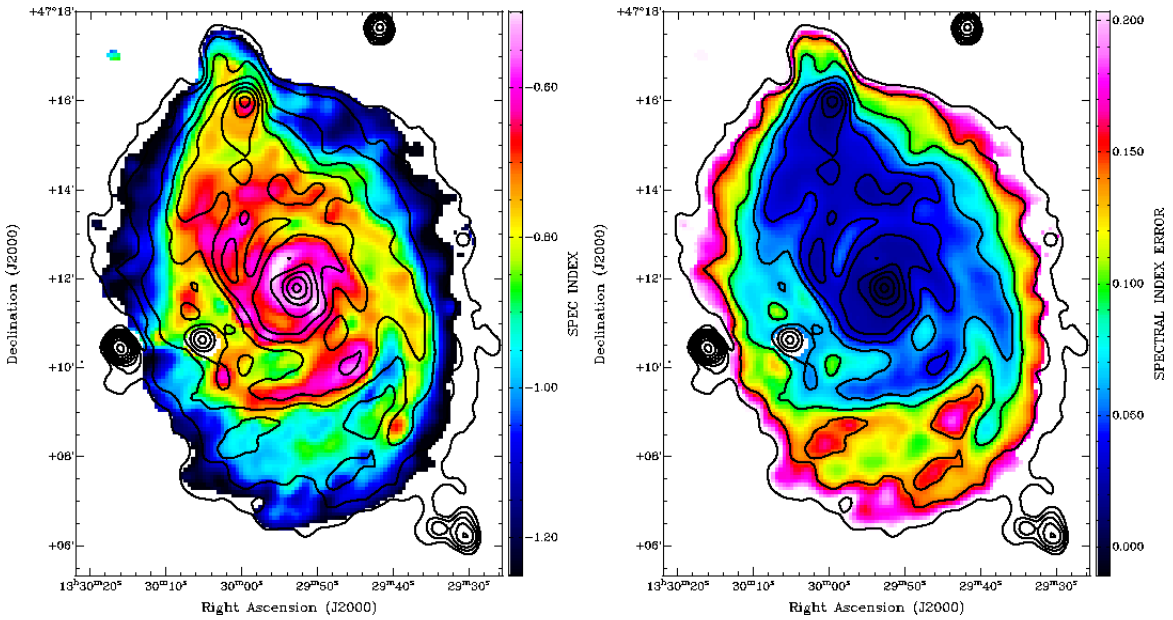

Figure 3.8: Spectral index map (left) & spectral index error map (right) made from the 1.4 GHz and 151 MHz maps at 20″ resolution the 151 MHz overlayed in contours.

Figure 3.9 shows the radial spectral index profile between 1.4 GHz and 151 MHz. We see several features including a slight dip at around r $\sim$ 2 kpc and a larger dip at r $\sim$ 3.5 kpc. These depressions show the interarm regions of M51. The spectral index rises again as the spiral arm region becomes more dominant. From 4 kpc $<$ r $\leq$ 10 kpc we see a gentle decrease in spectral index with a slight upturn at around r $\sim$ 10 kpc. This signifies the location of the companion galaxy NGC5195. The spectral index r $>$ 10 kpc drops very sharply indicating that the nonthermal emission is very much dominant in the extended disk and that the thermal fraction is very small. Also energy losses from the CREs is much

more significant in the extended disk compared to the inner star forming regions of the galaxy.

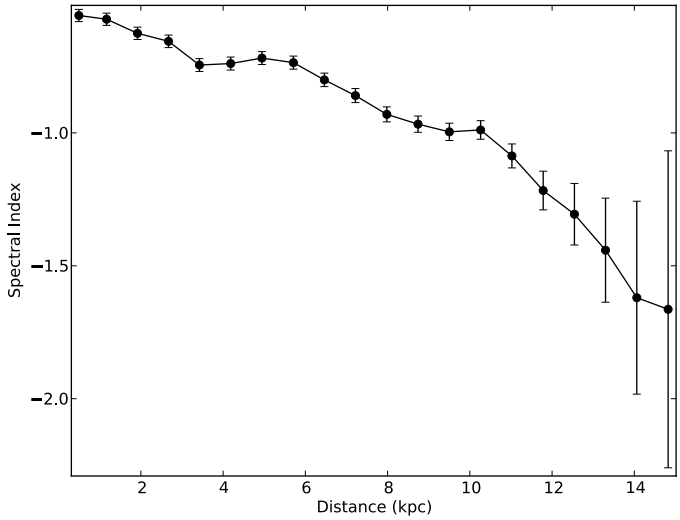

Figure 3.9: Radial spectral profile between 1.4 GHz and 151 MHz.

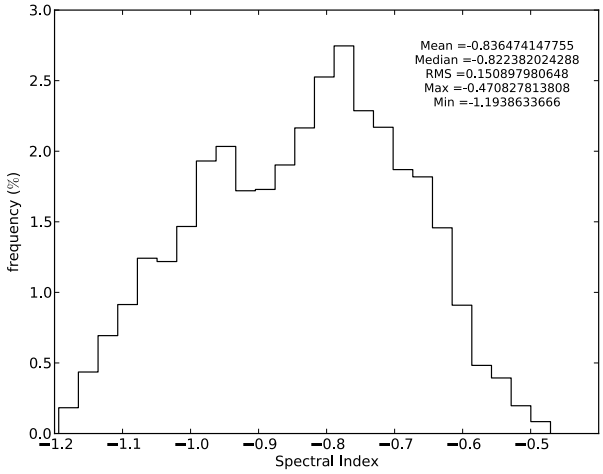

Figure 3.10: Histogram of the spectral index distribution grouped into 25 bins.

3.4.1 M51's total magnetic field

The total magnetic field of M51 can be determined from the non thermal synchrotron emission by assuming equipartition between the energy density of the cosmic rays and the magnetic field. The revised formula of Beck & Krause (2005)[115] was used. We used a nonthermal spectral index of -0.8 and an effective path length through the source to be 1064 pc. We also assumed that the polarized

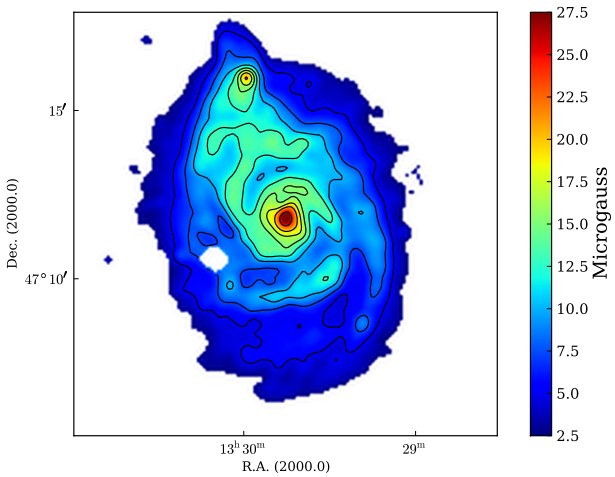

Figure 3.11: The total magnetic field of M51 in μG reaching up to R $\sim$ 10 kpc determined by assuming energy equipartition. Contours are in levels of 5,7.5,10,12.5,15,17.5,20,25 μG.

emission comes from ordered fields with all possible inclinations. Here we assume an proton and electron number density ratio of K=100, which is a fair assumption in the star forming regions in the disk. However, errors will become significant in regions away from these CREs sources especially in the outer disk as the observed K factor will increase. Assuming equipartition underestimates the total magnetic field by a factor of $(K/K_0)^{1/4}$ in these regions due to energy losses of CREs (Beck & Krause 2005) [115]. Fortunately, energy losses are generally weaker at these frequencies and therefore the equipartition estimate has a smaller error compared to higher frequencies. The total magnetic field strength was then scaled with the non thermal synchrotron intensity I_n using the following equipartition formula (Beck & Krause (2005)) [115]:

$$B \propto I_n^{1/(3+\alpha_{nt})} \tag{3.4}$$

Using these assumptions, we create a map of the total magnetic field in M51 shown in Figure 3.11. We see that the central region has magnetic field strength of between 20 and 30 μG while the arms have a strength of 10 to 20 μG. The interarm regions have a strength of between 8 and 11 μG. At regions R $\sim$ 10 kpc we observe field strengths of $\sim$ 5 μG. These values are lower than the values found in Fletcher et al. (2011)[93], but there a crude separation was performed to derive a nonthermal synchrotron map which was used to find the magnetic field strength. In this case, as the thermal component of the total emission is much smaller at 150 MHz than at 4.8 GHz, we would expect a smaller error in our estimation.

3.5 Cosmic ray propagation in M51

CREs lose their energies via a number of different processes such as losses from synchrotron radiation, inverse Compton (IC) losses, non-thermal bremsstrahlung, ionization losses and adiabatic losses. Out of these processes, synchrotron and inverse Compton losses have the same form and are therefore difficult to distinguish from the radio spectrum alone.

We take the equations from Pohl & Schlickeiser (1990)[116] to calculate the CREs energy E and the

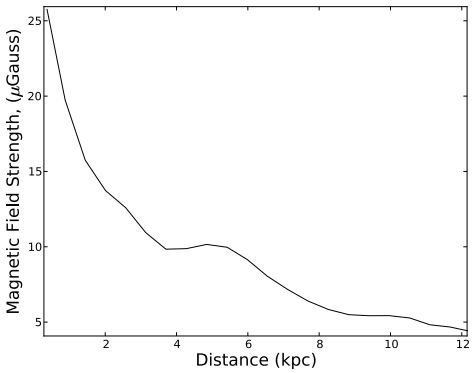

Figure 3.12: The radial profile of the total magnetic field of M51 in μG reaching up to 12 kpc.

synchrotron lifetime throughout M51 shown in figure 3.13:

$$E(\mathrm{GeV}) = (\nu/(16.1\mathrm{MHz}))^{1/2}\mathrm{B}(\mu\mathrm{G})^{-1/2} \tag{3.5}$$

$$\tau_{syn}(\mathrm{yr}) = 8.352 \times 10^{9}\mathrm{E}(\mathrm{GeV})^{-1}\mathrm{B}(\mu\mathrm{G})^{-2} \tag{3.6}$$

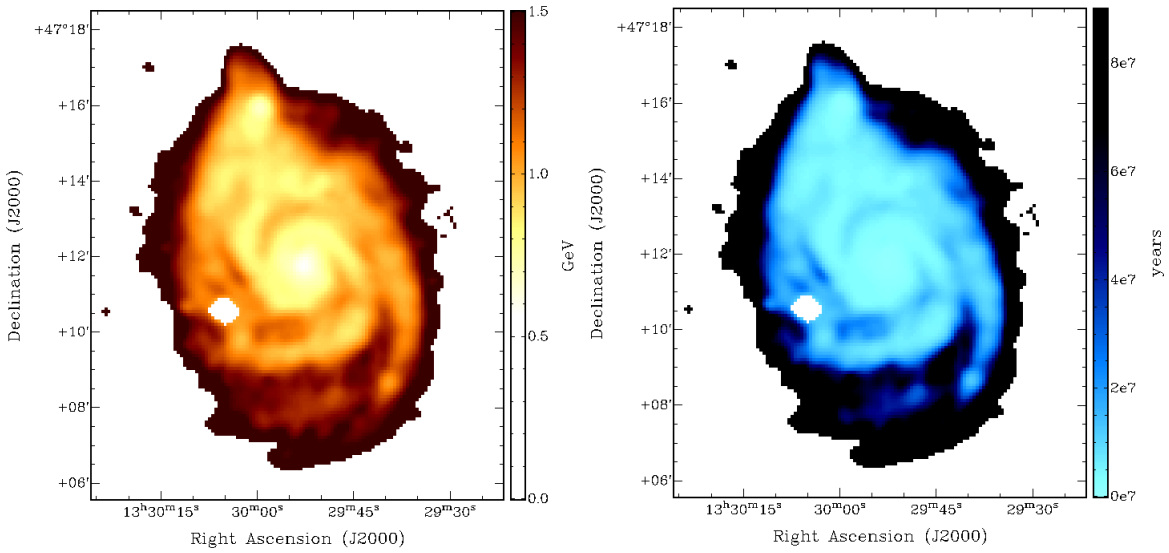

Figure 3.13: Cosmic Ray energy (left) and the synchrotron lifetime (right) maps of M51.

If we take $L = 1$ kpc as the normal distance that a CREs needs to travel from a SNR to the inter arm region of the galaxy then the diffusion coefficient D of the electrons is given by:

$$D = \frac{L^2}{\tau_{syn}} \tag{3.7}$$

In regions of high star formation within the spiral arms we calculate D to $\sim 7.5 \times 10^{28}$ cm^2 sec^{-1},

within the spiral arms but not in regions of high star formation we find D to be $\sim 3.8 \times 10^{28}$ cm^2 sec^{-1} and in the outer spiral arms D is found to be $\sim 1.5 \times 10^{28}$ cm^2 sec^{-1}. This agrees with the results of Fletcher et al. (2011) [93] as well as the values of $D \sim 1 - 10 \times 10^{28}$ cm^2 sec^{-1} found by Strong & Moskalenko (1998)[117] for the Milky Way.

Figure 3.13 shows us that at the edge of the extended disk r $\sim$ 10 kpc, the synchrotron lifetime for CREs is found to be approximately between $1 \times 10^8 < \tau_{syn} \leq 4 \times 10^8$ yr. Using a diffusion coefficient of $\sim 2.8 \times 10^{28}$ cm^2 sec^{-1}, and using equation 3.7, we see that the electrons at r $\sim$ 10 kpc are able to travel up to 3 - 6 kpc assuming no other energy losses. This takes us out to where we can detect the extended disk at 16 kpc with LOFAR.

3.5.1 The diffusion of cosmic ray electrons into the interarm regions

As mentioned in Basu et al. (2012)[81], at 333 MHz, the arm and inter regions were usually indiscernible for galaxies such as NGC6946. But in the case of M51 at 151 MHZ, we observe the arm and interarm regions very clearly. We would expect some amount of CREs diffusion into the interarms as the emission at 151 MHz are from a old population of CREs, which diffuses away from star forming regions in the spiral arms.

We took a Hα map, a 4.8 GHz, 1.4 GHz VLA maps from Fletcher et al. (2011)[93] in addition to the LOFAR 151 MHz and all maps were smoothed to a common resolution of 20″. All maps were made sure to be on the same grid. A slice was taken of M51 for all 4 maps at a region where the arm and interarm contrast could be studied. Finally, all fluxes from each map were normalized. The result of this can be seen in figure 3.14.

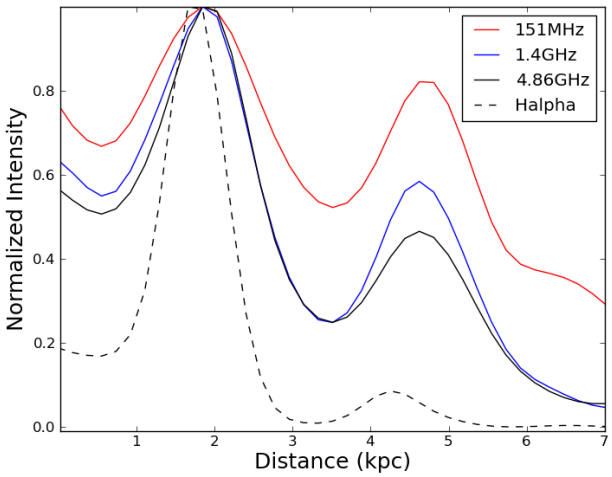

Figure 3.14: Intensity profile showing the arm and interarm contrasts of Hα and three different radio frequencies for a section of M51.

We see that the 4.8 GHz and 1.4 GHz profiles are very similar to each other, indicating that the CREs at 1.4 GHz which are 3.4 times less in frequency are not diffusing much further than at 4.8 GHz. But the CREs at 151 MHz which are 31.7 times less in frequency, a much smoother gradient is seen indicating that there is considerable more CREs diffusing fully into interarm region.

Therefore it must be explained that while we see considerable CREs diffusion in the interarm region

of M51, why don't we see CREs diffusing at the same extent as Basu et al. (2012)[81]? One reason could be a stronger and more turbulent spiral arm magnetic field seen in the M51 compared to galaxies like NGC6946. This could confine the CREs within the spiral arm making it harder for them to diffuse into the inter arm region.

3.6 Wavelet analysis of M51

Wavelet analysis is based on a space-scale decomposition using the convolution of the data with a family of self-similar basic functions that depend on the scale and location of the structure. The wavelet transform, like the Fourier transform, includes oscillatory functions, however, in the latter case these functions rapidly decay towards infinity. Frick et al. (2001) [118] showed that the wavelet is more resistant to noise and the smoother spectra allows better determination of the true frequency structure.

Wavelets have been applied to several galaxies for example M33 (Tabatabaei et al. 2007) [43] and M51 (Dumas et al. 2011) [104]. Wavelet transforms and cross correlation can enable one to separate the diffuse emission components from compact sources and compare the emission at different wavelengths which we shall perform in this section. It is also extremely useful to study the radio-IR correlation at various spatial scales especially when studying the differences of the correlation between the arm and interarm regions, for example Dumas et al. (2011)[104] & Basu et al. (2012)[119].

The wavelet coefficient of a 2D continuous wavelet transform is given by:

$$W(a, \mathbf{x}) = \frac{1}{a^{\kappa}} \int_{-\infty}^{+\infty} f(\mathbf{x}')\psi^*(\frac{\mathbf{x}' - \mathbf{x}}{a})d\mathbf{x}') \tag{3.8}$$

where $\psi(\mathbf{x})$ is the analysing wavelet, $\mathbf{x} = (x, y)$, $f(\mathbf{x})$ is a two-dimensional function which in this case is an image, a and κ are the scale and normalization parameters, respectively and finally * symbol denotes the complex conjugate.

The wavelet transform decomposes an image into maps of different scale which is given as a FITS cube. In each map of the cube, structures with the respective scales are prominent as they have larger coefficients than those with smaller or larger scales.

A LOFAR image at 151 MHz, a VLA map at 1.4 GHz and 70 μ meters from the SPITZER-MIPS (courtesy of F.Tabatabaei) were used for this analysis. The SPITZER-MIPS (Multiband Imaging Photometer for Spitzer, (Rieke et al. 2004) [120]). Infra-Red (IR) fluxes from normal galaxies are commonly taken to indicate the rate of recent star formation. (Hinz et al. 2004) [121] found that IR emission at 24 and 70 μm follows closely the structure of the ionized gas in M33, indicating that it is heated mostly by hot, ionizing stars.

All these maps were made sure to be on the same grid and smoothed to a PSF with FWHM of 20″. All images were of the same size which is important for the cross correlation. Bright background sources from the VLA and LOFAR maps were subtracted from the images.

The Mexican Hat wavelet was used as we wish to have more independent points and is a real isotropic wavelet with a minimal number of oscillations:

$$\psi(\rho) = (2 - \rho^2)e^{-\rho^2/2} \tag{3.9}$$

where $\rho = \sqrt{x^2 + y^2}$ This type of wavelet is shown in figure 3.15.

The periodic or gapped boundary conditions were compared and no difference could be seen so periodic boundary conditions was used. Gapped boundary conditions are usually important if there is not much blank space around the target being decomposed. The images have been decomposed into 10

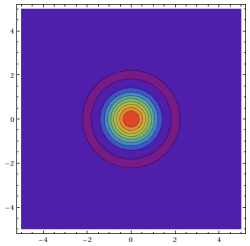

Figure 3.15: A 2D graphical representation of the Mexican hat wavelet.

different scales a in log space in order to compare the morphology between the three different images. The resulting wavelet decompositions can be seen in figure 3.16

We can see the individual HII regions within the spiral arms in the SPITZER and the VLA map quite well at smallest scale (a = 754 pc). However, these regions are not as visible in LOFAR at the same scale. The spiral arms are very visible at all three wavelengths at scales up to 1080 pc. The spiral arms are in discernible at a scales of 2212 pc but in the LOFAR map and to a smaller extent the VLA map, the lower spiral arm can be seen to extend much further out. This is probably due to the combination of the spiral arm and a kink in the southern inner spiral arm and several HII regions can be seen in the interarm region at this location. This is brought about due to fact of the interaction of M51 and NGC5195. This kink is also reproduced by (Dobbs et al. 2010) [91] in hydrodynamical simulations.

Once we get to a scale of 4440 pc, no discernible features can be seen in any of the wavelengths. All can be seen now is the underlying diffuse disk with a gentle radial decrease in intensity. It should be noted that the radial decrease is slower for M51 in the LOFAR dataset.

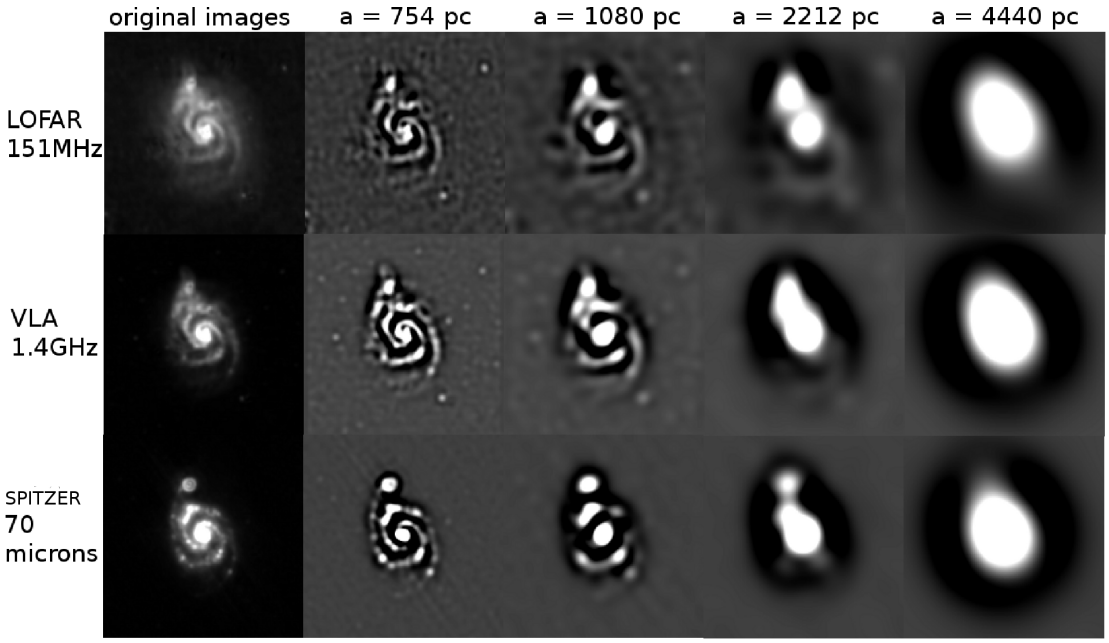

Figure 3.16: The original images of 151 MHz, 1.4 GHz & 70 μ meters are shown in the first column and their wavelet decompositions using a Mexican-hat wavelet for 4 different scales shown in parsecs.

In wavelet representation the scale distribution of the energy can be characterized by the wavelet

spectrum. This is defined as the energy of the wavelet coefficients of scale a of the whole physical plane:

$$M(a) = \int_{-\infty}^{+\infty} \int_{-\infty}^{+\infty} \left|W(a, \mathbf{x})|^2\right| d\mathbf{x} \tag{3.10}$$

The wavelet spectrum allows us to identify the dominant energy structures in our data and to qualitatively compare them. The wavelet spectrum for all three wavelengths are presented in figure 3.17.

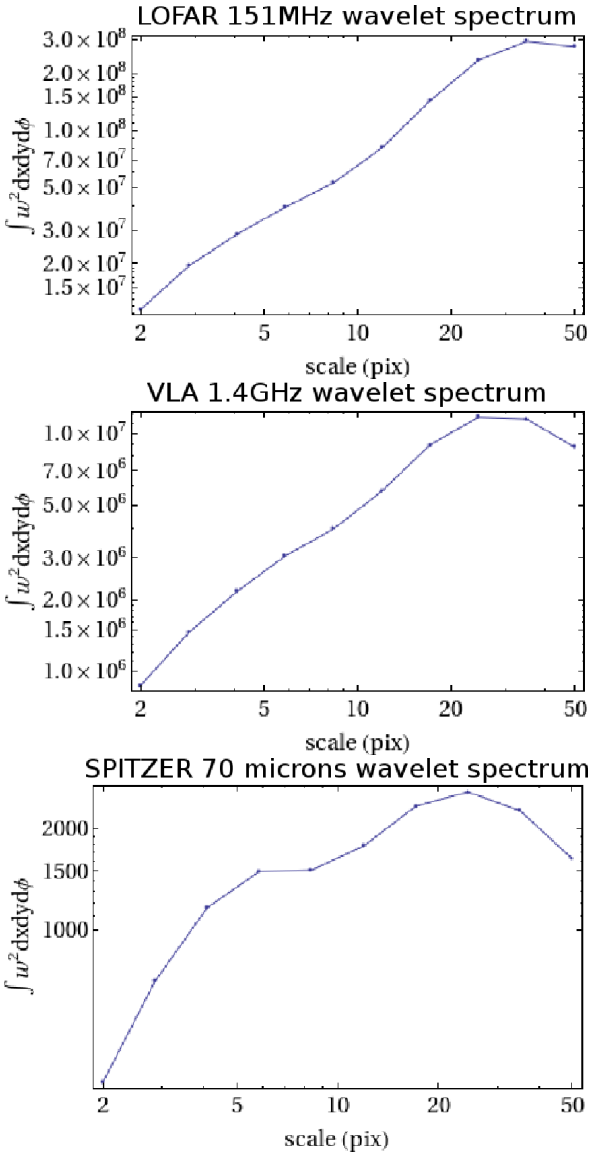

Figure 3.17: The wavelet spectrum for the three sets of data: LOFAR-151MHz (top), VLA-1.4GHz (middle), SPITZER-70 μmeters (bottom)

Due to the lack very high resolution it is hard to separate different features but we can see that the LOFAR wavelet spectrum reaches it's maximum energy at the highest scale compared to the other two wavelengths. LOFAR reaches it's maximum at 6.47 kpc while the VLA and SPITZER is 4.5 kpc. This

is due to the fact that the emission in LOFAR is able to extend further out due to CRE diffusion and the smaller synchrotron losses compared to higher frequencies. We also observe that the wavelet spectrum for the VLA data is very different to Dumas et al. (2011) [104] and could be due to an error in the combination of all 4 VLA configurations which were used.

3.6.1 Wavelet cross-correlations

The wavelet cross-correlation is a useful method to compare different images as a function of spatial scales as seen in Frick et al. (2001) [118], Dumas et al. (2011) [104] & Tabatabaei et al. (2007) [43]. Whilst normal cross-correlation anaylsis such as pixel to pixel correlation can be dominated by bright extended regions or large scale structure, the wavelet cross-correlation on the other hand, allows for the analysis of a scale-dependent correlation between two images.

The wavelengths cross-correlation coefficient at scale a is defined as:

$$r_w(a) = \frac{\int\int W_1(a,\mathbf{x})W_2^*(a,\mathbf{x})d\mathbf{x}}{[M_1(a)M_2(a)]^{1/2}} \tag{3.11}$$

A value of r_w can range between -1 (total anticorrelation) and +1 (total correlation). When one plots the value of r_w against scale one can see how well structures at different scales correlate in intensity and location.

The error is estimated by the degree of correlation and the number of independent points, n:

$$\Delta r_w(a) = \sqrt{\frac{1-r_w^2}{n-2}} \tag{3.12}$$

where, $n = 2.13(\frac{L}{a})^2$, and L is the size of the maps.

We define the value of $r_w > 0.75$ as a significant correlation (Frick et al. 2001) [118] & (Dumas et al. 2011) [104]. We see the cross correlation for our three different wavelengths in figure 3.18.

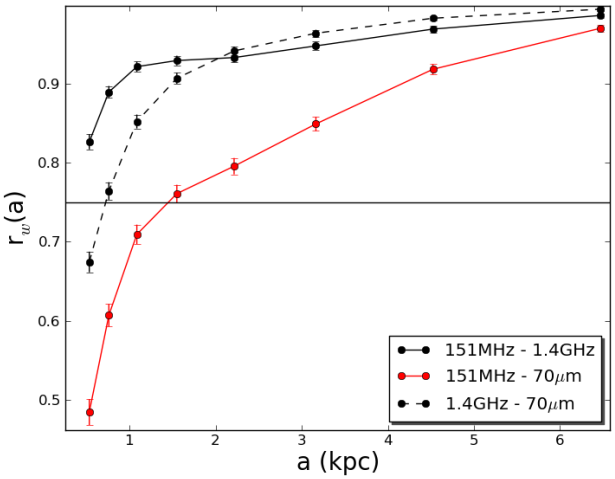

Figure 3.18: The cross correlation between our three different wavelengths with the solid black line showing the limit of significant correlation.

We observe that the cross correlation for the 1.4 GHz and 151 MHz data is extremely well correlated for all scales but we do see that the smaller scales less than 1 kpc do not correlate quite as well. Overall we see that r_w for 151 MHz - 70 μm is not as strong compared to 1.4 GHz - 70 μm

We see that the scale at $r_w = 0.75$ for the cross correlation between 151 MHz and 70 μm is approximately 1.45 kpc, which is about half for the cross correlation between 1.4 GHz and 70 μm at 720 pcs. This is a measure of the diffusion length l_{dif} which depends on the diffusion coefficient and CRE lifetime $l_{dif} = \sqrt{Dt_{CRE}}$. The diffusion coefficient can depend on the energy of the electrons, $D \propto D_E E^{0.5} \propto D_E \nu^{0.25} B_{tot}^{-0.25}$ with D_E being the energy dependent diffusion coefficient. These values correspond to (Dumas et al. 2011) [104] which found a value of $l_{diff} > 500$pc for M51. From (Tabatabaei et al. 2013) [46], this value is very similar to M31 ($l_{diff} > 730$pc $\pm$ 90) but considerable less compared to NGC6946 ($l_{diff} > 1700$pc $\pm$ 200). It should be noted that Tabatabaei et al. 2013 [46] used a value of 0.5 for r_w to signify a significant correlation.

This can simply interpreted as the CREs are diffusing from the star forming regions which can travel further at lower frequencies.

3.7 Detection of extragalactic background sources in polarization

3.7.1 Introduction

Up to present day very little has been done to study polarization at frequencies below 200 MHz and their characteristics cannot be extrapolated directly from higher frequencies. From previous observations at 350 MHz (Schnitzeler et al. 2009) [122], one would optimistically expect to detect a polarized source with a polarization degree of a few percent for every four square degrees (Bernardi et al. 2013) [123].

Fortunately, the study of polarization at low frequencies is now beginning to emerge partly due to the construction of LOFAR & the Murchison Widefield Array (MWA, Lonsdale et al. 2009 [70]) as well as the introduction of new techniques to analyse polarization such as RM synthesis (Brentjens & de Bruyn 2005)[124]. Recently, Bernardi et al. (2013) [123], performed a 2400 square degree polarization survey at 189 MHz with MWA with a 7′ beam. Out of a catalogue of 137 sources brighter than 4 Jy in total intensity, only one source was detected in polarization. Both beam depolarization and internal Faraday dispersion could cause this observed depolarization and therefore higher resolution observations are essential to discount the former effect. Gießübel et al. (2013) [82], whilst detecting diffuse polarization in the nearby galaxy M31 for the first time below 1 GHz, also created a catalogue of 33 polarized sources. Extrapolation of these results to even lower frequencies of LOFAR would result in very few source detections and no polarized diffuse emission detections. However, these observations are limited by a large angular resolution of 4′ and thus it needs to be seen if beam depolarization plays a large part in this. Farnes et al. (2013) [125] applied RM synthesis to data from the Giant Meterwave Radio Telescope (GMRT) and found that M51 was depolarized below the sensitivity limit.

LOFAR is a perfect instrument to measure Faraday depths to a very high accuracy and hence detect weak magnetic fields and low electron densities which are unobservable at higher frequencies. Importantly, LOFAR with it's high sensitivity and high angular resolution should be able to reduce depolarization. Already LOFAR is producing polarization results, Iacobelli et al. (2013) [126] was able to detect a faint and morphologically complex polarized foreground of the highly polarized Fan region which was in agreement with previous WSRT observations (Bernardi et al. 2009) [127].

3.7.2 Applying RM synthesis

For each channel Stokes Q and U were imaged with an area of 17.3 square degrees with CASA at 20″ resolution. Therefore, the primary beam is not applied which will lead to errors. However, using AW-imager for a field this size at this high resolution for every channel would require more processing time and power that is available. Each channel image was inspected and any channel with RFI contamination was discarded. This resulted in 3774 final images. RM Synthesis was performed on these images using software written by the LOFAR MKSP. The rms noise was found to be 79 μJy/beam where the angular resolution was 20″. The resulting Faraday cube was then cleaned using the RM Clean code written by Dr. George Heald (Heald et al. (2009)) [32] for MIRIAD (Sault et al. 1995)[128]. 1 σ level was used for the cutoff level and 1000 was the maximum number of iterations assigned. Usually instrumental polarization is located at a Faraday depth of 0 rad m^{-2}. However, due to the ionospheric RM correction that was performed, this instrumental polarization is shifted by the average RM correction implemented to the data. Therefore, for this observation, the instrumental polarization is located at a Faraday depth of approximately -1 rad m^{-2}.

The resolution in Faraday depth ϕ of this observation is given by the measured full width half maximum of the RM spread function (Brentjens & de Bruyn 2005)[124]:

$$\varphi = \frac{2\sqrt{3}}{\Delta\lambda^2} \tag{3.13}$$

where $\Delta\lambda^2$ is the width of the observed λ^2 distribution.

With a minimum frequency of 115.9 MHz and maximum of 176 MHz. This gives us $\varphi = 0.91$ rad m^{-2}. The largest detectable structure in Faraday spectrum (Brentjens & de Bruyn 2005) [124] is given by

$$\phi_{max} = \frac{\pi}{\lambda^2_{min}} \tag{3.14}$$

For this observation $\phi_{max} = 1.085$ rad m^{-2}. The error in Faraday depth is found by the following expression

$$\Delta\phi = \frac{\varphi}{2S/N} \tag{3.15}$$

where φ is the FWHM of the RMSF and the S/N is the signal-to-noise ratio of the peak of the component in the Faraday spectrum.

3.7.3 Extragalactic polarization detections

Unfortunately, no polarization from M51 was detected and must be strongly depolarized below the sensitivity limit. This is not surprising seeing that Farnes et al. (2013)[125] were unable to detect M51 in polarization at 610 MHz.

Taking five times the thermal noise as the detection threshold and assuming an average 1% degree of polarization, all sources with fluxes above a peak flux of 50 mJy were checked for polarization. From these sources, there were 6 polarized detections of background extragalactic radio galaxies in the field. Two of these sources are starting to become resolved with polarization detected in the lobe. This would result in a polarized source for every 2.9 square degrees.

Where data is available from higher frequencies notably Taylor et al. (2009)[129] we can determine the depolarization as in Beck (2007) [48]:

$$DP(150, 1400) = (PI_{150}/PI_{1400}) \times (\nu_{150}/\nu_{1400})^{\alpha_{nt}} \tag{3.16}$$

where α_{nt}=-1.0 is the non thermal spectral index and ν_i is the respective frequency.

Here we will address each source briefly. A summary of these detections can be seen in table 3.5 at the end of the chapter.

J133923+464008

This is a strong polarization detection in a radio galaxy where a single lobe is very dominant. The central component is detected in polarization (polarization degree of 7.7 ± 0.25%) at 1.4 GHz, but here at 151 MHz it is completely depolarized. The detected polarization comes solely from the single lobe. This single lobe contains two spatial components observable in both total and polarized intensity. The north component which is brighter is at a Faraday depth of 20.5 ± 0.1 rad m^{-2} while the southern component is 20.75 ± 0.1 rad m^{-2}. This is agreeable with the RM value found in Taylor et al. (2009)[129]. We find that the depolarization for this source is DP = 0.034. The Faraday spectra and total intensity map for this source can be seen in figure 3.19.

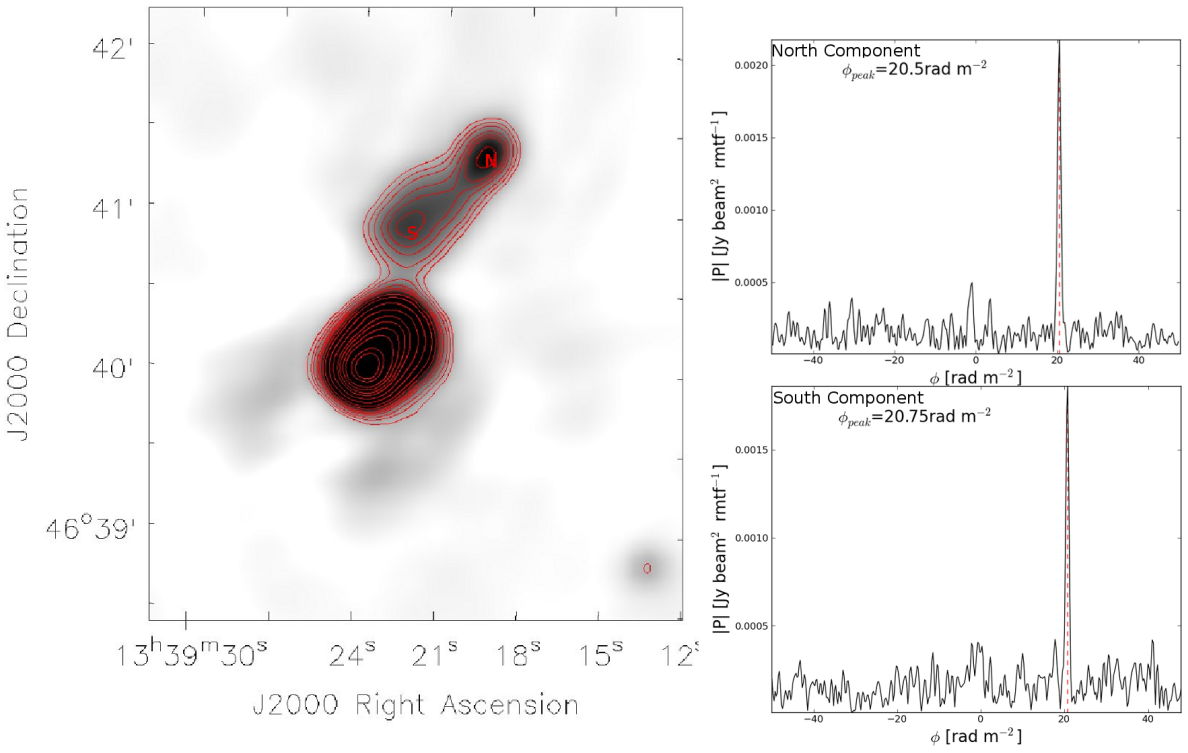

Figure 3.19: The radio lobe J133923+464008 seen in total intensity (left) with the two marked spatial components and the corresponding Faraday spectra (right).

This single lobe polarization fraction hardly decreases compared to the 1.4 GHz data of Taylor et al. (2009) [129]. This seems to suggest that we are seeing the Laing-Garrington effect (Garrington et al. 1988) [130] where the stronger jet is closer to us and is seen through a smaller amount of magneto-ionic material and thus shows less depolarization.

6CB1322467+483810

Once again this source is a single lobe radio galaxy with a strong polarization detection in the lobe at ϕ = +3.25 rad/m^{-2}. Unfortunately, this source is not seen in Taylor et al. (2009) [129] and therefore no comparison can be made at higher frequencies. At the peak of the lobe we see a polarization degree of 2.9%, very similar to the previous source J133923+464008. At this peak, we only see one clear component in the Faraday spectrum. Closer to the edge of the radio lobe marked 'O' in Figure, we see a secondary component at ϕ = +19.5 rad/m^2 with a polarized flux of 500 μJy/beam and possibly a third at ϕ = +30.5 rad m^{-2} with a polarized flux of 360 μJy/beam. The Faraday spectra and total intensity map for this source can be seen in figure 3.20.

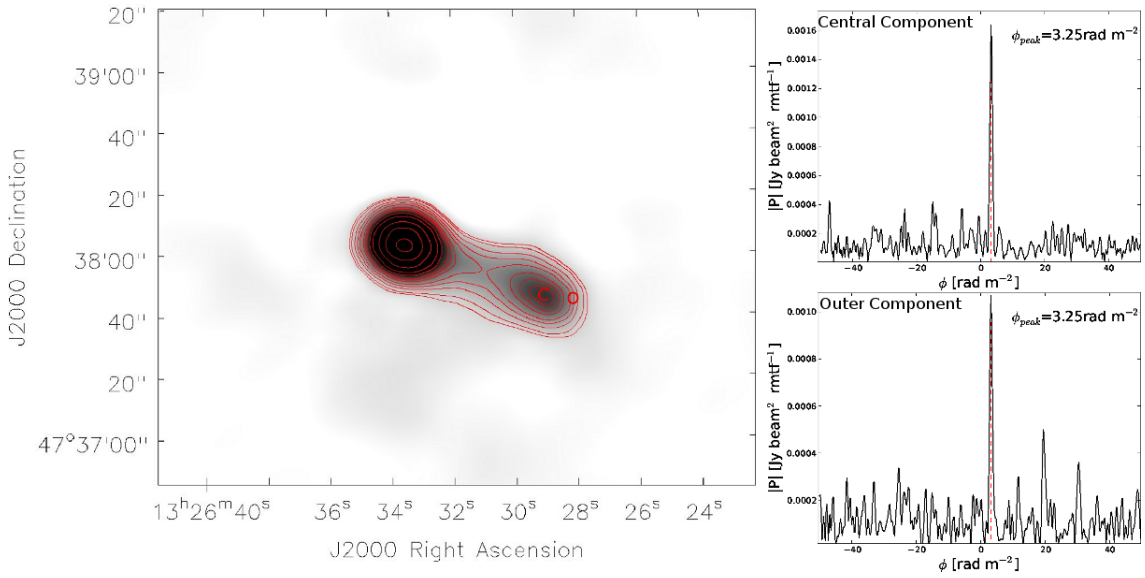

Figure 3.20: The radio lobe 6CB1322467+483810 in total intensity (left) with the two marked corresponding Faraday spectra (right).

J133707+485801

This unresolved source is detected in polarization at ϕ = +9.25 rad/m^{-2} with a polarized flux of 1.3 mJy/beam. Interestingly Taylor et al. (2009)[129] has a RM = -8.9±3.2 rad m^{-2}, while a similar value but with the wrong sign. This could be a sign error in the determination from Taylor et al.(2009)[129]. With a polarization fraction of just 0.2% at 151 MHz the depolarization ratio of this source is then 0.0082. The Faraday spectrum for this source can be seen in figure 3.21.

J133258+454201

This unresolved source is detected in polarization at ϕ = -5.25 rad/m^{-2} at 650.08 μJy/beam (S/N ratio is 8.2). This source is not detected in Taylor et al. (2009)[129]. The Faraday spectrum and for this source can be seen in figure 3.22.

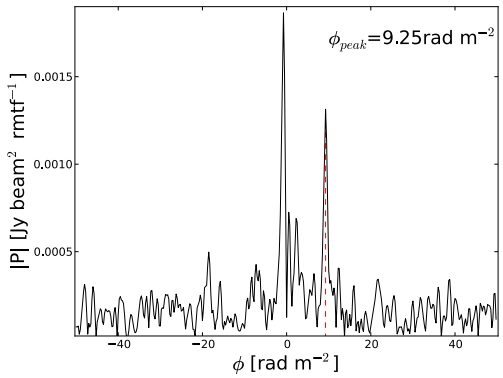

Figure 3.21: Faraday Spectrum of J133707+485801.

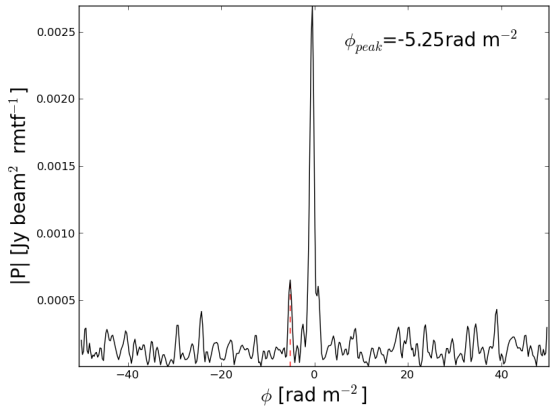

Figure 3.22: Faraday Spectrum of J133258+454201.

J133128+454002

This unresolved source is detected in polarization at two different Faraday depths, namely ϕ = -3.75 rad/m^{-2} with a polarized flux of 526 μJy/beam (S/N ratio is 6.6) and ϕ = +26.75 rad/m^{-2} with a flux of 507.79 μJy/beam (S/N ratio is 6.4). This source is not detected in Taylor et al. (2009)[129]. The Faraday spectrum for this source can be seen in figure 3.23.

4C+47.38

This unresolved source is detected in polarization at a Faraday depth of ϕ = 23.5 rad/m^{-2} with a polarized flux of 2.32 mJy/beam (S/N ratio is 29.36) This source was detected in Taylor et al. (2009)[129] with a RM of 30.6±1.4 rad/m^{-2}. With a polarization fraction of just 0.2% at 151 MHz the depolarization ratio of this source is then 0.00664. The Faraday spectrum for this source can be seen in figure 3.24

Several double lobe radio galaxies (for example see figure 3.25) detected in polarization by Taylor et al. (2009)[129] were not seen in polarization at 151 MHz.

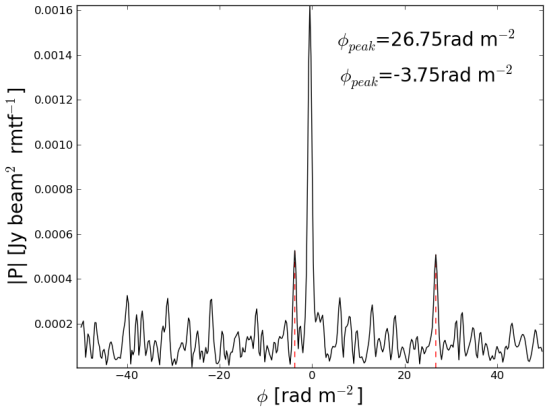

Figure 3.23: Faraday Spectrum of J133128+454002.

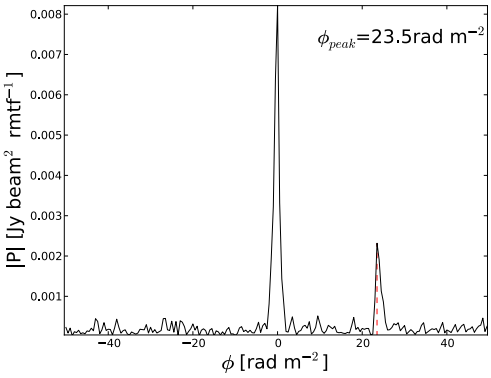

Figure 3.24: Faraday Spectrum of 4C+47.38.

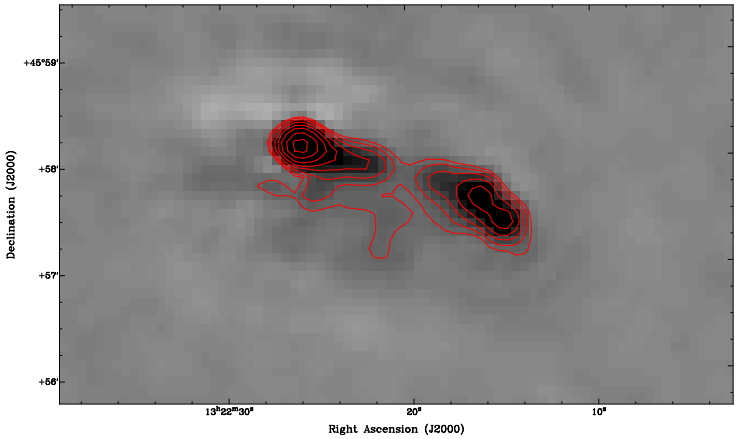

Figure 3.25: Double lobe radio galaxy while polarized at 1.4 GHz is not seen to be polarized at 151 MHz.

3.8 Discussion

In the analysis of the integrated flux, we see no spectral flattening and therefore disagree with Pohl et al. (1991) [131] (Figure. 11). It is obvious that inaccuracy of the flux from Israel and Mahoney (1990) [26] makes interpretation difficult and could be simply wrong. From these results it seems that the break energy is beyond 5 GeV (i.e. the energy of CREs emitting at about 5 GHz).

This puts the interpretation from Hummel (1991) [28] & Pohl et al. (1991) [131] less plausible. They argue that the break in the integrated spectrum is caused by the energy losses of the CREs due to the dynamic halo and this causes the spectrum to steepen at higher frequencies.

As seen in Pohl et al. (1991) [131], the break energy E_b is given by:

$$E_b = \frac{3.3 \times 10^{15}(\frac{\mathrm{div(v)}}{sec^{-1}}) + 8(\frac{n}{1cm^{-3}})}{(\frac{w(r)}{0.7eVcm^{-3}}) + 1/4(\frac{B_\perp}{3\mu G})^2} \tag{3.17}$$

where div(v) is the adiabatic expansion term, n represents the bremsstrahlung losses term with n being the total gas density, $w(r)$ is the radiation field representing inverse Compton losses and $1/4(B_\perp)^2$ is the synchrotron losses term with $B_\perp$ being the magnetic field strength in the line of sight.

However the model used did not take into account free free absorption and diffusion.

In M51, if this model is correct we should see a steepening at higher frequencies but this is not observed.

The spectral index at the central region of M51 indicates that thermal absorption is occurring but only at localized regions in the center of the galaxy. There is little thermal absorption at frequencies above 151 MHz, so that the integrated spectrum is not flattening.

As thermal absorption is not much of an issue in M51 we can use equation 3.17 from Pohl et al. (1991) [131] and neglecting inverse Compton losses (Heesen et al. in prep) and adiabatic expansion, and assuming an average total gas density of 1 cm^{-3} and an average field strength of 10 μG, we get E_b = 2.9 GeV. In order to shift this to greater than 5 GeV, either the gas density has to be greater than 2 cm^{-3} or we need a wind with div(v) $> 2 \times 10^{-15}$ sec^{-1}.

If we approximate div(v) $\sim \Delta v/\Delta z$, we need a vertical velocity gradient of $\Delta v > 60$ km/s/kpc, which seems too large. Heesen et al. (2009)[17] found a typical wind speed in the NGC253 halo of 300 km/s at several kpc height and no signs of acceleration. Instead the gas density has to be greater than 2 cm^{-3} which is very reasonable.

The radial profiles of 151 MHz and 1.4 GHz which consist mostly of non thermal emission are fitted by a flatter exponential profile at $R < 10$kpc than at $R > 10$kpc. Nonthermal emission mimics the distribution of the star forming regions in the disk and according to our findings, this still applies for low frequencies even though theoretically CREs should be able to travel further. As a result, the expectation that galaxies would be extremely large at low frequencies doesn't seem to hold. The break in the radial continuum profile will make it more difficult to see the extreme edges of the extended disk with LOFAR. The magnetic field strength beyond 10 kpc may become weaker than expected suggesting that neither turbulence from star formation nor magneto-rotational instability can create a sufficiently strong magnetic field for CREs to propagate along. Alternatively, the CREs may lose their energy much faster through some other loss process other than synchrotron losses and are not able to travel much further than we anticipated. What is still clear from our observation is that a significant magnetic field is present up to 16 kpc in the outer disk due to the fact that we simply observe synchrotron emission. The magnetic field would need to be ≥ 3.25 μG in order to be visible in the synchrotron instead of inverse Compton processes from the CMB.

Other face on galaxies with different properties such as NGC628 with an extended HI disk (Walter

et al. 2008) [132] need also to be examined to test if this kind of radial break is common in galaxies. Several more face-on galaxies have been been or will be shortly observed with LOFAR and should shed more light on this matter.

With regards to the polarization, we were able to detect 6 polarized background sources resulting in a density of one polarized source for every 2.9 square degrees. We have seen that the two resolved sources have a polarization fraction of approximately 3% at the radio lobe. Several polarized sources (at 1.4 GHz) where both radio lobes were resolved but completely depolarized at 151 MHz suggests that Faraday depolarization not beam depolarization is the dominant depolarization factor. Both of the resolved sources have one prominent radio lobe at 20″ resolution which suggest that the Laing-Garrington effect (Garrington et al. 1988) [130] is also relevant at 151 MHz which isn't suprising due to its dependence on frequency. The low density of background sources found in this work bodes ill for one of the main goals of the LOFAR Magnetism Key Science Project which was to create RM grids of polarized background sources behind galaxies which would be a more sensitive way to detect weak magnetic fields. Much more sensitivity is required to achieve this goal and probably won't be achievable with LOFAR.

The lack of a detection of diffuse polarization in M51 at low frequencies demonstrates that star forming galaxies produces significant turbulence that depolarizes any polarization signal completely. If we would have any chance to observe diffuse polarization it should be for a target with significant magnetic fields but little star formation for example, intergalactic fields in interacting galaxies or galaxy groups. However, this polarization sample is still small and more fields observed with LOFAR need to be processed for polarization.

Table 3.5: Summary table of the polarization detections in the M51 field

Name	RA	Dec	ϕ [rad/m^2]	PI [mJy]	p [%]	RM [rad/m^2]	PI [mJy] (Taylor et al. 2009)	p [%]
$J133923+464008$	$13^h39^m19^s$	$46°41'19''$	$+20.5 \pm 0.4$	2.2 ± 0.07	3.04	22.5 ± 0.1	6.8 ± 0.5	3.6 ± 0.1
$6CB1322467+483810$	$13^h26^m28^s$	$47°37'41''$	$+3.2 \pm 0.1$	1.6 ± 0.07	2.9			
$J133707+485801$	$13^h37^m07^s$	$48°58'04''$	$+9.2 \pm 0.3$	1.3 ± 0.07	0.2	-8.9 ± 3.2	16.9 ± 0.3	6.0 ± 0.1
$J133258+454201$	$13^h32^m58^s$	$45°42'2''$	-5.2 ± 0.3	0.65 ± 0.07	0.002			
$J133128+454002$	$13^h31^m28^s$	$45°40'4''$	-3.8 ± 0.3	0.53 ± 0.07	0.003			
$4C+47.38$	$13^h41^m45^s$	$46°57'16.8''$	$+23.5 \pm 0.1$	2.32 ± 0.07	0.2	-30.6 ± 1.4	37.25 ± 0.24	5.8 ± 0.04

CHAPTER 4

Modeling of the Cosmic Ray Diffusion in M51

4.1 Introduction to cosmic ray propagation

Cosmic ray electrons (CREs) are accelerated in the disk by shock waves induced by supernova explosions, a significant fraction of which occur in OB associations on a timescale of several 10^7 years (Reynolds et al. 2012) [133].

CR particles can propagate through the ISM by streaming with the Alfvén velocity along the ordered magnetic field lines or they can be scattered by the turbulent magnetic field. This leads to random walk diffusion which dominates in the Milky Way disk (Strong, Moskalenko & Ptsukin, 2007) [134] & (Dogiel & Breitschwerdt, 2012) [135]).

Cosmic ray diffusion explains why energetic charged particles have highly isotropic distributions and why they are well retained in the galaxy. The galactic magnetic field that tangles the trajectories of particles plays a crucial role in this process. Typical values of the diffusion coefficient found from fitting to CR data are around (3-5) $\times$ 10^{28} cm^2 s^{-1}, at a energy of approximately 1 GeV/n, and increases with rigidity (the particle's ability to resist bending its trajectory).

In order to model and describe the propagation of CREs we must construct an partial differential equation which describes the energy spectrum and particle density at different locations of the interstellar medium in the presence of continuous energy losses and with the continuous supply of fresh electrons from sources. This equation is known as the *diffusion-loss equation* for high energy electrons.

The derivation of this equation follows the simple approach from (Longair, 2010) [16]. We start an elementary volume of space, dV, into which electrons are injected at a rate $Q(E,t)dV$. The electrons within dV are subject to energy losses and can be written as:

$$-(\frac{dE}{dt}) = b(E) \tag{4.1}$$

In the absence of injection of electrons, the number of particles at time t that are in the energy range E to $E + \Delta E$ is $N(E)\Delta E$). At a later time $t + \Delta t$, these particles have been replaced with those electrons that have energies in the range E' to $E' + \Delta E'$, where

$$E' = E + b(E)\Delta t \tag{4.2}$$

$$E' + \Delta E' = (E + \Delta E) + b(E + \Delta E)\Delta t \tag{4.3}$$

Here we perform a Taylor expansion for ΔE and subtracting, we get:

$$\Delta E' = \Delta E + \frac{\mathrm{db(E)}}{\mathrm{dE}} \Delta E \Delta t \tag{4.4}$$

Therefore the change in $N(E)\Delta E$ in the time interval Δt is

$$\Delta N(E)\Delta E = -N(E,t)\Delta E + N[E + b(E)\Delta t, t]\Delta E' \tag{4.5}$$

If one performs another Taylor expansion for small $b(E)\Delta t$ and substituting for $\Delta E'$, we obtain:

$$\Delta N(E)\Delta E = \frac{\mathrm{dN(E)}}{\mathrm{dE}} b(E)\Delta E \Delta t + N(E)\frac{\mathrm{db(E)}}{\mathrm{dE}} \Delta E \Delta t \tag{4.6}$$

which is,

$$\frac{\mathrm{dN(E)}}{\mathrm{dt}} = \frac{\mathrm{d}}{\mathrm{dE}}[b(E)N(E)] \tag{4.7}$$

Now we add an injection term where the particles are continuously injected at a rate of $Q(E,t)$ per unit volume. We also add a gradient term with a scalar diffusion coefficient, D. With these additions, we can present the diffusion-loss equation for relativistic electrons:

$$\frac{\mathrm{dN(E)}}{dt} = \frac{\mathrm{d}}{\mathrm{dE}}[b(E)N(E)] + Q(E,t) + D\,\nabla^2\,N(E) \tag{4.8}$$

Segalovitz, (1977)[136] studied the radial variation of the spectral index of M51 using analytical solutions of equation 4.8. In this study, several different source functions were used. Firstly a spheroidal source function:

$$Q(r,z,E) = \begin{cases} Q_1 E^{-\gamma_0} exp(-z^2/b^2 - r^2/a^2)/\pi^{3/2}a^2 b & \text{for } E_1 \leq E_2 \\ 0 & \text{otherwise} \end{cases} \tag{4.9}$$

where a and b are the semi axes of spheroid where E_1 and E_2 are the limits on the range of injection energies. This failed to explain the observed spectral index. A step-like source function was found to be a better fit:

$$Q(r,z,E) = \begin{cases} Q_1 E^{-\gamma_0} exp(-z^2/b^2) & \text{for } E_1 \leq E_2 \text{ and } r \leq a \\ 0 & \text{otherwise} \end{cases} \tag{4.10}$$

Leakage of CREs out of the galactic magnetic field had a time scale shorter than the energy loss time of the electrons emitting at the observed frequency band.

These source functions are very dated and a source function extracted from the star formation of the galaxy should be used. Also, advances in computing would enable to solve equation 4.8 via approximation rather than analytical modeling. While analytical solutions for simple cases can give insight into the relations between the quantities involved and are good for rough estimates, they can become so complicated that no insight is gained. On the other hand, numerical models are very intuitive because they are able to generate the cosmic ray distribution over the galaxy for all species, the best example being the Galactic Propagation (GALPROP) code (Strong & Moskalenko, 1998) [137].

While our own Galaxy has been modeled extensively using the GALPROP code, external galaxies have not been modeled with both diffusion and energy losses of CREs since Segalovitz (1977) [136]. Several models have been performed for star forming galaxies but as homogeneous disks of gas which would enable to solve the steady state version of the diffusion-loss equation. Lacki et al. (2010) [138]

uses this form of the equation to predict the far-infrared (FIR) radio correlation. However, the authors note that in weaker starbursts, where the cooling and escape times are several megayears, the evolution of the CREs via diffusion and convection become important and the steady-state approximation will fail.

Therefore, for a galaxy like M51 the diffusion term becomes important and has to be modeled along with the energy losses of the CREs. Creating a code to solve this equation would enable us to investigate the importance of the different energy loss processes and estimate the magnitude of the diffusion coefficient for different galaxies. However, this code will need to be created from scratch.

In this chapter, I introduce the development and approximation methods used to solve the diffusion-loss equation. In addition, I show first results from this code and compare to observational results shown in the previous chapter.

4.2 Methods for solving the diffusion-loss equation

In order to solve the diffusion-loss equation numerically, one must employ several different approximation methods. Solving each term of the diffusion-loss equation is treated separately. The code is written entirely in PYTHON[1].

4.2.1 Solving the time derivative

Solving the the time derivative term of the diffusive equation $\frac{\delta N}{\delta t}$ requires the use of the Runge-Kutta methods which are families of systematic higher order improvements over the Euler method. The key idea is to evaluate the derivative $\frac{\delta N}{\delta t}$ not only at the end points t_n or t_{n+1} but also at intermediate points such as:

$$y_{n+1} = y_n + \Delta t f(t_n + \frac{\Delta t}{2}, y(t_n + \frac{\Delta t}{2})) + O(\Delta t^3) \tag{4.11}$$

The unknown solution $y(t_n + \frac{\Delta t}{2})$ is given by the second order Runge-Kutta algorithm:

$$\begin{aligned} k_1 &= \Delta t f(t_n, y_n) \\ k_2 &= \Delta t f(t_n + \Delta t/2, y_n + k_1/2) \\ y_{n+1} &= y_n + k_2 + O(\Delta t^3) \end{aligned} \tag{4.12}$$

The term $O(\Delta t^3)$ represents the local truncation error which is the error induced for each successive stage of the iterated algorithm. The most widely used Runge-Kutta algorithm is the fourth order method and will be used for our purposes. As this is a fourth-order method, the local truncation error is on the order of $O(\Delta t^5)$, while the total accumulated error is of order of $O(\Delta t^4)$. It is given by:

$$\begin{aligned} k_1 &= \Delta t f(t_n, y_n) \\ k_2 &= \Delta t f(t_n + \Delta t/2, y_n + k_1/2) \\ k_3 &= \Delta t f(t_n + \Delta t/2, y_n + k_2/2) \\ k_4 &= \Delta t f(t_n + \Delta t, y_n + k_3) \\ y_{n+1} &= y_n + 1/6(k_1 + 2k_2 + 2k_3 + k_4) + O(\Delta t^5) \end{aligned} \tag{4.13}$$

[1] http://www.python.org/

4.2.2 Solving the spatial derivative

When solving ordinary or partial differential equations, the first step is to discretized space and time and to replace differentials by differences. In solving the spatial derivatives we need to use the finite differences method for a second derivative. For a first derivative, the differential $\frac{\delta f}{\delta x}$ can be approximated to the first order by:

$$\frac{\delta f}{\delta x} = \frac{f(x_{n+1}) - f(x_n)}{\Delta x} + O(\Delta x) = \frac{f(x_n) - f(x_{n-1})}{\Delta x} + O(\Delta x) \tag{4.14}$$

where $O(\Delta x)$ is the truncation error.

From this we can get a second derivative estimator:

$$\frac{\delta^2 f}{\delta x^2} = \frac{f(x_{n+1}) + f(x_{n-1}) - 2f(x_n)}{\Delta x^2} + O(\Delta x^2) \tag{4.15}$$

For our simulations we shall use the fourth-order estimator for a second derivative:

$$\frac{\delta^2 f}{\delta x^2} = \frac{-f(x_{n-2}) + 16f(x_{n-1}) - 30f(x_n) - 16f(x_{n+1}) - f(x_{n-2})}{12\Delta x^2} + O(\Delta x^4) \tag{4.16}$$

However, the above estimator is not suitable for points near our spatial boundaries as points will become non-tabular (i.e. beyond the spatial boundaries) and therefore for the right hand side we use:

$$y_0'' = (35y_0 - 104y_{-1} + 114y_{-2} - 56y_{-3} + 11y_{-4})/12h^2 \tag{4.17}$$

using the notation $y_k = y(x + kh), h > 0$.

For the left hand side we use:

$$y_0'' = (11y_4 - 56y_3 + 114y_2 - 104y_1 + 35y_0)/12h^2 \tag{4.18}$$

The above methods were tested on solving the one-dimensional heat equation for a triangular initial temperature :

$$\frac{\delta f}{\delta t} = c^2 \frac{\delta^2 f}{\delta x^2} \tag{4.19}$$

as the heat equation is similar to the diffusion equation that we ultimately want to solve and is good test for functionality. Note that there is only one injection of heat at $t = 0$.

The spatial boundary conditions at $r = 0, 100$ are simply set to zero, at all times. These boundary conditions hence act as heat sinks and with time the heat should diffuse out making the triangular initial temperature go to zero. Applying the code to this triangular initial temperature works as it should be which can be seen in figure 4.1. It is seen that the initial temperature decreases to zero with time. Therefore we can be assured that the diffusive part of our code is working correctly.

As we are solving for a galaxy, it is more natural to use cylindrical coordinates rather than cartesian.

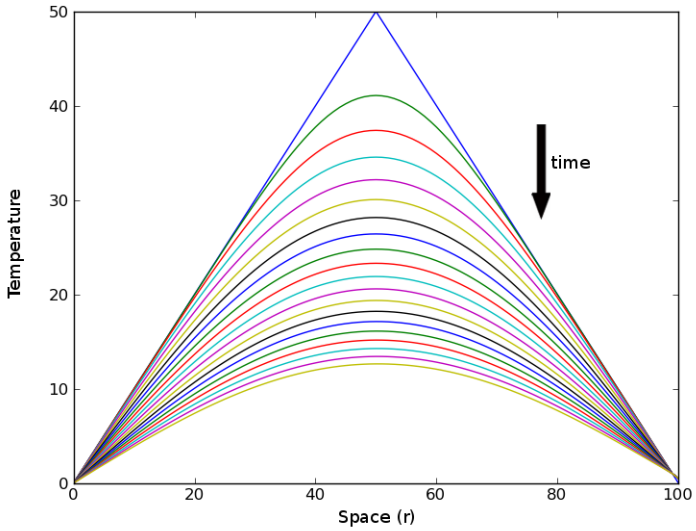

Figure 4.1: The diffusion of a triangular initial temperature with heat sinks as the boundary conditions. With time the heat diffuses into the heat sinks. The y-axis shows temperature while the x-axis is space.

In cylindrical coordinates, our diffusion term from equation 4.7 becomes:

$$\nabla.(D\nabla N(E))|_r = \frac{1}{r}\frac{\partial}{\partial r}(rD\frac{\partial N(E)}{\partial r}), \tag{4.20a}$$

$$\nabla.(D\nabla N(E))|_r \approx \frac{D}{r}\frac{\partial}{\partial r}(r\frac{\partial N(E)}{\partial r}), \tag{4.20b}$$

$$\nabla.(D\nabla N(E))|_r \approx \frac{D}{r}[\frac{\partial N(E)}{\partial r} + r\frac{\partial^2 N(E)}{\partial r^2}] \tag{4.20c}$$

4.2.3 Adding the Source Function

The radial distribution of the star formation rates for M51 of Kennicut et al. (2007) [108] and Schuster et al. (2007) [110] were used to determine the SN rate. The SFR from Kennicut et al. (2007) [108] were found using a combination of Hα and 24μm data, which gives reliable extinction corrected ionizing fluxes and SFR densities. Schuster et al. (2007) [110] used CO (2-1), HI and 20cm radio continuum data to determine the SFR. The data was extracted using DEXTER on the A&A website. However, the data from both Kennicut and Schuster only go out to 8 kpc and using the above method for extrapolation had poor results. Fortunately, SFR for regions with faint HI and infrared emission were determined by Thornley et al (2006) [96] up to 13 kpc from the center of the galaxy. Here we use the Hα corrected data and the results of the extended disk seen in figure 4.2. which seem to agree well with the Kennicut values. Therefore the values from Kennicut and Thornley are used for our source function. A power law of an index of -0.45 was fitted to the Thornley SFR values with a distance (see figure 4.2) from 7-10 kpc ignoring values greater than 10 kpc as the scatter gets quite large. A 3rd order univariate spline was used to interpolate SFR values in order to get an equal spaced grid of data points. This also important in order to smooth the SFR values. The reason being in that any sharp edges in the source function would

produce discontinuities and therefore no differentials would be found. Values were extrapolated for the central region of the galaxy using the same method which gave good results.

To determine the supernovae (SN) rate, we use the IMF power law using the Salpeter slope (Salpeter, (1955)) [139] of -7/3:

$$N(M) \propto M^{-7/3} \tag{4.21}$$

where M is the stellar mass. If we assume that stars with $> 8\ M_{\odot}$ become SNs then the fraction of mass that goes into SNs is:

$$f_M = \frac{\int_8^{20} M \times M^{-7/3} \mathrm{dM}}{\int_{0.1}^{20} M \times M^{-7/3} \mathrm{dM}}$$
$$f_M = 7.2\% \tag{4.22}$$

This fraction is applied to SFR rate profiles above to find the radial distribution of SNe output mass. If these distributions are summed up one would get 0.35 solar masses per year are converted to SN using Kennicut's SFR. Taking the mean mass of a SN to be 12 $M_{\odot}$, M51 should produce on average 1 SN per 34.5 years. For the Schuster data we get 0.44 solar masses per year are converted to SN which would produce 1 SN per 27 years. Our own Milky Way produces 1 SN per 50 years but one would expect M51 to have a greater SN rate due to the interaction with its companion. Furthermore it must be noted that 3 SN have been detected in M51 in the last 20 years (1994I, 2005cs, 2011dh). Therefore, these values found are quite realistic.

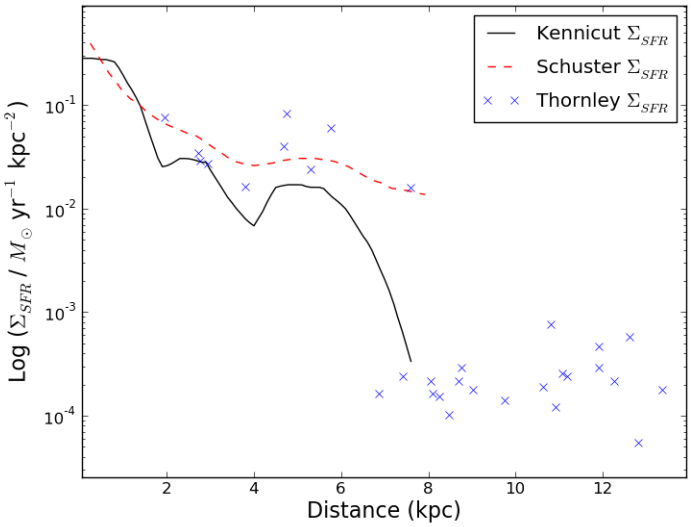

Figure 4.2: The star formation rates taken from Kennicut et al. (2007) [108], Schuster et al. (2007) [110] and Thornley et al (2006) [96].

The full source term is:

$$Q(E, R) = Q(R) \kappa E^{-p} \tag{4.23}$$

here the Q(R) is the radial profile of the SN rate which we have just found and p is the initial slope of the CRE energy spectrum which is taken as approximately 0.5 for our simulations.

We can now add the diffusion and source terms together and what we should see is initially a large increase in N(E) at a single energy with the injection of CREs. While this is happening diffusion will smooth the interarm and extended disk features. After a certain amount of time has elapsed, N(E) starts to stabilize as the diffusion and injection terms are canceling each other. This is what the code produces in figure 4.3.

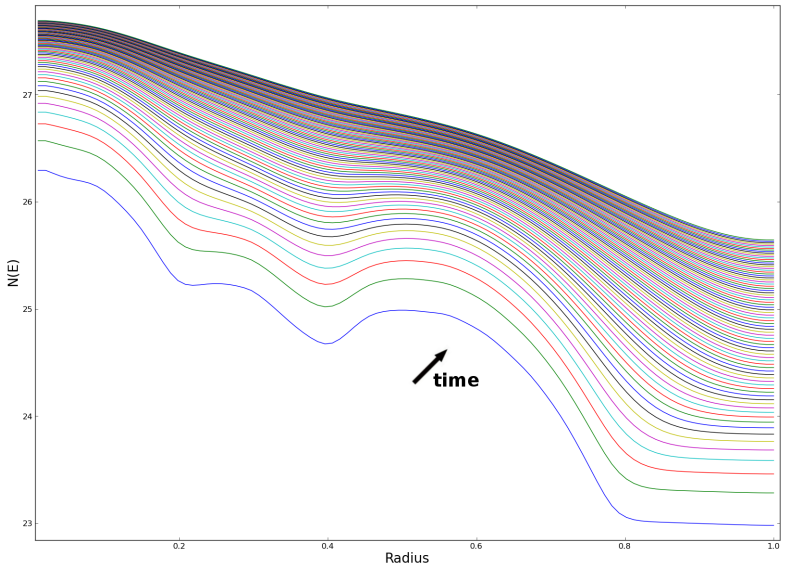

Figure 4.3: The evolution of N(E) against radius with time (2000 time iterations). Only the diffusion and source term are included in the code.

We can see the evolution of different regions of the galaxy increase with time in figure 4.4. The extended disk takes the longest to stabilize as the CREs takes a longer time to travel from the main star forming region (<8kpc).

4.2.4 Solving the energy derivative

When solving the energy part of the equation, $\frac{\delta}{\delta E}[b(E)N]$, where b(E) compromises of the energy loss processes, we will only take in account synchrotron and inverse Compton losses. Therefore:

$$b(E) = -(-\frac{\delta E}{\delta t}) = -(\frac{\delta E}{\delta t})_{sync} - (\frac{\delta E}{\delta t})_{IC}$$

$$b(E) = \frac{4}{3}\sigma_T c\gamma^2 U_{mag} + \frac{4}{3}\sigma_T c\gamma^2 U_{rad} \tag{4.24}$$

$$b(E) = \frac{4}{3}\sigma_T c\gamma^2 (U_{mag} + U_{rad})$$

where σ_T is the Thompson cross section, γ is the Lorentz factor, U_{mag} is the energy density of the magnetic field which is $B^2/8\pi$ and U_{rad} is the the energy density of the radiation field.

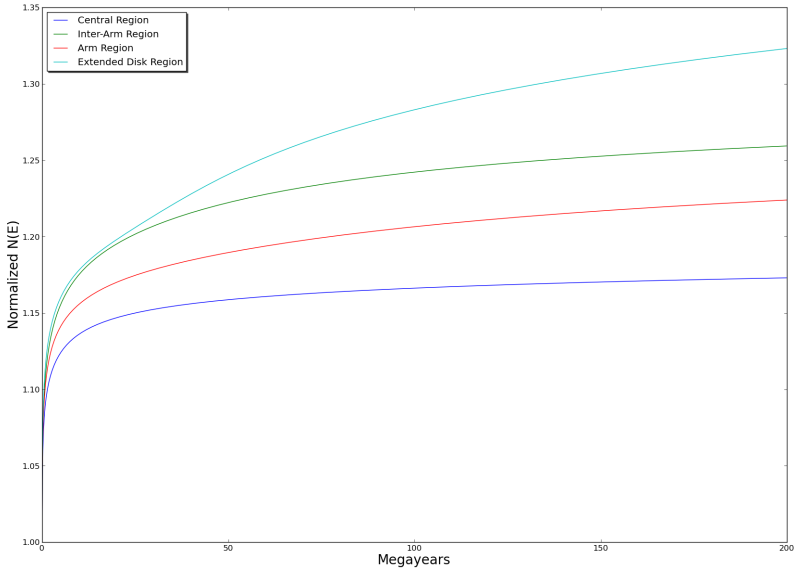

Figure 4.4: The evolution of normalized N(E) at different regions of the galaxy with the diffusion coefficient of $D = 2.8 \times 10^{28}$ cm^2 s^{-1} at a set energy. Energy losses are not included in the simulation.

To solve this energy term we employ a first order upwind scheme, given as:

$$\frac{u_j^{n+1} - u_j^n}{\Delta t} = -v_j^n \begin{cases} \frac{u_j^n - u_{j-1}^n}{\Delta x} & v_j^n > 0 \\ \frac{u_{j+1}^n - u_j^n}{\Delta x} & v_j^n < 0 \end{cases} \tag{4.25}$$

A very useful test is to compare this differential energy solution to an exact analytical solutions of the diffusion loss equation, ignoring the diffusion term. From Longair we can use the following analytical solution when an injection of electrons with a power law energy spectrum at t=0 only (i.e no continuous injection of electrons). Therefore we have $N(E) = \kappa E^{-p}\delta(t)$:

$$N(E) = \kappa E^{-p}(1 - aEt)^{p-2} \tag{4.26}$$

Not only does this help us compare and check if the code is working, it also helps us to understand the nature of the parameters and how they can change the overall evolution of the CRE energy. For the exact analytical solution, a is set in order that $aEt \leq 0$ and p is tested for $p \leq 2; p = 2; p \geq 2$. For $p = 2$, the solution stays constant. But if $p \geq 2$, we see the energy solution decreases quite rapidly after a certain period of time. In the case of $p \leq 2$, the opposite takes place, in that the energy distribution increases rapidly at higher energies. These analytical solutions can be seen in figure 4.5.

When we solve the differential in our code using the first order upwind scheme we can see the same behavior as the analytical solution except for $p = 2$. While the evolution stays constant for a period of time, a slight instability occurs and pushes the slope $p > 2$ and therefore the energy decreases. These results are presented in figs 4.6, 4.7 and 4.8.

Looking at these results, we can be confident that the energy loss part of equation 4.8 works properly.

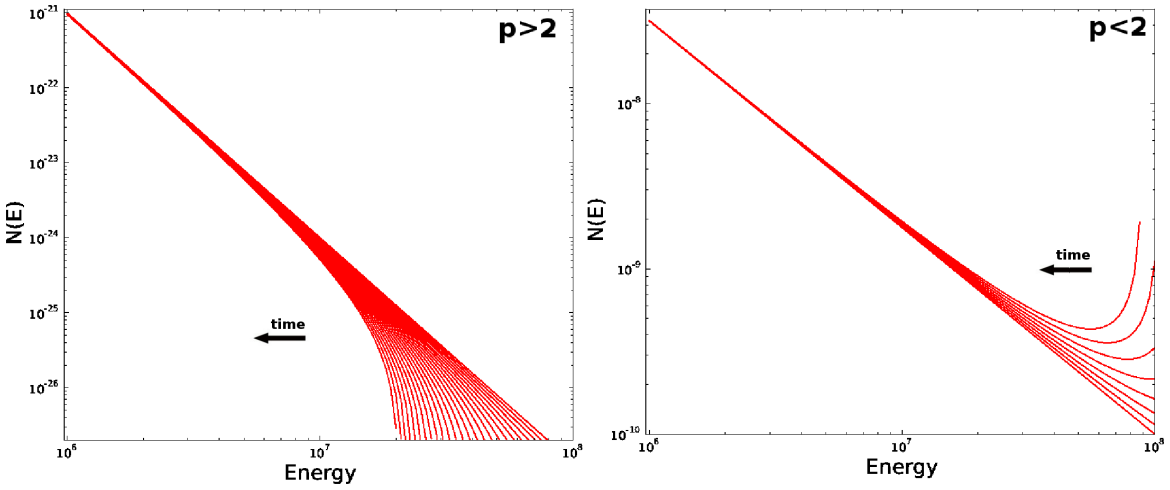

Figure 4.5: The analytical time evolution of a power-law energy distribution injected at $t = 0$ only for $p > 2$ (left) and $p < 2$ (right)

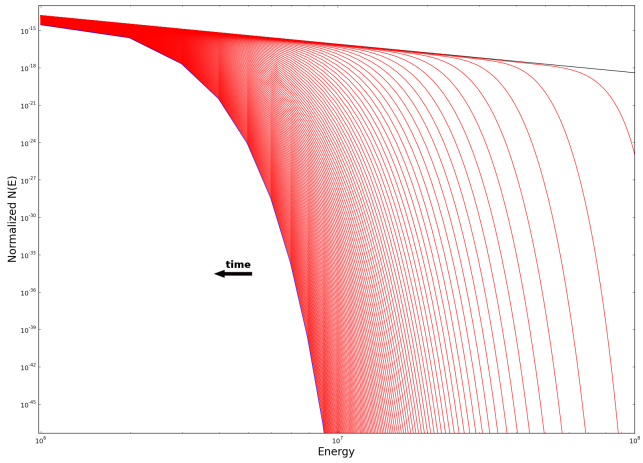

Figure 4.6: The evolution of energy with a single injection of CREs with a injection spectrum of p > 2. The red lines are in steps of 1000 iterations.

4.2.5 Selecting the boundary conditions

First attempts at creating a stable boundary condition were performed by letting:

$$\frac{\partial N}{\partial r} = \text{constant} \tag{4.27}$$

and

$$\frac{\partial N}{\partial E} = \text{constant} \tag{4.28}$$

This was done by creating a dummy point beyond the range of values for energy and radius by assuming a continuous slope. Using these dummy points we can solve the derivative by simply using the finite

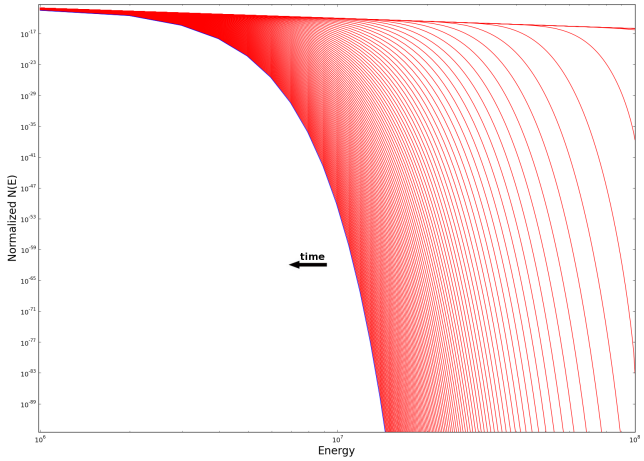

Figure 4.7: The evolution of energy with a single injection of CREs with a injection spectrum of p=2. The red lines are in steps of 1000 iterations.

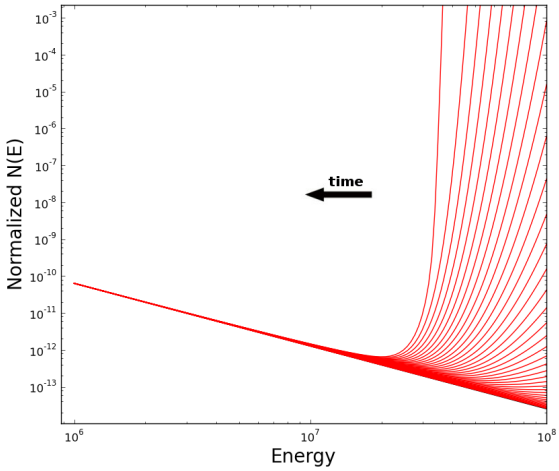

Figure 4.8: The evolution of energy with a single injection of CREs with a injection spectrum of p < 2. The red lines are in steps of 1000 iterations.

differences method for the diffusion and the upwind scheme for the energy losses.

It was seen that while this would produce stable solutions for the energy derivative, the spatial derivative, however, became very unstable after several hundred iterations. This can be seen in the top plot of figure 4.9. Therefore at R = 0,10 kpc the boundary condition:

$$\frac{\partial N}{\partial r} = 0 \tag{4.29}$$

was used. This was seen to be stable which is illustrated in the bottom plot of figure 4.9.

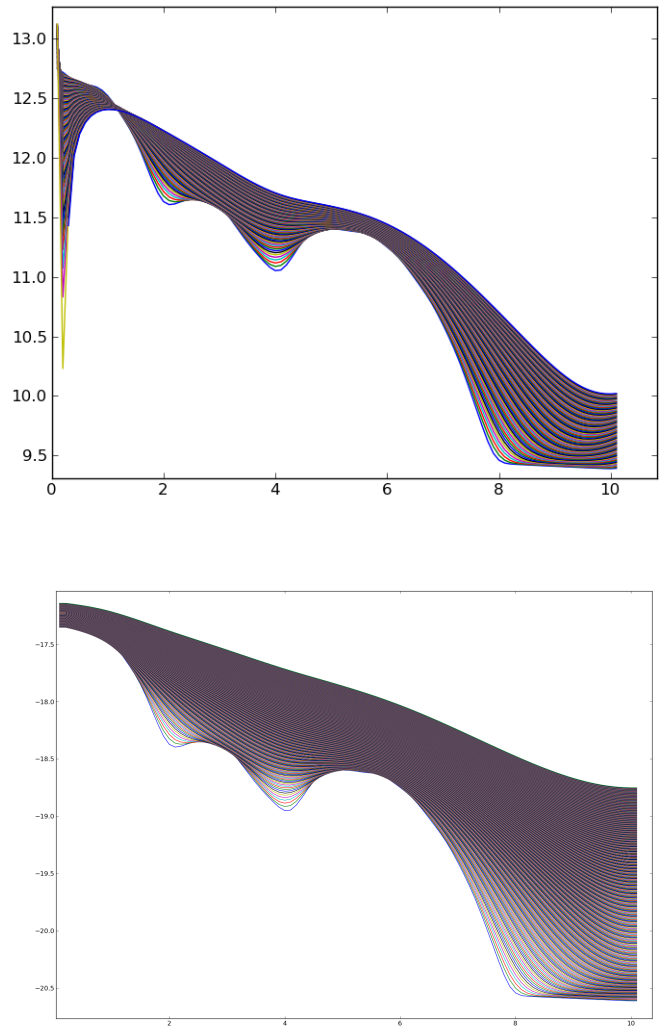

Figure 4.9: Showing the effects of different boundary conditions has on the radial distribution of CRe. The top plot shows the inadequacy of using a continuous derivative as a boundary condition. The bottom plot shows how letting the derivative equal to zero creates a stable solution.

4.2.6 Scaling the equation

As we are not interested in finding the total intensity of the synchrotron emission but rather the spectral index and scale lengths we are able to make everything dimensionless and not worry about units to a certain extent.

We introduce scalings of the form:

$$r = Rr'$$
$$t = t_0 t' \tag{4.30}$$
$$E = E_0 E'$$

R is taken as 10 kpc, t_0 is taken as 1×10^6 years and E_0 is taken as 5×10^{10} eV. All values used needed to be converted to cgs before making them dimensionless. The magnetic field is also scaled similarly.

The equation 4.8 when scaled becomes

$$\frac{\partial N}{\partial t'} = \frac{t_0 D}{R^2}\frac{1}{r'}\frac{\partial}{\partial r'}(r'\frac{\partial N}{\partial r'}) + \beta\frac{t_0 B_0^2}{E_0}\frac{\partial}{\partial E'}[E'^2 B'^2 N] + t_0 Q_0 Q(r' E^{-p}) \tag{4.31}$$

where

$$\beta = \frac{4}{3}\sigma_T c \frac{1}{m_e^2 c^4} \tag{4.32}$$

where σ_T is the Thompson cross section, c is the speed of light and m_e is the electron mass.

From the equation 4.31 we define the following coefficients:

$$\Theta = \frac{t_0 D}{R^2} \tag{4.33}$$
$$\Phi = \frac{\beta t_0}{E_0} \tag{4.34}$$
$$K = t_0 Q_0 \tag{4.35}$$

These coefficients will enable us to control the diffusion, energy losses and injection respectively.

$$\frac{\partial N}{\partial t} = \Theta\frac{1}{r'}\frac{\partial}{\partial r'}(r'\frac{\partial N}{\partial r'}) + \Phi B_0^2\frac{\partial}{\partial E'}[E'^2 B'^2] + KQ(r')E'^{-p} \tag{4.36}$$

Equation 4.36 is the final form the equation that is used in our simulations.

4.3 Investigation of cosmic ray diffusion without losses

In this section, a simulation will be run with the diffusion and source terms of equation 4.8 only. Therefore, energy losses are neglected. The source term is continuously injected at every iteration.

From this, the nature and effect of CR diffusion to the quantity of CREs with respect to the radius of M51 can be studied and compared to observations. Here we add two additional frequencies of M51 kindly supplied by Andrew Fletcher, the first being a GMRT 333 MHz map and the second being a 4.8 GHz map from the VLA (Fletcher et al, 2011) [93].

The radial profiles of all these frequencies can be seen in figure 4.10. The two extra frequencies were not included in the analysis of the previous chapter due to unreliability of the fluxes in the outer disk. The 4.8 GHz is not sensitive enough and combination with Effelsberg single dish data in order to fill in the missing spacings can lead to further inaccuracies, whilst the GMRT map contains some artifacts in the outer disk due to the calibration. Fortunately, the fluxes for the star forming disk for all frequencies are quite reliably and therefore we can use them to study the scale length of the inner

disk. An exponential profile of the form $I_0 exp(-r/l)$, where l is the scale length which was fitted to the inner 10 kpc of the disk but excluding the inner 1 kpc, due to the AGN in the central region. We see in table 4.1 the respective scale lengths for each frequency.

Frequency MHz	Scale length (R <10 kpc) kpc	Diffusion length kpc	Diffusion time $\times 10^7$ yrs
4800	2.98±0.2	2.1	8.9
1400	3.4±0.2	2.36	11.3
333	4.45±0.2	2.9	17.6
150	5.32±0.2	3.34	22.7

Table 4.1: Scale lengths of the radio continuum at four different frequencies with corresponding diffusion length and time found from simulations using $D = 2.8 \times 10^{28}$ cm^{-2} s^{-1}.

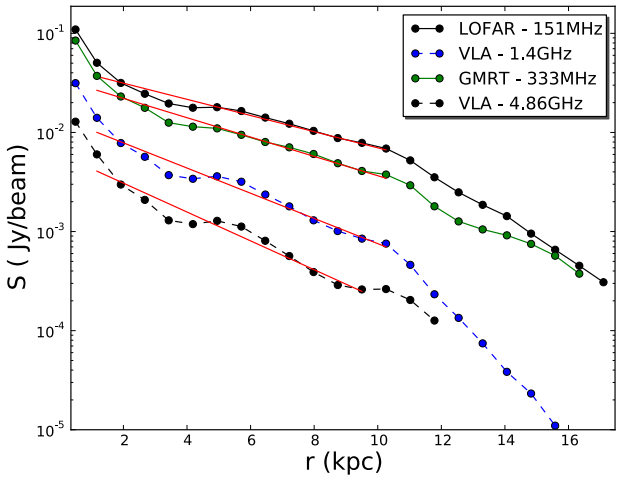

Figure 4.10: The radial profile of the radio continuum for M51 at several frequencies. The inner 10 kpc has been fitted with an exponential profile to determine the continuum scale length.

Comparing the scale lengths found here (see table 4.1) to the scale lengths found by (Dumas et al. 2011) [104] where the 4.8 GHz scale length (5.6±0.4) is larger than the 1.4 GHz scale length (4.5±0.5), it is obvious that there is a significant difference. It must be said that Dumas et al. (2011) had to combine all VLA configuration in addition to Effelsberg and this combination could have introduced significant errors in both frequencies.

The scale lengths found for each frequency are plotted in figure 4.11. It is found that a power law of the form $l = 1.2 \times 10^5 \nu^{-0.16\pm0.02}$ with ν being the observed frequency, fits the data quite well.

From Tabatabaei et al. 2013 [46], the diffusion length is:

$$l_d \propto \sqrt{D \cdot t_{syn}} \tag{4.37}$$

where:

$$t_{syn} \propto B^{-3/2} \nu^{-1/2} \tag{4.38}$$

$$D \propto \nu^{1/4} B^{-1/4} \tag{4.39}$$

combining both terms and solving the square root we get:

$$l_d \propto \nu^{-1/8} B^{-7/8} \tag{4.40}$$

This frequency dependence matches well to observed values, showing that diffusion is dominant along the inner disk.

We see the arm and interam regions are much more apparent at the higher frequencies but become smeared out with decreasing frequency.

We also observe the trend that the scale lengths increases with decreasing frequency which is what one would expect as the CREs at low frequencies lose their energies more slowly and therefore can travel much further, thus increasing the scale length.

Our model should be able to replicate this feature.

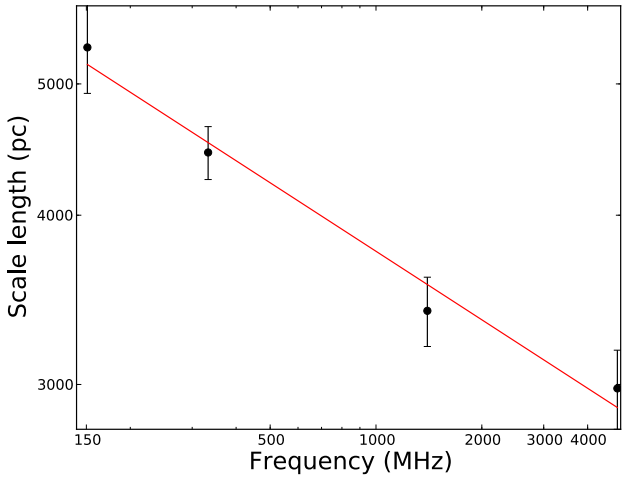

Figure 4.11: Scale lengths of M51 continuum emission from the inner disk against frequency. A power law is fitted shown in the figure by the solid red line.

The diffusion length is given by:

$$l_{diff}/pc = \sqrt{D/pc^2 yr^{-1}(t/2)/10^7 yr} \tag{4.41}$$

D is the diffusion coefficient and depends on the energy of the CRE as $D \propto E^p$ where $p \approx 0.5$ (Strong,Moskalenko & Ptuskin, 2007)[134]. Here D is set to 2.8×10^{28}cm^{2}sec^{-1} (Strong & Moskalenko. 1998) [137] and t is the time elapsed. We can see that the evolution of the radial profile of $N(E)$ in figure 4.12, with the respective diffusion length. We see that the interarm region is no longer visible with a diffusion length of approximately 1 kpc. This is the normal distance that a CRE needs to travel from a SNR to the interarm region. This corresponds to 2×10^7 years.

The simulation was run for 2.5×10^8 years and an exponential scale length was fitted to the $N(E)$ radial profile for many times in the evolution. The results of this can be seen in figure 4.13. We see that the scale length of $N(E)$ increase linearly with time and exponentially with diffusion length. From these we

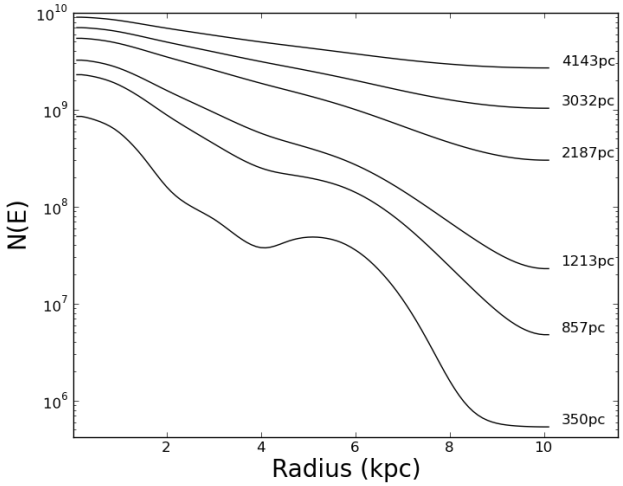

Figure 4.12: The radial profile of the distribution of CREs of a set energy at different diffusion lengths.

can estimate the diffusion length and time for our observations which are also shown in table 4.1. The diffusion length for 1.4 GHz is found to be 2.36 kpc which is not far off for what is typical for galaxy disks (1-2 kpc) (Murphy et al. 2006) [45].

4.4 Investigation of cosmic ray diffusion with losses

The energy loss term is now switched on with synchrotron losses only and determine the spectral index between the energy of the electrons at 151 MHz and 1.4 GHz. The energy corresponds to the observed frequency by the following equation:

$$E_{CRe} = \sqrt{\frac{\nu_{\mathrm{MHz}}}{16\mathrm{MHz\,B_{\perp}}}} \tag{4.42}$$

where ν_{MHz} is the resulting frequency in MHz and $B_{\perp}$ is the perpendicular magnetic field in μG.

We first test using different diffusion coefficients when running our simulation and we observe that a diffusion coefficient of 1 $\times 10^{28}$ cm^2 s^{-1} doesn't work as we get a very different shape for the radial spectral index which can be seen in figure 4.14. This is due to the fact that the CREs cannot diffuse far enough before losing their energy. We have also used a diffusion coefficient of greater than 1 $\times 10^{29}$ cm^2 s^{-1}, but the radial profile would become too smooth. Therefore we found 7.5 $\times 10^{28}$ cm^2 s^{-1} to be a good value for the diffusion coefficient as we were able to reproduce the shape of the observed radial spectral index profile.

The spectral index terms were averaged in regions of approximately 700 pc in order to match the resolution of the spectrum found from observation. In these simulations we use a diffusion coefficient of D = 7.5 $\times$ 10^{28} cm^2 s^{-1}.

We have used the radial magnetic field strength profile found from the LOFAR 151 MHz and VLA 1.4 GHz observations shown in the previous chapter.

What we see is that in figure 4.15 the model spectrum without an escape term is in the range of -0.8 to -1.2. The arm and interarm region of the spectral index can be seen although not as apparent as the

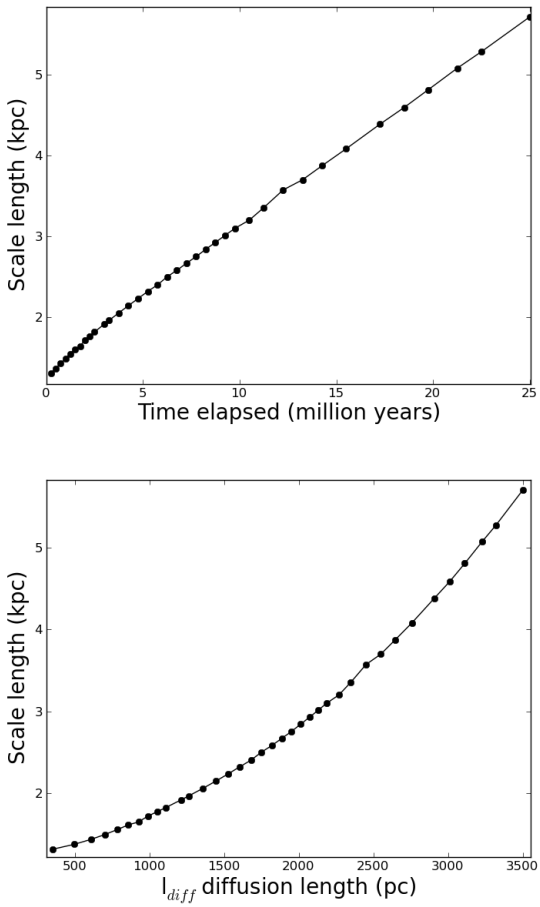

Figure 4.13: Scale length of $N(E)$ at a set energy obtained from simulations against time and diffusion length.

observed spectrum. This is a very good start for this model. We are not getting extreme values for the spectrum such as α = -2 or -3 but very reasonable values. We can also see from figure 4.16 that without an escape term, the simulation is stabilizing especially in central region of M51. It takes a longer time than the simulation time of 1.5 gigayears for the extended disk spectral index to stabilize.

Increasing κ from equation 4.26 in order to increase the injection rate may flatten the spectrum so this was tested. However, what was seen is that no matter what value κ is, the final radial spectrum is identical. The only difference is that the stabilization occurs much slower. The reason is that while we are injecting more fresh electrons, after several million years it will stop making a difference as the electrons in this simulation cannot leave the galaxy. Therefore an escape term is essential. A very simple escape term of the form $\frac{N(R,E)}{\tau_{esc}}$ where τ_{esc} which is taken to be 30 megayears. Thus equation 4.36 becomes:

$$\frac{\partial N}{\partial t} = \Theta \frac{1}{r'} \frac{\partial}{\partial r'}(r' \frac{\partial N}{\partial r'}) + \Phi \frac{\partial}{\partial E'}[E'^2 B'^2] + KQ(r')E'^{-p} - t_0 \frac{N(R,E)}{\tau_{esc}} \tag{4.43}$$

When adding this term we see in figure 4.15 that the overall spectrum has become flatter (i.e. increased) and in better agreement with observations. The region between 3 and 6 kpc agrees very well

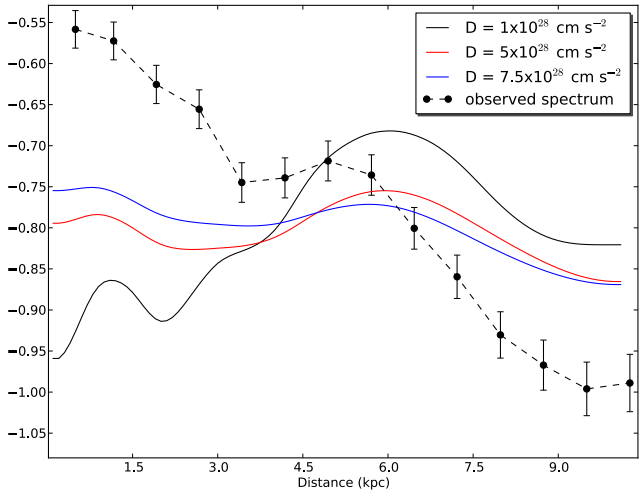

Figure 4.14: Comparing different diffusion coefficients used in our simulation. An escape term has been included for these simulations.

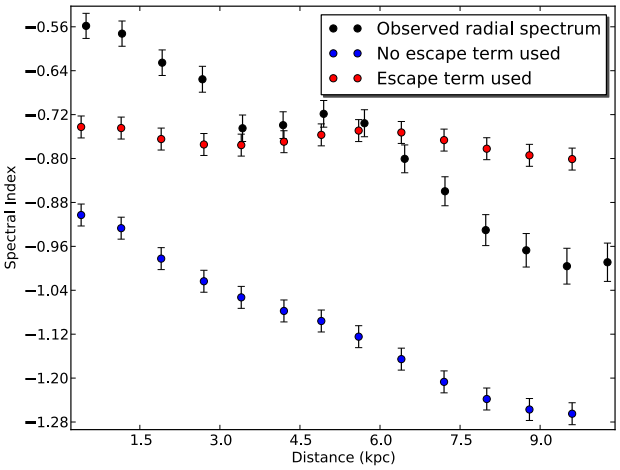

Figure 4.15: The model spectra (with and without an escape term) compared to the observed spectrum between 151 MHz and 1.4 GHz.

with observations. However, the inner region as well as the outer region of the galaxy seen in the simulation are not in very good agreement with observed spectrum. This would suggest that the escape and loss terms being used are probably too simplistic. Equipartion underestimates the magnetic field strength in the outer disk where CREs losses occur and hence the ratio of the proton and electron density becomes $K > 100$. Therefore synchrotron losses are also underestimated. Future modelling could allow to vary K with radius. With the escape time of CREs from the galaxy depends on diffusion we would need to have the escape term as a function of energy. But this dependence on energy is weak

$E^{-0.5}$ (Tabatabaei et al. 2013) [46]. So it is unclear how much more a complicated escape term would change the spectrum. It should be noted that from figure 4.16 that stabilization occurs much faster with an escape term present. The central region stabilizes only after 40 megayears and the spiral arm region takes longer to stabilize than the inter arm region. It is after 1 gigayear that the spectral index at the extended disk is stabilizing.

In addition, the observed spectral index contains thermal emission which would flatten (i.e increase) the spectrum, especially in the central region of the galaxy which was found to have a average thermal fraction of 20% in the previous chapter (when we assume the expected nonthermal spectrum is −0.8). If we take the observed spectral index in the central region of −0.55 and the expected non-thermal spectrum found from our simulations we get a smaller thermal fraction of 15%.

Taking this into account could easily make the model and observed spectrum in the central region more comparable.

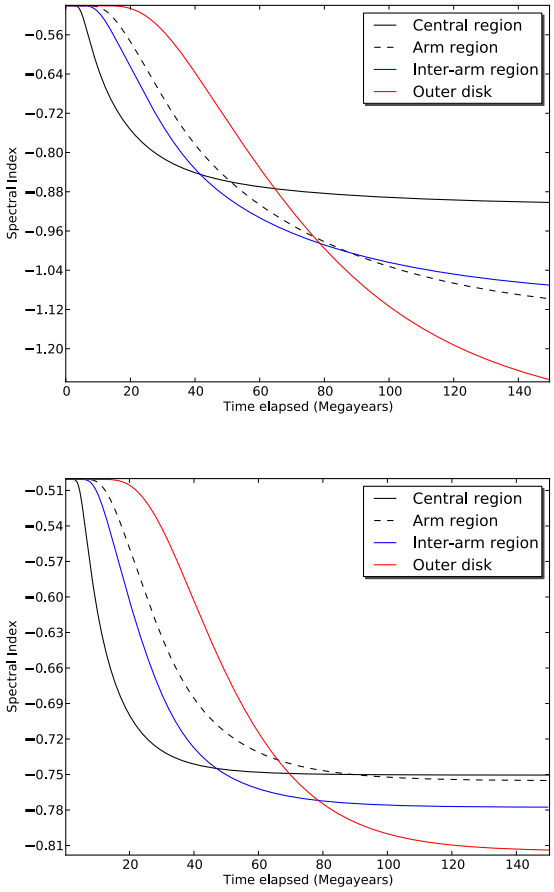

Figure 4.16: Evolution of the spectral index with time for different locations on the disk showed in the legend. Top: Evolution without an escape term, bottom: Evolution with an escape term.

Inverse Compton losses from the CMB can be added easily to code by altering the radial magnetic field profile using the following formula:

$$B_{eff} = \sqrt{B_{eq}^2 + B_{CMB}^2}$$
$$B_{eff} = \sqrt{B_{eq}^2 + (3.25\mu\mathrm{G})^2} \tag{4.44}$$

where B_{CMB} is the magnetic field strength equivalent to inverse Compton losses by the Cosmic Microwave Background (CMB). With this feature added we can see in figure 4.17 that the spectral index at all radii have decreased slightly. Interestingly, we see in the region beyond 6 kpc that the spectral index is decreasing more rapidly with the CMB term added. This illustrates that Inverse Compton losses from the CMB will become more important as the electrons move further from the star forming region where the synchrotron losses dominate.

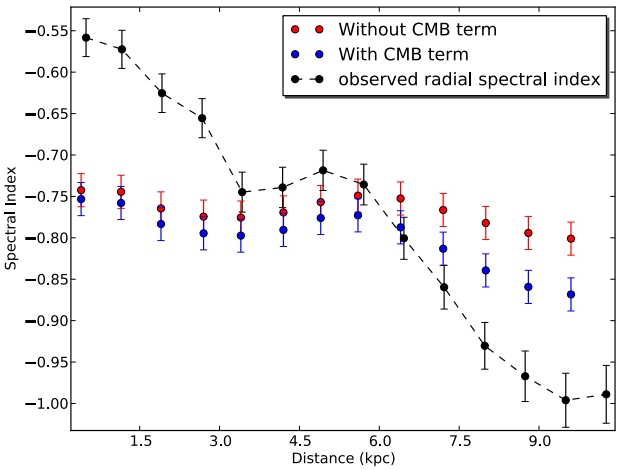

Figure 4.17: A plot showing the output of the model with and without a CMB inverse Compton term compared to the observed radial spectral index.

Inverse Compton losses resulting from the radiation field of the galaxy would be difficult to model exactly. A radial profile of the radiation field would be needed. Therefore it is easier to put an additional adjustable constant to the energy-loss term. This constant would be between 1 and 2. Setting it to one would mean no inverse Compton losses from the radiation field and setting it to two would mean that the inverse Compton losses from the radiation field would be equal to synchrotron losses. This needs to be tested.

4.5 Conclusions and outlook

This chapter has shown the development and testing of a simulation code that has the ability to predict the one dimensional radial distribution of the cosmic ray electron population at different energies and therefore the spectral index of that galaxy. In addition the scale lengths of the CRE population can be measured. We have also observed that already rough estimates of the diffusion coefficent for M51 can be obtained where we found a $7.5 \times 10^{28}\mathrm{cm}^2\mathrm{sec}^{-1}$ to be a good value. We have seen that the diffusion and energy-loss terms are working correctly when compared to analytical solutions.

In this case we have used M51 as our example galaxy but all galaxies could be simulated with this code as what is needed is the radial profile of the star formation and the magnetic field strength. This code could also be used for edge-on galaxies. An extra term representing convection could be implemented in the near future. This could be represented as an outflow with a bulk speed v_{wind}, which is possibly important for galaxies with high star formation. Several things need to addressed, however, including the simplistic form of the diffusion coefficient as well as the escape term. In addition, thermal effects need to be included or the subtraction of thermal emission from the VLA 1.4 GHz and LOFAR 151 MHz using the method from Tabatabaei et al. (2007) [140] in order to create an nonthermal spectral index map. This would give us a much better comparison. But it is important to note that with this diffusion model we obtain a nonthermal spectral index between -0.75 and -0.8 throughout most the galaxy which is very comparable to the integrated spectral index of M51 which is $\alpha = -0.81 \pm 0.02$.

While these additions need to be addressed the power of these models will enable us to compare the value of diffusion coefficient for different galaxies and to see the importance of inverse Compton losses in not only the star forming region of galaxies but also in the extended disks and haloes.

CHAPTER 5

Observations of NGC891 with LOFAR HBA

5.1 Introduction

Magnetic fields and cosmic rays are dynamically relevant in the disks of spiral galaxies because their energy density is similar to that of the turbulent motion of the cold gas (e.g. Beck 2007 [48]). Part of the energy input from supernova remnants goes into the acceleration of cosmic rays and into the turbulent amplification of magnetic fields. This scenario also explains the tight correlation between radio and far-infrared emission that holds for the integrated luminosities as well as for the local intensities within galaxies (e.g. Tabatabaei et al. (2013) [46]).

The physical relations of the various components of the interstellar medium (ISM) are less well understood in galaxy halos. Thick disks or halos are observed in the radio and X-ray spectral ranges, in the HI line of neutral hydrogen and in optical emission lines of ionized gas. If the major energy sources are located in the disk, warm and hot gas, cosmic rays and magnetic fields have to be transported from the disk into the halo. The required pressure could be thermal or nonthermal (cosmic rays and magnetic fields). Possible transport mechanisms are a "galactic wind" (e.g. Breitschwerdt et al. 1991 [141]), a "galactic fountain" (Shapiro & Field 1976 [142]) or "chimneys" (Norman & Ikeuchi 1989 [143]). Cosmic rays can propagate relative to the gas with the Alfvén speed via the streaming instability (Kulsrud & Pearce 1969) [144] or can diffuse along or across the magnetic field lines (e.g. Buffie et al. 2013 [145]). Especially unclear is the transport of magnetic fields. A turbulent field may be transported together with gas outflow, while an ordered field can support or suppress the outflow, depending on the field structure.

Edge-on galaxies are ideal laboratories to study the disk–halo connection and to investigate the driving forces of the outflow. The discovery of a huge radio halo around NGC4631 by Ekers & Sancisi (1977) [146] indicated that nonthermal processes play an important role. The theory of cosmic-ray propagation into the halos was developed in great detail (Lerche & Schlickeiser 1981 [147], 1982 [148], Pohl & Schlickeiser 1990 [116]), but comparisons with observations were inconclusive due to the limited quality of the radio data at that time. The Low Frequency Array (LOFAR) now opens a new era of such studies.

NGC891 is a galaxy similar to our own Milky Way in terms of optical luminosity (de Vaucouleurs et al. 1991 [149]), Hubble type Sb (van der Kruit & Searle , 1981 [150]) and rotational velocity of $225\,\mathrm{km\,s^{-1}}$ (Rupen 1991)[151], but has considerably more star formation due to the presence of approximately twice the amount of CO gas of the Milky Way, with the radial distribution of CO been remarkably similar in both galaxies (Scoville et al. 1993) [152]. Due to its proximity of 9.5 Mpc (van

der Kruit & Searle 1981)[150] and being a nearly edge-on galaxy with an inclination of 89.8° (Oosterloo et al. 2007) [153], NGC891 is an observational testing grounds for the study of disk and halo interactions and the galactic halo itself.

Rand et al. (1990) [154] and Dettmar (1990) [155] independently detected diffuse Hα emission 4 kpc away from the disk with an exponential scale height of about 1 kpc. Rand et al. (1990) [154] also detected many vertical Hα filaments or "worms" extending up to 2 kpc off the plane of the galaxy. They interpreted these "worms" as providing evidence for a galactic "chimney" mode [143, Norman & Ikeuchi 1989]. Howk & Savage (1997) [156] detected spectacular dust lanes emerging vertically into the halo of NGC891 which could not always be associated with energetic processes connected to massive star formation in the disk. Sofue (1987) interpreted such dust lanes as traces of vertical magnetic fields. Rossa et al. (2004) [157] speculated that the very narrow Hα filaments could be magnetically confined. The galactic fountain model is also invoked to explain the huge halo of neutral HI gas of NGC891 (Oosterloo et al. 2007) [153]. The extent is up to 22 kpc in the northwest quadrant. The exponential scale height increases from 1.25 kpc in the central regions to about 2.5 kpc in the outer parts. The bulk of the cold CO-emitting gas and the cold dust, on the other hand, are much more concentrated to the plane (Scoville et al. 1993 [152], Alton et al. 1998 [158]), but some CO emission could be traced up to 1.4 kpc height (García-Burillo et al. 1992 [159]).

X-ray observations performed by Bregman & Pildis (1994) [160] were able to detect a considerable amount of diffuse X-ray emission from the halo of NGC891. The vertical profile is Gaussian with a vertical scale height of 3.5 kpc, corresponding to a full width at half maximum of 5.8 kpc (Bregman & Houck, 1997 [161]). Temple et al. (2005) [162] observed X-ray emission protruding from the disk in the northwest direction up to approximately 6 kpc which showed a sharp cut-off, suggesting that this is the maximum extent that the gas has reached. Temple et al. (2005) also concluded from a comparison to other galaxies that NGC891 has more star formation than a normal spiral, but does not have properties as extreme as the starburst galaxy NGC253.

NGC891 has also been observed extensively in continuum throughout the past few decades. The first extensive investigation in radio continuum at 610, 1412 and 4995 MHz with the Westerbork Synthesis Radio Telescope (WSRT) by Allen et al. (1978) [163]. The profile of the radio disk at 1412 MHz was described by an equivalent thickness of 1.2 kpc. A strong steepening of the radio spectrum between 610 and 4995 MHz beyond about 0.7′ (2 kpc) distance from the plane was found, and an even more dramatic steepening between 1412 and 4995 MHz, inconsistent with simple models of CREs propagation (Strong 1978) [164]. Beck et al. (1979) [165] and Klein et al. (1984) [166] observed NGC891 at 8.7 GHz and 10.7 GHz with the Effelsberg single-dish telescope, but when comparing their data to 610 MHz found an almost constant spectral index until about 4 kpc and only a mild steepening beyond that distance, consistent with CRE propagation models. The reason of the discrepancy between those early data is the lack of large-scale structures ("missing spacings") when observing with a synthesis telescope like the WSRT. Hummel et al. (1991a) [167] observed NGC891 at 327 and 610 MHz with the WSRT and at 1490 MHz with the VLA, all of these did not suffer from the "missing spacings" problem. The resolution of 40″ showed that the inner and outer radio disks have a significantly different spectrum, partly due to the larger thermal fraction in the inner disk. The spectral steepening towards the halo is mild, and in the southwestern halo even a flattening may occur. The radio disk at 1490 MHz was described by an exponential scale height of 1.2 kpc. Dumke (1997) combined VLA and Effelsberg data at 4.8 GHz and found that the radio halo is more extended on the eastern side compared to the western one. The averaged vertical profile was described by two exponential scale heights of 270 pc and 1.8 kpc for the thin and thick disks, (Krause, 2011) respectively [33].

The structure of the magnetic field in the halo of NGC891 was investigated with help of linearly polarized radio synchrotron emission. From the VLA data at 1490 MHz, Hummel et al. (1991b) de-

tected polarized emission, but no overall orientation of the ordered magnetic field could be determined because Faraday rotation is strong at this frequency. The increase of the degree of polarization with distance above the plane indicates a general decrease of Faraday depolarization that could be modeled by exponential scale heights of the thermal gas and the turbulent magnetic field of 0.9 and 3.6 kpc, respectively. Sukumar & Allen (1991) [168] found polarized emission with the VLA at 4.86 GHz, where Faraday rotation and Faraday depolarization are smaller and an orientation of the disk field parallel to the plane could be measured, while the halo field has significant vertical components. Dumke et al. (1995) [169] observed a sample of edge-on galaxies, including NGC891, with the Effelsberg telescope at 10.55 GHz and detected polarized emission from the plane with an orientation predominately parallel to the plane. Such a field structure is to be expected from magnetic field amplification by the action of a mean-field $\alpha\omega$ - dynamo (Beck et al. 1996) [37]. From Effelsberg observations at 8.35 GHz, Krause (2009) [38] showed that the large-scale magnetic field appears "X-shaped" away from the plane. From data of Faraday rotation measures, Krause (2009) [38] also found indication for a large-scale toroidal field within the disk.

However, studying the non-thermal emission emanating from cosmic-ray electrons (CREs) gyrating around magnetic field lines within a galaxy is hampered at higher frequencies due to the contribution of thermal free-free emission that is predominately seen at recent sites of star formation. Also, the effect of galactic winds on the spectral index gradients can be only observed at frequencies less than 1 GHz. At high frequencies the dynamic halo model predicts a smooth break in the spectrum of the integrated radio emission which is defined by the equality between losses due to bremsstrahlung and adiabatic expansion and those by synchrotron emission and the inverse Compton effect (Pohl et al. 1991)[131]. Pohl et al. (1991) showed that the spectral break in NGC891 occurs at about 400 MHz; a static halo model (no outflow) was ruled out.

Israel & Mahoney (1991) [26] observed that the total fluxes of 68 galaxies at 57.5 MHz are systematically lower when one extrapolates from 1.4 GHz flux measurements, assuming a power-law spectrum with a constant slope. Israel & Mahoney (1991) [26] also reported that the fluxes of galaxies at 57.5 MHz would decrease with increasing inclination which they interpreted as increasing free-free absorption caused by a clumpy medium with an electron temperature of $T_s \approx 1000\,\mathrm{K}$ and a clump density of the order of $1\,\mathrm{cm}^{-3}$. However, no direct observational evidence of such medium exists, even in our own Galaxy. Hummel (1990) [28] performed a reanalysis of the data and did not confirm the correlation with the inclination of the galaxies.

Therefore, more reliable observations of galaxies need to be performed to clear up some of these issues.

LOFAR (van Harleem et al. 2013) [68] offers the opportunity to produce reliable measurements at lower frequencies and already imaging results are being produced (Mulcahy et al. 2011) [170], (van Weeren et al. 2012) [171], (de Gasperin et al. 2012) [172]).

Table 5.1: Physical parameters of NGC891

Morphology	Sb/SBb
Position of the nucleus	$\alpha(2000) = 02^{\mathrm{h}}22^{\mathrm{m}}33^{\mathrm{s}}.4$
	$\delta(2000) = +42^{\circ}20'57''$
Position angle of major axis	23°
Inclination	89.8° (0° is face on)
Distance	9.5 Mpc

In this chapter, we will present the first images of the edge-on spiral galaxy, namely NGC891. In

section 5.2 we will detail how the observation and data reduction were performed. Section 5.4 will show the total power image of NGC891 and present the integrated flux of the galaxy. In section 5.5 the spectral index and magnetic field map will be presented. We will then show results from the analysis of the scale height in section 5.6. Finally discuss our findings in section 5.8.

5.2 Observation description and data reduction

NGC891 was observed with LOFAR for polarization commissioning purposes. The observation took place on November 1st-2nd 2012 for a duration of approximately 10 hours during the night with a configuration of 55 high band antenna (HBA) stations. This configuration consisted of 23 core HBA stations (CS) and 9 HBA remote stations (RS). The core stations comprise of two ears of 24 tiles making effectively 55 stations. LOFAR has the novel ability to be able to observe the target and calibrator simultaneously with its dual beam mode, however as the nearest flux calibrator 3C48 ($\alpha = 01^h37^m41^s.3$, $\delta = +33°09'35''$) is more than 10 degrees from the target and therefore not within the HBA tile beam, NGC891 and 3C48 had to be observed consecutively, with 11 minute scans for the target and 1 minute for the calibrator. The total frequency range from 114 MHz to 189.84 MHz was split into 244 subbands (SBs) each with a bandwidth of 0.195 MHz. Each SB is divided into 64 channels each consisting of $\simeq$ 3 kHz of bandwidth. The first and final 2 channels in each SB were left out to remove the edges of the subband bandpass. These 244 SBs were grouped into 8 frequency blocks covering the entire range of frequencies. This is simply due to data management and calibrating/imaging the entire data set would be impractical in terms of processing.

Table 5.2: Parameters of the NGC891 LOFAR observation

Start Date (UTC)	1st-November-2012/18:08:08.0
End Date (UTC)	2nd-November-2012/04:06:52.9
Frequency Range	114-189.84 MHz
Total Bandwidth on Target	43.92 MHz

Firstly, it was seen that the shortest baselines between the ears of the core stations had a high proportion of RFI due to cross-talk. All these baselines were flagged. No interference from any of the A-Team was seen. As a test, demixing (Van der Tol et al. 2007) [74] was performed on 1 subband but no improvement was seen in the phases and therefore not implemented. For RFI detection and removal, the AOFlagger (Offringa et al. 2010) [73] was then used on the raw data. The data was then averaged by factors of 10 in time and 10 in frequency resulting in 6 channels per subband.

5.2.1 Initial Calibration

The calibrator scans for each subband of 3C48 were calibrated using a skymodel from Scaife & Heald (2012) using the Black Board Selfcal (BBS) software (Pandey et al. 2009) [75].

From Scaife & Heald (2012) [66], this skymodel which has a spectral model of the form:

$$\log S = \log A_0 + A_1 \log \nu + A_2 \log^2 \nu + ... \tag{5.1}$$

was used. The model was applied in linear frequency space, ie

$$S[\mathrm{Jy}] = A_0 \prod_{i=1}^{N} 10^{A_i \log^i[\nu/150\mathrm{MHz}]} \tag{5.2}$$

in order to retain Gaussian noise characteristics. Both determination of the optimal order (N) of polynomial model and maximum likelihood parameter estimation were performed using a Markov Chain Monte Carlo (MCMC) implementation.

The BBS software was used in all calibration steps. Only the parallel correlations of the gain Jones matrix were solved for, with the station beam switched on. All calibrator scans were calibrated in this fashion.

The gain amplitudes from each calibrator scan were read from the instrument table. Any outlier gain amplitude solutions caused by RFI were flagged using a MAD (Median Absolute Deviation) threshold of 2.5 and a median gain amplitude value was assigned. The gains for the target snapshots were found using simple interpolation in time. These interpolated gain amplitudes for each target snapshot and each subband were then written to an instrument table and applied using BBS.

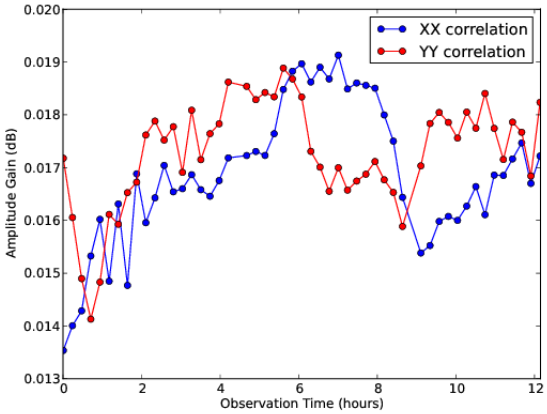

Figure 5.1: The median gain amplitudes for each snapshot of the calibrator throughout the full 12 hour observation for one station (CS24HBA0), the first 2 hours were not used.

After this amplitude calibration, subbands were combined in frequency for every snapshot for a greater signal to noise ratio to enable superior phase calibration. These blocks of 20-30 subbands were then phase calibrated using a global sky model. This global skymodel consists of positions of sources from the NVSSS catalogue (Condon et al. 1998) [7] with fluxes obtained from a power spectral fitting with data from the NVSS (1.4 GHz), WENSS (325 MHz) (Rengelink et al 1997) [76] and VLSS (74 MHz) (Cohen et al. 2007) [4] surveys. NGC891 itself is described as a simple Gaussian source. However, it was found that a spurious source was contained in the skymodel at the location of NGC891 due to inconsistencies between the 3 different catalogs. More on this will be discussed in section 5.3. This source was taken out of the skymodel before the phase calibration.

Directional dependent calibration or 'peeling' while been very beneficial in decreasing the overall noise especially with regards to the NGC891 field with the close proximity of 3C65 and 3C66 A/B. These sources create large sidelobes in the image but fortunately don't distort our target source. We decided not to apply peeling to our data due to the loss of flux of 5-10% to the target source that would incur. This is due to the fact that to get a complete model of the target source is extremely difficult and due to the sheer number of parameters, flux loss is inevitable at high resolution.

Due to this, only a simple phase selfcal was performed using a skymodel containing clean components obtained from AWimager which applies the primary beam, for sources away from the phase center. For NGC891 which is at the phase center and not affected greatly by the primary beam, clean components

from a CASA image were used. The reason for this is that AWimager in its current form doesn't have multiscale cleaning (Cornwell, 2008) [77] available. The two skymodels were combined to create a skymodel for self calibration again using BBS. All blocks showed an approximate 10% decrease in noise and the peak flux of point sources increased.

While it would be ideal to image the entire data set to get a final image, however due to its sheer data size, this is impracticable. Therefore, each frequency block was imaged separately with uniform weighting with similar uv coverage using multiscale clean with 20000 clean iterations at a resolution of 15″ with a cell size of 5″. The highest frequency block suffered from RFI due to Digital Audio Broadcast (T-DAB) (Offringa et al. 2013) [71] and therefore the image quality was quite poor and discarded. Each of the remaining blocks were checked so that the astrometry was correct. The remaining images were averaged in the image plane using an inverse variance weighting scheme. We checked the final map again to make sure that the astrometry was correct and in addition a 2-D Gaussian was fitted on several point sources to check if any of the sources were smeared. All points sources were nearly exactly the size of the convolved beam.

5.3 False detection of a Radio Supernova

When first calibrating this data an interesting source which had not being seen before in NGC891 could be seen in the north region of the galaxy. This mysterious source was located in an interesting part of the disk (see figure 5.2) where there is increased star formation. A previous LOFAR observation of this field was taken in 2011, with the phase center located at PSR J0218+4232 (located less than a degree away from NGC0891) and the source was not detected. This object ($\alpha = 02^h22^m33^s$ $\delta = +42°21'53''$) could be seen in all HBA frequencies and is present during the entire 2012 observation which had a duration of 12 hours.

This transient like object is seen north of the central region of the galaxy and no counterpart could be seen when comparing to older observations of this galaxy at higher frequencies.

It was seen with preliminary investigations of this LOFAR observation that this source had a flux of approximately 0.088 ± 0.004 Jy/beam at 173MHz with an inverted spectrum of slope 0.98 , i.e. the flux decreases with decreasing frequency. Also different time sections of the observation were analyzed and the transient object was present in all these time sections, ruling out that it is a very short lived transient.

NGC891 was again observed with LOFAR HBA on the 31st of March 2013 for a duration of 8 hours along with 3C66 and again it was detected. The so called transient could be seen in the target beam and the beam of 3C66. However it was observed with WSRT at 20 cm by Dr. George Heald for 7.5 hours on the same date and not detected (see figure 5.3). It was also observed at 15 GHz by Dr. Anna Scaife with the AMI interferometer but it also wasn't detected. In addition, recent JVLA data on NGC891 at L-Band from the summer of 2012 (B-array) and March 2013 (D-array) had not detected this object (P.Schmidt, priv communication).

These negative results at higher frequencies indicated that this is not a Radio Supernova as one would expect to have a detection at the higher frequencies before LOFAR frequencies. It could be a result of the afterglow from a Gamma Ray Burst (GRB).

However, when the previous 2011 LOFAR observation was reanalyzed with the same skymodel for calibration, the transient source appeared. This led us to believe that the source was instrumental in nature.

The LOFAR skymodel had erroneously contained a point source located at the same location of the so called transient source. It was seen that while the NVSS and WENSS catalogues showed NGC891 as a Gaussian source, the VLSS catalogue had a point source only. This is due to the fact that only the A-B

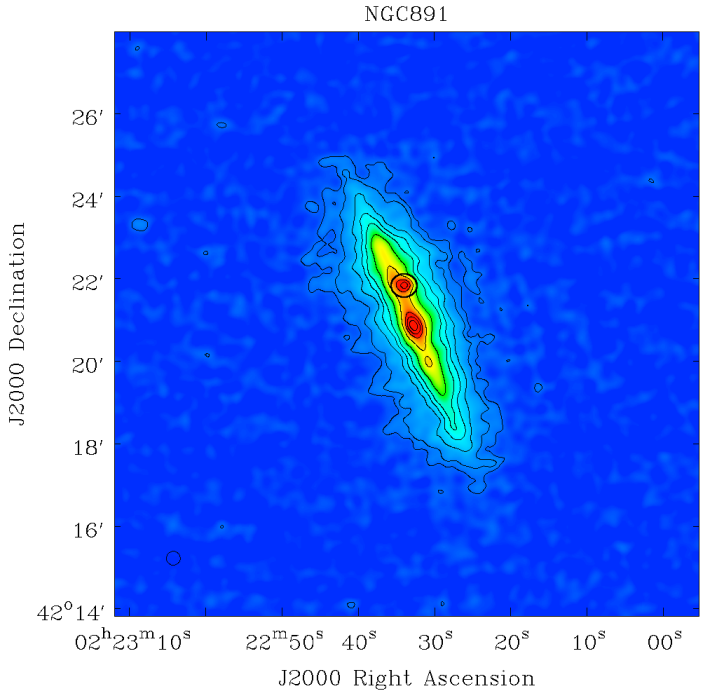

Figure 5.2: A preliminary image of NGC891 at 146 MHz with LOFAR with potential supernovae circled in black.

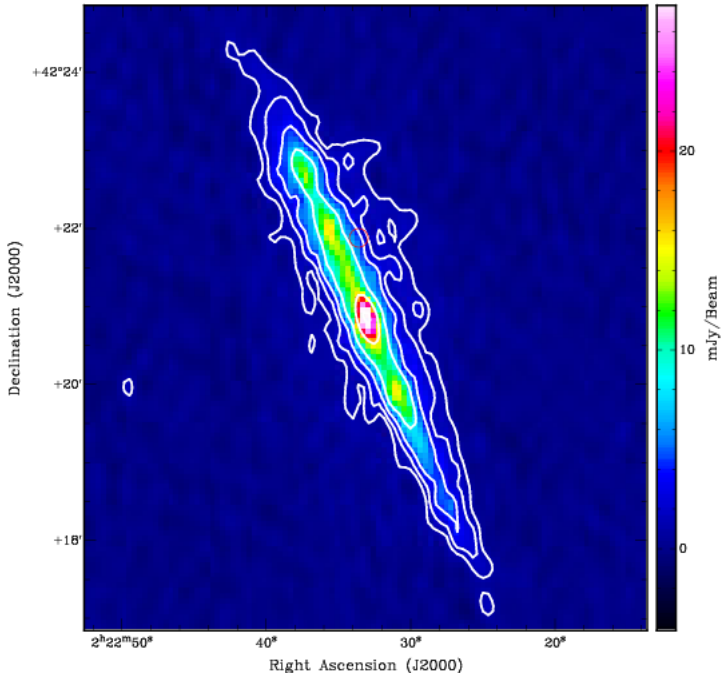

Figure 5.3: A WSRT 1.4 GHz image of NGC891 observed and reduced by Dr. George Heald. No detection could be seen where the so called transient source was located (shown with the red circle).

configurations were used in the survey and therefore not sensitive to extended emission of NGC891. Therefore it only detected the central region of NGC891. Furthermore as the VLSS survey is at 74 MHz, ionospheric phase fluctuations can cause to move sources from their true position, in our case to the location of the transient source. Figure 5.4 shows the region of NGC891 in the VLSS survey with the cross at the location of the so called transient source. As one can see, it corresponds to a slightly extended object.

The software that creates a skymodel from the above three catalogues identified the source from the VLSS catalogue as a different point source rather than the central region of NGC891.

Overall, the inconsistencies of the three catalogues contributed to a creation of a fake source through the LOFAR skymodel builder software and sadly the so called transient source was spurious.

This incident showed the need for correct starting models and using a model from different catalogues which came from different instruments can be extremely hazardous. Also the importance of at least one cycle of self calibration becomes apparent. If self calibration was performed, this spurious source would have decreased further in flux and its falseness would have been discovered sooner. It also shows that all starting skymodels used for self calibration should always be checked without exception.

On a positive side, it showed the great response of the scientific community when a potential exciting discovery was possible. 15 to 20 other astronomers from several different institutes were involved in this experience and showed how rapid developments can occur. It was comforting to see how real collaboration can happen so easily and naturally from the scientific community.

While personally, the experience was demoralizing in several respects, the lessons were learned and the NGC891 LOFAR data was recalibrated using a skymodel without the spurious source included.

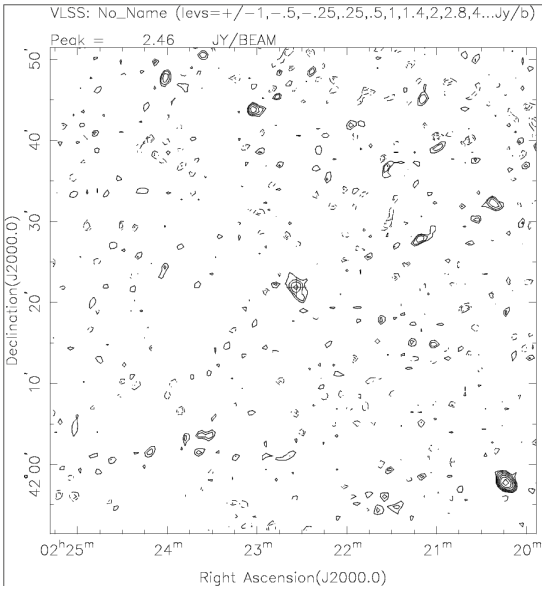

Figure 5.4: The region where NGC891 is located in the VLSS survey with only the central region visible with inaccurate position.From the VLSS survey (Cohen et al. 2007)[4]

5.4 NGC891 total power image

The final image of NGC891 at 146 MHz with a bandwidth of 36 MHz is shown in Figure 5.5.

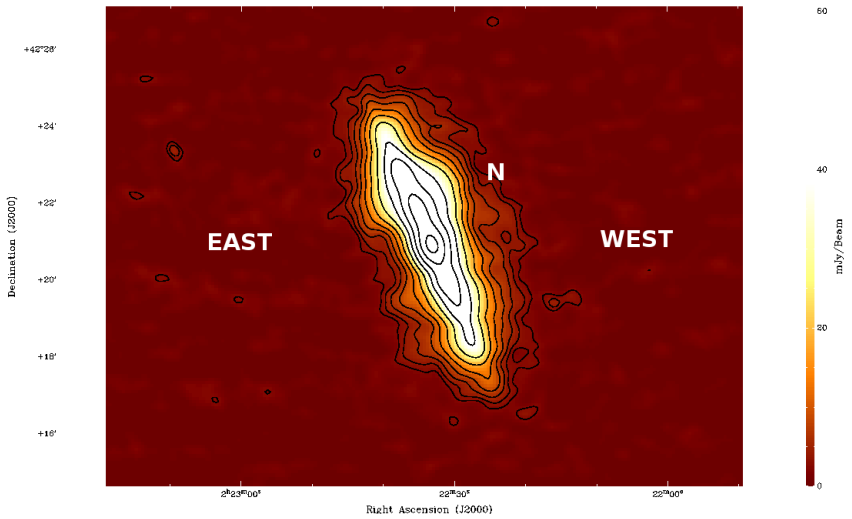

Figure 5.5: Final map of NGC891 observed at a central frequency 146 MHz with a bandwidth of 36 MHz at a resolution of 25 arcsecs. Contours start at 3σ level and increase by increments of 1.5.

The mean noise around NGC891 was found to be 765 μJy/beam while the noise in a quiet region was found to be 370 μJy/beam.

The morphology of NGC891 at this low frequency is quite similar to higher frequencies seen in Hummel et al. (1991) [167]. A peanut shape exists, bulging out in the northern sector of the galaxy. It is well know that this northern half has a greater star formation rate occurring compared to the southern half. Additionally it is known from Osterloo et al. (2007) [153] that HI extends up to 20 kpc in a filamentary structure to the northeast. We see the continuum emission at 146 MHz extending out to between 7-8 kpc from the disk. We also see an interesting bulge marked N in figure 5.5, which seems to be emanating from the disk. Interestingly, this observed at higher frequencies for example Hummel et al. (1991)[173]. It also seen in Hummel et al. (1991) [173] that this region is polarized.

When smoothed to a larger beam in order to detect the most extended emission, we detect that the halo extends as far out as 1.4 GHz observations but there is no indication that the halo extends further out than this. We also observe that the radial extent of the the disk is not seen to increase from the 1.4 GHz map. This tells us that the CREs are not able to reach so far from the plane or that we simply not sensitive enough. One would expect these low energy CREs to reach further out than what is observed at higher frequencies as they are thought not to be as affected by energy loss processes as higher energy CREs. Calculating the scaleheights for both frequencies is essential to get a true sense of how far the halo extends out to.

Additionally we observe that at least three galactic spurs in the east side of the galaxy which are similar to the ones found in NGC 5775 (Soida et al. 2011) [174]. These galactic spurs are signs of galactic winds which eject gas from galaxies and enrich the local interstellar medium.

NGC891 was imaged again, but on this occasion the uv coverage of the inner core is not used in the image so that we can see the the details of the disk better.

What we observe (see figure 5.7) is the disk and increased fluxes in the north, showing clearly the higher star formation in this region. In the south region of the disk, we have detected SN1986J at the location of ($\alpha = 02^h22^m30^s\delta = +42°20'00''$) at a flux of 6.6 ± 0.3 mJy. No other flux measurements can be found at this frequency for this supernova, the closest being from Bietenholz et al. (2010)[175] which was at 320 MHz at a flux of 8.9±1.8 mJy, measured in August 2007.

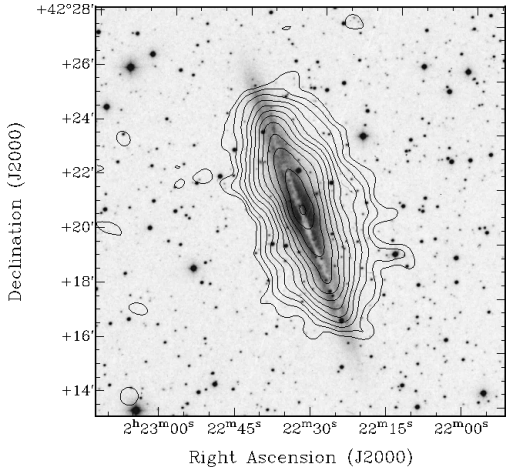

Figure 5.6: LOFAR image smoothed to a resolution of 40 arcsecs overlayed onto a Digital Sloan Survey image.

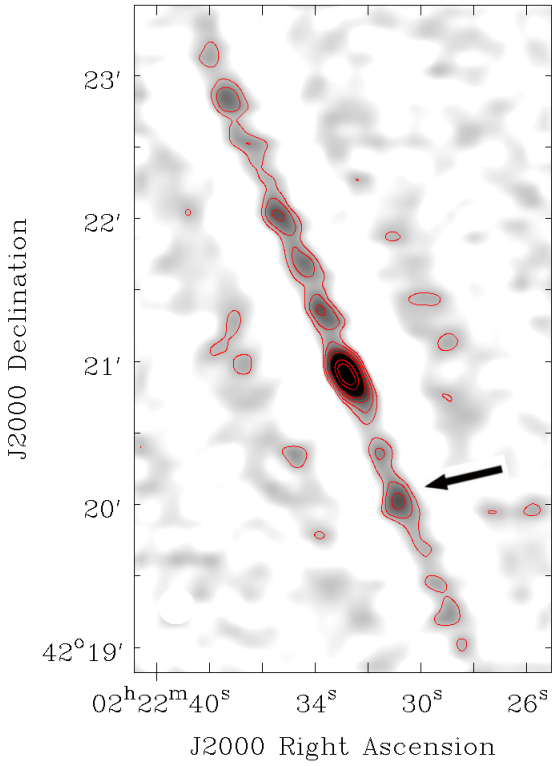

Figure 5.7: LOFAR image of NGC891 imaged without the inner uv coverage. RMS noise is 800 μJy. Contours are 3, 5, 7.5, 10, 15, 17.5 times the rms. SN1986J is marked with an arrow. Resolution is 25″

5.4.1 Integrated radio continuum spectrum

Here like M51 the uncertainties in the beam model of LOFAR make the transferring of gains the greatest cause of error which we take as 5%. We obtain an integrated flux measurement of NGC891 to be 3.14

± 0.15 Jy. This value agrees very well with the value at 151 MHz by Howarth (1990) [176]. Many of the flux measurements were taken from Hummel et al. (1991) [167], Gioia et al. (1982) [177], Israel & Van der Hulst (1983) [178] , Gregory & Condon (1991) [179], Stil et al. (2009) [180], Kazès et al. (1970), [181], Heeschen & Wade (1964) [182] and Gioia & Gregorini (1980) [107].

Table 5.3: Integrated Fluxes for NGC891 on the RBC scale [65, Roger, Costain & Bridle (1973)]

ν (GHz)	Flux Density (Jy)	Ref
10.07	0.148 ± 0.026	Gioia et al. (1982)
8.7	0.177 ± 0.023	Israel & Van der Hulst (1983)
4.85	0.239 ± 0.03	Gregory & Condon (1991)
4.8	0.271	Stil et al. (2009)
2.695	0.43	Kazes (1970)
1.4	0.76 ± 0.02	Hummel (1991)
0.75	1.4	Heeschen & Wade (1964)
0.61	1.6 ± 0.02	Hummel (1991)
0.408	1.8 ± 0.05	Gioia & Gregorini (1980)
0.327	2.1 ± 0.2	Hummel (1991)
0.151	3.35 ± 0.6	Howarth (1990)
0.146	3.14 ± 0.1525	This work

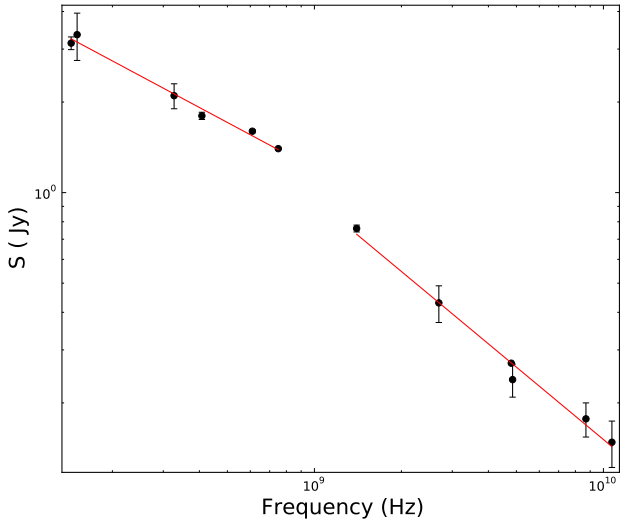

Figure 5.8: Integrated spectrum of NGC891 with two separate power laws fitted.

These values were plotted as can be seen in fig 5.8. The value of Israel & Mahoney (1990)[26] 57.5 MHz was deemed very unreliable due to large errors and not used in our analysis. There is obvious break in the spectrum between 1.4 GHz and 750 MHz. We fit a two power laws, the first to the high frequency data (above and including 1.4 GHz) which gives a spectral index α_{highfreq} = -0.79±0.04. This is very similar to the spectral index of M51. In addition, this is consistent with our CREs propagation code discussed in the previous chapter which gave spectral indices of approximately −0.75. The second

power law is fitted to the low frequency data (below 1.4 GHz). This gives a spectral index α_{lowfreq} = -0.51±0.03.

5.5 NGC891 spectral and magnetic field properties

An image of NGC891 from the VLA at 1.4 GHz used by Hummel et al. (1991) [167] was used together with the LOFAR map to produce a spectral index map. The LOFAR image was made sure to be on the same grid as well as the same resolution of 25″ in order to have the same image characteristics as the 1.4 GHz map. The spectral index map between these two frequencies can be seen in figure 5.9 with an error map.

At first glance the spectral index map contains much more structure than the total intensity map suggesting outflows from star formation regions in the disk or variations of the thermal fraction.

Firstly, in the center part of the disk, it is observed that the spectral index is as low as -0.4. In the north region of the disk, where there is higher star formation, the spectral index is -0.44. This is significantly lower than the median injection spectrum of -0.5 signifying thermal absorption. It also could signify thermal emission which would mean thermal fractions greater than 30% at 146 MHz which very high for this frequency.

Two interesting features can be detected in the west side of NGC891 indicated by letters N & C. At the location C, shows an extended region emanating from the disk where the spectral index is flatter where we observe a spectral index of approximately -0.6. This feature corresponds to a jet of diffuse X-ray emission observed by Bregman & Pildis, (1994) [160]. Bregman & Pildis, (1994) [160] say this could be evidence of a broken superbubble or a starburst event near the center.

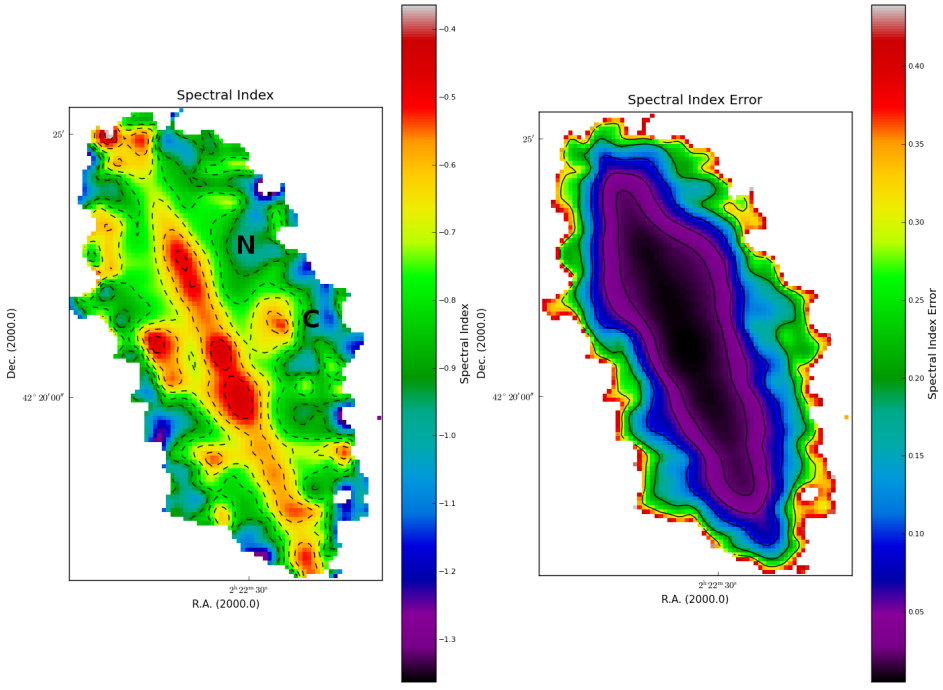

Figure 5.9: Spectral index and spectral index error map created from a power law between 146 MHz and 1.4 GHz.

At location N we observe a region which is quite the opposite, we observe a region of extreme

steepening from -0.6 to -1 indicating extreme CRE energy losses in this region of the galaxy. This region is directly above the star forming region of the disk seen in HII [154, Rand et al. 1990] and matches the region of flat spectral index in disk exactly.

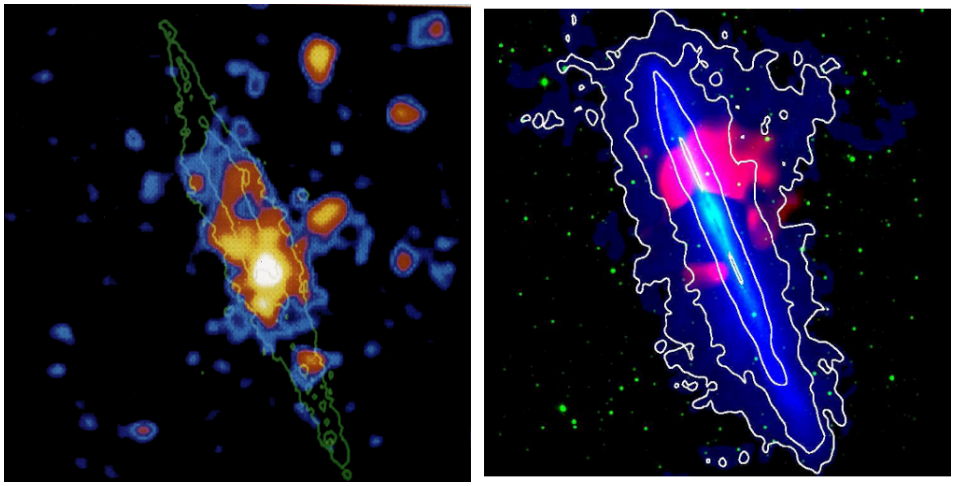

Figure 5.10: Left: X-ray emission in the 0.47-2.47 keV band of NGC891 detected with ROSAT with the green contours showing HII emission. (Bregman & Pildis, 1994) [160] Right: red emission shows 0.5-0.6 keV emission detected from XMM-Newton. (Hodges-Kluck & Bregman 2013) [183].

Looking at the change of spectral index with height above the disk (z), we see a general decrease in all sections. In some regions, the spectral index decreases nearly linearly, notably +/- 2.9 kpc on the east side of the galaxy where the radio spurs are located. A linear slope can be explained by a constant CR bulk speed (Heesen et al. 2009) [17]. Many of the regions flatten especially near the center of the galaxy, which would be explained by outflows from the central region.

The total magnetic field of NGC891 can be determined from the non thermal synchrotron emission by assuming equipartition between the energy density of the CREs and the magnetic field. The revised formula of Beck & Krause (2005) [115] was used. We used a nonthermal spectral index of -0.8, an effective path length through the source to be 3000 pc. We also assumed that the polarized emission comes from ordered fields with all possible inclinations. Here we assume an proton and electron number density ratio of K=100, which is a fair assumption in the star forming regions in the disk. However, errors will become significant in regions away from these CR sources especially in the halo as the observed K factor will increase. Assuming equipartition underestimates the total magnetic field by a factor of $(K/K_0)^{1/4}$ in these regions due to energy losses of CREs (Beck & Krause 2005) [115]. Therefore, the magnetic field strength estimated in the halo would be quite inaccurate. Fortunately, energy losses are generally weaker at these frequencies and therefore the equipartition estimate has a smaller error compared to higher frequencies. The total magnetic field strength was then scaled with the non thermal synchrotron intensity I_n using the following equipartition formula (Beck & Krause 2005) [115]:

$$B \propto I_n^{1/(3+\alpha_{nt})} \tag{5.3}$$

Using these assumptions, we created a map of the total magnetic field of NGC891 shown in Figure 5.12. The magnetic field strength in the disk should be more accurate than the field strength found in the halo. The strength of magnetic field at the center is approximately 19 μGauss. To the north we

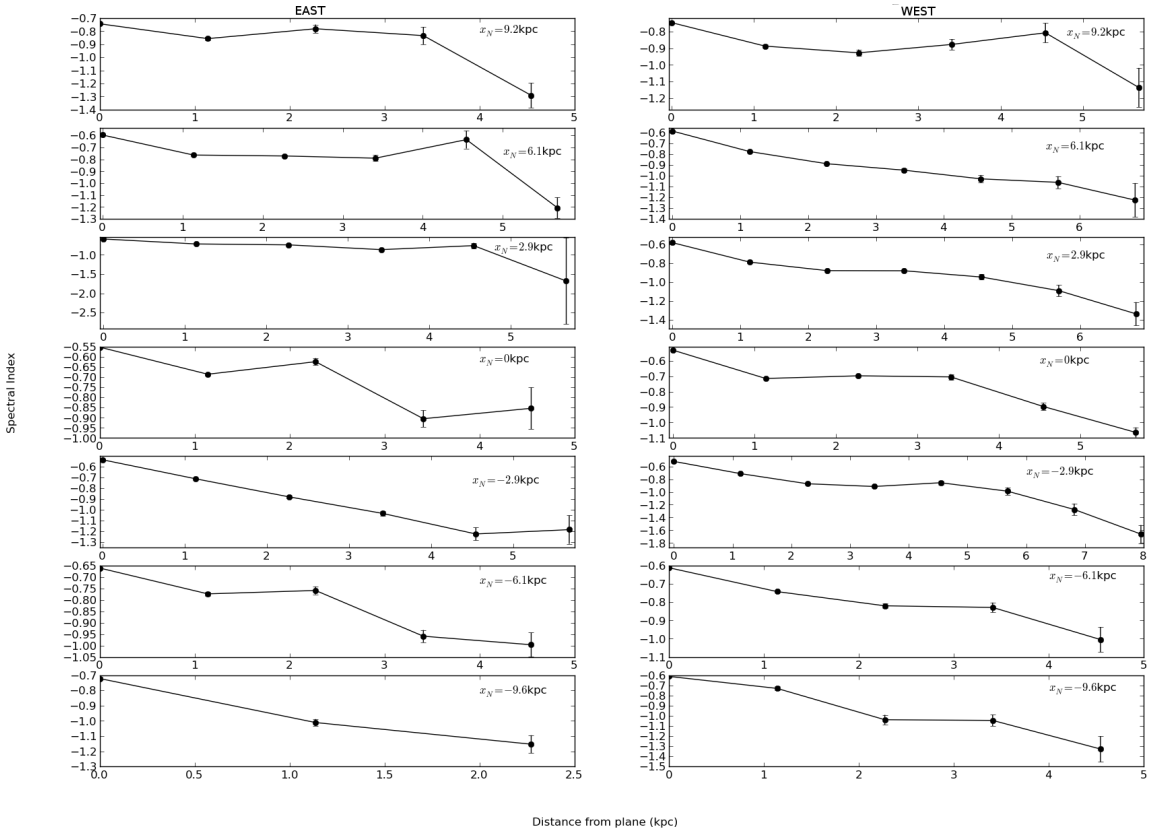

Figure 5.11: The vertical spectral index between 146 MHz and 1.4 GHz of the 7 different slices of NGC891.

see due to turbulence caused by increased star formation that the magnetic field strength is greater than 16 μGauss. In the south at the same distance from the central region we observe that the magnetic field strength is approximately 14 μGauss.

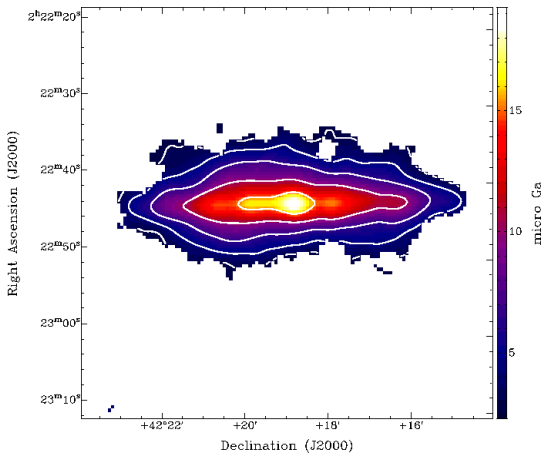

Figure 5.12: The estimated equipartition magnetic field strength for NGC891. The contours start at 3 μGauss and increase in multiples of 1.5.

5.6 Radio emission profiles in the z-direction

To obtain the z-distributions, we performed strip integration on the map with slices with an average width of 3 kpc and a length of 8 kpc. This strip integration was performed on both sides of the galaxy separately in order that the differences between the two sides of the galaxy could be investigated. Each data point is separated by a beamwidth to ensure that each data point is independent. The error σ_s for each data point is calculated by:

$$\sigma_s = \sqrt{\sigma_{rms}^2 + \sigma_B^2} \tag{5.4}$$

where the σ_{rms}^2 is the error due to noise in the image. This was found from the standard deviation of a region near the galaxy free from emission. σ_B, the calculated baselevel error was found from $\sigma_B = \sigma_{rms}\sqrt{n}$ with n being the number of integrated beam areas that are contained in each area of integration. Furthermore, in cases that the standard deviation in an area of integration is greater than the σ_B, then the standard deviation value was used instead. This becomes important in regions further from the plane of the galaxy.

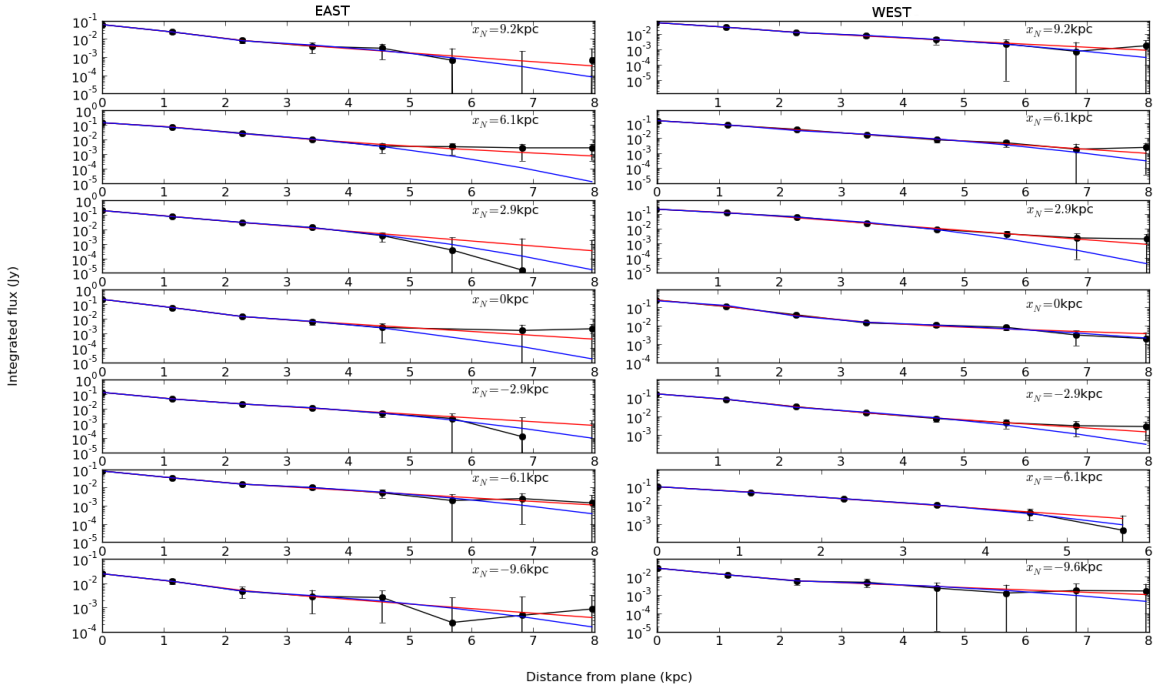

Figure 5.13: Profiles of the total radio emission in the z-direction for 7 slices for the east and west of the galaxy. A 2 component exponential (red) and 2 component Gaussian (blue) have been fitted

It is important to note that the observed profiles are actually the intrinsic distribution on the sky convolved with the telescope beam. Here we followed a similar approach as shown in Dumke et al. (1995) [169], where we assume two possible distributions convolved by the main beam which can be approximately described by a Gaussian: an exponential intrinsic distribution

$$W_{\exp}(z) = \frac{w_0}{2}\exp(\frac{-z^2}{2\sigma^2}) \cdot[\exp((\frac{\sigma^2 - zz_0}{\sqrt{2}\sigma z_0})^2 \mathrm{erfc}(\frac{\sigma^2 - zz_0}{\sqrt{2}\sigma z_0}) + \exp((\frac{\sigma^2 + zz_0}{\sqrt{2}\sigma z_0})^2 \mathrm{erfc}(\frac{\sigma^2 + zz_0}{\sqrt{2}\sigma z_0})] \tag{5.5}$$

with the complementary error function:

$$\mathrm{erfcx} = 1 - \mathrm{erfx} = \frac{2}{\sqrt{\pi}} \int_x^\infty \exp(-r^2)dr \tag{5.6}$$

and for a Gaussian intrinsic distribution

$$W_{\mathrm{gauss}}(z) = \frac{w_0 z_0}{\sqrt{2\sigma^2 + z_0^2 2}}\exp(\frac{-z^2}{(2\sigma^2 + z_0^2}) \tag{5.7}$$

where σ is the effective beam size. The free parameters are the maximum of the intensity distribution w_0 and the scale height z_0. These distributions are fitted by least-square fits. This was performed using a code kindly supplied by Dr. Marita Krause which doesn't supply errors at this time. Therefore a proper error analysis will be done in the near future.

These profiles cannot be described by single component exponential or Gaussian distribution which was also seen in Dumke et al. (1995)[169] at 2.8 cm. This is due to NGC891 possessing an extended halo. We observed in most regions of the galaxy that the halo is reaching out to 8 kpc. We found that in nearly all regions, a two component exponential fitted best to the halo continuum emission save two locations, the +2.9 kpc region to the north of the central region.

Table 5.4: Fitted scale heights for the west side of NGC891 at 146 MHz. $z_{0,2e}$ $z_{1,2e}$ correspond to the scaleheights of the first and second component exponential fit. $z_{0,2g}$ $z_{1,2g}$ correspond to the scaleheights of the to first and second component Gaussian fit. A positive location from the plane signifies the north half of the galaxy whereas negative is south.

Location from center (kpc)	$z_{0,2e}$ (kpc)	$z_{1,2e}$ (kpc)	$z_{0,2g}$ (kpc)	$z_{1,2g}$ (kpc)	Better Fit
+9.23	**0.42**	**2.11**	0.81	3.84	exponential
+6.08	**0.09**	**1.57**	0.89	3.47	exponential
+2.9	1.35	1.35	**0.59**	**2.71**	Gaussian
0	**0.73**	**3.94**	1.19	5.05	exponential
-2.93	**0.7**	**2.03**	0.95	3.52	exponential
-6.08	**0.11**	**1.40**	0.67	2.81	exponential
-9.23	**0.4**	**3.33**	0.71	4.68	exponential

We observe that the exponential scale heights of the thick disk (i.e the second component) can vary from 1.35 kpc to nearly 4 kpc. We observe a scale height of nearly 4 kpc on the west side of the central regions which correspond to the outflow emanating from the central region seen in our spectral index map. It is found that the average synchrotron scale height at 146 MHz to the west to be 2.42 kpc and 2.06 kpc in the east yielding a magnetic field scale height of 9.68 and 8.24 kpc respectively assuming equipartition. Assuming equipartition, the magnetic field scale height is (3-α_n) times the synchrotron

Table 5.5: Fitted scale heights for the east side of NGC891 at 146 MHz. $z_{0,2e}$ $z_{1,2e}$ correspond to the scaleheights of the first and second component exponential fit. $z_{0,2g}$ $z_{1,2g}$ correspond to the scaleheights of the to first and second component Gaussian fit. A positive location from the plane signifies the north half of the galaxy whereas negative is south.

Location from center (kpc)	$z_{0,2e}$ (kpc)	$z_{1,2e}$ (kpc)	$z_{0,2g}$ (kpc)	$z_{1,2g}$ (kpc)	Better Fit
+9.23	**0.41**	**1.8**	0.73	3.48	exponential
+6.08	**0.89**	**2.22**	0.75	2.65	exponential
+2.9	-	1.26	**0.54**	**2.68**	Gaussian
0	**0.32**	**1.63**	0.56	2.84	exponential
-2.93	**0.13**	**1.67**	0.51	3.18	exponential
-6.08	**0.3**	**2.14**	0.67	3.85	exponential
-9.23	**0.52**	**2.29**	0.86	4.07	exponential

scale height where α_n is the nonthermal spectral index which is negative. This is compared to the average synchrotron scale height at 1.4 GHz for the west side to be 1.71 kpc and 1.12 kpc in the east. We can compare the scale heights and magnetic field strength at the base of the disk with distance from the central region of the galaxy. We perform this for both the east and west side of the galaxy at 146 MHz.

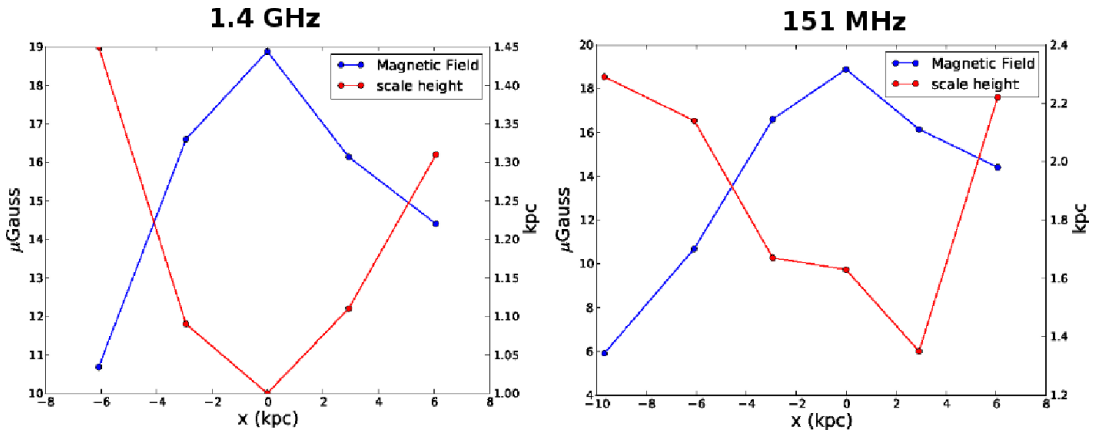

Figure 5.14: A plot of the magnetic field strength (blue) and synchrotron scale height (red) with respect to the distance from the central region on the east side of the galaxy.

We can see clearly in figure 5.14 that while the magnetic field strength and synchrotron scale height are anti correlated which was also seen in NGC253 [17, Heesen et al. (2009)]. This anticorrelation occurs as a larger magnetic field results in higher synchrotron losses which in turn creates smaller scale heights if there is a constant bulk speed. However, in that analysis, both sides of the galaxy were measured together where we are treating both sides separately. The west side is shown in figure 5.15, we observe something very different from the east side and not the obvious anticorrelation. This shouldn't be surprising as with the outflows detected on this side of the disk, we shouldn't expect a constant bulk CR outflow speed as seen in NGC253.

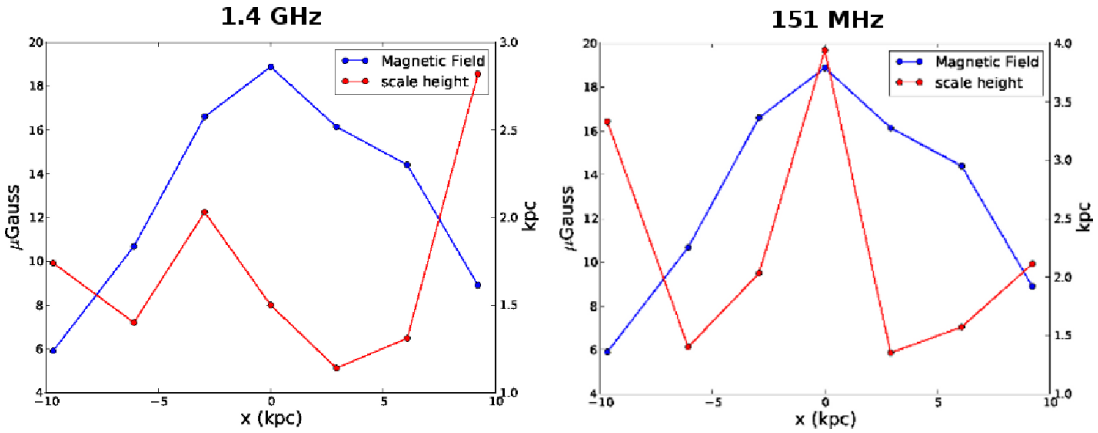

Figure 5.15: A plot of the magnetic field strength (blue) and synchrotron scale height (red) with respect to the distance from the central region on the west side of the galaxy.

5.7 RM synthesis

RM synthesis [124, Brentjens & de Bruyn, 2005] was performed on this data set but it was quickly seen that the instrumental polarization from the three 3C sources in the field was far too great. The whole field was checked but the only detection was from the pulsar PSRJ0218+4232 [90, Navarro et al. 1995]. This highlights the serious problem of instrumental polarization for LOFAR especially in fields where bright sources are present. More commissioning tests using PSRJ0218+4232 to calibrate for the instrumental polarization needs to be performed to devise the best strategy.

5.8 Discussion

The halo of NGC891 observed at 146 MHz is observed not to extend much further out compared to higher frequencies but the scaleheights fitted are found to be larger. Therefore, the sensitivity of this observation is limiting us in observing a larger halo. More sensitive observations could be proposed but, due to galaxy's proximity to 3C 66 A/B and 3C65, achieving very low noise would be a challenge.

The outflow on the northern western side of NGC891 is an interesting feature. When referring to HI maps from Oosterloo et al. (2007) [153] we see no signs of outflow within the first 2-3′ from the disk. This indicates that while the ionized gas being less dense is being forced out of the plane due to pressure while the HI being denser is more constrained by the galactic gravity potential. We see in our spectral index map that this region's spectral index steepens extremely quickly, indicating high energy losses. The magnetic field may be much stronger here as the higher star formation located in the disk could be creating a galactic fountain flow in this region. Brandenburg et al. (1995)[184] showed the horizontal field in the disk can be pumped into the halo to a height of several kpc. This pumped magnetic field would contribute to stronger synchrotron losses and thus we are not seeing this feature at higher frequencies. At low frequencies, the low energy electrons with longer synchrotron lifetimes are able to spread out further and thus why we observe this bulge at low frequencies.

The eastern side of the galaxy shows similarities to what Heesen et al. (2009) [17]: in that we found that the scale heights are increasing with increasing radius at 151 MHz and 1.4 GHz. However, the 1.4 GHz map from Hummel et al. (1991) [167] contains some negative artifacts at the edges. This analysis will be repeated with an extremely deep 1.4 GHz WSRT map reduced by Dr. Bjorn Adebahr in his PhD

thesis. This will give us a better determination of the scale lengths of the halo at the edges of the disc.

Heesen et al. (2009) [17] assumed that the galactic wind speed is the same for the entire galaxy but here we show that this not the case. The western side doesn't show this at all but this is not surprising as we know that many outflows in X-ray and HI exist on this side, the galactic wind cannot be the same in this region of the galaxy. Therefore, we can say that NGC253 and NGC891 are different cases to each other.

We see much more evidence of thermal absorption in NGC891 compared to M51 when comparing both spectral index maps. In M51 we only observe very small regions with thermal absorption in the galactic center and no other evidence in the spiral arms. NGC891, on the other hand, shows much more thermal absorption all across the disk, especially in the central region, in the north half of the galaxy and also the region around SN1986J. It should be noted that SN1986J has not being subtracted in the LOFAR map at this moment of time but it has been subtracted in the 1.4 GHz. Therefore, it would be natural to assume that the spectra in this region should be steeper than the true value but we see values of $\alpha = -0.44$. In other regions of the disk such as the south half we still observe a relatively flat slope $\alpha = -0.55$ to -0.6. This thermal absorption would be contributing to the flattening of the spectra of integrated emission seen in NGC891, whereas M51 had no significant flattening in its integrated spectrum. This is very similar to M82 which is a much more extreme case where thermal absorption flattens the integrated spectral index below 1 GHz to -0.26 ± 0.01 (Klein et al. 1988) [21].

Therefore, the inclination of the galaxy is obviously important. As our line of sight has to pass through the disk for NGC891, it is more likely the emission passes through HII regions and becomes thermally absorbed. The pathlength through the disk is much larger in NGC891 than in M51 and this would explain the flattening of the integrated spectra and why we see more signs of thermal absorption in the disk of NGC891 compared to M51. The resolution of the observation should be taken into account, with a 25″ beam any patchness expected with thermal absorption (eg in M82: Wills et al. (1997)[23]) would be completely smoothed over. Therefore, higher resolution observations of edge on galaxies with LOFAR are essential to study the local effects of thermal absorption.

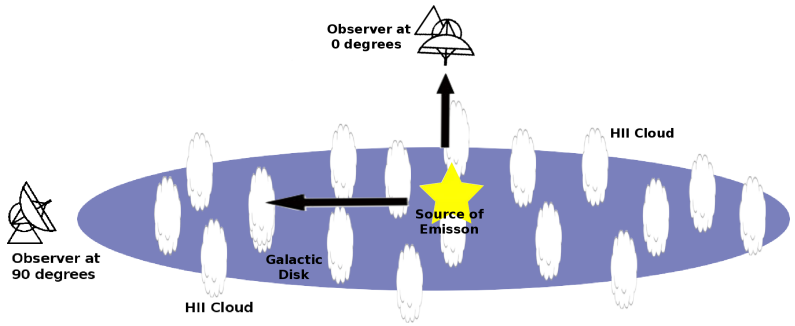

Figure 5.16: This diagram shows how the inclination of the galaxy would increase the path length of the emission. The emission observed needs to pass through more HII regions and thus increasing the likelihood of thermal absorption.

As Lacki (2013) [20] points out for M82 that free free absorption from HII regions are the most important absorption process down to 10 MHz. Therefore, we propose that the flattening of the integrated spectrum could be simply due to the inclination of the galaxy and line of sight through the star forming disk of the galaxy.

This is further evidence that the interpretation from Hummel (1991) [28] & and the model put forward from Pohl et al. (1991) [131] are mistaken. Hummel (1991) [28] discounted thermal absorption due to

not seeing a dependence of spectral flattening on galaxy inclination but here we observe the opposite.

While we agree with the proposal of Israel and Mahoney (1990) [26] that thermal absorption causes the flattening of the integrated spectrum of galaxies, we do not need diffuse ionized gas with a low temperature to explain it. No such gas has been observed in our own Milky Way. If this gas existed then signs of thermal absorption would have been more widespread in the spectral index maps of M51 and NGC891. We see signs of greater thermal absorption in the star forming regions of both galaxies, thus supporting the idea that the thermal absorption is caused by classical HII regions.

An important test case for these ideas is M33 (inclination of about 60°) (Israel et al. 1992[27]) where a break in the integrated emission spectrum was seen at around 600 MHz. The authors claim that this is due to again thermal absorption due to this low temperature ionized gas but the low frequency fluxes are again very undependable and all fluxes were placed on the Baars scale (Baars et al [63]) which is known to have errors at low frequencies as explained in Scaife & Heald (2012) [66]. LOFAR observations of this galaxy will be indispensable and already observations have taken place and are awaiting reduction.

However, more galaxies need to be observed with LOFAR with a variety of inclinations to fully investigate this. MSSS will be the perfect opportunity to see if this proposal is valid.

CHAPTER 6

Searching for vertical magnetic fields and outflows in NGC628

6.1 Introduction

The understanding of disk-halo interaction is vital to explain the evolution of spiral galaxies. Several theories exist that describe how star formation expels hot gas vertically into the halo, namely the galactic fountain model (Shapiro & Field, 1976) [142] (Bregman, 1980) [185], the chimney model (Norman & Ikeuchi, 1989) [143] and galactic wind (Breitschwerdt et al. 1991) [141]. HI holes (Bagetakos et al. 2011) [186] are created usually from stellar winds and supernovae from young massive stars in OB associations and super star clusters (SSCs) drive outflows.

These disk-halo outflows have important consequences for dynamo theory. Brandenburg et al. (1995) [184] studied a simple model of a galactic fountain flow and found that the horizontal field in the galactic disk can be pumped out into the halo to a height of several kpcs. The magnetic strength at a height of several kpcs was found to be comparable to that of the disk. Galactic MHD models with cosmic ray driven winds (Hanasz et al. 2009) [187] show that vertical flows may carry small scale magnetic fields of one polarity. Shukurov et al. (2006) [188] showed that the galactic fountain flow is efficient in removing magnetic helicity from galactic discs. Suppression of the α-effect can come from the conservation of magnetic helicity in a medium of high electric conductivity. This allows the mean magnetic field to saturate at a strength comparable to equipartition with the turbulent kinetic energy.

As a result, RM gradients or reversals across these HI holes features would be expected if the magnetic field is pushed up by the gas. Therefore being able to observe such RM gradients would help support mean-field dynamo and chimney theories.

Heald (2012) [189] detected an RM gradient in NGC6946 across a 600pc HI hole which indicated a vertical magnetic field. However, there is an obstacle with interpreting the above observational results in that the RM fluctuations in inclined galaxies can be due to variations of field strengths either parallel or vertical to the disk. The former effect can be due to compressive gas motions (density waves) or shearing, while vertical fluctuations can be due to Parker loops which are on a kpc scale or gas outflows.

Studying a face-on galaxy like NGC628 is essential so that the magnetic field components can be separated in 3D. RMs are only sensitive to vertical fields, while polarized emission traces the fields along the disk.

NGC628 = M 74 is a large, grand-design, isolated spiral galaxy. It is one of the nearest ($\sim$ 8 Mpc

distance) and brightest face-on spiral galaxy (inclination ~ 10°). The diameter of the star-forming disk is about 10′ and the HI disk about 30′, more than 3 times the Holmberg diameter (Kamphuis & Briggs 1992)[190]. The spiral structure is grand-design, but with broad spiral arms. The apparent absence of strong density waves is related to the lack of a strong bar or an interacting companion, leaving the disk largely undisturbed (seen in optical, UV and kinematics). NGC628 is similar to NGC6946 in many respects and hosts many HI holes (Bagetakos et al. 2011) [186]. NGC628 actually contains nearly twice the number of HI holes (102 holes) compared to NGC6946 (54 holes). These holes in NGC628 have a wide range of properties including diameter, hole expansion velocity and kinetic age. The age of the hole must be within a certain range in order to observe a RM gradient. Namely the hole must be old enough in that the field configuration has had time to gain a significant vertical offset, but young enough that vertical shear has not yet destroyed the observational signature. This is why HI holes are usually greater in size at larger radii.

The high star-formation rate of NGC628 leads to a bright disk in radio (synchrotron) continuum of about $10' \times 8'$ extent (Condon 1987) [191]. Marcum et al (2001) [192] observed NGC628 in UV, bright knots embedded in diffuse emission trace the spiral pattern and many of these knots are also bright in Hα. In addition the authors also suggest that the entire disk of NGC628 has undergone active star formation within the past 500 Myr and that the inner regions have experienced more rapidly declining star formation than the outer regions. It was part of the SINGS survey (Heald et al, 2009) [32] and was also observed in polarized radio continuum at 1.5 GHz with moderate resolution. The polarized emission is restricted to the outer disk and the observed RMs are small, due to strong Faraday depolarization at this frequency, similar to NGC6946 at the same frequency. With the exception of these observations, NGC628 has been poorly studied in radio continuum polarization.

Table 6.1: Observational data of NGC628

Morphology	SAc
Position of the nucleus	$\alpha(2000) = 01^h36^m41^s.74$
	$\delta(2000) = +15°47'01.1''$
Position angle of major axis	25°
D_{25}	10.5′
Inclination	5 − 10° (0° is face on)
Distance	8 Mpc

Due to the small inclination and large angular size of NGC628, it is one of the best galaxies to study the magnetic field of the disk as the fluctuations in Faraday rotation found in inclined galaxies (M 51 is 20°) can be due to variations of the field parallel or perpendicular to the disk. In NGC628, any resulting Faraday rotation found is mostly purely from the vertical field.

In this short chapter, I will present new Effelsberg Observations at 2.6 and 8.35 GHz including both total power and polarization. I will also show initial results from new JVLA (Jansky Very Large Array) S-Band observations for this galaxy. Data Reduction has yet to be complete but already impressive images can be presented. Finally future work and the outlook for this project will be discussed.

6.2 Effelsberg observations of NGC628

NGC628 was observed for the KINGFISHER project at 4.8 GHz with the Effelsberg 100 m telescope. This was reduced by the author using the NOD software. However, the region observed was too small and the entire galaxy did not fit. Therefore, integrated flux measurements would be inaccurate. It was

observed again by the author at 2.6 GHz and 8.35 GHz in October 2011 and again reduced with the NOD software. RFI was a big problem at 8.35 GHz and NGC628 was only observed at higher elevations at this frequency. 4 out of 32 scans had to discarded due to extremely bad RFI. At lower elevations it was observed at 2.6 GHz as the RFI was not as severe. However, significant RFI was still present and had to be flagged in Stokes I, Q & U.

A simple flux scaling was applied to the 8.35 GHz data using two calibrators, 3C286 and 3C48. Using values from the VLA calibrator handbook a common scale factor of 1374.5 was found and was applied to the target data. For both calibrators, the linearly polarized intensity and polarization angle were found by fitting a Gaussian over the Stokes Q & U values and calculating from the following equations:

$$P_{lin} = \sqrt{U^2 + Q^2 - \sigma^2} \tag{6.1}$$

where σ is the noise in Stokes Q and U.

$$\phi = \frac{1}{2} \cdot \arctan(\frac{U}{Q}) \tag{6.2}$$

For the seven scans of 3C48, one scan had a very different value and was discarded. The remaining scans gave a degree of polarization 5.5% and a polarization angle of $-65°$. This agrees very well with values found by Perley & Butler (2013) [193], which had values of 5.3% and $-64°$ for 8.1 GHz respectively. In addition, for 2 scans of 3C286, the degree of polarization was 11.65% and polarization angle was 33.8°. Again in excellent agreement to P & B which had values of 11.7% and 33°. Therefore, we can be very confident that the polarization we are seeing in our target is accurate.

As the 2.6 GHz receiver is a 8 channel polarimeter, an additional bandwidth calibration had to be performed along with the normal flux scaling. For each of the eight channels, the flux of the calibrator 3C295 was compared to it's theoretical value using a power law with a spectral index of -1.04. A scale factor was then determined from the difference of the two and applied to each channel. The final images for both frequencies can be seen in figure 6.1.

The integrated flux found for NGC628 at 8.35 GHz was 37.6 ± 1 mJy while 2.6 GHz was found to be 110 ± 10 mJy. Measurements from other sources were also used to determine the spectral index of the galaxy (see table 6.2). All these measurements are tied to the Baars scale (Baars et al. 1977) [63].

A single power law was fitted to this and a spectral index of $\alpha = -0.78 \pm 0.02$ was found. A plot of this data can be seen in figure 6.2. This value not only agree with Paladino et al. (2009) [194] ($\alpha = -0.78$) but is a normal value for spiral galaxies as the average spectral index for galaxies is $\alpha = -0.74 \pm 0.03$ (Gioia et al. 1982) [177].

Table 6.2: Integrated Fluxes for NGC628 on the Baars scale (Baars et al. 1977) [63]

ν (GHz)	Flux Density (Jy)	Ref
8.35	0.0376 ± 0.0007	This work
4.85	0.06 ± 0.005	Paladino et al. (2009)
2.614	0.11 ± 0.01	This work
1.515	0.16 ± 0.01	Paladino et al. (2009)
1.4	0.15 ± 0.01	Condon et al. (1998)
0.324	0.49 ± 0.03	Paladino et al. (2009)
0.057	2 ± 1	Israel & Mahoney (1990)

From the images shown in figure 6.1, NGC628 has a very striking axisymmetric galactic magnetic field. The ground mode of a $\alpha\omega$-dynamo is capable of generating such a field structure and is the easiest

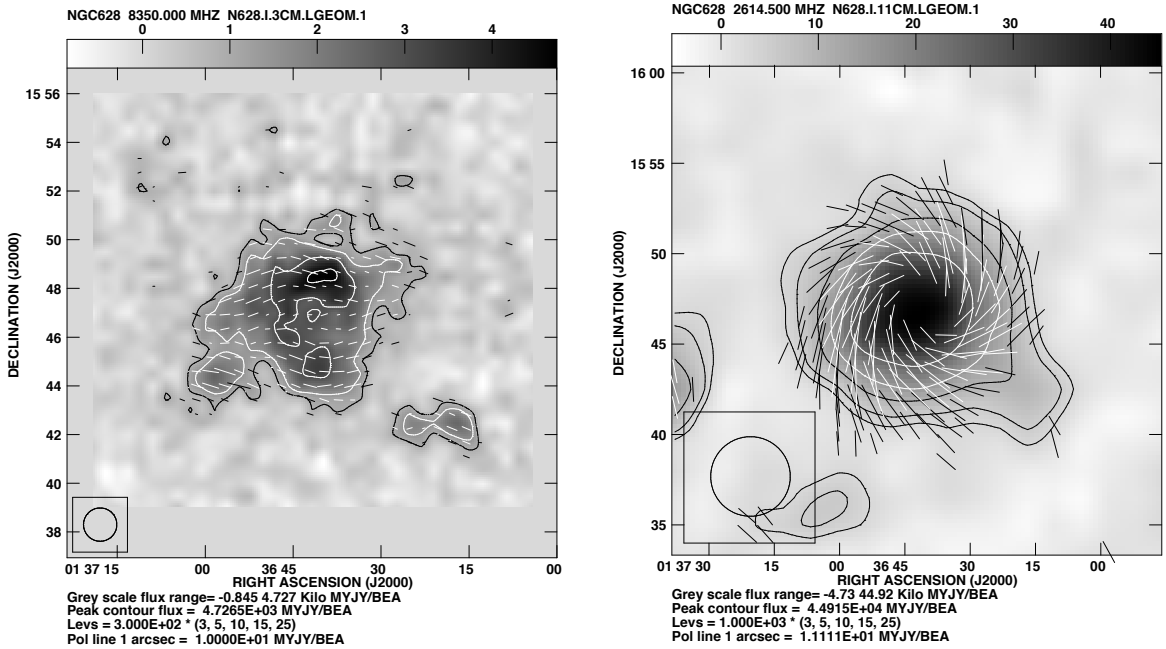

Figure 6.1: Left: NGC628 observed with the Effelsberg 100 meter telescope at 8.35 GHz at a resolution of 81″ and has an rms noise of 282 μJy/beam. The vectors show $E + 90°$ and is not corrected for Faraday Rotation which is very small at this frequency. Contours are at 3,5,10,15,25 $\times$ 300μJy. Right: NGC628 at 2.6 GHz, at a resolution of 4.6′ with a rms noise of 1.1mJy/beam. The vectors show $E + 90°$ and not corrected for Faraday Rotation which is small at this frequency. Contours are at 3,5,10,15,25 $\times$ 1 mJy.

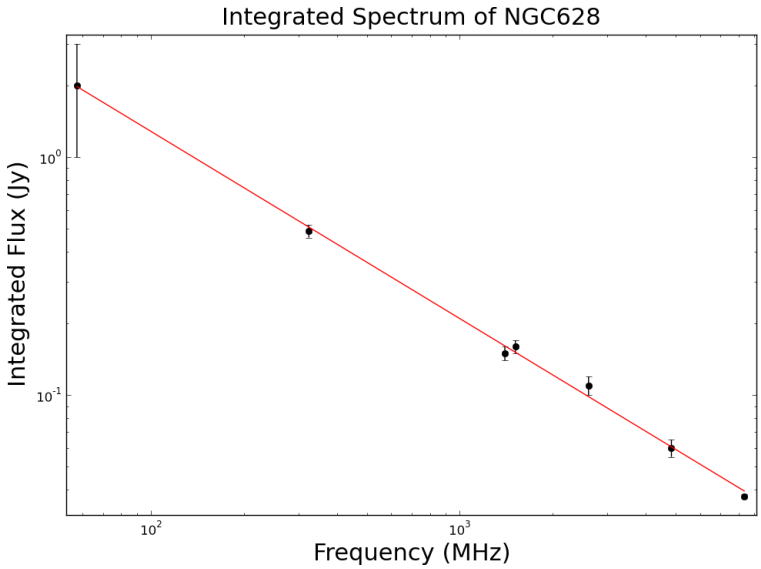

Figure 6.2: Plot showing the integrated fluxes of NGC628 including new measurements from this work. A single power law was fitted with a spectral index of $\alpha = -0.78 \pm 0.02$.

mode for the dynamo to produce.

6.3 Data reduction and imaging of S-band JVLA data

In this section, I will show briefly discuss how this JVLA S-Band observation was set up and including the data reduction. Preliminary images will be shown as well as interesting first results from performing RM Synthesis on the D-configuration data.

The JVLA (Perley et al. 2011) [195] is an upgraded version of the VLA with new receivers and electronics which gives a full frequency coverage from 1 to 50 GHz. This is provided by 8 frequency bands with cryogenic receivers. It can deliver up to 8 GHz of instantaneous bandwidth for some frequency bands. The JVLA can give an improvement of a factor of 10 in continum sensitivity. Also with a new correlator frequency resolution has increased by a factor of 3180. Already many interesting results and spectular images are being produced.[1]

6.3.1 Setting up the observation

NGC628 was observed by the JVLA (Jansky Very Large Array) in D and C configuration on February and June 2013 in S-Band (2-4 GHz) The synthesized beamwidth for this observation is approximately 23″ for D-configuration at 3 GHz and 7.0″ for C-configuration. Of course, this depends on the weighting scheme used. The ultimate factor limiting the field of view is the diffraction-limited response of the individual antennas, not on the array configuration. An approximate formula for the full width at half power in arcminutes is: PB = $45/\nu_{GHz}$. Therefore at it's highest frequency (4 GHz) in S-Band, the primary beam is approximately 10′. As NGC628 is over 12′ in angular size, a single pointing will not suffice, therefore mosaicing must be performed.

For this a hexagonal grid was chosen for both D and C configurations. Therefore the distance between two pointings is

$$\text{Distance} = \frac{2}{\sqrt{3}\frac{\lambda}{2D}} \tag{6.3}$$

where D is the dish diameter. While the galaxy is oversampled, this is a safer approach as every position in the galaxy is at least covered three times. This is best for uniform noise but the downside is that many pointings are needed. In this case 7 pointings were essential to create a hexagonal grid like the one shown in figure 6.3.

S-Band is subject to very strong RFI from a number of satellites in particular those providing satellite radio service. A satellite passing through the initial slew will cause unwanted erroneous attenuator settings. Therefore, in order to prevent this from occurring, the observation was started with a quick L band scan on 3C48 which was in a satellite free zone at this time. After this, the S-Band was switched on.

3C48 was observed at the start of the observation so it could be used as the main flux calibrator to calibrate bandpass and absolute fluxes. The source J0240+1848 was used as the phase and polarization leakage calibrator and was observed at least once every hour. 3C138 was observed twice during the observation in order to calibrate the polarization angle. Between these calibrator scans, all 7 pointings of the NGC628 were performed several times. The D-configuration observation was in total 5 hours and C-configuration was 6 hours.

[1] For a recent overview please refer to the presentation by Rick Perley: http://www.alma.ac.uk/events/past-events/advancedradioastronomymaterial/Perley-Exemplar.pdf

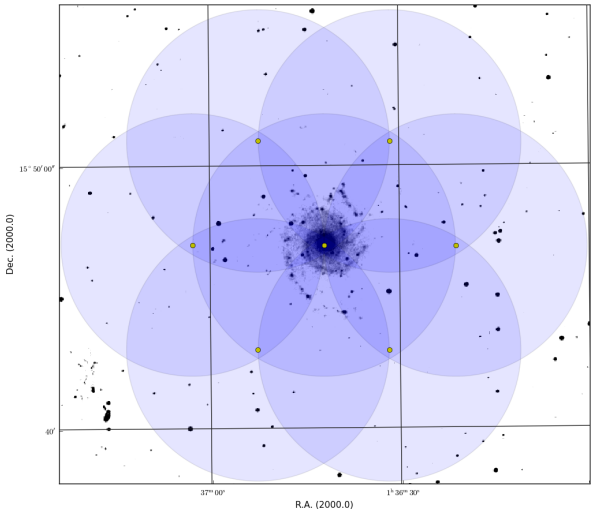

Figure 6.3: The JVLA pointing setup showing all 7 pointings overlayed onto an optical image of NGC628.

6.3.2 Reducing the data

The VLA pipeline performs basic flagging and calibration to the data but it is only for Stokes I. Therefore the calibration needs to be repeated for polarization but already some initial flag tables and calibration tables can be retained.

As the RFI can be extremely strong in S-Band and as this RFI can produce a sharp edge in the spectrum, this can introduce an oscillation across the frequency channels where no RFI is present. This is called Gibbs' phenomenon and can be brought under control by using Hanning smoothing. Hanning smoothing is a running mean across the spectral axis with a triangle as the smoothing function.

The residual delays of each antenna relative to the reference antenna were found and applied when finding the bandpass correction. 3C48 was used as the main calibrator for the flux density and bandpass calibration.

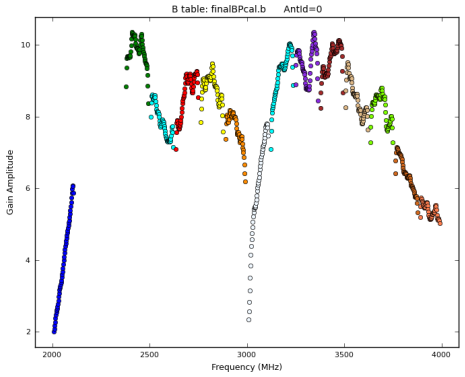

Figure 6.4: The bandpass correction applied to one antenna. One point represents the correction for one channel and every color represents a spectral window. Spectral windows 17 and 18 are flagged due to RFI.

Next, the corrections for the complex antenna gains were found. The absolute magnitude of the gain amplitudes were determined by referencing our standard flux density calibrator. To determine the

appropriate complex gains for the target source, we used our phase calibrator, in this case J0240+1848. This was the closest and most appropriate phase calibrator that could be found to our target in order to minimize the differences through the atmosphere between the phase calibrator and the target source.

The JVLA utilizes circular polarizers as it is easier to calibrate the gains and the imaging of Q and U are simpler. Circular feeds give good linear polarization but poor circular polarization measurements. In addition, as the circular feeds are placed next to each other and both are a little out of focus, this can produce large circular polarization (so called 'beam squint'). This is shared by all Cassegrain dishes. The effect becomes large beyond the beam's FWHM. Therefore, circular polarization work is not recommended.

For polarization calibration, the cross-hand delays due to the residual difference between the R and L on the reference antenna were solved using 3C138 which has more polarization signal than 3C48. Before this, the Q and U values were assigned to 3C138.

To solve for the polarization leakage, which is usually 5%, the phase calibrator was used as it is unpolarized. 3C138 was then used to solve for the polarization angle. Once this was done all calibration tables were applied to the calibrators and each pointing for the target.

6.3.3 Preliminary images and results

Figures 6.5, 6.6, 6.7 show preliminary images of NGC628 from the JVLA data in S-Band. The entire bandwidth was not used for any of these images as more editing of the data for RFI still needs to be performed. Therefore only the RFI quiet regions of bandwidth were used, namely from 2.4 GHz to 3.2 GHz.

These images were made using a normal Clark-clean algorithm with multiscale clean (Cornwell, 2008)[77] rather than multi-frequency multi-scale clean deconvolution (Sault & Wieringa, 1994)[196] (Rau & Cornwell, 2011)[197]. This is due to the long processing time of multi-frequency multi-scale clean deconvolution but this will be performed when all the data is ready for imaging

In total intensity at D-configuration (Fig 6.5), the two spiral arms are observed very clearly at this resolution. One of the spiral arms is observed to extend far out to the north (shown in the figure as 'A') which extends up to 417″ or 16.2 kpc from the center of NGC628. In HI, the spiral arm can be seen to extend out even further than this (Dutta et al, 2008) [198]. Also, at the location marked with 'B' in the north, the brightest region in the galaxy can be observed and is quite elongated along the spiral arm. Images from C-configuration will start to resolve this region of the galaxy.

In polarization at D-configuration (Fig 6.6), a clear axisymmetric pattern can be observed just like the Effelsberg observation but now the magnetic spiral arms can be resolved. The brightest emission is associated from these magnetic spiral arms which are very similar to the ones seen in NGC6946 (Beck, 2007)[48]. Much more polarization is observed in the central regions of the galaxy compared to Heald et al 2009 [32]. This is due to the fact that the Faraday depolarization is less severe at this wavelength compared to 18cm-22cm wavelengths used in Heald et al. (2009) [32]. Significant amounts of polarization from these magnetic arms are observed much further out in the northern region of the galaxy than observed in Heald et al. (2009) [32] and extends out nearly as far as the total emission in north. Heald et al. (2009) [32] found that the minimum in polarized intensity occurs at the receding major axis of the galaxy (PA = 25°), at S-Band this kind of depolarization has not been detected. Due to the low inclination of this galaxy, one wouldn't expect major depolarization due to this effect. In the central regions of the galaxy, a polarization fraction of 10 – 20% can be observed, increasing to 30 – 40% at larger radii. This indicates that the magnetic field is exceptionally well ordered especially in the extended disk.

Finally, in total intensity at C-configuration (Fig 6.6), we are missing a lot of the extended emission

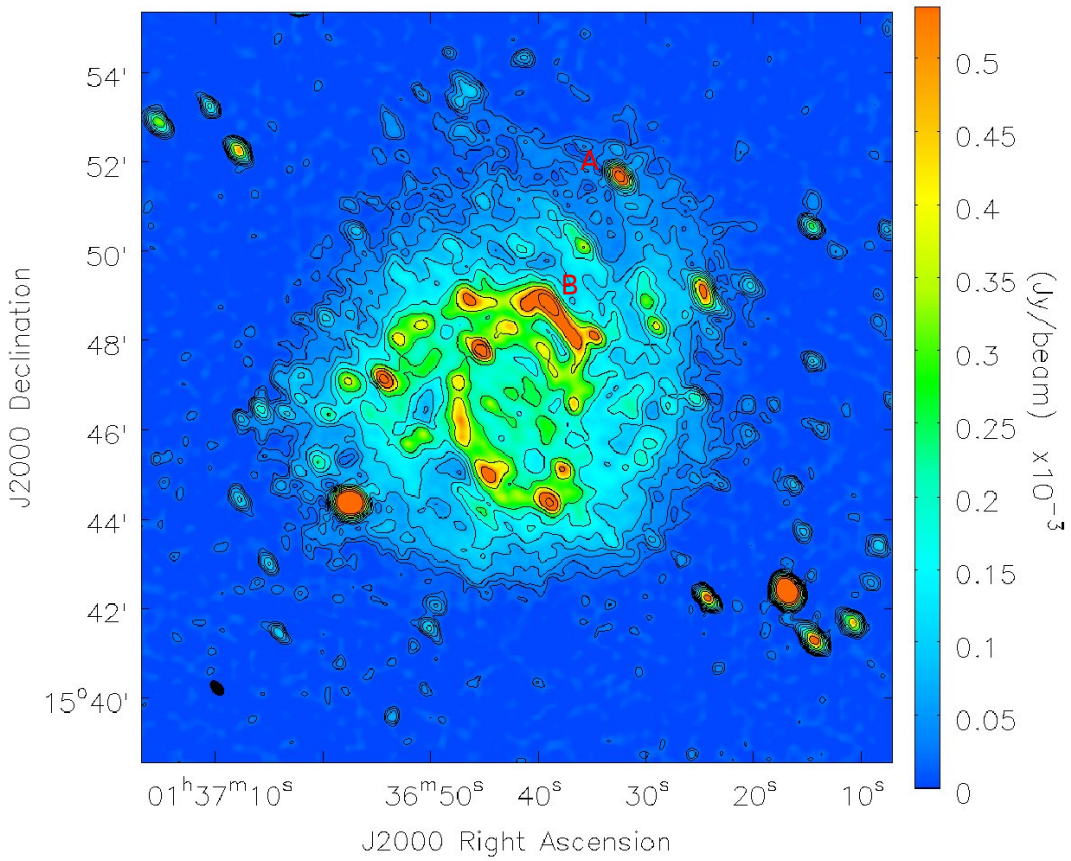

Figure 6.5: NGC628 observed at D configuration in total intensity. Noise is approximately 6 μJy/beam. Contours are in levels of 3,5,8,12,18,27,40,60,90,135 $\times\sigma$. Resolution is 22″ × 13″.

due to missing spacings, but we can now see the spiral arms in much greater detail thanks to the longer baseline length of this configuration. We can see the major star forming regions in the spiral arms, notably the regular chain of HII complexes in the South West spiral arm. The brightest structure seen in the North East is now starting to become resolved. This region is made up of many individual HII complexes located very close to each other as seen in Sonbaş et al. (2010) [199].

6.3.4 Preliminary RM synthesis results

RM Synthesis (Brentjens & deBruyn 2005)[124] has been performed on NGC628 in the WSRT SINGS survey at a 30″ resolution (Braun et al. 2010)[55] where a main component near −30 rad m^{-2} was detected. In addition to this, two secondary components were detected centered near -213 and +145 rad m^{-2} at a 90″ resolution. These secondary components are important to confirm as they could be instrumental in nature. Each channel was imaged and smoothed to 30″. The Q and U channels were separated and every channel was inspected for RFI. This resulted in several channels been discarded and the final number of channels used in RM Synthesis was 441. Available channels in spectral window 16 (around 2 GHz) that were not corrupted were also used in order to minimize the FWHM of the Rotation Measure Transfer Function (RMSF).

The bandwidth from 2.5 GHz to 3.5 GHz were used which results Faraday depth resolution was found

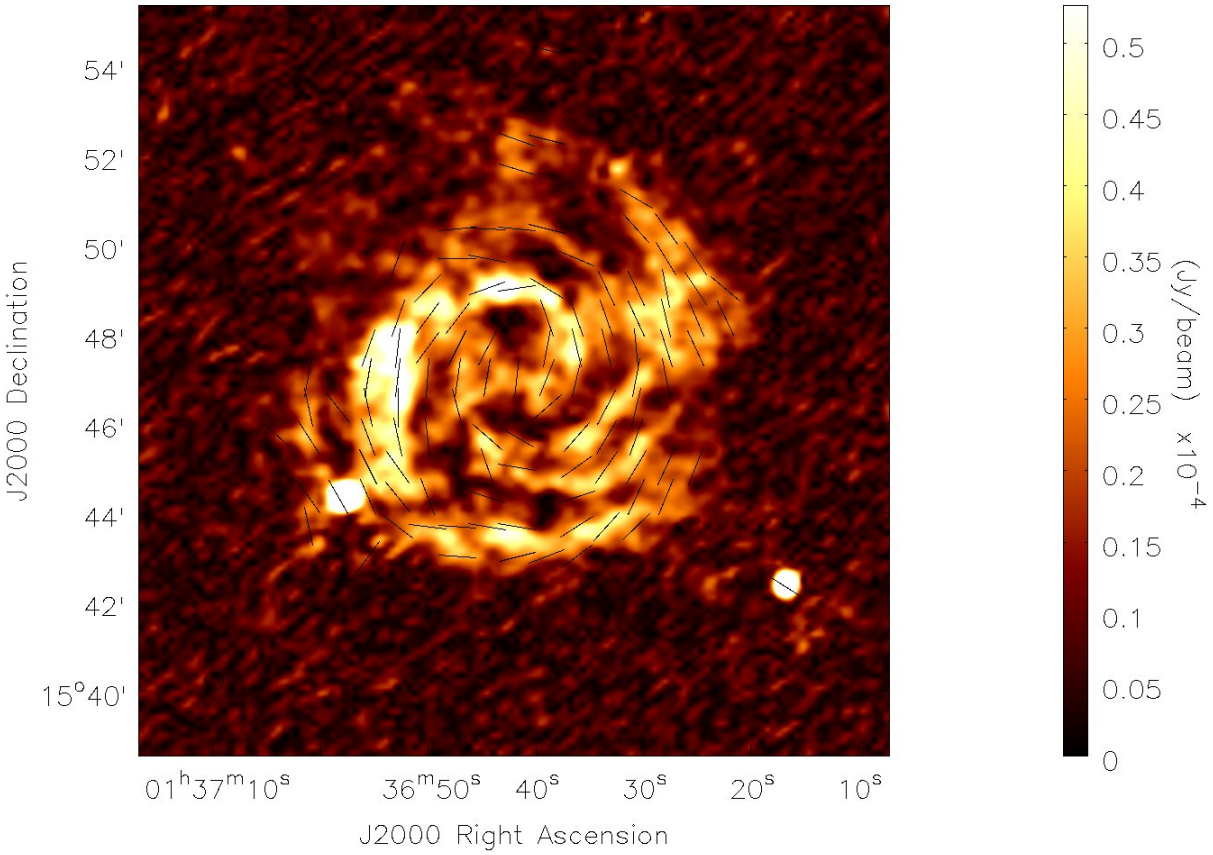

Figure 6.6: NGC628 observed at D configuration in polarized intensity. Noise is approximately 4.5 μJy/beam. Vectors have been rotated by 90° to show the direction of the B field and have not been corrected for Faraday rotation which is small at this frequency. Resolution is $24'' \times 24''$.

to be 232.1 rad m^{-2} and the largest observable scale is 426 rad m^{-2}. The RMSF can be seen in figure 6.8.

As polarized intensity has Ricean, rather than Gaussian statistics (Heald et al. 2009)[32], the noise has a Rayleigh distribution with a mean ('the Ricean bias') and variance of

$$\langle P \rangle_n = \sigma_{Q,U} \sqrt{\frac{\pi}{2}} = 1.25 \cdot \sigma_{Q,U} \tag{6.4}$$

and

$$\sigma_P = \sqrt{\frac{4-\pi}{2}} \sigma_{Q,U} = 0.66 \cdot \sigma_{Q,U} \tag{6.5}$$

for an rms noise in Q and U of $\sigma_{Q,U}$.

$\sigma_{Q,U}$ was found to be 5.8 μJy/beam and therefore in polarized intensity, σ_P was found to be 3.8 μJy/beam.

While this is not all the available bandwidth that could be used for RM Synthesis, another 400 MHz could be extracted. However, due to extremely strong RFI at frequencies of 2.1-2.3 GHz as well as the bandwidth between 3.7-4 GHz will not be usable. This will limit our final achievable FD resolution and sensitivity.

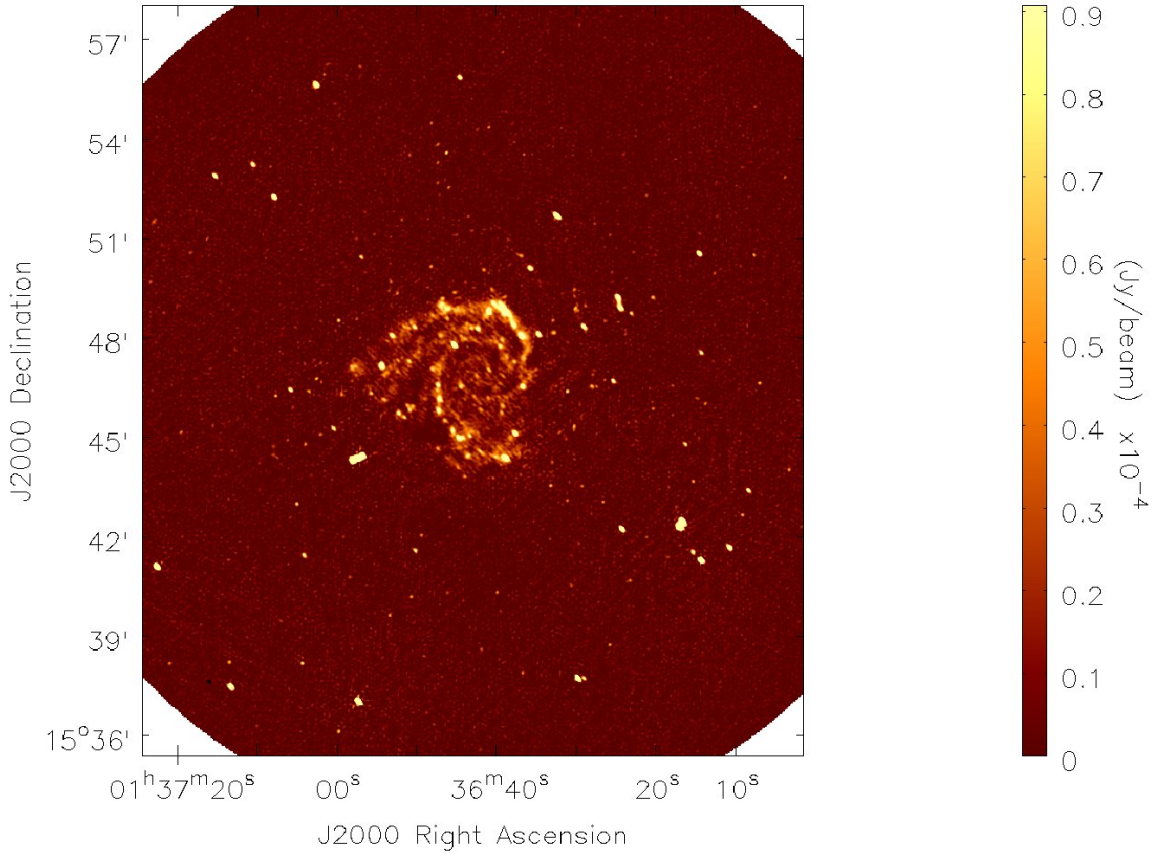

Figure 6.7: NGC628 observed at C configuration in total intensity. Noise is approximately 6 μJy/beam. Resolution is $7'' \times 4''$.

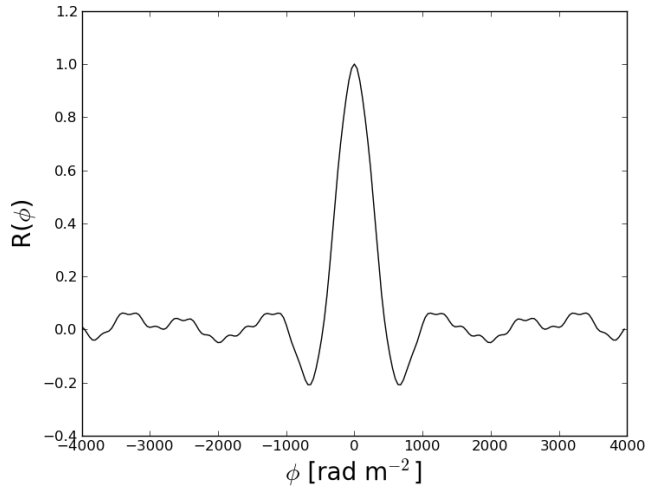

Figure 6.8: The RMSF from JVLA S-Band data, not all the available data is used.

RM Synthesis was performed using software for LOFAR and RM Clean (Heald et al. 2009) [32] was performed using software from George Heald. For the RM Clean, 5000 iterations were used.

It was seen that the main component of NGC628 is seen at around -40 rad m^{-2} (see fig 6.9) which agrees with Braun et al. (2010) [55]. But much more interestingly is we see regions in the galaxy with a clear Faraday depth of approximately ϕ = -200 rad m^{-2}. As we have 3 times better resolution than Braun et al. (2010) [55]. we can see that these structures are more discrete in nature. We also see that these regions observed at ϕ = -200 rad m^{-2} are NOT visible in the main component where ϕ = -40 rad m^{-2}. In addition we also see a discrete, weak component at a Faraday depth of ϕ = +160 rad m^{-2}. This again agrees with the secondary component seen at +145 rad m^{-2} by Braun et al. (2010) [55]. Faraday spectra of these components can be seen in figure 6.11.

This is interesting as there has recently been debate on whether these secondary components were real detections especially with regards to M51 where new JVLA observations fail to detect them. The detection of this highly dispersed and heavily depolarized 'second disk' is thought to support the model that the polarized intensity observed at GHz frequencies from nearby galaxies is mainly the region of emissivity located above the mid plane closest to the observer. As this polarized emission only passes through the extended halo it experiences little Faraday rotation amounting to only a few tens of rad m^{-2}. But polarized emission from the farside of the galaxy has to pass through the mid plane, resulting in Faraday Rotation of plus and minus 150-250 rad m^{-2}.

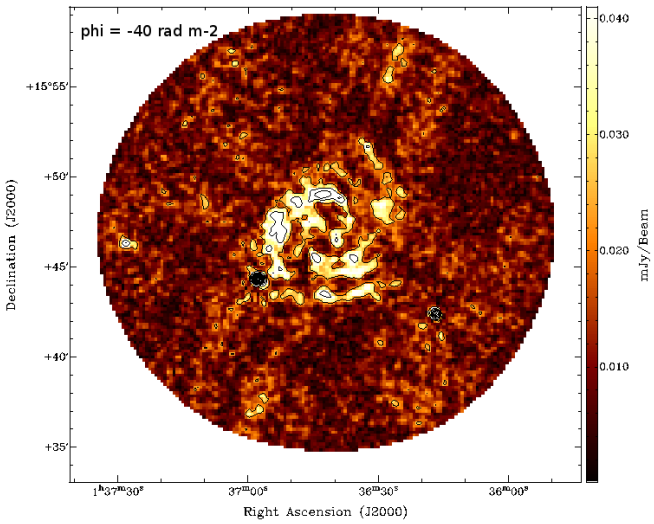

Figure 6.9: The main component seen in the Faraday cube centered at -40 rad m^{-2}.

But then why do we not see this emission at -40 rad m^{-2} as well? This polarized emission would need to pass through the extended halo as well as the disk. and we should see two components in the RM cube if the halo is emitting too. One possibility is that the polarization is in fact coming from disk but coming from a region with a greater vertical magnetic field or electron density. As Brandenburg et al. (1995) [184] showed, a fountain flow could produce magnetic field strengths comparable to the base of the flow in this case the disk and thus produce a higher Faraday depth. Figure 6.10 shows two Faraday slices at a fixed right ascension, and it is very clear that a RM gradient is visible and this could be a sign of the outflows needed to transport magnetic helicity from the galactic disc.

These secondary components are quite widespread and can be seen throughout most of the disk as can be seen in figure 6.11. It can be seen that most of these secondary components can be seen in west where

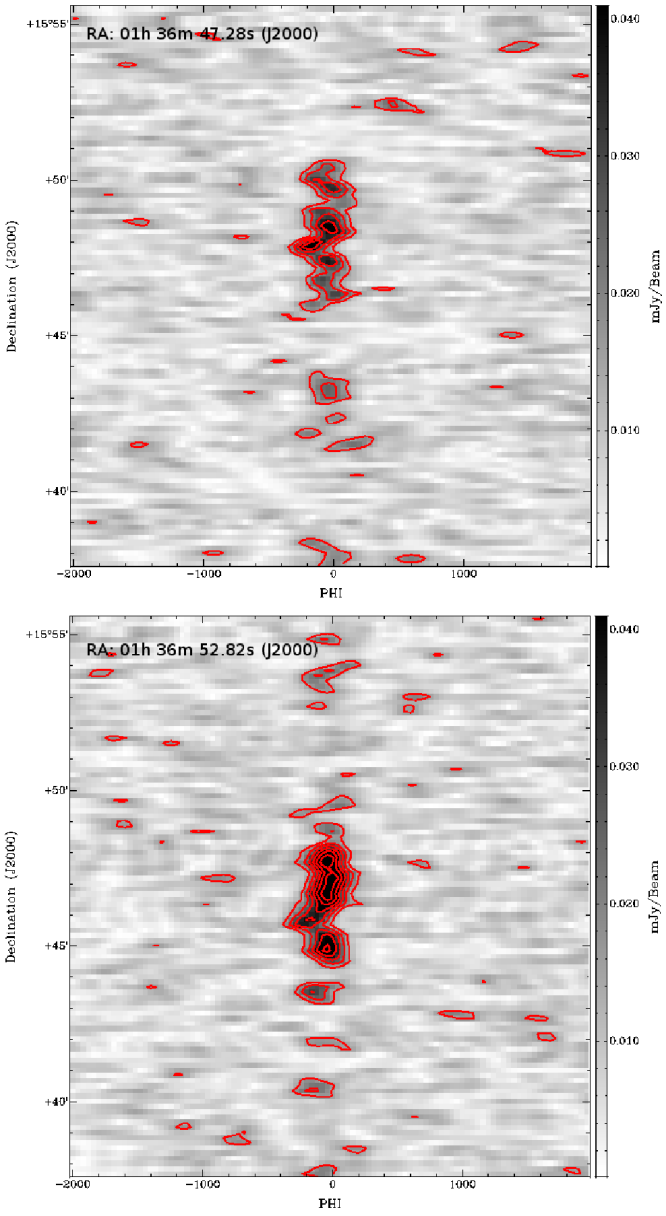

Figure 6.10: Two different slices at different Right Ascensions of the Faraday cube showing that while most emission is seen at -40 rad m^{-2}, we can see that some emission comes from a Faraday depth of -200 rad m^{-2}.

the spiral arms are more promiment. Some of these secondary components are also seen at +150-250 rad m^{-2} which would indicate magnetic field reversals.

Greater resolution in angular resolution and Faraday depth is sorely needed to investigate the secondary components further and the C-configuration data on hand will be essential to achieve this.

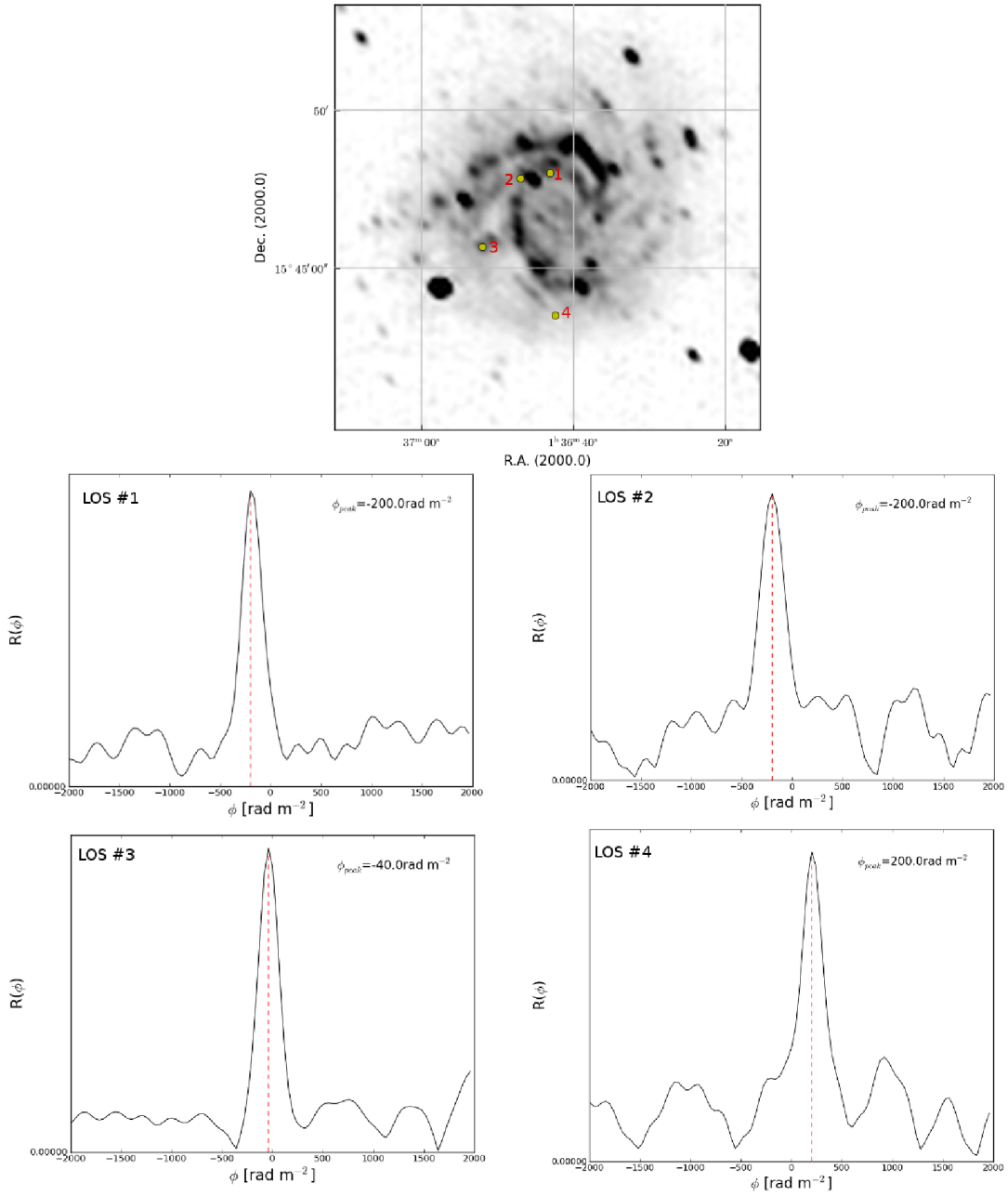

Figure 6.11: Four different Faraday spectra from the Faraday cube at different locations in the galaxy which illustrate the presence of the two secondary components. The image on top shows the location of each line of sight in the galaxy and below the corresponding spectra.

6.4 Outlook and future work

Firstly, initial polarization calibration of the JVLA C-configuration need to be completed. Once this is completed both C and D configurations need to be combined. As our 2 configurations have the same pointings, this should make combination easier. Once this is done, self calibration will be implemented

which should bring the noise down further and enable us to detect more of the extended disk.

Also the full possible amount of data will be usable for RM-Synthesis. With better FD resolution, sensitivity and angular resolution the secondary components seen in the RM cube will be better resolved and more apparent.

An 8 hour LOFAR observation has taken place with the main aim of the study of extended disk of NGC628 which in HI extends to 30′.

Magnetic fields are an important component of the interstellar medium (ISM) in galaxies as they contribute significantly to the pressure of interstellar gas, are essential for star formation and can also control the density and distribution of cosmic rays. Low frequency emission from galaxies out to a redshift of about 3 is almost purely non thermal and therefore a perfect tracer of cosmic ray electrons (CREs) and the large scale magnetic field.

There is increasing evidence that magnetic fields can extend deep into intergalactic space; however as it is far from regions of acceleration, the synchrotron emission is weak due to lack of cosmic rays electrons which suffer from various loss processes. Fortunately, low energy electrons which emit emission at low frequencies suffer less from energy loss processes and are expected to travel further, especially in the presence of ordered magnetic fields. We have seen already in this thesis that M51's disk has been detected to 16 kpc at 150MHz and here, NGC628 with an extended HI disk, total and polarized emission can be seen up to 16kpc at 2-3 GHz.

Also it is know that CRe diffusion parallel to the magnetic field has a higher diffusion coefficient than diffusion perpendicular to the field (Buffie et al. 2012) [145]. Also galaxies with extended HI disks can be even more beneficial as HI can be partially ionized. Generally, in the galaxies studied with sufficient resolution, the outer HI layers show spiral features. The extent of M51's disk observed with LOFAR is seen to increase significantly in radius compared to higher frequencies, even though it possesses no extended HI disk.

The scale length of the total synchrotron emission in the disks of spiral galaxies is usually $\sim$ 4 kpc, but the scale length of the magnetic energy is about 8 kpc (Beck 2007) [48]. This is larger than any other energy with the exception of global rotation. It follows from this that the scale length of the equipartition total magnetic field strength is $\sim$ 16 kpc.

The relative importance of various competing forces in the interstellar medium can be estimated by comparing the corresponding energy densities or pressures. Beck (2007) [48] shows that with increasing radius of NGC 6946, the turbulence energy density decreases quite drastically while the ordered magnetic field energy density decreases much slower than the total magnetic field energy density. However, the total magnetic energy density in the outer galaxy is an underestimate due to energy losses of the cosmic-ray electrons. Although the star-formation activity is low, turbulence caused by magneto-rotational instability (MRI) could keep dynamo action functioning far out into the disk (Sellwood and Balbus 1999) [99].

The main aims of the LOFAR observation are:

1. Detection of the outer disk that NGC628 is known to possess from HI and Hα observations. This will provide us with much needed data on the magnetic field and CREs distribution at extreme distances from the optical radius.

2. Detection of diffuse polarized emission in the outer disk. The magnetic field becomes more regular in outer parts of galaxies which can be detected from the polarized emission of non-thermal radiation using RM-Synthesis. However, from experience this will be technically difficult due to strong depolarization at low frequencies but depolarization should be smaller outside the star formation regions. Fortunately, 7 $\sim$ 8 polarized background sources exist within the extended

disk. These sources start to become resolved at around 15 arcsecs (as seen in the JVLA data) and with LOFAR's potentially high resolution, beam depolarization is reduced. These sources could help us probe the magnetic field at different radii.

3. The radio-far-infrared correlation can be investigated and compared between the arm and inter-arm regions where the slope of the Radio-FIR correlation differs (Basu et al. 2012) [119]. In addition,Tabatabaei et al. (2013) [46] found that the propagation length of CREs in galaxies increase as a ratio of ordered and turbulent magnetic fields can be deduced by the Radio-FIR cross correlation as a function of scale. The propagation length of CRes are very different below 1GHz and about 5GHz. LOFAR observations will enable us to measure the diffusion coefficient and will provide constraints for models of cosmic-ray propagation.

4. Using available data from Effelsberg, VLA (Paladino et al. 2010) [194] and JVLA at a wide range of frequencies will enable us to study the radio spectral energy distribution within NGC 628, and with other galaxies observed in LOFAR cycle 0 & 1 will help to answer questions concerning thermal absorption and the existence of $T_e < 1000K$ ionized gas (Israel and Mahoney 1990)[26]. The radio specta may also show outflows from the star forming regions into the disk.

5. This observation can also be used to detect diffuse polarized foreground emission. This galaxy's Galactic latitude is low ($b = -45°$) and will be compared to other LOFAR observations at different latitude.

CHAPTER 7

MSSS- Multi-frequency Snapshot Sky Survey

7.1 Introduction to the MSSS survey

The Multi-frequency Snapshot Survey (MSSS) is the first all sky survey with LOFAR. The primary aim of MSSS is to produce a global sky model (GSM) to replace the 'Mark-0' skymodels, namely skymodels based on cataloged values from the VLSS, WENSS, and NVSS. As was seen in Chapter 5, these type of models can have serious discrepancies not even including the fact that the spectral index information is oversimplified. The 'Mark-1' LOFAR GSM is being generated by MSSS which is a broadband survey of the northern sky ($\delta > 0°$) but due to the large field of view, sources $\delta > -2°$ can be detected.

MSSS is in fact two surveys, one in LBA range which covers a frequency range from 30 to 74 MHz and the other in HBA spanning from 120 to 160 MHz. The overall overview of MSSS can be seen in Table 7.1.

Survey	MSSS-LBA	MSSS-HBA
Station configuration	LBA INNER	HBA DUAL-INNER
Field of view per field (FWHM)	5.77° at 60 MHz	2.42° at 150 MHz
Bandwidth (MHz) per field	16	16
Number of simultaneous field observed	5(+ calibrator)	6
Time per field	9×11 min	2×7 min
Required number of fields	660	3616
Required on-source observing time (hr)	218	141

Table 7.1: MSSS overview

While the full LOFAR array including international stations are being used for MSSS, initially only the core 3km will be processed for the MSSS-HBA and 10km baselines for MSSS-LBA. This ensures a similar resolution of 2 arcminutes for both surveys. Fortunately, the data could easily be reprocessed to achieve higher resolution for a more accurate skymodel and an increased science capability. While time smearing nor frequency smearing doesn't provide a hindrance to higher resolution imaging, the sparse uv-coverage does, as well as the longer processing time especially with regards to the imaging. Initial tests have shown that for a normal 2.2×2.4 arcmin image would take 8 minutes to process, However, imaging a MSSS field at a resolution of 28×17 arcsec would take 54 minutes. Therefore, due to processing limitations a higher resolution MSSS would probably be limited in scope if done at all.

Survey Name (Telescope)	Frequency Range (MHz)	Sensitivity (mJy/beam)	Angular resolution (arcsec)	Sky Area (sq deg)
MSSS-LBA	30-74	≤ 15	≤ 100	20,000
VLSS (VLA)	74	100	80	30,000
MSSS-HBA	120-160	≤ 5	≤ 120	20,000
TGSS (GMRT)	140-156	7-9	20	32,000
WENSS (WSRT)	330	3.6	54	10,000
NVSS (VLA)	1400	0.45	45	35,000

Table 7.2: MSSS characteristics compared with existing surveys

Band Number	LBA central frequency	HBA central frequency
0	31 MHz	120 MHz
1	37 MHz	125 MHz
2	43 MHz	129 MHz
3	49 MHz	135 MHz
4	54 MHz	143 MHz
5	60 MHz	147 MHz
6	66 MHz	151 MHz
7	74 MHz	157 MHz

Table 7.3: MSSS Band frequencies

This chapter presents work done for MSSS during this PhD including creating and testing calibration schemes, detection of polarization and preliminary work done on a low frequency survey of nearby galaxies.

7.2 Creating and testing initial calibration techniques

During the first weeks of MSSS, the LBA survey was observed first as there are fewer fields to observe, however, processing MSSS LBA data proved to be far more difficult than HBA data.

Initial calibration of LBA MSSS data had to be tested in three different ways, namely, creating an image from data processed fully through the pipeline (demixed and calibrated from a sky model), data that is demixed only and calibrating it from the preceding 2 minute calibration pointing and finally data that is demixed only and is calibrated using the calibrator beam via direct transfer of gain solutions. This final method of calibration can be done for every LBA field as the LBA antenna have whole sky coverage unlike the HBA which is constrained by the size of the tile beam.

For these tests, one field (phase center: $\alpha = +9^h00^m00^s, \delta : +63°28'21''$) was tested with 3C196 as the calibrator.

It was seen early on, whilst imaging the processed data that RFI can become a major problem, therefore flagging with RFI-console (Offringa et al. 2013) [72] becomes important when the individual subbands are merged to create a band of 10 subbands. Band 3 (49 MHz) and 5 (60 MHz) were found to be heavily affected by RFI mainly due to one pointing. When this pointing was excluded, the image quality was better. Only the core stations were imaged. With MSSS, a rms noise of 15 mJy/beam is hoped to be achieved. However it had a noise of approx 1 Jy/beam, which is far too high.

Therefore, it was decided to start again from the demixed data and calibrate the target field from the 2

minute pointing before the main pointings. RFI console was used after demixing and after the subbands are merged into a single band. The resulting image was not much different from method 1, in that the noise was not really affected. The rms noise was approximately 0.95-1 Jy/beam. Again, far from the target sensitivity.

Finally, starting again from the demixed data, the gain amplitudes from the calibrator beam were directly transferred to the target field. An image was created, however it was quite poor. Inspection of the total electron content (TEC) solutions showed that station CS032 had bad solutions and was therefore flagged. The data was then flagged in RFI-console (Offringa et al. 2013) [72] and it was then re-calibrated with BBS TEC calibration. The data was then imaged once again and the image obtained had a better noise than the previous methods. Baselines up to 10 km were imaged which showed very promising results for the future of MSSS.

From these results, it is apparent that method 3 was the superior method of calibration resulting in the lowest noise with the 10 km baseline image having a rms noise of 175 mJy/beam. This noise could be easily reduced with several iterations of self calibration including directional dependent calibration bringing it closer to the target noise of 15 mJy/beam. This method of initial calibration was adopted for the calibration of MSSS LBA data with some minor improvements.

Also as seen in figure 7.1, real sources that were not included in the skymodel appear using method 3.

Method of calibration	rms noise value
Method 1: Imaging Processed data	1 Jy/beam
Method 2: Imaging demixed data with gain transfer from 2 minute scans	0.9-1 Jy/beam
Method 3: Transferring Gains from Calibrator Beam to target Beam	485 mJy/beam
Method 3: Imaged with a uv-coverage up to 6km	377 mJy/beam
Method 3: Imaged with a uv-coverage up to 10km	175 mJy/beam

Table 7.4: Noise achieved for each calibration method

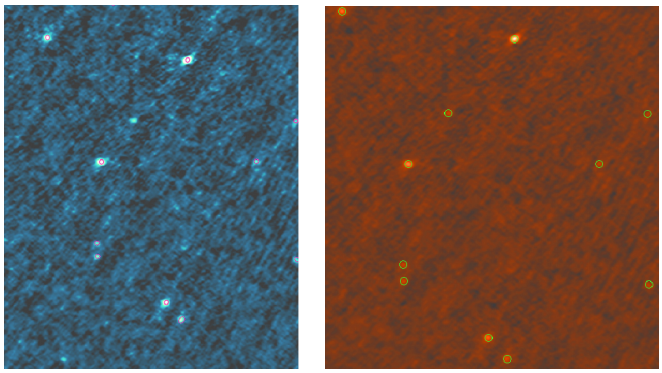

Figure 7.1: Left figure shows a region of the image created from Method 3 with the red circles showing the skymodel used for the BBS TEC calibration. The right figure shows the same area with the green circles showing VLSS sources. One visible source can be seen to be not included in the skymodel but is contained in VLSS catalogue. This is not the only case with several more real sources appearing than were not included in the skymodel.

7.3 Testing directional dependent calibration on MSSS LBA data

It was found from other members of the MSSS team that using directional dependent calibration would lower the rms noise by a 20-30%. This short section shows results of further tests of the directional dependent calibration of LBA data and its effect on extended sources.

Already initial calibrated data was used in testing the directional dependent calibration scripts. Each of the 7 bands were calibrated separately and it was found that peeling 4-5 sources takes 20-30 minutes for each band. Inserting more sources than this increases processing time exponentially which has major implications to processing the entire survey. A significant improvement could be seen from the resulting images.

The noise was determined for the restored image with no primary beam correction. One can see in table 7.5 that a different number of sources were peeled for each band which are automatically by a script. However, it is clear that the peeling has reduced the noise in all bands. However, BAND 0 shows little improvement, compared to the other bands that have an equal number of sources peeled. BAND 5 shows the greatest reduction in noise (24.6%) with 6 sources peeled, however BAND 7 had six sources peeled as well but only shows a 11% percent decrease.

It can been seen in the closeups (see figure 7.2) that artifacts from around the sources are reduced in the peeled data. Overall the image quality is much better compared to the unpeeled data. Large scale and small scale noise around sources disappear with the addition of the noise decreasing, however, this depends on which band is peeled.

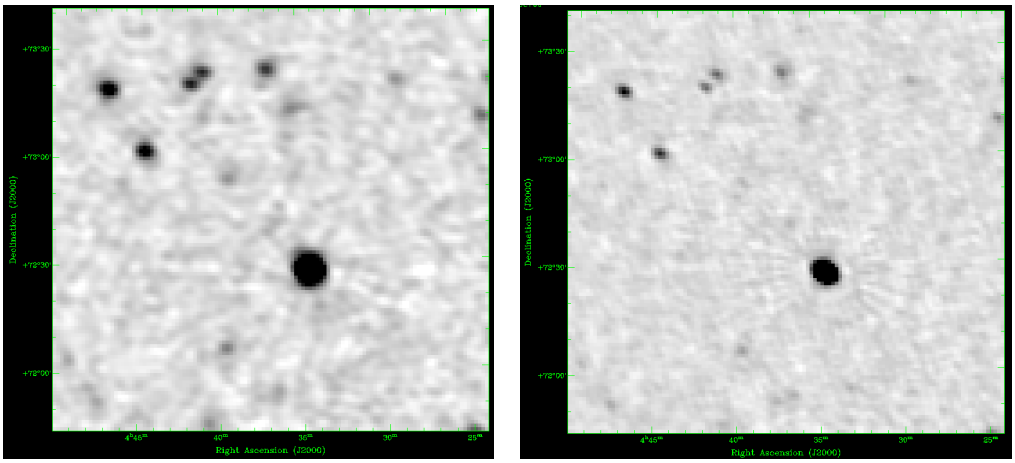

Figure 7.2: Closeup of a region from a field in LBA with the left figure showing before peeling and the right figure after peeling.

The face on spiral galaxy IC342 is located at the edge of the field and was compared to the unpeeled image. Quite a difference can be seen between the peeled image and unpeeled image (see figure 7.3). The peak flux in the unpeeled image is 2 times greater than the peeled image. Also IC342 is more extended in the unpeeled image. This seems to be a serious problem, namely that when performing directional dependent calibration, the integrated flux of extended sources always decreases. This problem has been explored already in section 2.8.3, however the countermeasures found there to minimize this effect cannot work due to the lack of multiscale clean of AWimager (Tasse et al. 2013) [101]. AWimager is essential for MSSS unlike NGC891 and M51 in previous chapters as we are interested in entire field and therefore the primary beam correction is vital.

Band number	Prepeeled (mJy/beam)	Peeled (mJy/beam)	Difference	Number of peeled sources
Band 0	620	609	1.7%	4
Band 1	542	496	8.5%	4
Band 2	388	318	18.0%	4
Band 3	298	255	14.4%	4
Band 4	216	166	23.2%	5
Band 5	203	153	24.6%	6
Band 6	172	132	23.3%	5
Band 7	142	126	11.3%	6

Table 7.5: Noise achieved for each band before and after peeling

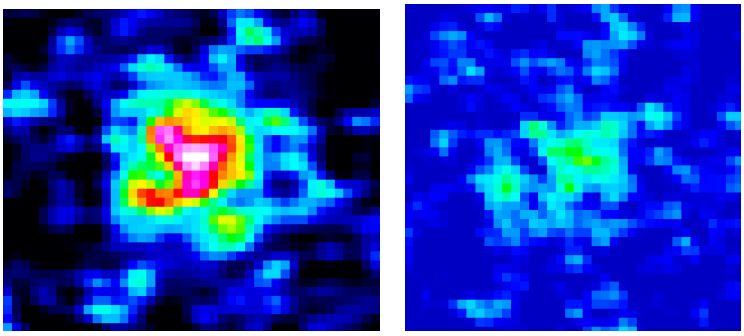

Figure 7.3: The face on spiral galaxy IC342 shown before (left) peeling and after (right) peeling. The color scale is the same for both images.

7.4 Investigation of the gains solutions derived from Cygnus-A and compared with 3C196

As mentioned in section 2.2.2, the Scaife & Heald (2012) [66] models of six 3C sources are mostly used for the calibration of LOFAR, but Cygnus-A was also checked as a calibrator and compared to another 3C source, in this case 3C196. While Cygnus-A is an extremely strong source in LBA, it would need a complex model especially for a longer baselines. This section outlines this small investigation to see if Cygnus-A is a suitable calibrator for MSSS.

First of all, the gain solutions from 3C196 were compared to the Cygnus gains in the frequency domain for one snapshot. In terms of amplitude, both calibrators show similar gain bandpasses with a peak at around 58 MHz as expected. However, the Cygnus-A gains change much smoother over the entire frequency range compared to the 3C196 gains. Also we can see that the standard deviation found for each subband is substantially higher for 3C196 compared to Cygnus-A (see figure 7.4).

The same data was used to compare how the gains behave in a single snapshot. The processed data had to be re-calibrated as the normal MSSS calibration script will clip extreme gain amplitude values and change them to the median which would skew the results. The parset used for calibration is the parset normally used in MSSS LBA calibration script. Figure 7.5 shows the Cygnus-A gains (blue) and 3C196 (red). It is easy to see that the Cygnus-A gain solutions are much more stable in time than this snapshot of 3C196.

A comparison to a skymodel with no spectral information and a skymodel with spectral information

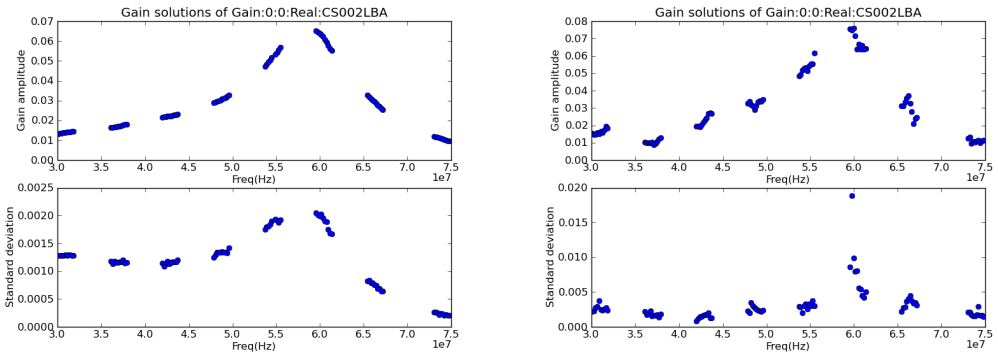

Figure 7.4: Plots showing the average gain amplitude and std. deviation for each subband for the entire frequency range used for MSSS for the XX correlation of station CS002. Left shows gains obtained from Cygnus-A and right is from 3C196.

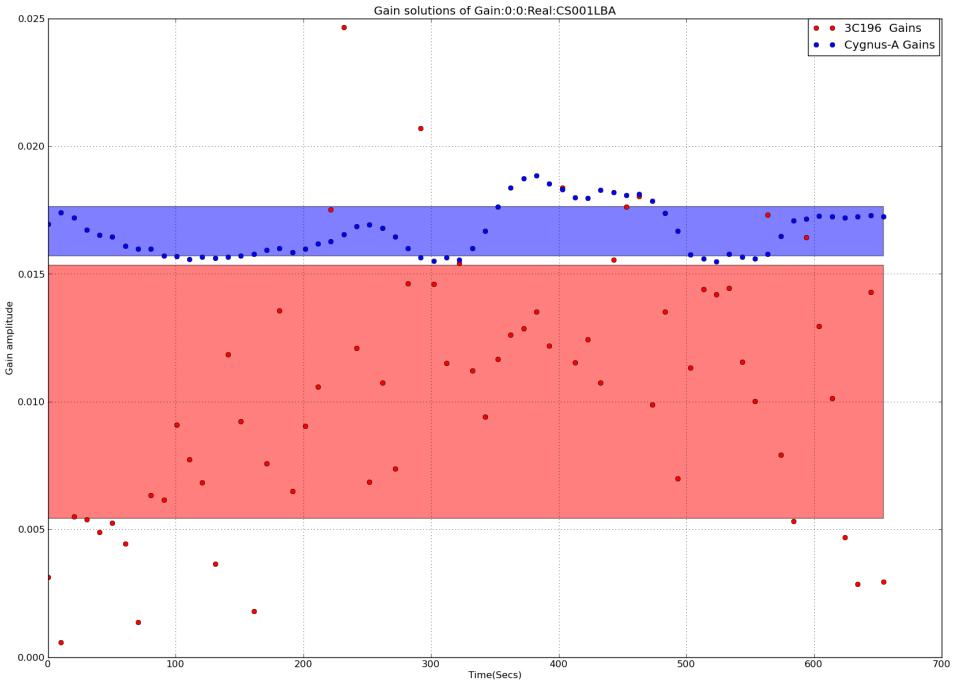

Figure 7.5: Plots showing the variation of gain solutions of the XX correlation for station CS002 for Cygnus-A and 3C196 with the shaded region showing the standard deviation around the gain average.

was performed and it was seen that the amplitude is lower in amplitude for a sample subband, as well as the standard deviation for the new spectral skymodel, but other than that no other differences could be seen.

In conclusion it was seen that:

1. In terms of frequency, the Cygnus-A gain solutions were better defined than 3C196 gains. The gain curve for Cygnus-A is much better defined.

2. In terms of time, the Cygnus-A gain solutions were much better behaved than the 3C196 gain. This can be seen for different subbands and snapshots.

3. Adding the spectral information doesn't degrade the gains but shifts the amplitude which would be expected.

4. In terms of the gain amplitudes, Cygnus-A is a better calibrator than other of the 3C sources due to it's extreme brightness. As the resolution of MSSS is only $2'$, errors due to an imperfect skymodel should not be severe, however, when going to higher resolutions this could impact results and should be kept in mind.

7.5 Detection of nearby spiral galaxies in the MSSS survey

LOFAR for the first time enables us to conduct a systematic survey of nearby galaxies at moderate resolution and a reasonable S/N ratio at very low frequencies.

Israel and Mahoney (1991) [26] observed that the total fluxes of 68 galaxies at 57.5 MHz are systematically lower when one extrapolates from 1.4 GHz flux measurements assuming a single power law. Israel and Mahoney also reported that the fluxes of galaxies at 57.5 MHz would decrease with increasing declination which they interpreted as increasing free-free absorption caused by a clumpy medium with an electron temperature of $T_s \approx 1000K$ and a electron density of the order of 1cm^{-1}. However, no direct observational evidence (which would be difficult) of such medium exists, even in our own Galaxy. Hummel (1991) [28] performed a reanalysis of the data and did not confirm the correlation with the inclination of the galaxies. It was argued that the observed curved spectra were consistent with electron diffusion models without free-free absorption. The survey carried out by Israel and Mahoney was done with the Clark Lake telescope (Erickson et al. 1982) [2] and had poor resolution of $7'$ as well as poor S/N ratio. Therefore, there is a need for more reliable measurements with greater resolution, which MSSS can deliver.

Even though MSSS has not being finished yet, preliminary work has begun regarding a creation of a sample of 60 galaxies. This sample includes (i) all known galaxies inside a sub-volume bounded by 3.5 Mpc, (ii) an unbiased sample of spiral and irregular galaxies within the 11 Mpc sphere in the Spitzer Local Volume Legacy Survey (LVL, Dale et al (2009)[200]) and (iii) additional interesting galaxies between 11 Mpc and the Virgo Cluster.

Many of these galaxies have been already detected at the time of writing, a sample of these detected galaxies can be in seen in figure 7.6.

While the resolution achieved prohibits detailed study of most galaxies, structures can be seen in several galaxies for example, IC342 and M81, where a spiral arm is visible. This work will be continued with collegues from Krakow, Poland, Bochum University, ASTRON and the MPIfR and will continue most likely for the next 2 years.

7.6 First detections of polarization in the MSSS survey

Detection of polarization with MSSS would enable an all sky survey of the northern sky in polarization at low frequencies for the first time. This would be very exciting as Galactic polarized emission below 200 MHz is poorly understood and their characteristics cannot extrapolated from higher frequencies.

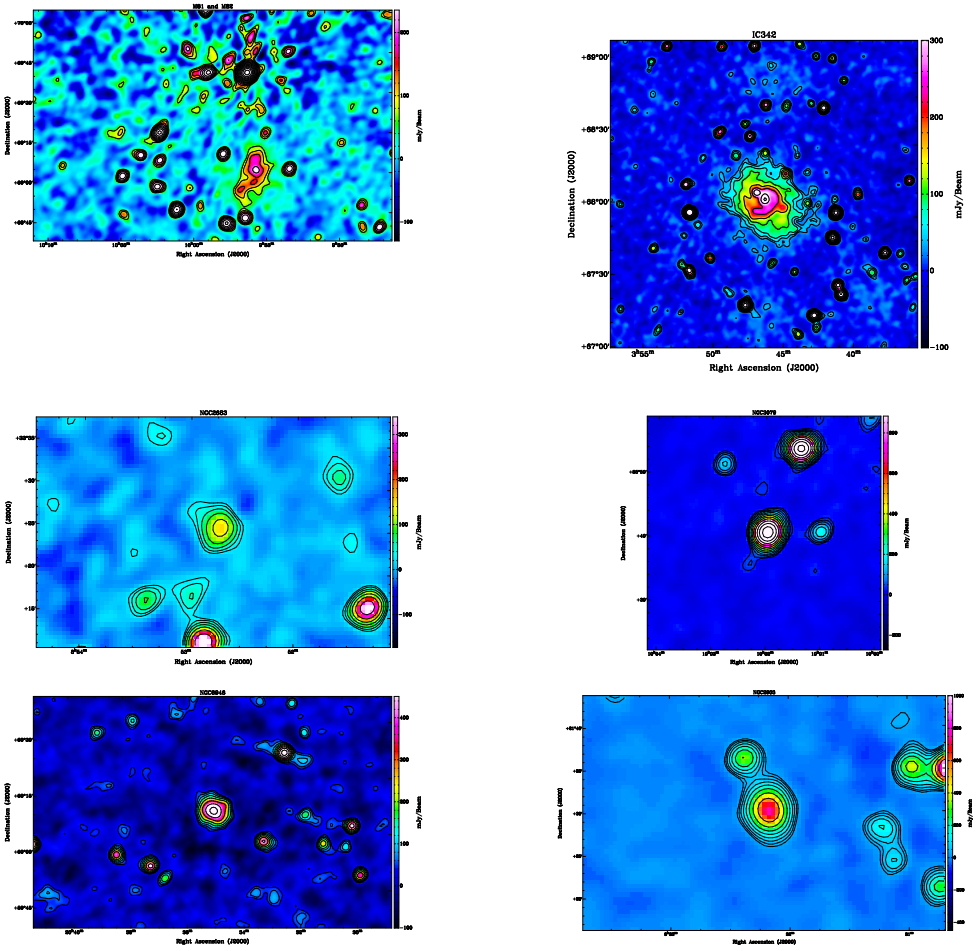

Figure 7.6: A selection of galaxies detected with MSSS HBA, from top left, M81 & M82, IC342, NGC2683, NGC3079, NGC6946 and NGC2903.

Recently Bernardi et al. (2013)[123] with the MWA (Lonsdale et al. 2009)[70] at 189 MHz performed a 2400 square degree polarization survey in the southern sky with 15.6′ resolution and a noise of 15 mJy/beam. This survey resulted in only a single detection out of a catalogue of 137 sources brighter than 4 Jy in total intensity. This means that the remaining sources have polarization fractions of less than 2%. This in comparison to the average value of 7% at 1.4 GHz, meaning that the polarization fraction decreases drastically at low frequencies. Both beam depolarization and internal Faraday dispersion could generate the observed depolarization. Higher resolution observations could improve this.

The scientific value of a polarization survey with MSSS would be invaluable and with greater resolution, better sensitivity and a greater survey area, it would help greatly in furthering our understanding of polarization at low frequencies. In theory, MSSS has excellent Faraday resolution [124, Brentjens & de Bruyn (2005)] of 1.5 rad m^{-2} and a maximum Faraday depth [124, Brentjens & de Bruyn (2005)] of approximately 330 rad m^{-2}. The RMSF from MSSS can be seen in figure 7.7. Until now, no polarization detection had been performed on MSSS. The detection of polarization in MSSS had to be achieved before planning future steps for a polarization survey.

This section shows a definite polarization detection in the Fan region as well as for PSRJ0218+4232

at the correct Faraday Depth. With these results, the MKSP can now plan for the processing of MSSS data for a polarization survey.

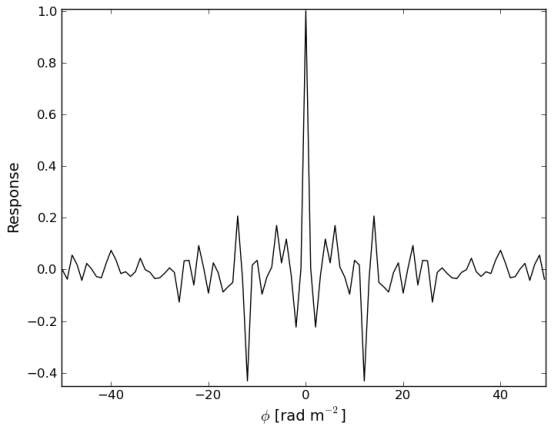

Figure 7.7: The RMSF produced from the frequency coverage of MSSS.

7.6.1 Summary on pipeline for polarization processing

Calibration for the ionspheric Faraday rotation is essential to detect polarization at the correct Faraday depth and therefore an additional pipeline had to be implemented to already calibrated data.This needed to be created in order to detect polarization in MSSS. The outline for this pipeline is as follows:

1. Firstly, all the visibility data from the separate snapshots had to split up into channels, this is 8 bands by 40 channels, resulting in 320 channel CASA Measurement Sets[1] (MS) for each snapshot. Naturally, the CORRECTED-DATA column was copied into new MS's DATA column. This step has to be performed as the current implementation of AWimager (Tasse et al. (2013)) [101] cannot image seperate channels. It is hoped that this functionality will be added in the near future making this step redundant.

2. The RM correction for the ionospheric Faraday rotation was determined using CODE[2] TEC data and was applied to each channel MS with BBS.

3. The snapshots were then concatenated for each channel.

4. Each channel was then imaged in the usual MSSS imaging mode with exceptions, namely, the element beam is switched on to avoid any beam projection depolarization and all Stokes parameters were imaged.

5. Once every channel has been imaged, the images are split into it's Q and U components and converted to FITS files. If a mosaic is been made, there is no need to separate the Stokes parameters.

[1] http://casa.nrao.edu/docs/UserMan/UserMansu82.html
[2] http://aiuws.unibe.ch/ionosphere/

6. George Heald's RM Synthesis and RM Clean software (Heald et al. 2009) [32] was then used to perform RM Synthesis. For RM Clean, the same parameters were always used namely a gain of 0.1, 1000 clean iterations and clean cutoff of 0.01 Jy/beam.

The initial steps of separating and calibrating doesn't take much time, however, the concatenation can take 1-2 hours to concatenate all channels. Unsurprisingly, the imaging takes the largest amount of processing time, approximately 6-7 hours. Overall, it would take 1 day to process a field mosiac (like figure7.10). A diagram of the polarization pipeline can be seen in figure 7.8.

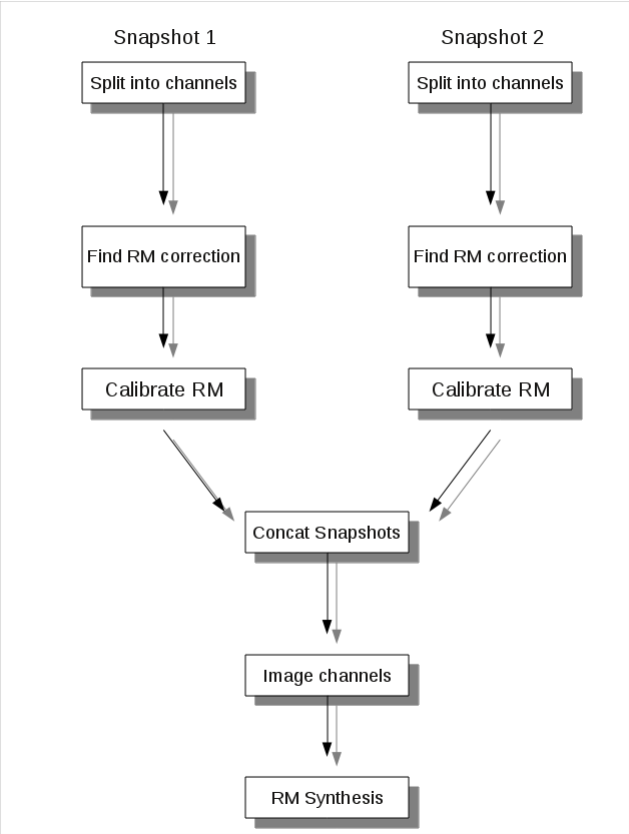

Figure 7.8: The polarization pipeline for one field, note that once AWimager has the capability to image channels, splitting the original Measurement Sets will not be needed. Also RM calibration will only need to be applied to each band rather than each channel. Finally each band could be concatenated rather than each channel further saving time.

7.6.2 Detection of polarized Galactic foreground emission

Processed data of one mosaic (six fields) from the Fan Region was processed for polarization which can be seen in figure 7.10. Each field was processed and imaged separately. Finally each channel image were then made into the six field mosaic. Clear detections of polarized emission can be seen in several slices in the Faraday cube seen in figure 7.11. Several features can be seen which agree with Iacobelli et al. (2013) [85]. These include the ring structure at ϕ = -2 rad m^{-2} which is a local bubble feature at 100pc (Bernardi et al. 2009 [127], Iacobelli et al. 2013 [126]) and the bubble structure at ϕ = -5 rad m^{-2}

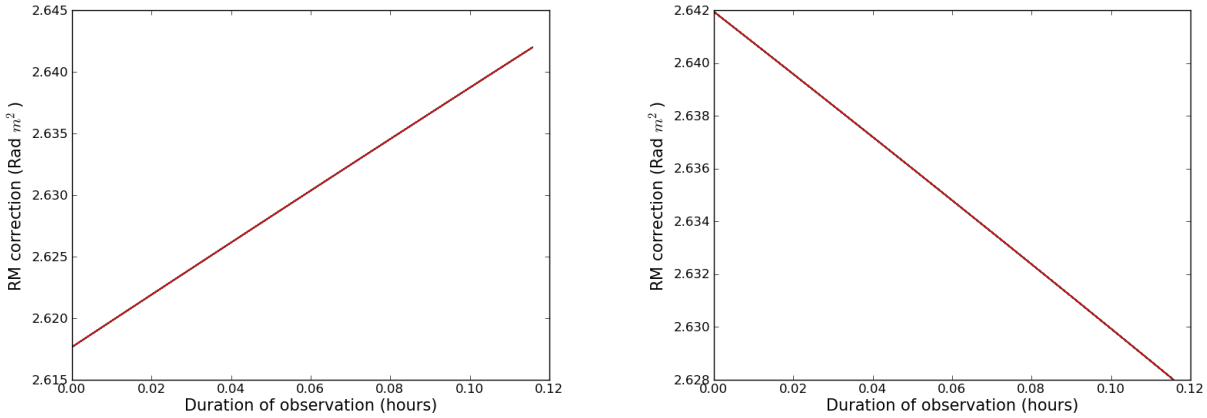

Figure 7.9: The values for the RM correction using CODE TEC data. CODE TEC data is recorded every hour and therefore the resolution is insufficient to see any fluctuations in TEC.

which is nearby relic Stromgren sphere at 200pc. Unfortunately, no confident detection of polarization from an extragalactic source can be seen. Iacobelli et al.(2013) [85] notes that polarization can be seen in both the spiral galaxy IC342 and the giant double-lobe radio galaxy WNB 0313+683. It should be said that the radio galaxy does have an interesting peak in it's southern lobe at ϕ = -9 rad m^{-2}, which would be agreement with Iacobelli et al. (2013) [85], but it is more likely sidelobes of the instrumental response.

From these results, a shallow survey of diffuse Galactic foreground structures is possible and should be planned for.

7.6.3 Detection of PSRJ0218+4232 in polarization

PSRJ0218+4232 is a pulsar with a high degree of polarization with a Faraday depth of ϕ = -61 rad m^{-2} (Navarro et al. 1995) [90] was observed with MSSS and reduced in the normal MSSS pipeline. The processed data was then further processed for polarization. The pulsar is clearly detected at the correct Faraday depth with a polarization degree of 51% as shown in figures 7.12 & 7.13. This shows that MSSS can detect polarization for point sources but more importantly it is at the correct Faraday depth. As an extra test, RM Synthesis software developed by Mike Bell was used and compared to George Heald's software and the dirty Faraday spectrum were seen to be identical, however, MB's completely fails for RM Clean compared to GH's RM Clean software which can be seen in figure 7.14. This effect was also seen for the M51 commission dataset. This was repeated again with a gain of 1 with 1 clean iteration where one would expect the main component to be subtracted, however, this is not seen.

7.6.4 3C208

The field around the double lobed QSO 3C208 was also processed for polarization. In front of this QSO is a known MgII galaxy (Bernet et al. 2013) [201] and the aim was to see if a different polarized components could be seen in the Faraday spectrum. However, no polarization could be detected. Bridle et al (1994) [202] show that both lobes of 3C208 are polarized and therefore at this low resolution could be depolarizing each other. 3C208 is approximately 15 arcsecs across and therefore would need a

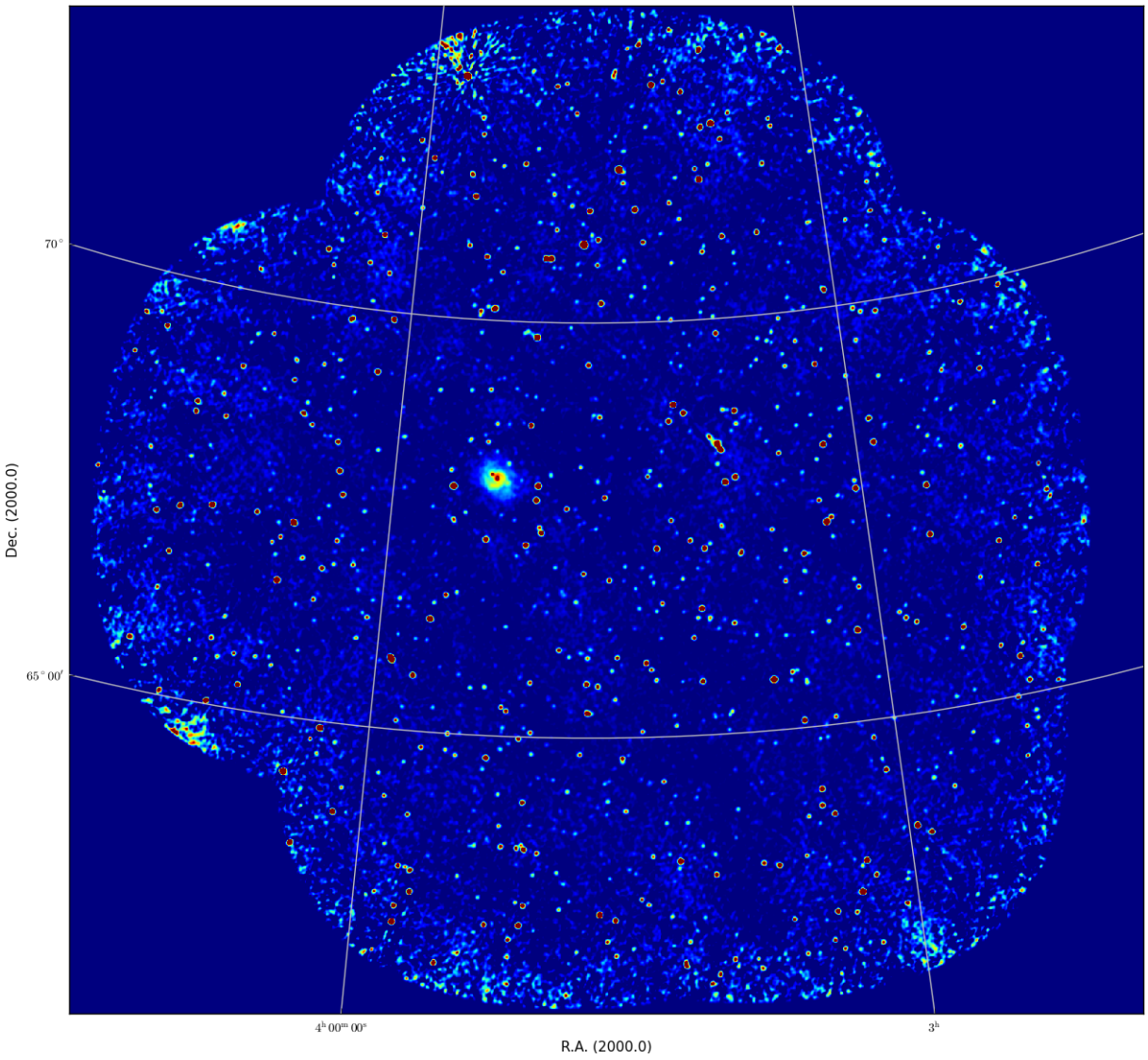

Figure 7.10: The processed data of the FAN region which went through the normal MSSS pipeline. The spiral galaxy IC342 can be easily seen. No self calibration has been performed.

resolution far beyond what MSSS can do to resolve the lobes. Therefore a dedicated observation would be required.

7.7 Summary

The main results and findings from this work include:

1. An initial calibration strategy was devised for the LBA survey which could achieve a noise of 175 mJy/beam. It was also seen that sources from previous catalogues appeared without the need of being specified in the skymodel used. This method of initial calibration was adopted for all LBA observations with more fine tuning.

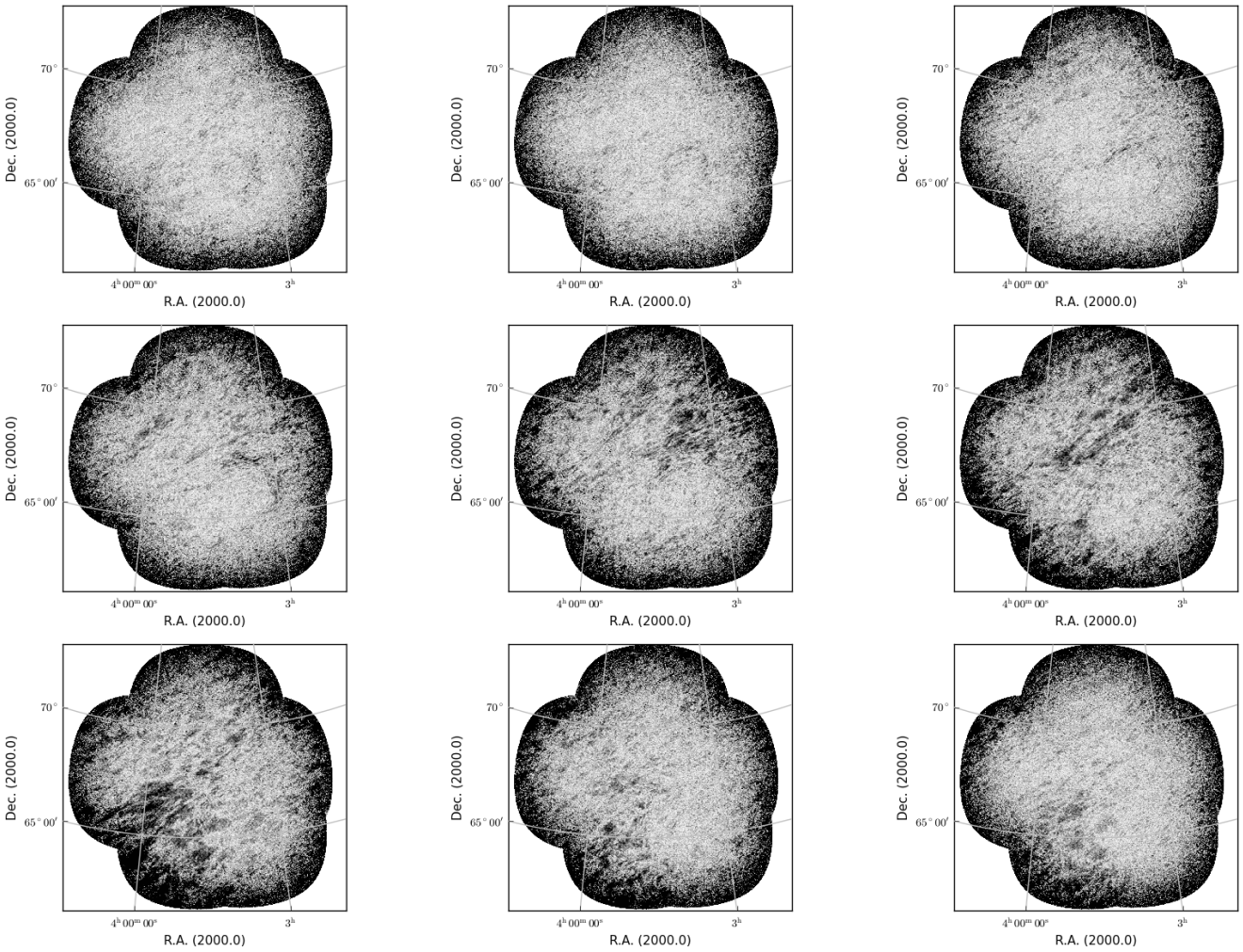

Figure 7.11: Slices of the Faraday Cube from ϕ = -5 rad m^{-2} (upper left) to +4 rad m^{-2} (lower right) in steps on 1 rad m^{-2}. The ring structure can be seen as well the very large scale curtain polarized feature.

2. Directional dependent calibration was tested in an LBA field and was shown to produce much improved images with an increase in overall and local dynamic range. However, it was seen that the integrated flux of IC342 decreases substantially. This is mainly due to an incomplete model of the extended emission and due to vast number of parameters in the calibration process.

3. Cygnus-A was compared to 3C196 and proved to be a better calibrator with the existing skymodel in terms of gains, both in frequency and time.

4. Many nearby galaxies have been detected in the HBA part of the survey as well as IC342 in the LBA part. The spectral analysis of these galaxies will either prove or disprove the findings of Israel & Mahoney (1990)[26] to whether or not a low temperature clumpy medium in galaxies exist.

5. A polarization pipeline was created for MSSS HBA data and through it polarization was detected in the Fan Region matching similar structures seen in previous publications. PSRJ0218+4232

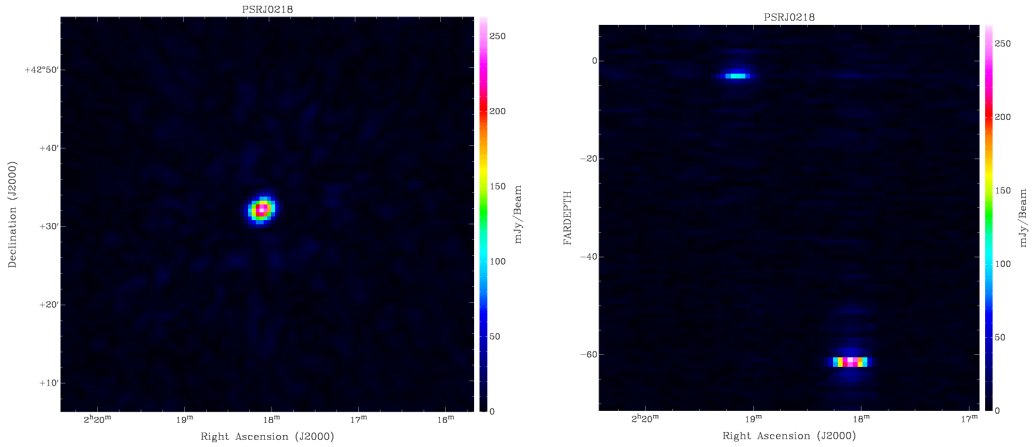

Figure 7.12: Left: A slice taken from the cleaned Faraday cube at -61 rad m^{-2} showing a clear detection of PSRJ0218+4232. Right: This figure shows the same Faraday cube with Faraday depth on the Y-axis and Right Ascension on X-axis at a set declination. PSRJ0218 can be seen again at -61 rad m^{-2} and another source at around -2 rad m^{-2} which is instrumental.

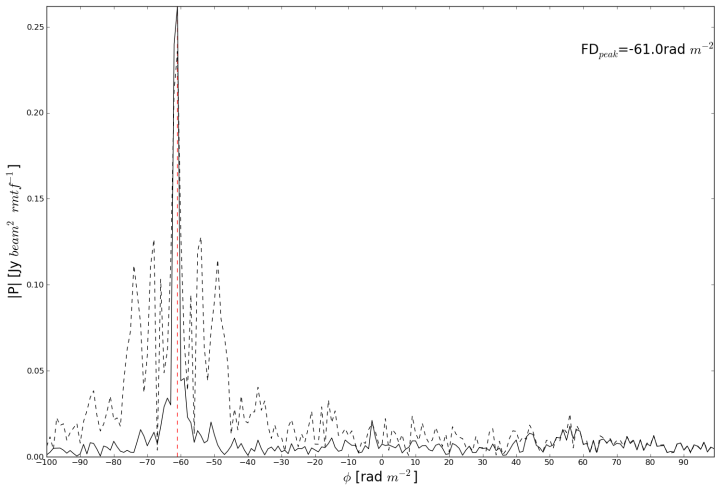

Figure 7.13: Left: The Faraday spectra of PSRJ0218+4232. The dashed line is the dirty Faraday Spectra and the solid line is the cleaned Farday Spectra. As expected the peak is found at -61 rad m^{-2}. A small peak can be seen at -2 rad m^{-2} which is the instrument response. Usually the instrumental response is located at 0 rad m^{-2} but correction for ionspheric Faraday rotation can make it non zero.

was also detected at the correct Faraday depth. This is the first step towards an all polarization sky survey of the northern sky with LOFAR.

6. Finally, it was found that the main RM synthesis software used by the MKSP doesn't work. There are plans that this software will be fixed and usable for data from all instruments.

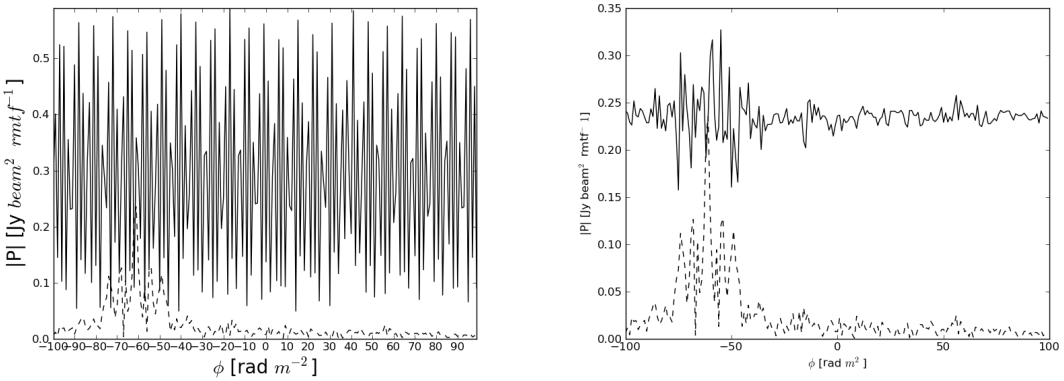

Figure 7.14: Left: A Faraday spectra created with Mike Bell's RM Synthesis code. The dashed line is the dirty Faraday Spectra which is identical to the result produced by George Heald's code. However the solid line shows the cleaned spectrum which is incorrect. The same clean parameters were gain=0.1,niter=1000,cutoff=0.01. Right: Identical to the left figure with the exception of different clean parameters used, namely gain=1, niter=1, cutoff=0.01.

CHAPTER 8

Conclusions & Outlook

We are currently at the cusp of the golden age of radio astronomy with exciting new radio telescopes being currently built including Meerkat, ASKAP and many others, all pathfinders to the Square Kilometre Array. For the low frequency part ($\leq$ 300 MHz) of the SKA, LOFAR (Low Frequency Array) is the critical pathfinder. Low frequency interferometry has been fraught with many difficulties, most importantly, distortion of the receiving signals due to ionospheric fluctuations. As a result, low frequency astronomy is relatively unexplored. With the construction of LOFAR, we are able to finally explore this uncharted region. However, throughout this thesis, LOFAR was still been constructed and commissioned. Therefore considerable commissioning activities needed to be performed.

In these commissioning activities, development of software to interpolate the complex gain solutions in frequency in order to increase the sensitivity of the observation was successfully implemented. This method of calibration is now being used by many users of LOFAR. In addition, studies and tests were performed on directional dependent calibration as well as correction for the ionospheric Faraday rotation of polarized signals.

The main achievement resulting from these commissioning activities are the first images of galaxies observed with LOFAR HBA at arcsec resolution and μJy sensitivity. Never before have nearby galaxies been observed at such low frequencies at such high resolution. We are able for the first time to explore the physical nature of low energy electrons and magnetic fields.

8.1 Observation and modelling of M51 at low frequencies

We observed M51, an interacting face-on spiral galaxy which is ideal to explore the nature and extent of the extended disk and its magnetic field. We were able to detect synchrotron emission in the outer disk out to 16 kpc showing that a significant magnetic field exists at these large distances. The spiral arms of M51 are still observable at 151 MHz but signs of cosmic ray diffusion of low energy cosmic ray electrons are obvious. For example, the wavelet cross correlation between 151 MHz and 70μm is seen to have a significant correlation at scales greater than 1.45 kpc compared to 0.72 kpc for 1.4 GHz and 70μm. This is a measure of the propagation length of cosmic ray electrons that decreases with increasing frequency. The radial scalelengths l were found to have a frequency dependence of $l \propto \nu^{-0.16\pm0.02}$ which is as expected from our diffusion model.

We observed a break in the scale length of the synchrotron emission at 151 MHz at approximately 10 kpc from the center of the galaxy, just beyond the star forming disk of the galaxy (see figure 3.6). The

scale length of the outer disk is found to be two times lower. This break is also observed at 1.4 GHz at the same location but is steeper which is expected due to greater energy losses at higher frequencies. This break makes it much more difficult to detect the extended disk, even at low frequencies. The cause of this break is likely due to the increased prominence of inverse Compton losses from the galaxy's radiation field and the Cosmic Microwave Background as the magnetic field is weaker due to inefficient star formation in the outer disk.

There is found to be no flatting of the spectrum of integrated radio emission for M51. This puts the interpretation from Hummel (1991) [28] & Pohl et al. (1991) [131] less plausible that the break in the integrated spectrum is caused by the energy losses of the CREs and this causes the spectrum to steepen at higher frequencies. Evidence of thermal absorption is seen in localized regions in the center of the galaxy.

These results badly need simulations of the distribution, propagation and energy losses of cosmic ray electrons. While our own Galaxy has been studied extensively with the GALPROP code, external galaxies have been seldomly studied. In order to rectify this, a new code was developed from scratch in order to simulate the diffusion-loss equation for M51. Our simulations are able to reasonably match the observed spectral index in some respects such as the arm and interarm contrast. We showed that with a diffusion coefficient of approximately 7.5×10^{28} cm^2 s^{-1} we can replicate the shape of the spectral index profile of M51.

We find that in order to match observations, we need to take into account the thermal contribution in the central region as well inverse Compton losses from the Cosmic Microwave Background in the outer disk. However, it becomes clear that the equipartition magnetic fields derived from the observations are too weak away from star forming regions. Therefore, this code can help us constrain the magnetic field strength in regions where little star formation is present, ie the extended disk or halo.

While M51 was not detected in linear polarization due to severe depolarization, we were able to find six extragalactic sources in polarization at a resolution of 20″ at a frequency of 151 MHz. This would result in a detection of a polarized source on average for every 2.9 square degrees. This is important information for future polarization surveys at low frequencies and limits the possibility of using RM grids of background polarized sources to probe weak magnetic fields.

8.2 Observation of NGC891 with LOFAR HBA

We also observed the edge on galaxy NGC891, with LOFAR HBA achieving a rms noise of approximately 0.8 mJy/beam at a resolution of 20″. We confirm earlier studies that NGC891 has a significant break in its spectrum of integrated radio emission. The spectral index at high frequencies is very similar to that in M51, while at low frequencies significant indications of thermal absorption are visible. In particular, the northern half and the central region show significant thermal absorption. The thermal absorption in NGC891 is much more widespread compared to M51 and suggests that the path length of the emission is important and thus the inclination of the galaxy.

While we cannot see an extended halo we do see larger scale heights for 151 MHz compared to higher frequencies, thereby suggesting that better sensitivity is needed. NGC891 is different from NGC253 in that only one side of the galaxy shows a constant bulk outflow speed through the anticorrelation of synchrotron scale height and magnetic field and the linearity of the spectral index. The other side of the galaxy does not show similar results. We suggest, through X-ray observations and the spectral index map produced in this work, that outflows from the disk would produce a variety of bulk speeds.

We also detect a new feature not seen at higher frequencies, which is located just above a region of high star formation. We believe this to be an outflow with a stronger magnetic strength due to extreme

steepening of the spectral index at this region.

8.3 Detection of Faraday gradients in the disk of NGC628

The nearly face on galaxy NGC628 was observed with the Effelsberg 100m telescope at 2.6 & 8.35 GHz and the JVLA at 2-4 GHz. With the Effelsberg observations we find that NGC628 is described by a spectral index of $\alpha = -0.78 \pm 0.02$, confirming previous observations. We also see that from these low resolution images that NGC628 possess a striking axisymmetric galactic magnetic field which is is the easiest mode for the $\alpha\omega$-dynamo to produce. We present preliminary images of the D-configuration JVLA of this galaxy and are able to show that NGC628 contains magnetic arms, very similar to NGC6946. We also perform RM synthesis and we can confirm the main component seen in Braun et al. (2010) [55] at a Faraday depth of approximately -40 rad m^{-2}. Excitedly, we detect gradients and reversals in Faraday depth within the disk of NGC628. These gradients could signify the magnetic field being pushed up from the disk into the halo. This is extremely important as this would help to remove small scale magnetic helicity from the disk as the conservation of magnetic helicity can suppress a dynamo. Therefore this would support both mean-field dynamo and 'chimney' theories in one go.

8.4 Multi Frequency All Sky Survey

MSSS (Multi-frequency Snapshot Sky Survey) is the first all sky survey performed by LOFAR, spanning a frequency range of 30-70 MHz for LBA and 120-160 MHz for HBA. During this thesis, several activities were performed which helped complete this survey. This included creating and testing the first draft of the initial calibration cycle for MSSS data, testing the viability of different calibrators including Cygnus-A and testing directional dependent calibration. Most importantly from a cosmic magnetism point of view, linear polarization from the Galactic foreground was detected in the Fan region. Also, polarization was detected from the millisecond pulsar PSRJ0218+4232 at the Faraday depth of -61 rad m^{-2}. These results will enable us to perform an all sky shallow polarization survey at low frequencies for the first time.

8.5 The main findings of this thesis

To summarize this thesis we can see there are three main findings:

Diffusion is the main process of cosmic ray electron propagation in the disk.
We found that the dependence of the inner disk scale length with frequency ($\nu^{-0.16\pm0.02}$) corresponds nearly exactly to the theoretical frequency dependence of the diffusion length ($\nu^{-1/8}$). Our diffusion-loss model of M51 was able to roughly reproduce the features of the radial spectral index and agrees with the integrated spectral index. Also the break scale shown in the FIR-radio correlation has approximately doubled from 1.4 GHz and 151 MHz, again showing the effects of diffusion. Finally we could detect a smoother gradient in the arm interarm contrasts at 151 MHz compared to higher frequencies. All these findings point to the fact that diffusion is the most dominant process of cosmic ray electron propagation in the star forming disk of M51.

The flattening of the integrated spectrum of galaxies at low frequencies is due to thermal absorption.
We have observed no spectral flattening in M51 but confirm a significant flattening in NGC891 which we believe is caused by thermal absorption by classical HII regions. Much more thermal

absorption in the disk is observed in NGC891 from the spectral index maps produced whereas M51 only shows this effect in small regions in the center of the galaxy. Therefore this signifies that the path length becomes important and thus the inclination of the galaxy. The interpretation of the flattening by Pohl et al. (1991) [131] is false due to not including thermal absorption and diffusion in their model. We also discount that the thermal absorption is caused by a low temperature ionized gas component proposed by Israel & Mahoney (1990) [26]. Further observations of galaxies at a range of inclinations is essential to validate this finding. In addition, modelling thermal absorption would be of great benefit.

Detection of diffuse polarization in star forming galaxies at low frequencies is unrealistic.
Finally, the non-detection of polarization of M51 shows us that detection of diffuse polarization in star forming galaxies at low frequencies is unrealistic. If we would have any chance to observe diffuse polarization it should be for a target with significant magnetic fields but little star formation. Also the chance of detecting weak magnetic fields with a RM grid of background polarized sources will also be very difficult due to the insufficient density of polarized sources detected.

Bibliography

[1] T. L. Landecker and R. Wielebinski, "The Galactic Metre Wave Radiation: A two-frequency survey between declinations +25^o and -25^o and the preparation of a map of the whole sky", in: *Australian Journal of Physics Astrophysical Supplement* 16 (1970), p. 1.

[2] W. C. Erickson, M. J. Mahoney, and K. Erb, "The Clark Lake Teepee-Tee telescope", in: *ApJs* 50 (Dec. 1982), pp. 403–419, DOI: 10.1086/190831.

[3] N. E. Kassim et al., "The 74 MHz System on the Very Large Array", in: *ApJs* 172 (Oct. 2007), pp. 686–719, DOI: 10.1086/519022, arXiv: 0704.3088.

[4] A. S. Cohen et al., "The VLA Low-Frequency Sky Survey", in: *The Astronomical Journal* 134 (Sept. 2007), pp. 1245–1262, DOI: 10.1086/520719, arXiv: 0706.1191.

[5] W. M. Lane et al., "VLSS redux: Software improvements applied to the Very Large Array Low-Frequency Sky Survey", in: *Radio Science* 47, RS0K04 (Jan. 2012), DOI: 10.1029/2011RS004941, arXiv: 1205.4695 [astro-ph.IM].

[6] N. E. Kassim et al., "The VLA Low-frequency Sky Survey (VLSS)", in: *American Astronomical Society Meeting Abstracts*, vol. 35, Bulletin of the American Astronomical Society, Dec. 2003, p. 1301.

[7] J. J. Condon et al., "The NRAO VLA Sky Survey", in: *The Astronomical Journal* 115 (May 1998), pp. 1693–1716, DOI: 10.1086/300337.

[8] S. J. Tingay et al., "The Murchison Widefield Array: The Square Kilometre Array Precursor at Low Radio Frequencies", in: *Publications of the Astronomical Society of Australia* 30, e007 (Jan. 2013), p. 7, DOI: 10.1017/pasa.2012.007, arXiv: 1206.6945 [astro-ph.IM].

[9] S. Zaroubi et al., "Imaging neutral hydrogen on large scales during the Epoch of Reionization with LOFAR", in: *MNRAS* 425 (Oct. 2012), pp. 2964–2973, DOI: 10.1111/j.1365-2966.2012.21500.x, arXiv: 1205.3449 [astro-ph.CO].

[10] B. W. Stappers et al., "Observing pulsars and fast transients with LOFAR", in: *A&A* 530, A80 (June 2011), A80, DOI: 10.1051/0004-6361/201116681, arXiv: 1104.1577 [astro-ph.IM].

[11] A. D. Kuzmin and B. Y. Losovsky, "No low-frequency turn-over in the spectra of millisecond pulsars", in: *A&A* 368 (Mar. 2001), pp. 230–238, DOI: 10.1051/0004-6361:20000507.

[12] M. Kramer et al.,
"The Characteristics of Millisecond Pulsar Emission. III. From Low to High Frequencies",
in: *ApJ* 526 (Dec. 1999), pp. 957–975, DOI: 10.1086/308042, eprint: astro-ph/9906442.

[13] A. Noutsos, "The Magnetic Field of the Milky Way from Faraday Rotation of Pulsars and Extragalactic Sources", in: *Space Science Reviews* 166 (May 2012), pp. 307–324,
DOI: 10.1007/s11214-011-9860-2.

[14] A. Asgekar et al.,
"LOFAR detections of low-frequency radio recombination lines towards Cassiopeia A",
in: *A&A* 551, L11 (Mar. 2013), p. L11, DOI: 10.1051/0004-6361/201221001,
arXiv: 1302.3128 [astro-ph.GA].

[15] R. P. Fender et al., "The LOFAR Transients Key Project",
in: *VI Microquasar Workshop: Microquasars and Beyond*, 2006, eprint: astro-ph/0611298.

[16] M. S. Longair, *High Energy Astrophysics*, 2010.

[17] V. Heesen et al., "Cosmic rays and the magnetic field in the nearby starburst galaxy NGC 253. I. The distribution and transport of cosmic rays", in: *A&A* 494 (Feb. 2009), pp. 563–577,
DOI: 10.1051/0004-6361:200810543, arXiv: 0812.0346.

[18] T. A. Thompson et al.,
"Magnetic Fields in Starburst Galaxies and the Origin of the FIR-Radio Correlation",
in: *ApJ* 645 (July 2006), pp. 186–198, DOI: 10.1086/504035, eprint: astro-ph/0601626.

[19] M. C. Begelman, R. D. Blandford, and M. J. Rees, "Theory of extragalactic radio sources",
in: *Reviews of Modern Physics* 56 (Apr. 1984), pp. 255–351,
DOI: 10.1103/RevModPhys.56.255.

[20] B. C. Lacki, "Interpreting the low-frequency radio spectra of starburst galaxies: a pudding of Strömgren spheres", in: *MNRAS* 431 (June 2013), pp. 3003–3024,
DOI: 10.1093/mnras/stt349, arXiv: 1206.7100 [astro-ph.CO].

[21] U. Klein, R. Wielebinski, and H. W. Morsi, "Radio continuum observations of M82",
in: *A&A* 190 (Jan. 1988), pp. 41–46.

[22] B. Adebahr et al., "M 82 - A radio continuum and polarisation study. I. Data reduction and cosmic ray propagation", in: *A&A* 555, A23 (July 2013), A23,
DOI: 10.1051/0004-6361/201220226, arXiv: 1209.5552 [astro-ph.GA].

[23] K. A. Wills et al., "Low-frequency observations of supernova remnants in M82",
in: *MNRAS* 291 (Nov. 1997), p. 517.

[24] G. B. Rybicki and A. P. Lightman, *Radiative processes in astrophysics*, 1979.

[25] R. Schlickeiser, *Cosmic Ray Astrophysics*, 2002.

[26] F. P. Israel and M. J. Mahoney,
"Low-frequency radio continuum evidence for cool ionized gas in normal spiral galaxies",
in: *ApJ* 352 (Mar. 1990), pp. 30–43, DOI: 10.1086/168513.

[27] F. P. Israel, M. J. Mahoney, and N. Howarth, "The integrated radio continuum spectrum of M33 - Evidence for free-free absorption by cool ionized gas",
in: *A&A* 261 (July 1992), pp. 47–56.

[28] E. Hummel, "On the low frequency radio spectrum of spiral galaxies",
in: *A&A* 251 (Nov. 1991), pp. 442–446.

[29] M. Krause, E. Hummel, and R. Beck,
"The magnetic field structures in two nearby spiral galaxies. I - The axisymmetric spiral magnetic field in IC342. II - The bisymmetric spiral magnetic field in M81",
in: *A&A* 217 (June 1989), pp. 4–30.

[30] R. Beck and P. Hoernes, "Magnetic spiral arms in the galaxy NGC6946",
in: *Nature* 379 (Jan. 1996), pp. 47–49, DOI: 10.1038/379047a0.

[31] J. L. Han, R. Beck, and E. M. Berkhuijsen,
"New clues to the magnetic field structure of M 31", in: *A&A* 335 (July 1998), pp. 1117–1123,
eprint: astro-ph/9805023.

[32] G. Heald, R. Braun, and R. Edmonds,
"The Westerbork SINGS survey. II Polarization, Faraday rotation, and magnetic fields",
in: *A&A* 503 (Aug. 2009), pp. 409–435, DOI: 10.1051/0004-6361/200912240,
arXiv: 0905.3995 [astro-ph.GA].

[33] M. Krause, "Magnetic fields and star formation as seen in edge-on galaxies",
in: *ArXiv e-prints* (Nov. 2011), arXiv: 1111.7081 [astro-ph.GA].

[34] M. Dahlem, U. Lisenfeld, and G. Golla, "Star formation activity in spiral galaxy disks and the properties of radio halos: Observational evidence for a direct dependence",
in: *ApJ* 444 (May 1995), pp. 119–128, DOI: 10.1086/175587.

[35] J. Rossa and R.-J. Dettmar,
"An Hα survey aiming at the detection of extraplanar diffuse ionized gas in halos of edge-on spiral galaxies. I. How common are gaseous halos among non-starburst galaxies?",
in: *A&A* 406 (Aug. 2003), pp. 493–503, DOI: 10.1051/0004-6361:20030615,
eprint: astro-ph/0304452.

[36] E. Hummel and R.-J. Dettmar,
"Radio observations and optical photometry of the edge-on spiral galaxy NGC 4631",
in: *A&A* 236 (Sept. 1990), pp. 33–46.

[37] R. Beck et al., "Galactic Magnetism: Recent Developments and Perspectives",
in: *Annual Review of Astronomy and Astrophysics* 34 (1996), pp. 155–206,
DOI: 10.1146/annurev.astro.34.1.155.

[38] M. Krause, "Magnetic Fields and Star Formation in Spiral Galaxies",
in: *Revista Mexicana de Astronomia y Astrofisica Conference Series*, vol. 36,
Revista Mexicana de Astronomia y Astrofisica Conference Series, Aug. 2009, pp. 25–29,
arXiv: 0806.2060.

[39] R. Tüllmann et al., "The thermal and non-thermal gaseous halo of NGC 5775",
in: *A&A* 364 (Dec. 2000), pp. L36–L41, eprint: astro-ph/0010267.

[40] T. de Jong et al.,
"Radio continuum and far-infrared emission from spiral galaxies - A close correlation",
in: *A&A* 147 (June 1985), pp. L6–L9.

[41] J. J. Condon, "Radio emission from normal galaxies",
in: *Annual review of astronomy and astrophysics* 30 (1992), pp. 575–611,
DOI: 10.1146/annurev.aa.30.090192.003043.

[42] R. Beck and G. Golla, "Far-infrared and radio continuum emission of nearby galaxies",
in: *A&A* 191 (Feb. 1988), pp. L9–L12.

[43] F. S. Tabatabaei et al.,
"A multi-scale study of infrared and radio emission from Scd galaxy M 33",
in: *A&A* 466 (May 2007), pp. 509–519, DOI: 10.1051/0004-6361:20066731,
eprint: astro-ph/0701897.

[44] M. Harwit and F. Pacini, "Infrared galaxies - Evolutionary stages of massive star formation",
in: *ApJL* 200 (Sept. 1975), pp. L127–L129, DOI: 10.1086/181913.

[45] E. J. Murphy et al., "An Initial Look at the Far-Infrared-Radio Correlation within Nearby Star-forming Galaxies Using the Spitzer Space Telescope",
in: *ApJ* 638 (Feb. 2006), pp. 157–175, DOI: 10.1086/498636, eprint: astro-ph/0510227.

[46] F. S. Tabatabaei et al., "Multi-scale radio-infrared correlations in M 31 and M 33: The role of magnetic fields and star formation", in: *A&A* 557, A129 (Sept. 2013), A129,
DOI: 10.1051/0004-6361/201218909, arXiv: 1307.6253 [astro-ph.GA].

[47] E. Le Roux, "Étude théorique du rayonnement synchrotron des radiosources",
in: *Annales d'Astrophysique* 24 (Feb. 1961), p. 71.

[48] R. Beck, "Magnetism in the spiral galaxy NGC 6946: magnetic arms, depolarization rings, dynamo modes, and helical fields", in: *A&A* 470 (Aug. 2007), pp. 539–556,
DOI: 10.1051/0004-6361:20066988, arXiv: 0705.4163.

[49] B. J. Burn, "On the depolarization of discrete radio sources by Faraday dispersion",
in: *MNRAS* 133 (1966), p. 67.

[50] T. G. Arshakian and R. Beck, "Optimum frequency band for radio polarization observations",
in: *MNRAS* 418 (Dec. 2011), pp. 2336–2342, DOI: 10.1111/j.1365-2966.2011.19623.x.

[51] R. J. Rand and A. G. Lyne,
"New Rotation Measures of Distant Pulsars in the Inner Galaxy and Magnetic Field Reversals",
in: *MNRAS* 268 (May 1994), p. 497.

[52] P. Frick et al., "Faraday rotation measure synthesis for magnetic fields of galaxies",
in: *MNRAS* 414 (July 2011), pp. 2540–2549, DOI: 10.1111/j.1365-2966.2011.18571.x,
arXiv: 1102.4316 [astro-ph.GA].

[53] R. Beck et al., "Recognizing magnetic structures by present and future radio telescopes with Faraday rotation measure synthesis", in: *A&A* 543, A113 (July 2012), A113,
DOI: 10.1051/0004-6361/201219094, arXiv: 1204.5694 [astro-ph.IM].

[54] M. R. Bell and T. A. Enßlin,
"Faraday synthesis. The synergy of aperture and rotation measure synthesis",
in: *A&A* 540, A80 (Apr. 2012), A80, DOI: 10.1051/0004-6361/201118672,
arXiv: 1112.4175 [astro-ph.IM].

[55] R. Braun, G. Heald, and R. Beck,
"The Westerbork SINGS survey. III. Global magnetic field topology",
in: *A&A* 514, A42 (May 2010), A42, DOI: 10.1051/0004-6361/200913375,
arXiv: 1002.1776 [astro-ph.CO].

[56] J. P. Hamaker, J. D. Bregman, and R. J. Sault,
"Understanding radio polarimetry. I. Mathematical foundations.",
in: *A&As* 117 (May 1996), pp. 137–147.

[57] R. J. Sault, J. P. Hamaker, and J. D. Bregman,
"Understanding radio polarimetry. II. Instrumental calibration of an interferometer array.",
in: *A&As* 117 (May 1996), pp. 149–159.

[58] O. M. Smirnov,
"Revisiting the radio interferometer measurement equation. I. A full-sky Jones formalism",
in: *A&A* 527, A106 (Mar. 2011), A106, DOI: 10.1051/0004-6361/201016082,
arXiv: 1101.1764 [astro-ph.IM].

[59] O. M. Smirnov, "Revisiting the radio interferometer measurement equation. II. Calibration and direction-dependent effects", in: *A&A* 527, A107 (Mar. 2011), A107,
DOI: 10.1051/0004-6361/201116434, arXiv: 1101.1765 [astro-ph.IM].

[60] H. T. Intema et al., "Ionospheric calibration of low frequency radio interferometric observations using the peeling scheme. I. Method description and first results",
in: *A&A* 501 (July 2009), pp. 1185–1205, DOI: 10.1051/0004-6361/200811094,
arXiv: 0904.3975 [astro-ph.IM].

[61] C. J. Lonsdale, "Configuration Considerations for Low Frequency Arrays",
in: *From Clark Lake to the Long Wavelength Array: Bill Erickson's Radio Science*,
ed. by N. Kassim et al., vol. 345, Astronomical Society of the Pacific Conference Series,
Dec. 2005, p. 399.

[62] S. Wijnholds et al., "Calibration challenges for future radio telescopes",
in: *IEEE Signal Processing Magazine* 27 (Jan. 2010), pp. 30–42,
DOI: 10.1109/MSP.2009.934853, arXiv: 1004.0156 [astro-ph.IM].

[63] J. W. Baars et al., "The absolute spectrum of CAS A - an accurate flux density scale and a set of secondary calibrators", in: *A&A* 61 (Oct. 1977), pp. 99–106.

[64] N. Rees, "A deep 38-MHz radio survey of the area delta greater than + 60 degrees",
in: *MNRAS* 244 (May 1990), pp. 233–246.

[65] R. S. Roger, C. H. Costain, and A. H. Bridle,
"The low-frequency spectra of nonthermal radio sources",
in: *The Astronomical Journal* 78 (Dec. 1973), p. 1030, DOI: 10.1086/111506.

[66] A. M. Scaife and G. H. Heald, "A broad-band flux scale for low-frequency radio telescopes",
in: *MNRAS* 423 (June 2012), pp. L30–L34, DOI: 10.1111/j.1745-3933.2012.01251.x,
arXiv: 1203.0977 [astro-ph.IM].

[67] K. I. Kellermann, I. I. Pauliny-Toth, and P. J. Williams,
"The Spectra of Radio Sources in the Revised 3c Catalogue", in: *ApJ* 157 (July 1969), p. 1,
DOI: 10.1086/150046.

[68] M. P. van Haarlem et al., "LOFAR: The LOw-Frequency ARray",
in: *A&A* 556, A2 (Aug. 2013), A2, DOI: 10.1051/0004-6361/201220873,
arXiv: 1305.3550 [astro-ph.IM].

[69] S. W. Ellingson et al., "The LWA1 Radio Telescope",
in: *IEEE Transactions on Antennas and Propagation* 61 (May 2013), pp. 2540–2549,
DOI: 10.1109/TAP.2013.2242826, arXiv: 1204.4816 [astro-ph.IM].

[70] C. J. Lonsdale et al., "The Murchison Widefield Array: Design Overview",
in: *IEEE Proceedings* 97 (Aug. 2009), pp. 1497–1506, DOI: 10.1109/JPROC.2009.2017564,
arXiv: 0903.1828 [astro-ph.IM].

[71] A. R. Offringa et al., "The LOFAR radio environment", in: *A&A* 549, A11 (Jan. 2013), A11, DOI: 10.1051/0004-6361/201220293, arXiv: 1210.0393 [astro-ph.IM].

[72] A. R. Offringa, J. J. van de Gronde, and J. B. M. Roerdink, "A morphological algorithm for improving radio-frequency interference detection", in: *A&A* 539, A95 (Mar. 2012), A95, DOI: 10.1051/0004-6361/201118497, arXiv: 1201.3364 [astro-ph.IM].

[73] A. R. Offringa et al., "A LOFAR RFI detection pipeline and its first results", in: *ArXiv e-prints* (July 2010), arXiv: 1007.2089 [astro-ph.IM].

[74] S. van der Tol, B. D. Jeffs, and A.-J. van der Veen, "Self-Calibration for the LOFAR Radio Astronomical Array", in: *IEEE Transactions on Signal Processing* 55 (Sept. 2007), pp. 4497–4510, DOI: 10.1109/TSP.2007.896243.

[75] V. N. Pandey et al., "Calibrating LOFAR using the Black Board Selfcal System", in: *The Low-Frequency Radio Universe*, ed. by D. J. Saikia et al., vol. 407, Astronomical Society of the Pacific Conference Series, Sept. 2009, p. 384.

[76] R. B. Rengelink et al., "The Westerbork Northern Sky Survey (WENSS), I. A 570 square degree Mini-Survey around the North Ecliptic Pole", in: *A&As* 124 (Aug. 1997), pp. 259–280, DOI: 10.1051/aas:1997358.

[77] T. J. Cornwell, "Multiscale CLEAN Deconvolution of Radio Synthesis Images", in: *IEEE Journal of Selected Topics in Signal Processing* 2 (Nov. 2008), pp. 793–801, DOI: 10.1109/JSTSP.2008.2006388.

[78] S. Bhatnagar et al., "Correcting direction-dependent gains in the deconvolution of radio interferometric images", in: *A&A* 487 (Aug. 2008), pp. 419–429, DOI: 10.1051/0004-6361:20079284, arXiv: 0805.0834.

[79] J. M. Silverman, A. V. Filippenko, and S. B. Cenko, "PTF Discovery of a Type II Supernova in M51", in: *The Astronomer's Telegram* 3398 (June 2011), p. 1.

[80] I. Arcavi et al., "SN 2011dh: Discovery of a Type IIb Supernova from a Compact Progenitor in the Nearby Galaxy M51", in: *ApJl* 742, L18 (Dec. 2011), p. L18, DOI: 10.1088/2041-8205/742/2/L18, arXiv: 1106.3551 [astro-ph.CO].

[81] A. Basu et al., "GMRT 333-MHz observations of six nearby normal galaxies", in: *MNRAS* 419 (Jan. 2012), pp. 1136–1152, DOI: 10.1111/j.1365-2966.2011.19764.x, arXiv: 1109.0369 [astro-ph.GA].

[82] R. Gießübel et al., "Polarized synchrotron radiation from the Andromeda galaxy M 31 and background sources at 350 MHz", in: *A&A* 559, A27 (Nov. 2013), A27, DOI: 10.1051/0004-6361/201321765, arXiv: 1309.2539 [astro-ph.CO].

[83] A. G. de Bruyn et al., "Radio polarization and RM structure at high Galactic latitudes", in: *Astronomische Nachrichten* 327 (June 2006), pp. 487–490, DOI: 10.1002/asna.200610566.

[84] A. G. de Bruyn and M. A. Brentjens,
"Diffuse polarized emission associated with the Perseus cluster",
in: *A&A* 441 (Oct. 2005), pp. 931–947, DOI: 10.1051/0004-6361:20052992,
eprint: astro-ph/0507351.

[85] M. Iacobelli, M. Haverkorn, and P. Katgert, "Rotation measure synthesis at the 2 m wavelength of the FAN region: unveiling screens and bubbles", in: *A&A* 549, A56 (Jan. 2013), A56, DOI: 10.1051/0004-6361/201220175, arXiv: 1210.6801 [astro-ph.GA].

[86] R. N. Manchester et al., "ATNF Pulsar Catalog (Manchester+, 2005)",
in: *VizieR Online Data Catalog* 7245 (Aug. 2005),

[87] M. A. Brentjens, "Deep Westerbork observations of Abell 2256 at 350 MHz",
in: *A&A* 489 (Oct. 2008), pp. 69–83, DOI: 10.1051/0004-6361:20077174,
arXiv: 0807.4467.

[88] R. F. Pizzo et al.,
"Deep multi-frequency rotation measure tomography of the galaxy cluster A2255",
in: *A&A* 525, A104 (Jan. 2011), A104, DOI: 10.1051/0004-6361/201014158,
arXiv: 1008.3530 [astro-ph.CO].

[89] C. Sotomayor-Beltran et al., "Calibrating high-precision Faraday rotation measurements for LOFAR and the next generation of low-frequency radio telescopes",
in: *A&A* 552, A58 (Apr. 2013), A58, DOI: 10.1051/0004-6361/201220728,
arXiv: 1303.6230 [astro-ph.IM].

[90] J. Navarro et al., "A Very Luminous Binary Millisecond Pulsar",
in: *ApJl* 455 (Dec. 1995), p. L55, DOI: 10.1086/309816.

[91] C. L. Dobbs et al., "Simulations of the grand design galaxy M51: a case study for analysing tidally induced spiral structure", in: *MNRAS* 403 (Apr. 2010), pp. 625–645,
DOI: 10.1111/j.1365-2966.2009.16161.x, arXiv: 0912.1201 [astro-ph.GA].

[92] D. S. Mathewson, P. C. van der Kruit, and W. N. Brouw,
"A High Resolution Radio Continuum Survey of M51 and NGC 5195 at 1415 MHz",
in: *A&A* 17 (Mar. 1972), p. 468.

[93] A. Fletcher et al., "Magnetic fields and spiral arms in the galaxy M51",
in: *MNRAS* 412 (Apr. 2011), pp. 2396–2416, DOI: 10.1111/j.1365-2966.2010.18065.x,
arXiv: 1001.5230 [astro-ph.CO].

[94] C. Horellou et al., "Faraday effects in the spiral galaxy M 51",
in: *A&A* 265 (Nov. 1992), pp. 417–428.

[95] A. Segalovitz, "High resolution observations of M 51 at 21 and 49 CM",
in: *A&A* 54 (Feb. 1977), pp. 703–711.

[96] M. D. Thornley, J. Braine, and E. Gardan, "Infrared Dust Emission in the Outer Disk of M51",
in: *ApJl* 651 (Nov. 2006), pp. L101–L105, DOI: 10.1086/509719,
eprint: arXiv:astro-ph/0610256.

[97] J. Braine and F. Herpin,
"Molecular hydrogen beyond the optical edge of an isolated spiral galaxy",
in: *Nature* 432 (Nov. 2004), pp. 369–371, DOI: 10.1038/nature03054,
eprint: astro-ph/0412283.

[98] F. Bigiel et al., "Extremely Inefficient Star Formation in the Outer Disks of Nearby Galaxies", in: *The Astronomical Journa* 140 (Nov. 2010), pp. 1194–1213, DOI: 10.1088/0004-6256/140/5/1194, arXiv: 1007.3498 [astro-ph.CO].

[99] J. A. Sellwood and S. A. Balbus, "Differential Rotation and Turbulence in Extended H I Disks", in: *ApJ* 511 (Feb. 1999), pp. 660–665, DOI: 10.1086/306728, eprint: astro-ph/9806307.

[100] G. Heald et al., "Progress with the LOFAR Imaging Pipeline", in: *ArXiv e-prints* (Aug. 2010), arXiv: 1008.4693 [astro-ph.IM].

[101] C. Tasse et al., "Applying full polarization A-Projection to very wide field of view instruments: An imager for LOFAR", in: *A&A* 553, A105 (May 2013), A105, DOI: 10.1051/0004-6361/201220882, arXiv: 1212.6178 [astro-ph.IM].

[102] T. J. Cornwell, K. Golap, and S. Bhatnagar, "W Projection: A New Algorithm for Wide Field Imaging with Radio Synthesis Arrays", in: *Astronomical Data Analysis Software and Systems XIV*, ed. by P. Shopbell, M. Britton, and R. Ebert, vol. 347, Astronomical Society of the Pacific Conference Series, Dec. 2005, p. 86.

[103] C. C. Finlay et al., "International Geomagnetic Reference Field: the eleventh generation", in: *Geophysical Journal International* 183 (Dec. 2010), pp. 1216–1230, DOI: 10.1111/j.1365-246X.2010.04804.x.

[104] G. Dumas et al., "The Local Radio-IR Relation in M51", in: *ApJ* 141, 41 (Feb. 2011), p. 41, DOI: 10.1088/0004-6256/141/2/41, arXiv: 1012.0212 [astro-ph.CO].

[105] U. Klein, R. Wielebinski, and R. Beck, "High frequency radio continuum investigation of M51", in: *A&A* 135 (June 1984), pp. 213–224.

[106] U. Klein and D. T. Emerson, "A Survey of the Distributions of 2.8-CM Radio Continuum in Nearby Galaxies - Part One - Observations of 16 Spiral", in: *A&A* 94 (Jan. 1981), p. 29.

[107] I. M. Gioia and L. Gregorini, "Radio observations of a complete sample of spiral galaxies at 408 MHz", in: *A&As* 41 (Sept. 1980), pp. 329–334.

[108] J. R. C. Kennicutt et al., "Star Formation in NGC 5194 (M51a). II. The Spatially Resolved Star Formation Law", in: *ApJ* 671 (Dec. 2007), pp. 333–348, DOI: 10.1086/522300, arXiv: 0708.0922.

[109] F. S. Tabatabaei, M. Krause, and R. Beck, "High-resolution radio continuum survey of M 33. I. The radio maps", in: *A&A* 472 (Sept. 2007), pp. 785–796, DOI: 10.1051/0004-6361:20077461, arXiv: 0706.0261.

[110] K. F. Schuster et al., "A complete ^{12}CO 2-1 map of M 51 with HERA. I. Radial averages of CO, H I, and radio continuum", in: *A&A* 461 (Jan. 2007), pp. 143–151, DOI: 10.1051/0004-6361:20065579, eprint: astro-ph/0609670.

[111] R. Kothes et al., "A catalogue of Galactic supernova remnants from the Canadian Galactic plane survey. I. Flux densities, spectra, and polarization characteristics", in: *A&A* 457 (Oct. 2006), pp. 1081–1093, DOI: 10.1051/0004-6361:20065062.

[112] D. A. Green, "A revised Galactic supernova remnant catalogue",
in: *Bulletin of the Astronomical Society of India* 37 (Mar. 2009), pp. 45–61,
arXiv: 0905.3699 [astro-ph.HE].

[113] N. Z. Scoville et al.,
"High-Mass, OB Star Formation in M51: Hubble Space Telescope Hα and Paα Imaging",
in: *The Astronomical Journal* 122 (Dec. 2001), pp. 3017–3045, DOI: 10.1086/323445,
eprint: astro-ph/0108248.

[114] B. Greenawalt et al., "Diffuse Ionized Gas in M51/NGC 5195 and M81",
in: *ApJ* 506 (Oct. 1998), pp. 135–151, DOI: 10.1086/306232.

[115] R. Beck and M. Krause, "Revised equipartition and minimum energy formula for magnetic field strength estimates from radio synchrotron observations",
in: *Astronomische Nachrichten* 326 (July 2005), pp. 414–427,
DOI: 10.1002/asna.200510366, eprint: astro-ph/0507367.

[116] M. Pohl and R. Schlickeiser,
"Implications of the unification of cosmic ray transport and Galactic wind models",
in: *A&A* 239 (Nov. 1990), pp. 424–436.

[117] I. V. Moskalenko and A. W. Strong,
"Production and Propagation of Cosmic-Ray Positrons and Electrons",
in: *ApJ* 493 (Jan. 1998), p. 694, DOI: 10.1086/305152, eprint: astro-ph/9710124.

[118] P. Frick et al., "Scaling and correlation analysis of galactic images",
in: *MNRAS* 327 (Nov. 2001), pp. 1145–1157, DOI: 10.1046/j.1365-8711.2001.04812.x,
eprint: astro-ph/0109017.

[119] A. Basu, S. Roy, and D. Mitra,
"Low-frequency Radio-FIR Correlation in Normal Galaxies at ˜1 kpc Scales",
in: *ApJ* 756, 141 (Sept. 2012), p. 141, DOI: 10.1088/0004-637X/756/2/141,
arXiv: 1207.2555 [astro-ph.GA].

[120] G. H. Rieke et al., "The Multiband Imaging Photometer for Spitzer (MIPS)",
in: *ApJs* 154 (Sept. 2004), pp. 25–29, DOI: 10.1086/422717.

[121] J. L. Hinz et al., "Energy Sources of the Far-Infrared Emission of M33",
in: *ApJs* 154 (Sept. 2004), pp. 259–265, DOI: 10.1086/422558.

[122] D. H. M. Schnitzeler, P. Katgert, and A. G. de Bruyn, "WSRT Faraday tomography of the Galactic ISM at λ ˜ 0.86 m. I. The GEMINI data set at (l, b) = (181deg, 20deg)",
in: *A&A* 494 (Feb. 2009), pp. 611–622, DOI: 10.1051/0004-6361:20078912,
arXiv: 0810.4211.

[123] G. Bernardi et al., "A 189 MHz, 2400 deg^2 Polarization Survey with the Murchison Widefield Array 32-element Prototype", in: *ApJ* 771, 105 (July 2013), p. 105,
DOI: 10.1088/0004-637X/771/2/105, arXiv: 1305.6047 [astro-ph.CO].

[124] M. A. Brentjens and A. G. de Bruyn, "Faraday rotation measure synthesis",
in: *A&A* 441 (Oct. 2005), pp. 1217–1228, DOI: 10.1051/0004-6361:20052990,
eprint: astro-ph/0507349.

[125] J. S. Farnes, D. A. Green, and N. G. Kantharia,
"Probing Magnetic Fields using the Giant Metrewave Radio Telescope",
in: *ArXiv e-prints* (Sept. 2013), arXiv: 1309.4646 [astro-ph.IM].

[126] M. Iacobelli et al., "Studying Galactic interstellar turbulence through fluctuations in synchrotron emission. First LOFAR Galactic foreground detection", in: *A&A* 558, A72 (Oct. 2013), A72, DOI: 10.1051/0004-6361/201322013, arXiv: 1308.2804 [astro-ph.GA].

[127] G. Bernardi et al., "Foregrounds for observations of the cosmological 21 cm line. I. First Westerbork measurements of Galactic emission at 150 MHz in a low latitude field", in: *A&A* 500 (June 2009), pp. 965–979, DOI: 10.1051/0004-6361/200911627, arXiv: 0904.0404 [astro-ph.CO].

[128] R. J. Sault, P. J. Teuben, and M. C. Wright, "A Retrospective View of MIRIAD", in: *Astronomical Data Analysis Software and Systems IV*, ed. by R. A. Shaw, H. E. Payne, and J. J. Hayes, vol. 77, Astronomical Society of the Pacific Conference Series, 1995, p. 433, eprint: arXiv:astro-ph/0612759.

[129] A. R. Taylor, J. M. Stil, and C. Sunstrum, "A Rotation Measure Image of the Sky", in: *ApJ* 702 (Sept. 2009), pp. 1230–1236, DOI: 10.1088/0004-637X/702/2/1230.

[130] S. T. Garrington et al., "A systematic asymmetry in the polarization properties of double radio sources with one jet", in: *Nature* 331 (Jan. 1988), pp. 147–149, DOI: 10.1038/331147a0.

[131] M. Pohl, R. Schlickeiser, and E. Hummel, "A statistical analysis of cosmic ray propagation effects on the low frequency radio spectrum of spiral galaxies", in: *A&A* 250 (Oct. 1991), pp. 302–311.

[132] F. Walter et al., "THINGS: The H I Nearby Galaxy Survey", in: *The Astronomical Journal* 136, 2563 (Dec. 2008), pp. 2563–2647, DOI: 10.1088/0004-6256/136/6/2563, arXiv: 0810.2125.

[133] S. P. Reynolds, B. M. Gaensler, and F. Bocchino, "Magnetic Fields in Supernova Remnants and Pulsar-Wind Nebulae", in: *Space Science Reviews* 166 (May 2012), pp. 231–261, DOI: 10.1007/s11214-011-9775-y, arXiv: 1104.4047 [astro-ph.GA].

[134] A. W. Strong, I. V. Moskalenko, and V. S. Ptuskin, "Cosmic-Ray Propagation and Interactions in the Galaxy", in: *Annual Review of Nuclear and Particle Science* 57 (Nov. 2007), pp. 285–327, DOI: 10.1146/annurev.nucl.57.090506.123011, eprint: astro-ph/0701517.

[135] V. A. Dogiel and D. Breitschwerdt, "Cosmic Rays in the Disk and Halo of Galaxies", in: *EAS Publications Series*, ed. by M. A. de Avillez, vol. 56, EAS Publications Series, Sept. 2012, pp. 61–71, DOI: 10.1051/eas/1256007.

[136] A. Segalovitz, "The spectral index distribution of M51", in: *A&A* 61 (Oct. 1977), pp. 59–67.

[137] A. W. Strong and I. V. Moskalenko, "Propagation of Cosmic-Ray Nucleons in the Galaxy", in: *ApJ* 509 (Dec. 1998), pp. 212–228, DOI: 10.1086/306470, eprint: astro-ph/9807150.

[138] B. C. Lacki, T. A. Thompson, and E. Quataert, "The Physics of the Far-infrared-Radio Correlation. I. Calorimetry, Conspiracy, and Implications", in: *ApJ* 717 (July 2010), pp. 1–28, DOI: 10.1088/0004-637X/717/1/1, arXiv: 0907.4161 [astro-ph.CO].

[139] E. E. Salpeter, "The Luminosity Function and Stellar Evolution.", in: *ApJ* 121 (Jan. 1955), p. 161, DOI: 10.1086/145971.

[140] F. S. Tabatabaei et al.,
"High-resolution radio continuum survey of M 33. II. Thermal and nonthermal emission",
in: *A&A* 475 (Nov. 2007), pp. 133–143, DOI: 10.1051/0004-6361:20078174,
arXiv: 0708.2484.

[141] D. Breitschwerdt, J. F. McKenzie, and H. J. Voelk,
"Galactic winds. I - Cosmic ray and wave-driven winds from the Galaxy",
in: *A&A* 245 (May 1991), pp. 79–98.

[142] P. R. Shapiro and G. B. Field,
"Consequences of a New Hot Component of the Interstellar Medium",
in: *ApJ* 205 (May 1976), pp. 762–765, DOI: 10.1086/154332.

[143] C. A. Norman and S. Ikeuchi,
"The disk-halo connection and the nature of the interstellar medium", in: *The Outer Galaxy*,
ed. by L. Blitz and F. J. Lockman, vol. 306, Lecture Notes in Physics, Berlin Springer Verlag,
Jan. 1988, p. 155.

[144] R. Kulsrud and W. P. Pearce,
"The Effect of Wave-Particle Interactions on the Propagation of Cosmic Rays",
in: *ApJ* 156 (May 1969), p. 445, DOI: 10.1086/149981.

[145] K. Buffie, V. Heesen, and A. Shalchi, "Theoretical Explanation of the Cosmic-Ray
Perpendicular Diffusion Coefficient in the Nearby Starburst Galaxy NGC 253",
in: *ApJ* 764, 37 (Feb. 2013), p. 37, DOI: 10.1088/0004-637X/764/1/37,
arXiv: 1212.5721 [astro-ph.GA].

[146] R. D. Ekers and R. Sancisi, "The radio continuum halo in NGC 4631",
in: *A&A* 54 (Feb. 1977), p. 973.

[147] I. Lerche and R. Schlickeiser,
"On the transport and propagation of relativistic electrons in galaxies",
in: *ApJs* 47 (Sept. 1981), pp. 33–85, DOI: 10.1086/190751.

[148] I. Lerche and R. Schlickeiser, "On the transport and propagation of relativistic electrons in
galaxies The effect of adiabatic deceleration in a galactic wind for the steady state case",
in: *A&A* 107 (Mar. 1982), pp. 148–160.

[149] G. de Vaucouleurs et al.,
Third Reference Catalogue of Bright Galaxies. Volume I: Explanations and references. Volume II: Data for galaxies between 0^h and 12^h. Volume III: Data for galaxies between 12^h and 24^h.
1991.

[150] P. C. van der Kruit and L. Searle, "Surface Photometry of Edge-On Spiral Galaxies. II - the
Distribution of Light and Colour in the Disk and Spheroid of NGC891",
in: *A&A* 95 (Feb. 1981), p. 116.

[151] M. P. Rupen, "Neutral hydrogen observations of NGC 4565 and NGC 891",
in: *The Astronomical Journal* 102 (July 1991), pp. 48–106, DOI: 10.1086/115858.

[152] N. Z. Scoville et al., "The scale height and radial distribution of molecular gas in NGC 891",
in: *ApJl* 404 (Feb. 1993), pp. L59–L62, DOI: 10.1086/186743.

[153] T. Oosterloo, F. Fraternali, and R. Sancisi, "The Cold Gaseous Halo of NGC 891",
in: *The Astronomical Journal* 134 (Sept. 2007), p. 1019, DOI: 10.1086/520332,
arXiv: 0705.4034.

[154] R. J. Rand, S. R. Kulkarni, and J. J. Hester,
"The distribution of warm ionized gas in NGC 891", in: *ApJl* 352 (Mar. 1990), pp. L1–L4, DOI: 10.1086/185679.

[155] R.-J. Dettmar, "The distribution of the diffuse ionized interstellar medium perpendicular to the disk of the edge-on galaxy NGC 891", in: *A&A* 232 (June 1990), pp. L15–L18.

[156] J. C. Howk and B. D. Savage, "Extraplanar Dust in the Edge-On Spiral NGC 891",
in: *The Astronomical Journal* 114 (Dec. 1997), p. 2463, DOI: 10.1086/118660,
eprint: astro-ph/9709197.

[157] J. Rossa et al.,
"A Hubble Space Telescope WFPC2 Investigation of the Disk-Halo Interface in NGC 891",
in: *The Astronomical Journal* 128 (Aug. 2004), pp. 674–686, DOI: 10.1086/422489,
eprint: astro-ph/0405401.

[158] P. B. Alton et al.,
"Deep Submillimeter Images of NGC 891-Cold Dust at Larger Galactic Radii",
in: *ApJl* 507 (Nov. 1998), pp. L125–L129, DOI: 10.1086/311692.

[159] S. Garcia-Burillo et al., "Molecular gas distribution and dynamics of the edge-on spiral galaxy NGC 891 - Discovery of a molecular halo", in: *A&A* 266 (Dec. 1992), pp. 21–36.

[160] J. N. Bregman and R. A. Pildis, "X-ray-emitting gas surrounding the spiral galaxy NGC 891",
in: *ApJ* 420 (Jan. 1994), pp. 570–575, DOI: 10.1086/173587.

[161] J. N. Bregman and J. C. Houck, "The Hot Gas Surrounding the Edge-on Galaxy NGC 891",
in: *ApJ* 485 (Aug. 1997), p. 159, DOI: 10.1086/304397.

[162] R. F. Temple, S. Raychaudhury, and I. R. Stevens,
"X-ray observations of the edge-on star-forming galaxy NGC 891 and its supernova SN1986J",
in: *MNRAS* 362 (Sept. 2005), pp. 581–591, DOI: 10.1111/j.1365-2966.2005.09336.x,
eprint: astro-ph/0506657.

[163] R. J. Allen, R. Sancisi, and J. E. Baldwin,
"Radio continuum observations of the edge-on disc galaxy NGC 891",
in: *A&A* 62 (Jan. 1978), pp. 397–409.

[164] A. W. Strong, "The radio halo of NGC 891", in: *A&A* 66 (May 1978), pp. 205–209.

[165] R. Beck et al., "Radio continuum observations of NGC 891 and NGC 253 at 8.7 GHz",
in: *A&A* 77 (Aug. 1979), pp. 25–30.

[166] U. Klein, R. Wielebinski, and R. Beck, "A survey of the distribution of 2.8 cm-wavelength radio continuum in nearby galaxies. V - A small sample of edge-on galaxies",
in: *A&A* 133 (Apr. 1984), pp. 19–26.

[167] E. Hummel et al.,
"The large-scale radio continuum structure of the edge-on spiral galaxy NGC 891",
in: *A&A* 246 (June 1991), pp. 10–20.

[168] S. Sukumar and R. J. Allen,
"Polarized radio emission from the edge-on spiral galaxies NGC 891 and NGC 4565",
in: *ApJ* 382 (Nov. 1991), pp. 100–107, DOI: 10.1086/170697.

[169] M. Dumke et al.,
"Polarized radio emission at 2.8cm from a selected sample of edge-on galaxies.",
in: *A&A* 302 (Oct. 1995), p. 691.

[170] D. D. Mulcahy et al.,
"Probing the Magnetic Fields of Nearby Spiral Galaxies at Low Frequencies with LOFAR",
in: *ArXiv e-prints* (Dec. 2011), arXiv: 1112.1300 [astro-ph.CO].

[171] R. J. van Weeren et al., "First LOFAR observations at very low frequencies of cluster-scale non-thermal emission: the case of Abell 2256", in: *A&A* 543, A43 (July 2012), A43, DOI: 10.1051/0004-6361/201219154, arXiv: 1205.4730 [astro-ph.CO].

[172] F. de Gasperin et al., "M 87 at metre wavelengths: the LOFAR picture",
in: *A&A* 547, A56 (Nov. 2012), A56, DOI: 10.1051/0004-6361/201220209,
arXiv: 1210.1346 [astro-ph.GA].

[173] E. Hummel, R. Beck, and M. Dahlem,
"The magnetic field structure in the radio halos of NGC 891 and NGC 4631",
in: *A&A* 248 (Aug. 1991), pp. 23–29.

[174] M. Soida et al., "The large scale magnetic field structure of the spiral galaxy NGC 5775",
in: *A&A* 531, A127 (July 2011), A127, DOI: 10.1051/0004-6361/200810763,
arXiv: 1105.5259 [astro-ph.GA].

[175] M. F. Bietenholz, N. Bartel, and M. P. Rupen, "Supernova 1986J Very Long Baseline Interferometry. II. The Evolution of the Shell and the Central Source",
in: *ApJ* 712 (Apr. 2010), pp. 1057–1069, DOI: 10.1088/0004-637X/712/2/1057,
arXiv: 1002.0304 [astro-ph.HE].

[176] N. Howarth, PhD thesis, University of Cambridge, 1990.

[177] I. M. Gioia, L. Gregorini, and U. Klein,
"High frequency radio continuum observations of bright spiral galaxies",
in: *A&A* 116 (Dec. 1982), pp. 164–174.

[178] F. P. Israel and J. M. van der Hulst,
"A radio continuum survey of nearby galaxies. I - Observations at 0.4, 0.8, 4.8, and 10.7 GHz",
in: *The Astronomical Journal* 88 (Dec. 1983), pp. 1736–1748, DOI: 10.1086/113465.

[179] P. C. Gregory and J. J. Condon,
"The 87GB catalog of radio sources covering delta between O and + 75 deg at 4.85 GHz",
in: *ApJs* 75 (Apr. 1991), pp. 1011–1291, DOI: 10.1086/191559.

[180] J. M. Stil et al., "The Integrated Polarization of Spiral Galaxy Disks",
in: *ApJ* 693 (Mar. 2009), pp. 1392–1403, DOI: 10.1088/0004-637X/693/2/1392,
arXiv: 0810.2303.

[181] I. Kazès, A. M. Le Squeren, and Nguyen-Quang-Rieu,
"Structure of Normal Galaxies at 2695 MHz", in: *Astrophysical Letters* 6 (July 1970), p. 193.

[182] D. S. Heeschen and C. M. Wade, "A radio survey of galaxies",
in: *The Astronomical Journal* 69 (May 1964), p. 277, DOI: 10.1086/109269.

[183] E. J. Hodges-Kluck and J. N. Bregman,
"A Deep X-Ray View of the Hot Halo in the Edge-on Spiral Galaxy NGC 891",
in: *ApJ* 762, 12 (Jan. 2013), p. 12, DOI: 10.1088/0004-637X/762/1/12,
arXiv: 1211.1669 [astro-ph.CO].

[184] A. Brandenburg, D. Moss, and A. Shukurov, "Galactic Fountains as Magnetic Pumps",
in: *MNRAS* 276 (Sept. 1995), p. 651.

[185] J. N. Bregman, "The galactic fountain of high-velocity clouds", in: *ApJ* 236 (Mar. 1980), pp. 577–591, DOI: 10.1086/157776.

[186] I. Bagetakos et al., "The Fine-scale Structure of the Neutral Interstellar Medium in Nearby Galaxies", in: *The Astronomical Journal* 141, 23 (Jan. 2011), p. 23, DOI: 10.1088/0004-6256/141/1/23, arXiv: 1008.1845 [astro-ph.CO].

[187] M. Hanasz, D. Wóltański, and K. Kowalik, "Global Galactic Dynamo Driven by Cosmic Rays and Exploding Magnetized Stars", in: *The Astrophysical Journal Letters* 706 (Nov. 2009), pp. L155–L159, DOI: 10.1088/0004-637X/706/1/L155, arXiv: 0907.4891 [astro-ph.GA].

[188] A. Shukurov et al., "Galactic dynamo and helicity losses through fountain flow", in: *A&A* 448 (Mar. 2006), pp. L33–L36, DOI: 10.1051/0004-6361:200600011, eprint: astro-ph/0512592.

[189] G. H. Heald, "Magnetic Field Transport from Disk to Halo via the Galactic Chimney Process in NGC 6946", in: *ApJl* 754, L35 (Aug. 2012), p. L35, DOI: 10.1088/2041-8205/754/2/L35, arXiv: 1206.6569 [astro-ph.CO].

[190] J. Kamphuis and F. Briggs, "Kinematics of the extended H I disk of NGC 628 - High velocity gas and deviations from circular rotation", in: *A&A* 253 (Jan. 1992), pp. 335–348.

[191] J. J. Condon, "A 1.49 GHz atlas of spiral galaxies with B(T) = +12 or less and delta = -45 deg or greater", in: *ApJs* 65 (Dec. 1987), pp. 485–541, DOI: 10.1086/191234.

[192] P. M. Marcum et al., "An Ultraviolet/Optical Atlas of Bright Galaxies", in: *ApJs* 132 (Feb. 2001), pp. 129–198, DOI: 10.1086/318953.

[193] R. A. Perley and B. J. Butler, "An Accurate Flux Density Scale from 1 to 50 GHz", in: *ApJs* 204, 19 (Feb. 2013), p. 19, DOI: 10.1088/0067-0049/204/2/19, arXiv: 1211.1300 [astro-ph.IM].

[194] R. Paladino, M. Murgia, and E. Orra, "Radio spectral index images of the spiral galaxies NGC 0628, NGC 3627, and NGC 7331", in: *A&A* 503 (Sept. 2009), pp. 747–754, DOI: 10.1051/0004-6361/200911870, arXiv: 0905.3643 [astro-ph.CO].

[195] R. A. Perley et al., "The Expanded Very Large Array: A New Telescope for New Science", in: *ApJl* 739, L1 (Sept. 2011), p. L1, DOI: 10.1088/2041-8205/739/1/L1, arXiv: 1106.0532 [astro-ph.IM].

[196] R. J. Sault and M. H. Wieringa, "Multi-frequency synthesis techniques in radio interferometric imaging.", in: *A&As* 108 (Dec. 1994), pp. 585–594.

[197] U. Rau and T. J. Cornwell, "A multi-scale multi-frequency deconvolution algorithm for synthesis imaging in radio interferometry", in: *A&A* 532, A71 (Aug. 2011), A71, DOI: 10.1051/0004-6361/201117104, arXiv: 1106.2745 [astro-ph.IM].

[198] P. Dutta et al., "HI power spectrum of the spiral galaxy NGC628", in: *MNRAS* 384 (Feb. 2008), pp. L34–L37, DOI: 10.1111/j.1745-3933.2007.00417.x, arXiv: 0711.1234.

[199] E. Sonbaş et al.,
"A search for supernova remnants in the nearby spiral galaxy M 74 (NGC 628)",
in: *A&A* 517, A91 (July 2010), A91, DOI: 10.1051/0004-6361/200913858,
arXiv: 1005.0149 [astro-ph.GA].

[200] D. A. Dale et al.,
"The Spitzer Local Volume Legacy: Survey Description and Infrared Photometry",
in: *ApJ* 703 (Sept. 2009), pp. 517–556, DOI: 10.1088/0004-637X/703/1/517,
arXiv: 0907.4722 [astro-ph.CO].

[201] M. L. Bernet, F. Miniati, and S. J. Lilly,
"The Extent of Magnetic Fields around Galaxies out to z ˜ 1",
in: *ApJl* 772, L28 (Aug. 2013), p. L28, DOI: 10.1088/2041-8205/772/2/L28,
arXiv: 1307.2250 [astro-ph.CO].

[202] A. H. Bridle et al., "Deep VLA imaging of twelve extended 3CR quasars",
in: *The Astronomical Journal* 108 (Sept. 1994), pp. 766–820, DOI: 10.1086/117112.

List of Figures

List of Tables